NBSIR 82-2484

Internal Strain, Deformation, and Failure of Large Scale Pullout Tests in Concrete

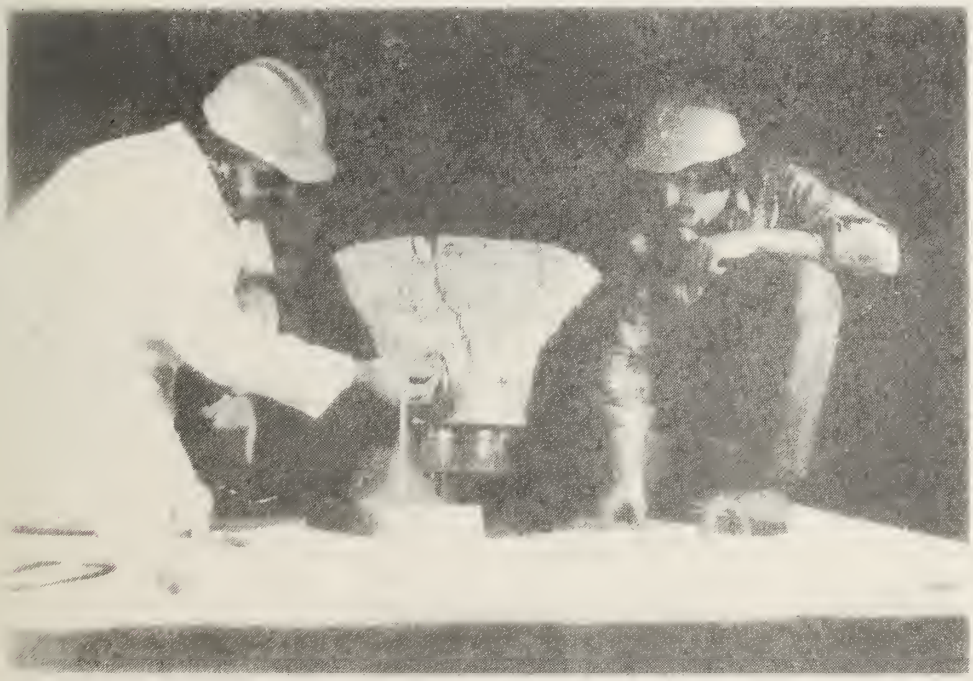

U.S. DEPARTMENT OF COMMERCE
National Bureau of Standards
National Engineering Laboratory
Center for Building Technology
Washington, DC 20234

March 1982

Issued May 1982

U.S. DEPARTMENT OF COMMERCE
NATIONAL BUREAU OF STANDARDS

NBSIR 82-2484

INTERNAL STRAIN, DEFORMATION, AND FAILURE OF LARGE SCALE PULLOUT TESTS IN CONCRETE

William C. Stone

U.S. DEPARTMENT OF COMMERCE
National Bureau of Standards
National Engineering Laboratory
Center for Building Technology
Washington, DC 20234

March 1982

Issued May 1982

U.S. DEPARTMENT OF COMMERCE, Malcolm Baldrige, *Secretary*
NATIONAL BUREAU OF STANDARDS, Ernest Ambler, *Director*

ABSTRACT

A study was performed to obtain detailed experimental data on crack propagation and internal strain distribution for the pullout test method for non-destructive strength evaluation of concrete. A 12:1 scaled-up pullout test was designed, using a commercial pullout insert for the prototype dimensions, and was instrumented with small waterproof embedment strain gages so as to obtain internal strain profiles at critical locations. Two large scale specimens were tested with apex angles falling at the upper and lower bounds currently recommended in ASTM C-900. Two dimensional axisymmetric finite element analyses were performed for the two experimental specimens and the results were compared with measured strains for load stages below the onset of internal cracking.

The results showed good correlation between the analytical and experimentally observed strains. The experimental data indicate that internal cracking, and the formation of the failure surface, are principally governed by the tensile strength of the concrete. The failure surface appears to be formed at 65 percent of ultimate load. Beyond this point, it is likely that the entire load is carried by the mechanism of aggregate interlock. Ultimate failure occurs when all aggregates mechanically bridging the failure surface pullout from the retaining cement paste. It is likely that the pullout test measures the shear strength of the cement paste or mortar which binds the concrete together.

Keywords: Concrete; crack propagation; failure surface geometry; failure theory; finite element method; internal strain; laboratory testing; large scale models; mathematical mode; pullout test; stress contours.

EXECUTIVE SUMMARY

A study was performed at the National Bureau of Standards to obtain detailed experimental data on crack propagation and internal strain distribution for method for non-destructive strength evaluation of concrete. A 12:1 scaled up pullout test was designed, using a common commercial pullout insert for the prototype dimensions, and was instrumented with small waterproof embedment strain gages so as to obtain strain profiles at critical locations. Two large scale concrete specimens were tested with apex angles falling at the upper and lower bounds currently recommmended in ASTM C 900. Two dimensional axisymmetric finite element analyses was performed for the two experimental specimens and the results were compared for load ranges below the onset of internal cracking.

The results of these tests indicate that there are two principal internal crack systems for the pullout test. Radial cracks form parallel to the vertical planes extending radially from the disk stem (r-z plane). These cracks initiate randomly along the circumference of the pulling stem at the top concrete surface and propagate away from the stem as a curved front towards the primary failure surface. Circumferential cracks form the primary failure surface--the outer surface of the pullout "cone". These cracks begin at the disk edge and propagate towards the reaction ring as the load is increased. Correlation between experimental and analytical studies have indicated that the circumferential failure surface very nearly follows the principal compressive stress trajectory from the disk edge to the reaction ring. This means that the principal tensile stresses act almost normal to the failure surface. Experimental data show that the compressive strains along this path are insufficient to cause failure of concrete by crushing, and additionally, that the tensile strains normal to the failure surface do substantially exceed the limiting tensile strain of concrete. Circumferential cracking is thus primarily governed by the tensile strength of the concrete. This, however, is not the principal strength property of concrete that is measured by the pullout test.

A study of the discontinuities (sharp changes in slope, or large strain excursions) in the load strain histories of the embedded strain gages revealed three distinct phases in the failure sequence of a pullout test. These occur between 30 to 40 percent of ultimate, 60 to 70 percent of ultimate, and from 80 to 100 percent of ultimate load. The three phases have been hypothesized in this report to constitute the initiation and propagation of circumferential cracking along the failure surface, completion of circumferential cracking along the failure surface, and a progressive ultimate failure by degradation of aggregate interlock across the failure surface. The second of these--that of completion of circumferential cracking--was experimentally shown to take place via propagation beginning at the disk edge and ending at the inside edge of the reaction ring. Completion of circumferential cracking occurs at approximately 65 percent of ultimate load, regardless of variation in apex angle. Beyond this load, the upward force is resisted by embedded sized aggregate particles mechanically bridging the circumferential failure surface. An idealized discrete failure model developed in this study, based on the assumption that failure occurs when all such aggregate particles shear through the retaining cement paste, gave ultimate load estimates that were encouraging. It is likely that the pullout test directly measures the shear strength of the cement paste which binds the concrete together.

ACKNOWLEDGMENTS

The author is greatly indebeted to Dr. Nicholas J. Carino for his persistent help in the experimental investigation and for his advice and counsel both in the planning of the project as well as the writing of this report.

Many thanks are extended to the technical staff of the laboratory, including Mr. Frank Rankin, Mr. Tom Ruschell, and Mr. Randy Williams, without whom the experimental investigation could not have been carried out.

Lastly, thanks are due to Dr. Kyle A. Woodward for making available the program TEXD used for data acquisition and reduction during the laboratory tests.

TABLE OF CONTENTS

ABSTRACT iii
EXECUTIVE SUMMARY iv
ACKNOWLEDGMENTS v
LIST OF TABLES viii
LIST OF FIGURES ix

1. Introduction 1

2. Procedure 9

2.1 General 9
2.2 Instrumentation 9

2.2.1 Micro Embedment Strain Gages 9
2.2.2 Slip Gages 18

2.3 Data Acquisition 25
2.4 Specimen Propagation 28
2.5 Loading System 37
2.6 In Place Strength of Concrete 41
2.7 Test Procedure 46

3. RESULTS 49

3.1 Load Deflection Curve 49
3.2 Shape of Failure Surface 53
3.3 Comparison of Experimental and Analytical Strain Distributions 53

3.3.1 Axial Strain 62
3.3.2 Radial Strain 62
3.3.3 Circumferential Strain 62
3.3.4 Vertical Strain Along Disk Edge 62
3.3.5 Radial Strain on Vertical Line Above Disk Edge 70
3.3.6 Radial Strain Along Disk Face 70

3.4 Elastic Behavior 70

3.4.1 Stress Contours 70
3.4.2 Principal Stress Profiles Along Failure Surface 76
3.4.3 Principal Stress Trajectories 76

3.5 Crack Propagation Analysis 88

3.5.1 Post Cracking Behavior 88
3.5.2 Discontinuity Histograms 94
3.5.3 Crack Propagation Sequence 100

TABLE OF CONTENTS (Continued)

		Page
4.	Discussion	107
	4.1 Failure Theory	107
	4.2 Aggregate Interlock Model	108
5.	Summary and Conclusions	115
	5.1 Failure Sequence	115
	5.2 Internal Strains	115
	5.3 Principal Stresses	117
	5.4 Failure Surface Shape	117
	5.5 Failure Mechanism	118
	5.6 Recommendations for Further Research	118
REFERENCES		120

LIST OF TABLES

Page

Chapter 2

2.1 Linear scale factors for direct modelling 10
2.2 Concrete mix specifications for as-placed material 37
2.3 Cylinder strength results 44

Chapter 3

3.1 Ranges in percent of ultimate load which mark pronounced changes ... 49
3.2 Ranges in percent of ultimate load of primary discontinuity zones observed by embedment gages 100

LIST OF FIGURES

Introduction

1.1 Schematic representation of the Pull-out test

1.2 Ottosen's finite element cracking analysis of the Pull-out test

1.3 Radial and Circumferential cracks in the Pull-out test

Chapter 2

2.0 Scale comparison between prototype and macro model

2.1 Steps in the fabrication of micro embedment gages

2.2 General view of instrumented pull-out disk showing, top to bottom: RV,RN (radial gages), TC (triaxial compression, radial) and CW (circumferential gages)

2.3 Close up view of RV (right) and RN (left) gages prior to casting

2.4 ET (edge tension) gages measure vertical strain along side face of disk

2.5 ANE (axial, north east quadrant) gages

2.6 Gages are wired to piano wire grid using flexible copper wire

2.7 Typical end detail for a circumferential gage string

2.8 Typical assembled gage strings ready for mounting on disk

2.9 Overall view of instrumented disk prior to casting

2.10 Slip wire details at disk connection

2.11 External hardware for slip gage

2.12 Alternate system for monitoring vertical displacement of disk

2.13 Pull-out insert specifications

2.14 Assembled loading tendon and pull-out insert (specifications)

2.15 Mating disk and loading head (with hydraulic jacks) prior to welding

2.16 Assembled loading tendon and pull-out insert (as built)

2.17 Supplemental reinforcement specifications

LIST OF FIGURES (continued)

2.18 As built supplemental reinforcement

2.19 Perforated angle frame used to support gage strings. Cross channel frame is used to stabilize and level disk prior to casting

2.20 Checking embedment gage resistance prior to casting

2.21 Jacking-Counter Pressure system (schematic)

2.22 Compression frame specifications

2.23 Jacking head and ram cluster specifications

2.24 Calibrating Jacking-Counter Pressure system

2.25 Seating Jacking-Counter Pressure system on hydrostone grout prior to leveling

2.26 Pre-tensioning loading tendon strands

2.27 Placing C.I.P.P.O.C.s in freshly cast specimen

2.28 Slave cylinders in temperature controlled water bath

2.29 Temperature histories in Pull-out specimen # 1

2.30 Temperature histories in Pull-out specimen # 2

2.31 Graphics terminal used to monitor real time strain profiles during testing of Specimens 1 and 2

2.32 Acoustic emmission device and amplifier used to provide advance warning of impending failure

2.33 Overall view of lab test set-up

Chapter 3

3.1 Vertical disk displacement vrs load, Specimen 1, $2\alpha = 70$

3.2 Vertical disk displacement vrs load, Specimen 2, $2\alpha = 54$

3.3 Normalized load deflection plot

3.4 Experimental macro pull-out "cones"

LIST OF FIGURES (continued)

3.5a Measured failure surface for Specimen 1, 2 α = 70

3.5b Measured failure surface for Specimen 2, 2 α = 54

3.6 Typical embedded strain gage history

3.7 2D axisymmetric finite element mesh for Specimen 1

3.8 2D axisymmetric finite element mesh for Specimen 2

3.9 Axial strain along (idealized) failure surface : experimental vrs FEM at P = 50 kips ; Specimen 1

3.10 Axial strain along (idealized) failure surface : experimental vrs FEM at P = 50 kips; Specimen 2

3.11 Radial strain along (idealized) failure surface : experimental vrs FEM at P = 50 kips; Specimen 1

3.12 Radial strain along (idealized) failure surface : experimental vrs FEM at P = 50 kips; Specimen 2

3.13 Circumferential strain along (idealized) failure surface: experimental vrs FEM at P = 50 kips; Specimen 1

3.14 Circumferential strain along (idealized) failure surface: experimental vrs FEM at P = 50 kips; Specimen 2

3.15 Vertical strain along disk edge: experimental vrs FEM at P = 50 kips; Specimen 1

3.16 Vertical strain along disk edge: experimental vrs FEM at P = 50 kips; Specimen 2

3.17 Radial strain along disk face: experimental vrs FEM at P = 50 kips; Specimen 1

3.18 Radial strain along disk face: experimental vrs FEM at P = 50 kips; Specimen 2

3.19 Radial strain along vertical line above disk edge: experimental vrs FEM at P = 50 kips; Specimen 1

3.20 Radial strain along vertical line above disk edge: experimental vrs FEM at P = 50 kips; Specimen 2

3.21 Maximum principal stress contours for Specimen 1

LIST OF FIGURES (continued)

3.22 Maximum principal stress contours for Specimen 2

3.23 Minimum principal stress contours for Specimen 1

3.24 Minimum principal stress contours for Specimen 2

3.25 Sigma Max (maximum principal stress) along failure surface (from axisymmetric FEM analysis)

3.26 Sigma Min (minimum principal stress) along fasilure surface (from axisymmetric FEM analysis)

3.27 Tau Max (maximum shearing stress) along failure surface (from axisymmetric FEM analysis)

3.28 Sigma Theta (circumferential stress) along failure surface (from axisymmetric FEM analysis)

3.29 Elastic state of stress along idealized failure surface

3.30 Principal stress trajectories for Specimen 1 (from axisymmetric FEM analysis)

3.31 Principal stress trajectories for Specimen 2 (from axisymmetric FEM analysis)

3.32 Elastic deformation of Specimen 1 at P = 50 kips (from axisymmetric FEM analysis)

3.33 Circumferential stress contour for Specimens 1 and 2 at P = 50 kips. (from axisymmetric FEM analysis)

3.34 Positive strain excursion indicating gage crosses crack surface

3.35 Negative strain excursion (reversal) indicating crack has gone around gage

3.36 Axial gage showing strain reversal -- crack has passed around gage, unloading it

3.37 Typical monotonic non-linear axial strain history

3.38 Discontinuity profiles for Specimens 1 and 2

3.39 Crack propagation sequence for Specimen 1

3.40 Crack propagation sequence for Specimen 2

3.41 Axial strain along failure surface (experimental) at ultimate load for Specimen 1

LIST OF FIGURES (continued)

3.42 Axial strain along failure surface (experimental) at ultimate load for Specimen 2

Chapter 4

4.1 Basis for aggregate shear failure calculations

4.2 Basis for calculation of n

4.3 Generalization of aggregate interlock failure

1. INTRODUCTION

The most critical period in the life of a reinforced concrete structure is during its construction. During this time the concrete is weak and, if unanticipated construction loads are applied, catastrophic collapse may occur. In the past the development of compressive strength of concrete in such structures has normally been determined by the testing of field cured specimens. However, it is now generally recognized that results obtained from such specimens may vary greatly from the in-place strength of the structure owing to different casting, compaction, and curing conditions. There exists, therefore, a need for a method to accurately measure the in-place strength of concrete.

In recent years the pullout test, initially proposed in the U.S.S.R. in 1934, has attracted much attention as a possible method for measuring in-place strength and a number of patents have been registered in various countries. In the U.S.A. Richards [17] has advocated the use of these tests on structural concrete members and a tentative standard method for such tests has been adopted by the American Society for Testing and Materials [22]. Briefly, a pullout test measures, with a specially constructed center pull tension jack which reacts against the concrete surface through a reaction ring of specified geometry, the force required to pull out a specially shaped steel insert (consisting of one or two pieces) whose enlarged end has been cast into the concrete. Because of its shape the steel insert pulls out a cone of concrete. The precise geometry of this "cone" is determined by a number of factors, including the diameter of the "disk" (enlarged portion), the depth of embedment, the diameter of the "stem" (pulling rod), and the diameter of the "counter-pressure" (reaction) ring which forms the base of the pulling apparatus (see figure 1.1). The method has a number of advantages over other methods for in-place strength evaluation. These advantages are:

1. The measurements are simple and easy to carry out.

2. It costs considerably less than other in-situ destructive tests, such as drilled cores.

3. The results are available within minutes after the test.

4. It is superior to other in-situ non-destructive methods such as the Rebound Hammer (ASTM C805) and the Windsor Probe (ASTM C803) because a greater depth and volume of concrete is tested. The pullout test is a direct measure of concrete strength, whereas the rebound Hammer and Windsor probe measure other properties that may be related to strength.

Contrasting these attributes it is generally noted that:

1. The pullout test must be planned in advance of concreting. Other methods, such as the Windsor Probe can be performed anywhere after the concrete has hardened.

2. The pullout test does not measure the strength of the interior of mass concrete because the typical insert usually does not extend further than

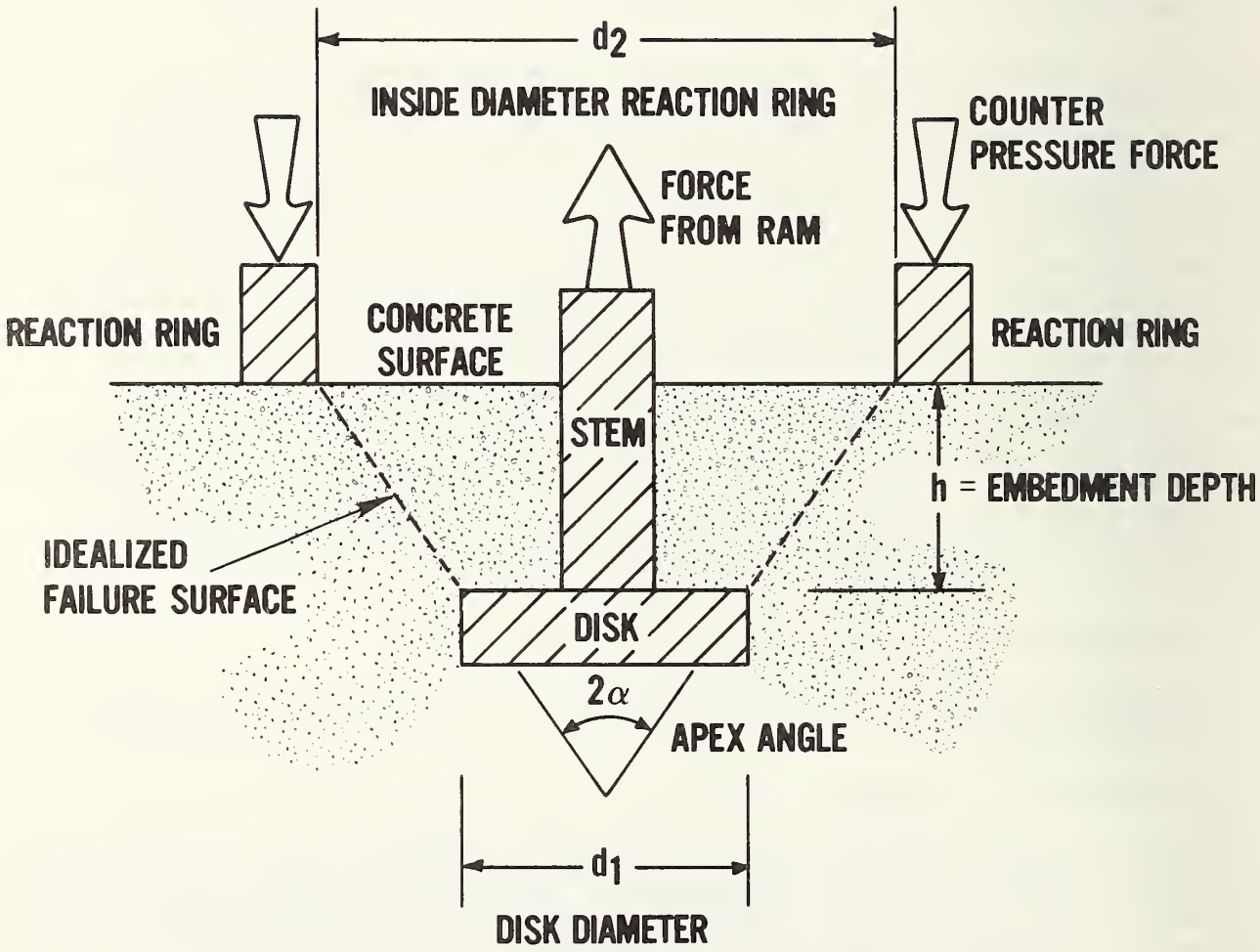

Figure 1.1 Schematic representation of pull-out test in concrete

1.5 inches (38 mm) below the surface. A novel technique for obtaining pullout measurements at greater depth has recently been proposed by Richards [8].

3. For accurate results it is presently recommended [6,22] that the relationship between the pullout strength and the compressive strength should be determined for each site and for each type of concrete and aggregate size. (For such calibrations the in-test variation of the pullout test is low and on the same order as for standard cylinder tests [6].) This requires development of a calibration curve before construction begins.

4. The resulting damage to exposed concrete surfaces must be repaired. It is still a non-destructive test since the structural member need not be discarded following the test.

The state of stress in the pullout test is complex and difficult to analyze. Considerable controversy has arisen over just what strength property of concrete is actually being measured, and what constitutes the physical mechanism of failure. Prior to 1975 it was generally believed that the concrete was simultaneously in tension and in shear [4], and it has been suggested that the pullout force is a measure of the direct shear strength of concrete. Alternatively, some believe[5] that the pullout test measures the punching shear strength of concrete and that the name should be changed to the Punching-Shear test. Interestingly, the Danish commercial version of the pullout test is called the Lok-Test; Lokning is Danish for punching. "Lok strength" was thus defined as the force required to punch out a small piece of concrete of specified geometry. In a recent survey of pullout tests conducted at a number of construction sites Bickley [6] reported a high degree of correlation between the pullout strength and the compressive strength of concrete. He went on to state that it is, therefore, likely that the pullout test measures a property of concrete which is either compressive strength, or has a constant relationship with compressive strength. Whatever the true strength property being measured is, it is clear that the pullout test, if it is to be widely accepted, must ultimately present its findings in the form of an equivalent compressive strength, since this is the basis of design. There are thus two avenues for improving the method: to determine the strength property being measured and develop a correlation between this strength property and the compressive strength; and to experimentally improve correlation with compressive strength by modifying the test. Using the latter technique Kierkgaard-Hansen [2] performed an extensive experimental investigation in Denmark during the 1960s. The results of this study indicated that by decreasing the apex angle (see figure 1.1), one could achieve a higher correlation between the pullout force and the compressive strength of concrete. This was achieved by varying the diameter of the counterpressure ring. Lacking a reaction device to control the upper diameter of the failure surface, a pullout specimen will fail in tension and exhibit a fracture surface with a trumpet shaped geometry rather than an approximately straight sided conic frustum. Kierkegaard-Hansen later adopted a fixed geometry with a 25 mm disk, 25 mm embedment depth, and a 55 mm I.D. reaction ring. Using this device, he established empirical equations for two concretes with differing aggregate sizes. These equations are now seeing wide commercial use in Europe. The questions of optimum geometry, the

reason for different equations for different aggregate sizes, and the ever debatable mechanism of failure gave rise to two important analytical works in the mid 1970s.

Jensen and Braestrup [1] showed by means of plasticity theory, that the pullout force is directly proportional to the compressive strength of concrete. Unfortunately, their analysis was based on a series of assumptions having questionable validity. First, there is some doubt that plasticity theory is applicable to an inherently brittle material, especially when tensile stresses are present as is the case of the pullout test. Secondly, their derivation assumes that concrete obeys the Mohr-Coulomb failure theory with a tension cut-off. The Mohr-Coulomb theory is not the most applicable failure theory for concrete subjected to multiaxial stresses [9,10,11]. Derivation further assumes that the state of stress on the assumed failure surface would result in "sliding" failure; the possibility of failure by separation is dismissed. There is no discussion on the actual stress state within the concrete during the test and, thus, there is no explanation of why "sliding" failure is the correct failure mode. Finally, it is assumed that the failure surface defines a conic frustum, whereas tests indicate that the failure surface is "trumpet shaped" [2]. These inconsistencies render their conclusion somewhat less convincing.

In a later study, Ottosen [7] analyzed the pullout test by means of an axisymmetric nonlinear finite element computer program. This analysis followed the progression of radial and circumferential cracking by means of an iterative smeared cracking procedure: small load increments were employed and at each step the state of stress was compared with a specified failure criterion for concrete. If cracking had occurred the iteration was repeated using the redistributed stress state until a stable crack configuration was achieved. Ottosen used both the Mohr-Coulomb failure criterion, as had Jensen and Braestrup, and a more accurate criterion which accounted for strain hardening and softening in the pre and post failure region, respectively. Failure was determined by lack of convergence after a specified number of interations. The analysis showed that circumferential cracks--the ones which form the surface of the pullout "cone"--begin at the disk edge at about 15 percent of ultimate and propagate towards the reaction ring with increased load. Furthermore, these cracks had reached to the reaction ring by 65 percent of ultimate load. Thereafter, Ottosen states that the load is carried by a "compression strut" (see figure 1.2)--a zone of uncracked concrete which extends from the disk to the reaction ring between two parallel circumferential cracks--and that ultimate failure is governed by compressive failure of this strut. From this he concluded that the pullout test directly measures the compressive strength of concrete. The analysis also indicated the formation of radial cracks which begin at low load levels at the intersection of the top concrete surface and the disk stem and propagate towards the the circumferential failure surface. These do not significantly influence the failure load since they form in planes perpendicular to the principal failure surface (see figure 1.3).

Ottosen's study is one of the most ambitious analytical attempts to date to resolve the internal behavior of the pullout test and the results are encouraging. However, a number of inconsistencies cast doubt on the basis for his primary conclusion: that the pullout test directly measures the compressive

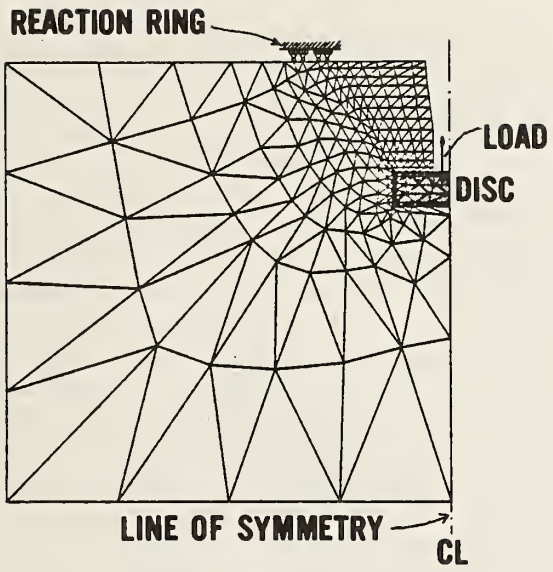

Figure 1.2a Ottosen's axisymmetric finite element mesh of the pull-out test

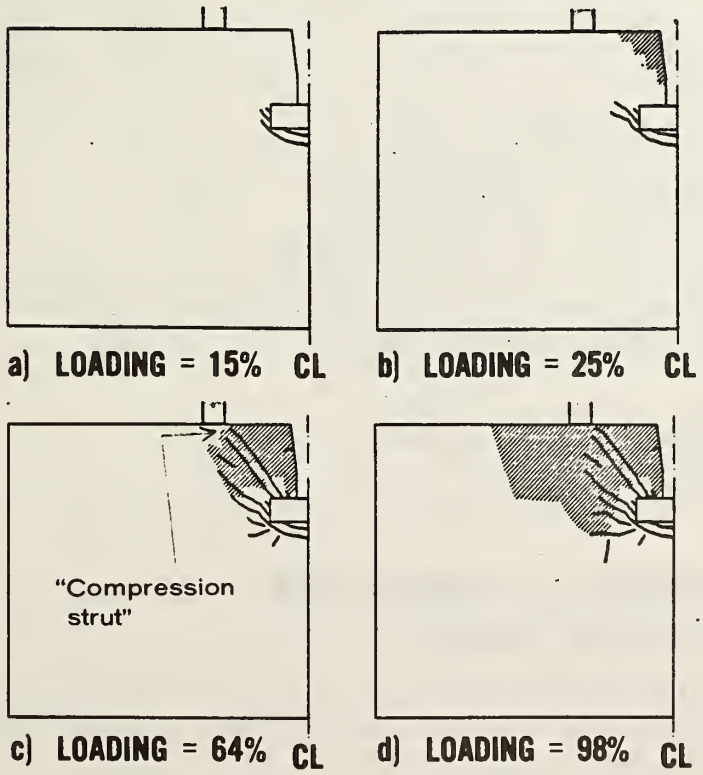

Figure 1.2b Crack development with increasing loadings. The loading is expressed in relation to the predicted failure load

Figure 1.2 Ottosen's finite element cracking analysis of the pull-out test

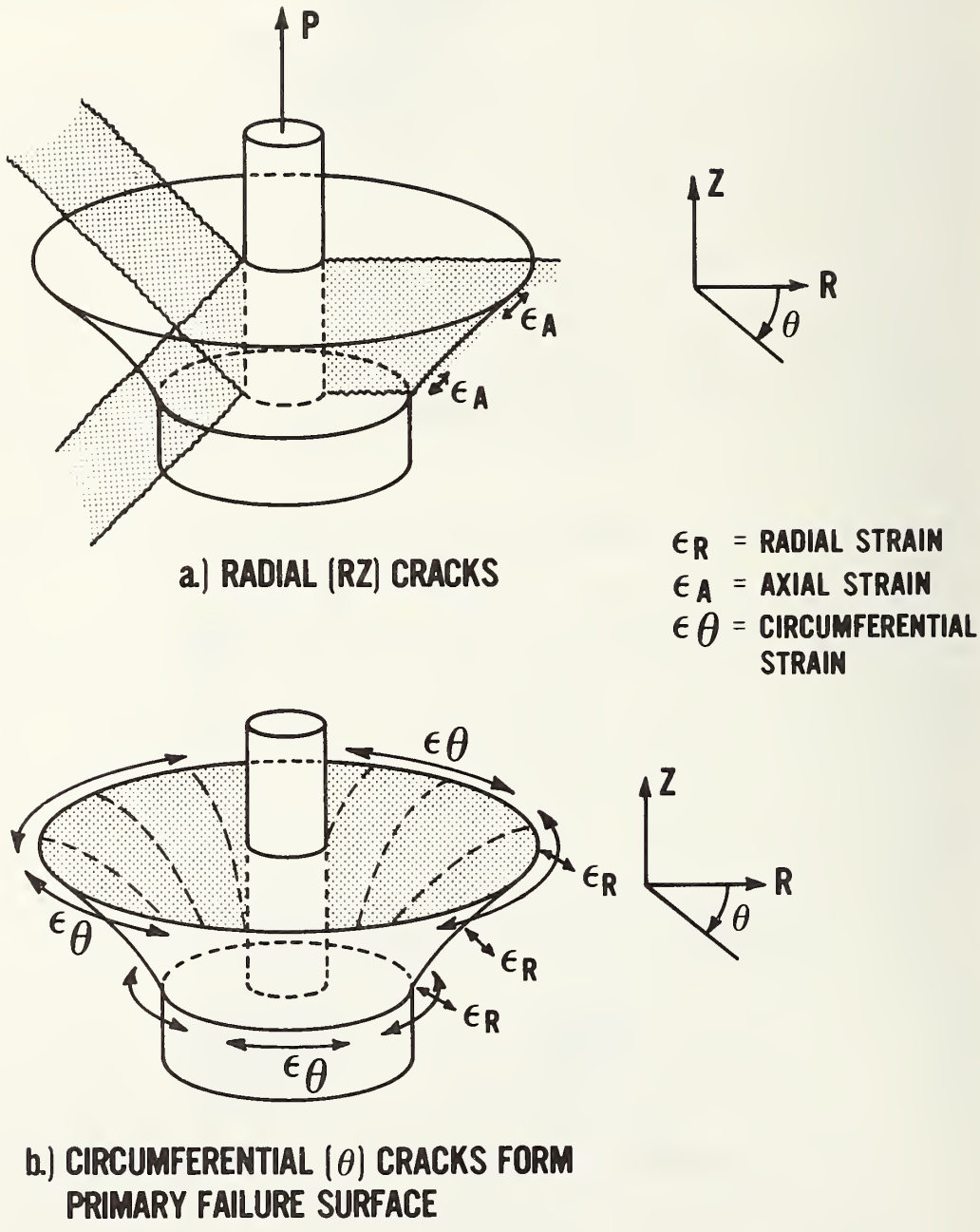

Figure 1.3 Radial and circumferential cracks in the pull-out test

strength of concrete. First, the model assumes perfect bond between the pullout disk and the surrounding concrete. This is an unlikely boundary condition, since most contractors coat the pullout inserts with oil prior to casting the concrete [8]. This serves as a bond breaker which would prohibit vertical load transmission through the side and bottom faces of the disk. The difference in the state of stress is significant. Lacking bond on the side and bottom faces, the load will be transmitted directly to a re-entrant corner in the concrete. Loading situation will give rise to a stress concentration in the concrete adjacent to the disk edge. Furthermore, no evidence of a compression strut failure has been detected in physical test. If such a compression strut did control failure, one would expect to find an annular frustum of crushed, powdered concrete sufficiently thick to have carried the ultimate load. For a typical commercial pullout test (reaction ring diameter: 2.16" (55 mm); disk diameter: 1" (25 mm); embedment depth: 1" (25 mm)) the thickness of such a strut would have to be on the order of 1/4 inch (6 mm) and it would be highly noticeable upon completion of the test. The fact that it is not present leads to the question: if the failure mechanism was incorrectly predicted by Ottosen's analysis, what assumptions and boundary conditions need to be modified for further study?

More imposing, however, can we use a continuum theory analysis to model the failure of the pullout test, or can it only be used up to a certain point before a discrete failure mechanism governs? An analytical model of a complex structure must be calibrated so as to reproduce both the actual internal strain distribution as well as the actual overall load deflection history if it is to have any validity. This can only be accomplished via calibration with known experimental data. No such internal strain or load deflection data on the pullout test existed at the time of Ottosen's study.

In order to provide an experimental basis for future analytical work and to gain an understanding of the failure mechanism during the pullout test it was necessary to perform a detailed experimental investigation on a level here-to-fore unattempted. The NBS study reported herein, sought to provide the following necessary data:

1. An experimental load-deformation history for the pullout test.

2. An experimental record of the internal strain distribution in the vicinity of the critical failure surface.

3. An experimental record of the internal crack propagation sequence as a function of load.

4. A comparison of the internally measured strains in the pre-cracked state with an axysymmetric linear elastic finite element analysis.

5. Experimental quantification of the change in the shape of the failure surface as a function of the apex angle.

Together with future experimental and analytical work to be performed in a second study, the ultimate objectives of the NBS investigation of the pullout are to answer the following questions:

1. What strength property of concrete is measured by the pullout test?

2. What modifications of the current standard test procedure are required to produce the most reliable results?

2. EXPERIMENTAL PROCEDURE

2.1 General

The primary impediments to gathering precise experimental data from "inside" a pullout test lay in the scale of the test subject. At present, the majority of the commercially available units have adopted about 1 inch (25 mm) diameter disk with an embedment depth of the same dimension. Operating within these geometric restrictions, instrumenting the specimens would prove difficult. To circumvent this obstacle a reverse-modelling procedure was employed. Scale modelling of structural systems in the laboratory is often utilized to increase the efficiency of an experimental investigation. Typically, the technique calls for a reduction in the size of the structure. For any given model, similitude requirements must be derived to relate the prototype to the model structure. If the requirements are accurately met the model can be tested and its results used to predict the behavior of the prototype. In direct modelling, where the material properties for the prototype and the model are the same, the prototype and model are related by only the linear scale factor, S_L. Table 2.1 shows the relationship generally adopted to relate the prototype properties to the model properties for the direct modelling case. The reverse (or "magnified") modelling procedure utilizes the same scale factors as shown in table 2.1, but S_L is now an integer rather than a fraction.

The object then was to "scale up" the prototype pullout test to the maximum possible degree, as this would facilitate the placement of the internal instrumentation. The "maximum degree" of scaling was limited primarily by cost considerations and available loading system components at NBS. The final scale adopted was 12:1 and the prototype dimensions were taken from a standard commercially available insert (see figure 2.0). This resulted in a pullout insert with a disk measuring 12 inch (305 mm) in diameter and 4 inch (102 mm) thick. The counterpressure ring had an inside diameter of 26 inch (660 mm). The depth of embedment, h, was varied so that the apex angles (see figure 1.1) for the two specimens tested fell at the upper and lower bounds specified in ASTM C900. Specimen #1 had h = 10" (254 mm) and specimen #2 had h = 13.5" (343 mm). For the lower limit of α =27° the pullout force was estimated at 900 kips (4005 kN) for concrete with a compressive strength of 4000 psi (27.6 MPa). This was considered to be the maximum desirable load while maintaining a sufficient safety factor on the loading apparatus.

2.2 INSTRUMENTATION

2.2.1 Micro-Embedment Strain Gages

To measure the internal strain distribution of the pullout test, it was necessary to develop a reliable method by which the strain could be monitored without disrupting the strain field. It was also desired to have a sufficient number of measurements along the critical path to completely define a particular strain profile between the disk edge and the counterpressure ring. This meant that the measuring device would have to be very small and capable of picking up the strain in the concrete; i.e. it would require a positive embedment in the concrete in such a manner as to preclude the possibility of slippage.

Table 2.1 Relationship Between Model and Prototype Structures (Direct Modeling Case)

Variable	K_1
Modulus of Elasticity	1
Strain, Stress	1
Linear Dimensions	S_L
Deformations	S_L
Pressure	1
Concentrated Load	$(S_L)^2$
Moment	$(S_L)^3$
Self-Dead Weight	$(1/S_L)$
Steel Reinforcement Area	$(S_L)^2$

S_L = Linear Scale Factor

Model Variable = K x prototype variable

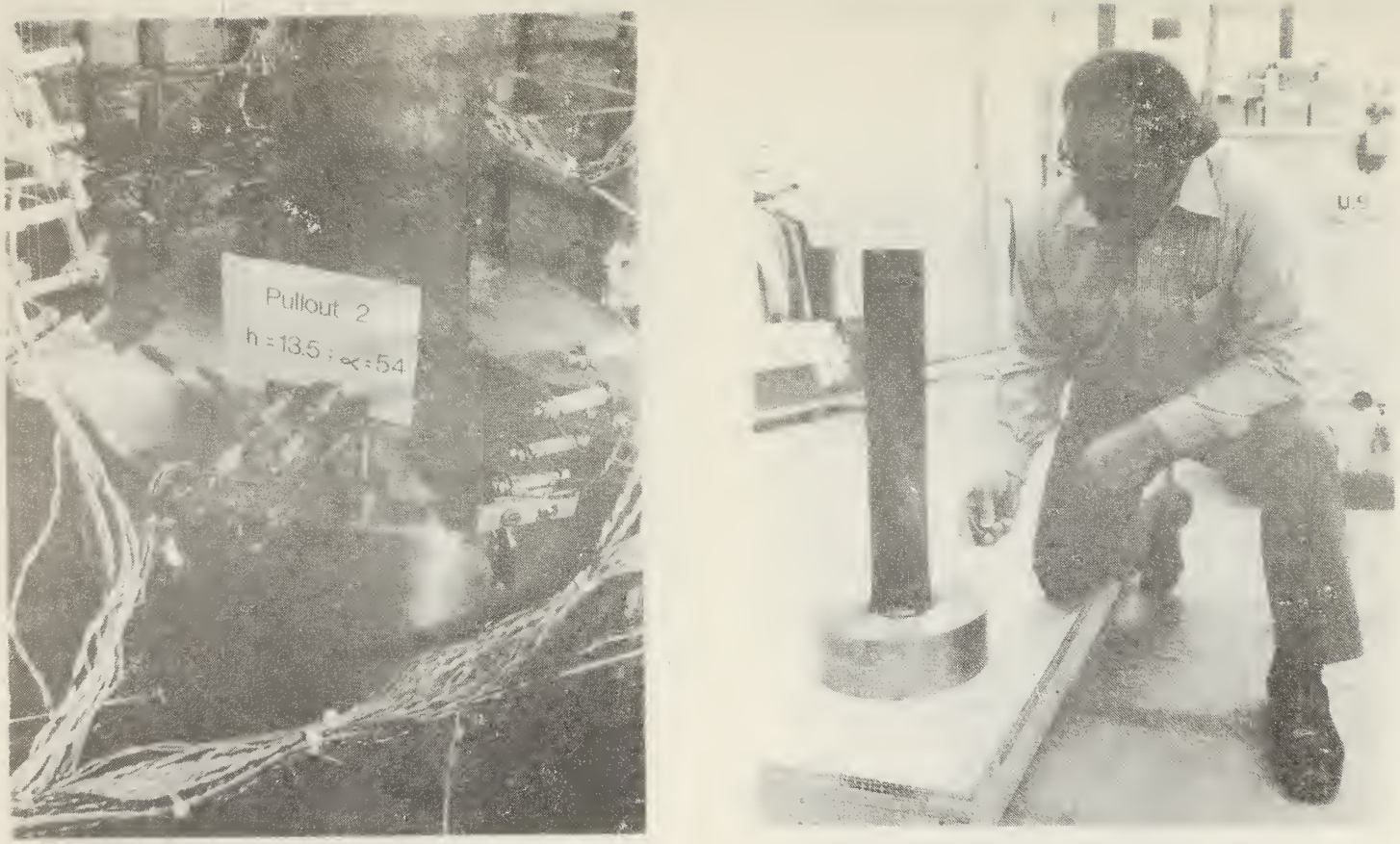

a) b)

Figure 2.0 Scale comparison between prototype commerciall pull+out insert and large scale

Figure 2.1a Begin fabrication with 70-75 TG aluminum rod, 1.25 inches long and 0.135 inch diameter

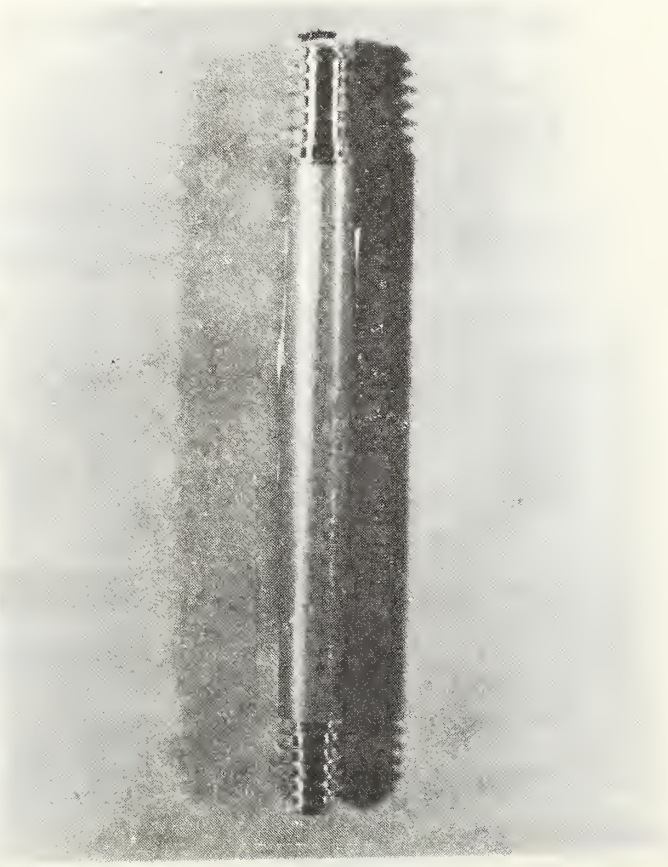

Figure 2.1b Thread end for 1/8 inch with 4-40 die

Figure 2.1 Fabrication of micro embedment gage

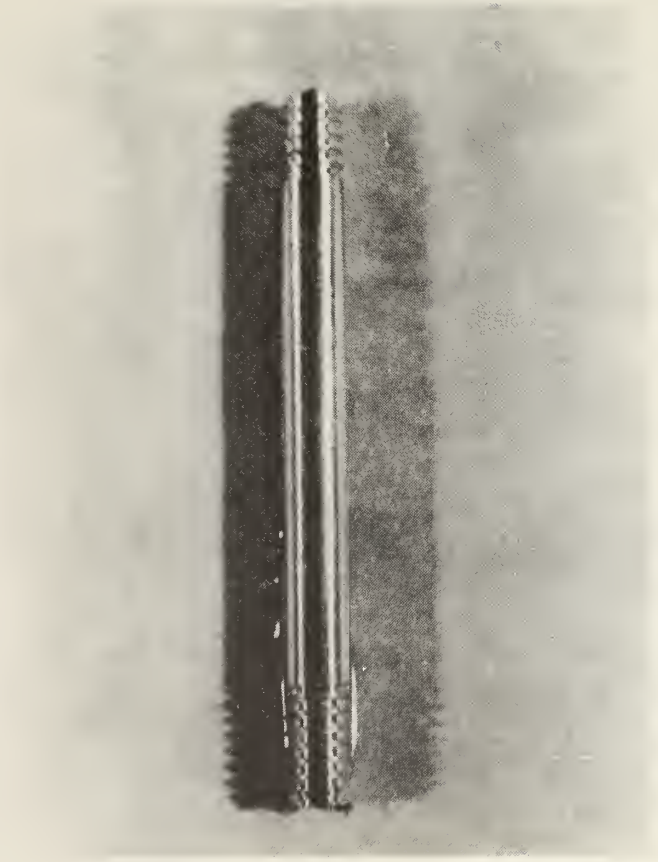

Figure 1.1c Prepare gaging surface with metal etching compound after fine sanding with emery cloth

Figure 1.1d Apply gage and lead tabs with high strength strain gage glue

Figure 2.1e Solder lead wires to soldering tabs

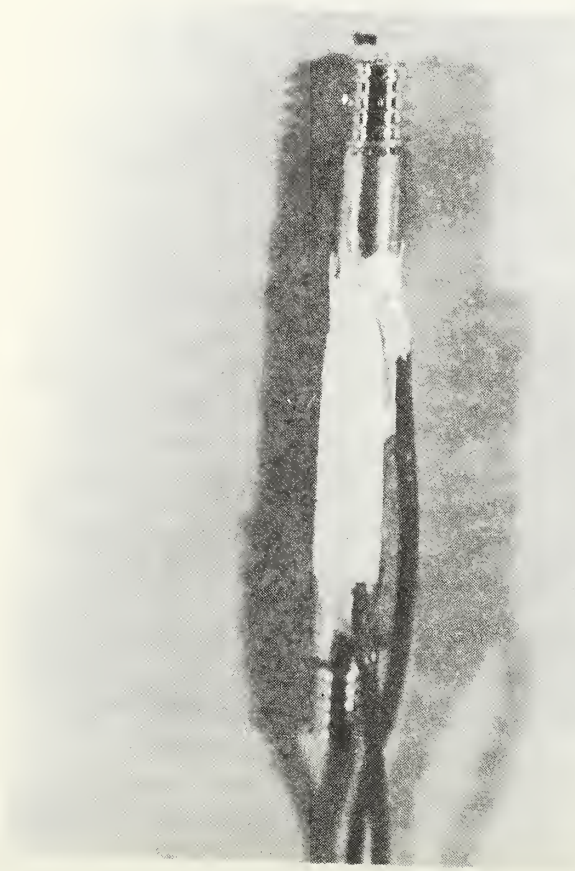

Figure 2.1f Apply coating of epoxy waterproofing compound to gage and lead tabs

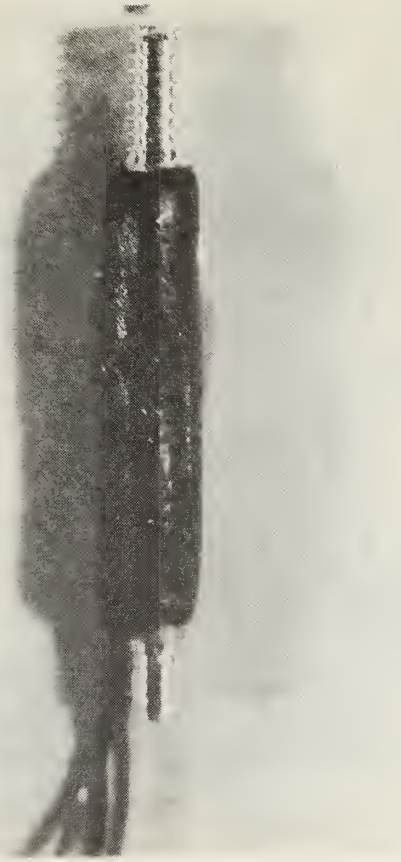

Figure 2.1g Apply thin layer of butyl rubber waterproofing compound over center portion of gage

Figure 2.1h Wrap butyl ruber with thin teflon sheet

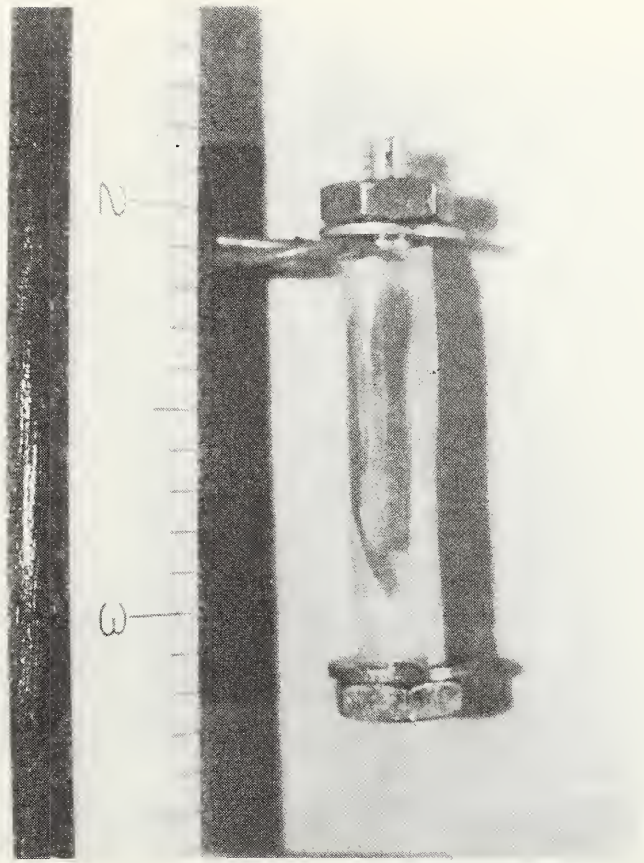

Figure 2.1i Insert gage into 1.25 inch length of 1/4 inch diameter heat shrink tubing and seal by heating. Attach nut and washer to each end

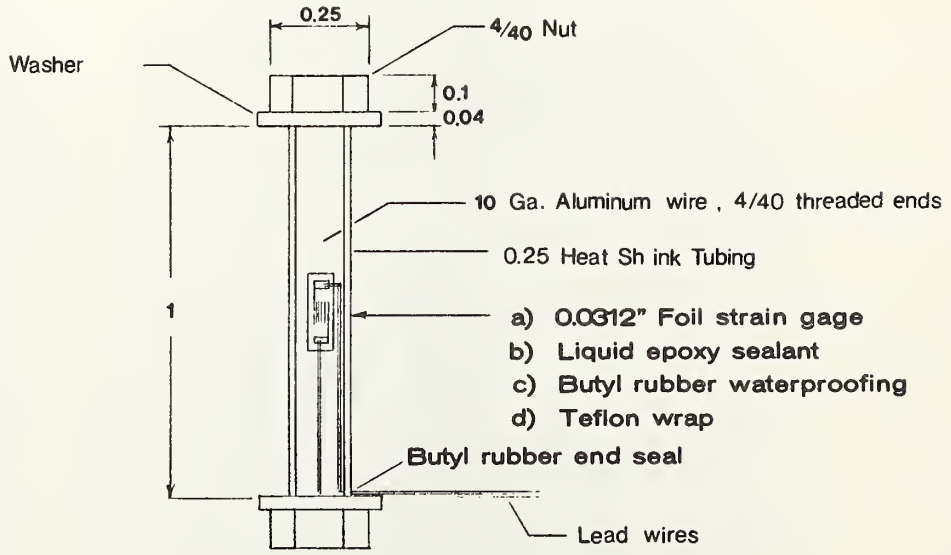

Figur 2.1j Schematic drawing of insert gage. All units are in inches

No such strain measuring devices were commercially available at the time of this study.

A simple micro-embedment strain gage was developed as shown in figure 2.1. The gage is composed of a foil strain gage bonded to an aluminum rod and represents a modified version of a similar gage first developed at the University of Texas at Austin by W.C. Stone [12]. To meet the requirement of negligible slippage, an enlarged anchor (consisting of a nut and washer assembly) was attached to each end of the aluminum rod. The length of the rod between these two anchors was 1 inch (25.4mm). Over this length the bond between the aluminum rod and the concrete was broken so that the foil gage measured the average strain in the concrete between the two end anchors. It should be noted that these gages measure only axial strain, parallel to the length of the rod. When linked to the data acquisition system described in section 2.3 the sensitivity of these gages was $\pm$6 microstrain. An extensive search of available foil strain gages showed that the smallest workable gages had a gage length of .031 inch (.78 mm) and a grid width of .032 inch (.81 mm). The backing was a flexible polyamide compound which permitted the foil gage to be glued to a round surface. Rigid backed foil gages using compounds such as bakelite should be avoided as they tend to crack when bent.

The foil gage was mounted on a 1.25 inch (32 mm) long, 0.130 inch (3.3 mm) diameter rod of 70-75 TG aluminum which was prethreaded for 1/8 inch (3.2 mm) on each end (see figures 2.1a through 2.1d). A two part methyl cyanoacrylate adhesive was used for the gluing. The foil gages were waterproofed with a liquid epoxy sealant after the lead wires had been soldered in place (see figures 2.1 e and f). The entire assembly was then encased in a thin shell of flexible butyl rubber barrier compound and overwrapped with teflon tape (figures 2.1g and h). A washer and nut (4-40 thread) were then attached on one end (where the lead wires exit) and the central portion of the gage was inserted into a 1-1/8 inch (28.5 mm) piece of 1/4 inch (6.35 mm) diameter heat shrink tubing which abutted against the washer. A heat gun was used to reduce this outer barrier so that a durable waterproof shell now encased the gage. The washer and nut for the opposite end were then screwed on until snug and the gage was tested to ensure proper electronic functioning.

Before committing the embedment gages to use in the model specimens, a number of trial runs were performed. Two 3 inch (76 mm) x 6 inch (152 mm) mortar cylinders were instrumented with a gage positioned parallel to the longitudinal axis in the center of each cylinder. The cylinders were loaded in a standard compression testing machine and the strain recorded using a manually balancing indicator at successive load stages. Likewise, two splitting tension tests were performed with internal gages oriented perpendicular to the splitting plane. Both types of tests exhibited acceptable linear behavior in the gage response.

When placed in the model these embedment strain gages can be classified into three primary categories: (a) "radial" gages, oriented perpendicular to the side of the conic frustum defined by the outer disk edge and the inner reaction ring edge, and parallel to the R-Z plane (figure 1.3); (b) "axial" gages, oriented tangent to the side of the same conic frustum and parallel to the R-Z

plane; and (c) "circumferential" gages, oriented tangent to the conic frustum but perpendicular to the R-Z plane. Figures 2.2, 2.3, 2.4, and 2.5 illustrate the different orientations. Additional gages were placed so as to monitor strains near the side and top faces of the disk, where first cracking was anticipated.

In order to define a particular strain profile it was necessary to have a string of closely spaced gages suspended along the orientation of interest. This was accomplished by attaching the gages with soft copper wires to a grid constructed from .016 inch (.4mm) stainless steel piano wire, as shown in figure 1.6. Each end of the grid was soldered to a brass bar measuring 2 inch (51 mm) by 1/2 inch (13 mm) by 1/8 inch (3.2 mm), which was machined so that it could be bolted to attachment points on the disk edge. Figure 2.7 shows the the brass end bar with additional hardware for achieving circumferential gage orientations. Typical assembled gage strings, ready for placement in the specimen, are shown in figure 2.8. An overall view of instrumented specimen #2 is presented in figure 2.9.

2.2.2 Slip Gages

In order to measure the load-deformation history of the pullout test, a method had to be devised to monitor the displacement of the disk with respect to its original position. Since the concrete surface above the disk would undergo deformation, the top concrete surface could not be used as an accurate a reference place for displacement measurements. Similarly, the stroke on the hydraulic ram loading system could not be used as a measure of disk movement since this includes the elastic deformation of the tendon transmitting the load to the disk. The method finally adopted was originally proposed by J. O. Jirsa [13] and has been used extensively at the University of Texas at Austin for measuring the absolute displacement of anchor bolts and the relative displacement of reinforcing bars used in splices. The device is known collectively as a slip gage, but really consists of about half a dozen commonly available parts.

For this study, the technique involves mounting a 0.045 inch (1.1 mm) diameter piano wire near the base of the disk as illustrated in figure 2.10. To do this, a 1/4 inch (6.35 mm) deep hole (approx. 0.046 inch (1.17 mm) diameter) is first drilled into the side of the disk, a 90° bend is placed in the end of the piano wire, the wire cleaned with a piece of emery cloth, and finally the bent portion is bonded into the hole with epoxy cement. This then, provides a positive mechanical attachment to the disk. The wire is encased in a snug fitting teflon sheath to prevent bonding to the cast concrete. The encased wire is then guyed into place so tat it leaves the disk parallel to the vertical axis (the anticipated direction of displacement), forms a smooth curve, and exits through the side of the specimen perpendicular to the face. As the disk displaces upwards, the wire will be drawn in from the side face by the same amount. A threadbar anchor is installed on the side form approximately 4 inch (102 mm) from the exit point of the slip wire. This is later used to mount the external instrumentation.

After casting and form removal, the exposed slip wires are trimmed to 1.25 inch (32mm) length and placed in tension by means of a spring loaded block which is

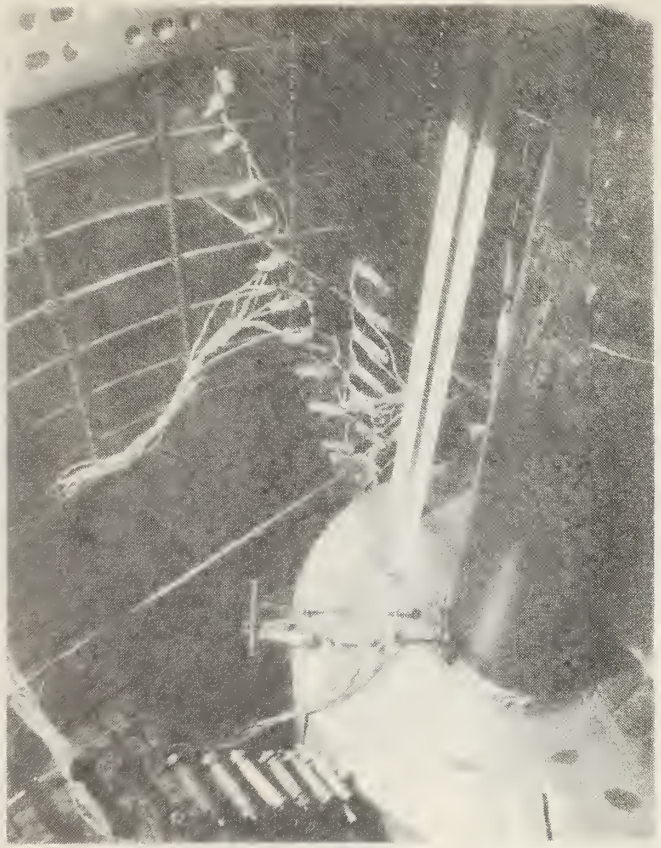

Figure 2.2 General view of instrumented pull-out disk showing, top to bottom: RV, RN (radial gages), TC (triaxial compression, radial), and CW (circumferential) gages

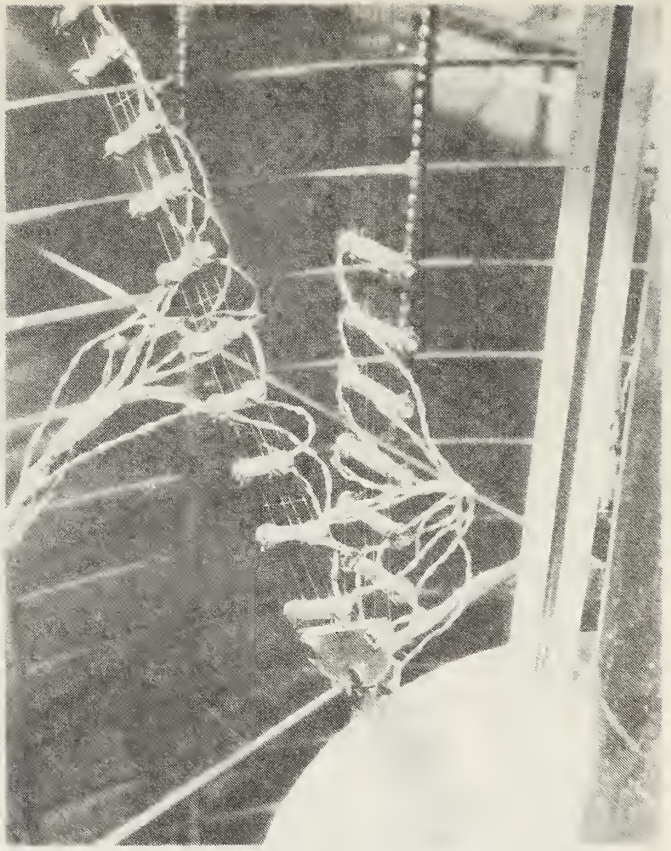

Figure 2.3 Close up view of RV (right) and RN (left) gages prior to casting

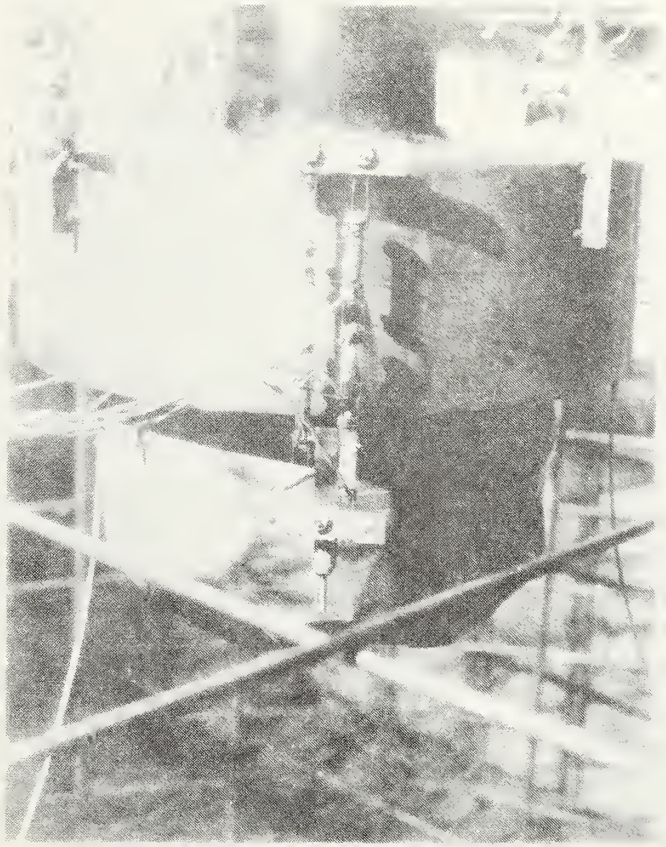

Figure 2.4 ET (edge tension) gages measure vertical strain along side face of disk

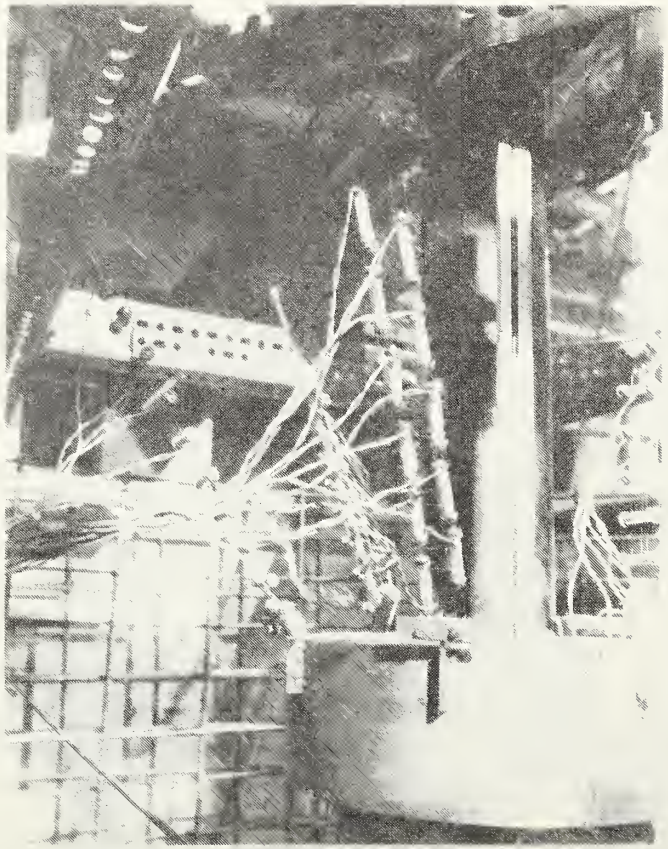

Figure 2.5 ANE (axial, northeast) gages measure compressive strain along the failure surface

Figure 2.6 Gages are wired to piano wire grid using soft copper wire

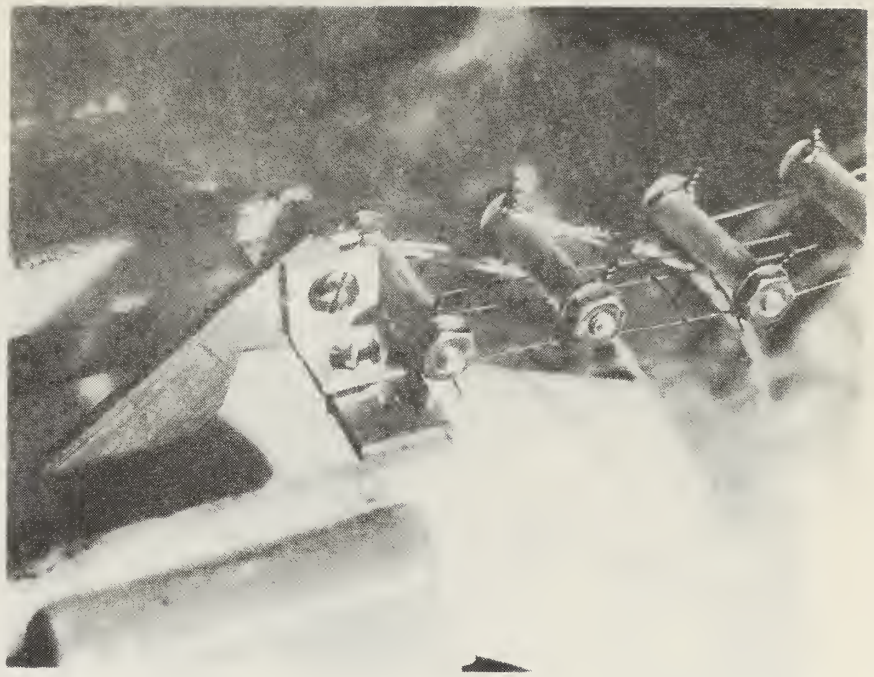

Figure 2.7 Typical end detail for a circumferential gage string

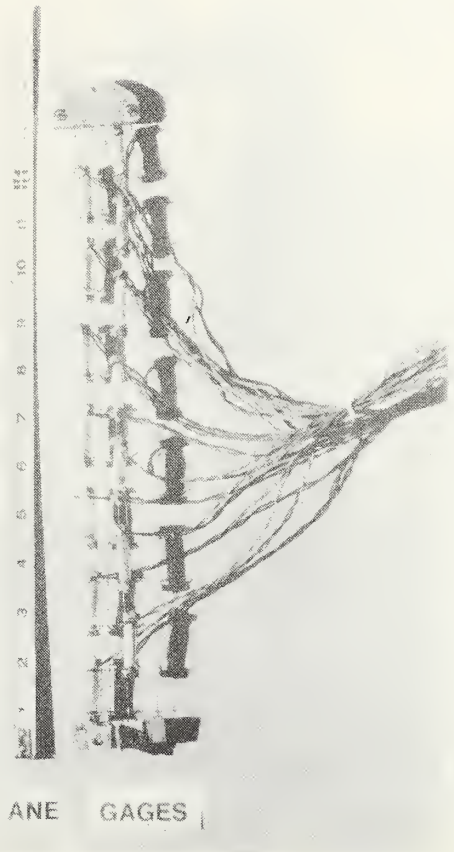

a) ANE gages

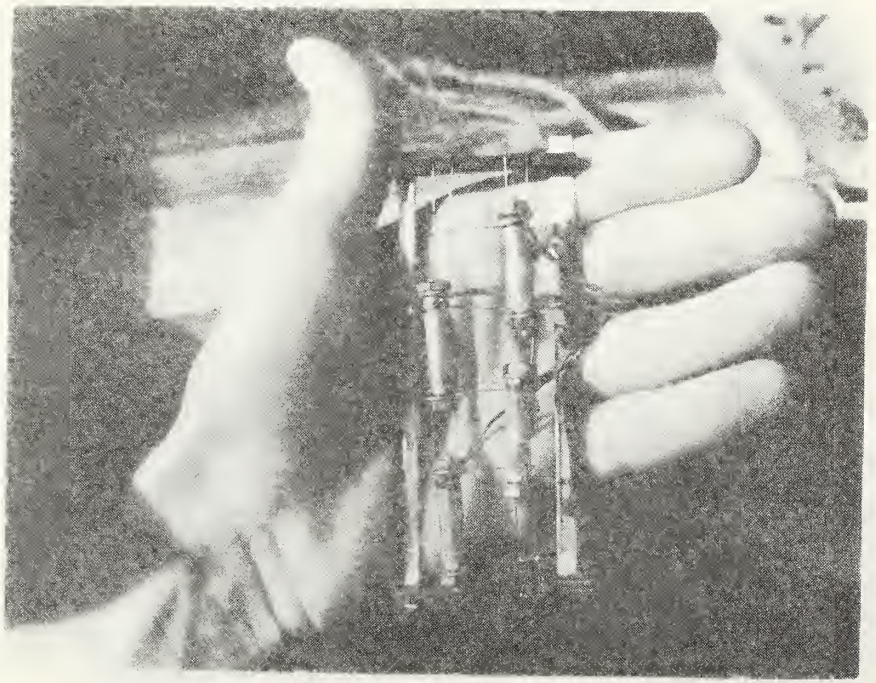

b) TC gages

Figure 2.8 Typical assembled gage strings ready for mounting on disk

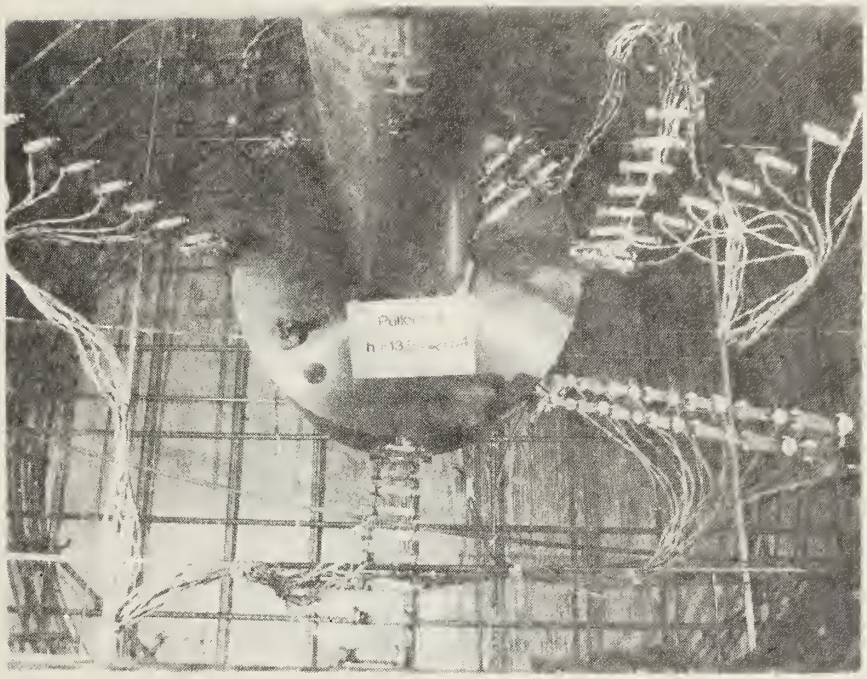

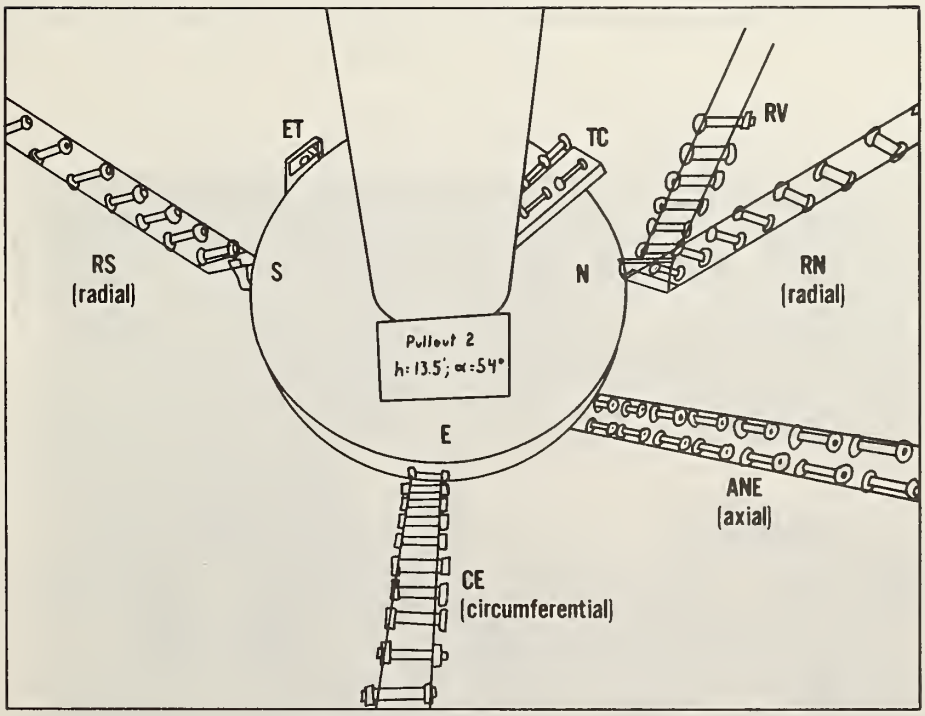

Figure 2.9 Overall view of instrumented specimen prior to casting

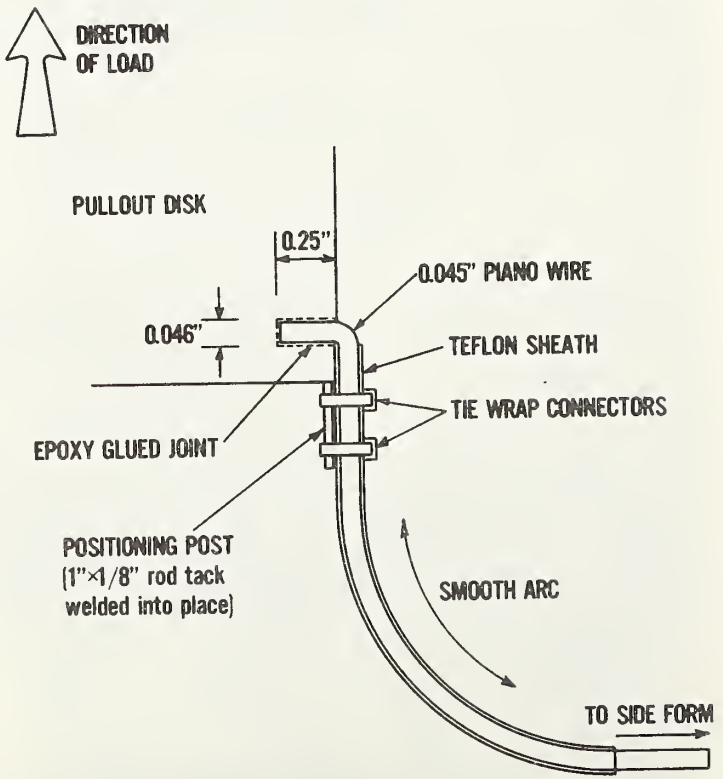

Figure 2.10 Slip wire details at the disk connection

securely clamped onto the end of the wire. This ensures that there will be no slack in the line and permits both "positive" (IN) and "negative" (OUT) displacement to be measured. The motion of the wire is measured to .0001 inch (.0025 mm) accuracy using a spring loaded linear voltage displacement transducer (LVDT). The LVDT is positioned using a clamping block attached to a support rod which has been screwed into the threadbar anchor in the side of the specimen. Figure 2.11 shows the external details of the slip gage mechanism.

As a backup to the primary slip gages (three were mounted on 120° arcs around the circumference of the disk on both specimens) two LVDT's measured the displacement of the "stem" of the pullout assembly with respect to the counterpressure ring base. This was accomplished by mounting the LVDT's on long bars that had beeen welded to the "stem" 4 inch (102 mm) above the concrete surface (figure 2.12). The two LVDT's were mounted 180° opposite one another to negate any errors due to lateral bending of the stem.

2.3 DATA ACQUISITION

Each specimen contained a total of 79 physical data channels--71 embedment strain gages, 5 displacement transducers (LVDTs), two 10,000 psi (69 MPa) pressure transducers and a 6 volt system excitation voltage. Manual monitoring was deemed prohibitive for all but a few key channels--primarily the pressure transducer readings from which the load was monitored. Automated data acquisition centered around a NEFF 620 unit driven by a PDP11 minicomputer. The advantage of this system lay in its speed: with a scan rate of 50,000 hertz the entire data set could be read in less than 2/1000 of a second. The data was stored on a 2.5 million word RK05 high speed removable diskpack and later transferred to a 9 track 1600 BPI magnetic tape.

Additionally, it was desired to be able to monitor--in real time--the strain profile along particular gage strings at various load stages. An interactive graphics/real time data reduction package known as "TEXD," written by K.A. Woodward of the NBS Structures Division, was utilized in conjunction with the data acquisition system mentioned above. This program represents a major advancement over previously available technology and permitted the unique capability of reviewing the test results in reduced form while the test was *still in progress*. In the interactive mode, graphics plots could be obtained on a Tektronics 4014 using predefined plot files which had been generated for each gage string. By obtaining a hard copy of the plot a direct comparison of what was happening inside the specimen (reduced to units of microstrain) could be made with an analytically derived (linear elastic) strain distribution. During the precracking load stages, it was thus possible to isolate anomalies in the experimental data and identify possible malfunctioning gages or wiring problems before going past the "point of no return"--internal cracking. This was of major importance since, due to the high cost of each test, it was desirable to minimize the number of erratic or malfunctioning gages. A number of bad channels--caused primarily by malfunctioning plug-in IC cards in the acquisition system--were thus detected, and corrected, prior to loading the specimen to first cracking. It should be noted that these bad channels would have gone unnoticed were it not for the graphics plots, since the gages exhibited correct electronic functioning where the wires exited the specimen.

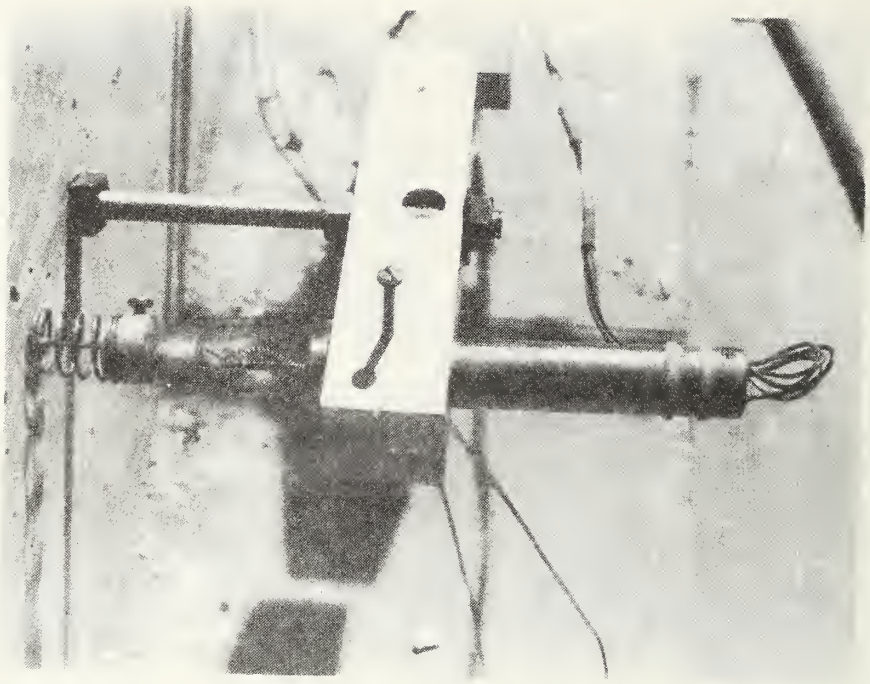

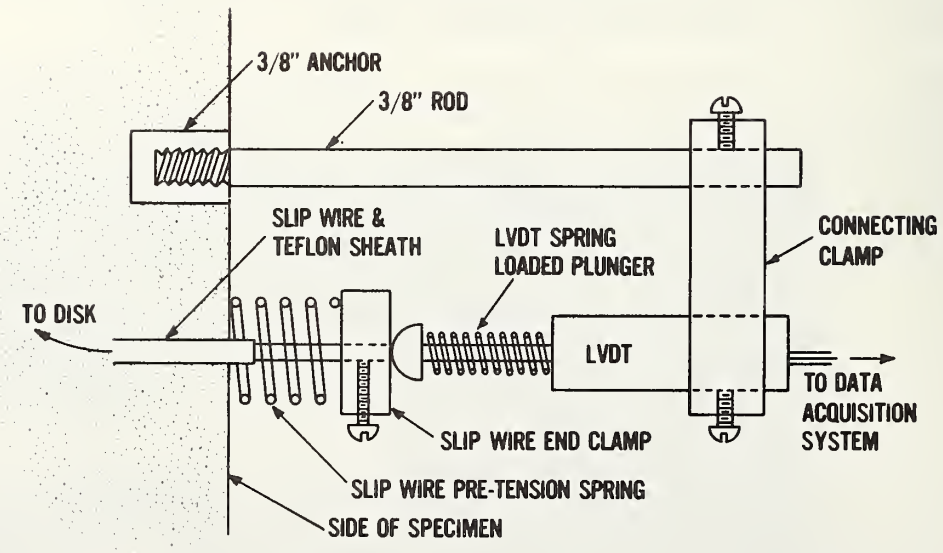

Figure 2.11 External hardware for slip gage

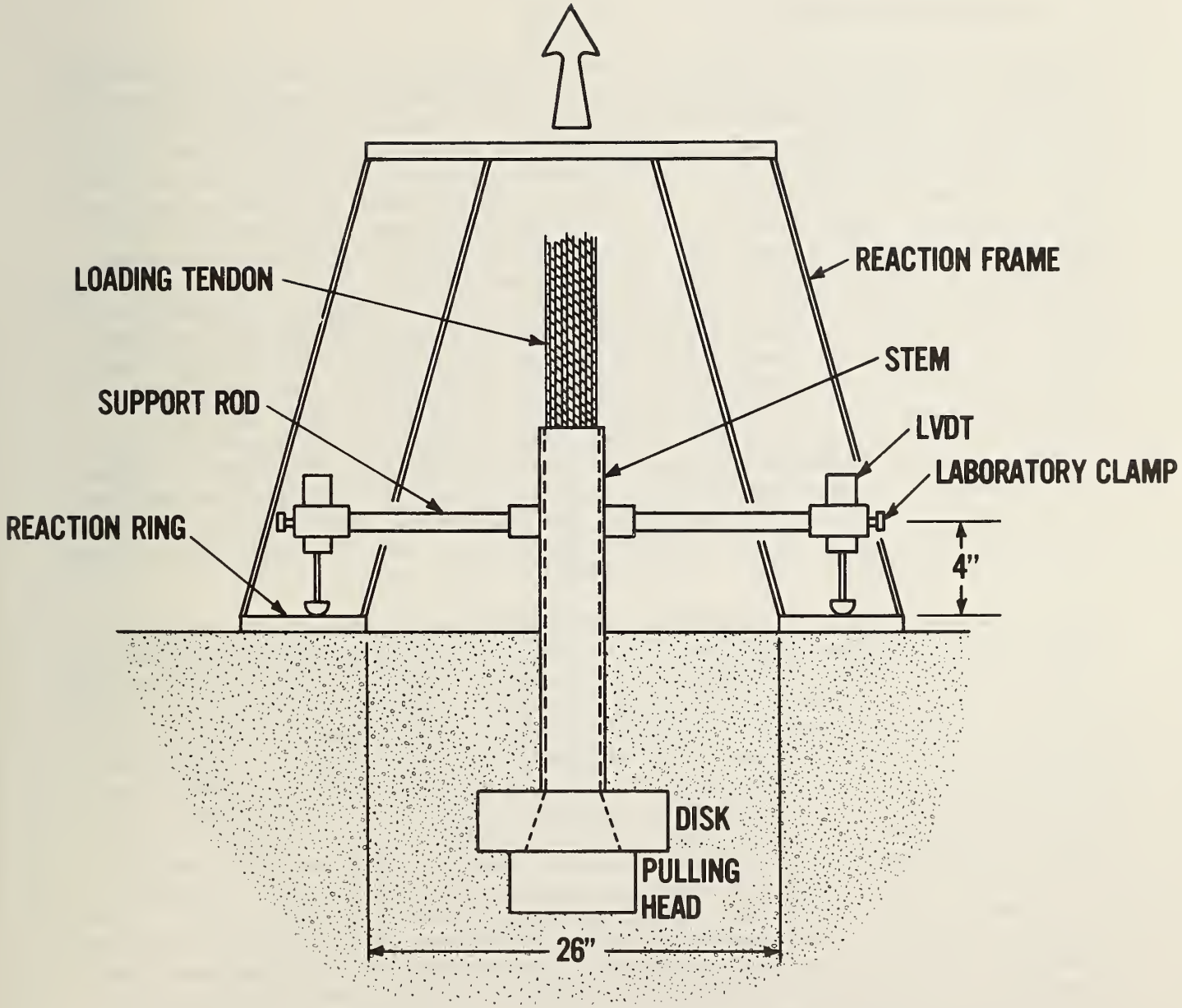

Figure 2.12 Alternate system for monitoring vertical displacement of disk

2.4 SPECIMEN PREPARATION

The central feature in each specimen was the pullout "disk" and "stem" assembly. The disk was machined from A36 mild steel to the dimensions shown in figure 2.13. A 3-1/2 inch (89 mm) diameter standard pipe (4.0 inch (102 mm) OD) was welded to the top of the disk to achieve the external geometry that was called for in the 12:1 scaled-up model. It should be noted, however, that there was a significant difference between the inner workings of the model test and actual commercial insert. Most commercial pullout inserts utilize a tapered mild steel stem for positioning of the disk during casting. Prior to testing this stem is removed--unscrewed--and a high strength (usually with f_y > 120 ksi (828 MPa)) pulling rod inserted for the subsequent load test. To utilize this same technique in the scaled-up model would have required a threaded 120 ksi (828 MPa) rod 4 inch (102 m) in diameter and 83 inch (2.1 mm) long. Price quotes ranged between $10,000 and $15,000, which was deemed prohibitive. An alternative solution--by machining a tapered hole in the bottom of the disk so that a 270 ksi (1863 MPa) post-tensioning tendon (31-1/2 inch 13 mm) diameter 7 wire strands) could be threaded through the pipe and up through the loading system to a standard 31 strand post-tensioning pulling head--allowed for transmission of the load at a substantial saving of time and funds. The tendon was anchored to the disk via a standard 31 strand pullling head, with the individual strands having been pre-seated (with conical chucks) at the factory.

Since it was desirable to maintain a low profile behind the disk, the preset pulling head was welded directly to the bottom of the pullout disk (figure 2.14). Due to the sharp curvature imposed on the outer tendons--a commercial 31 strand anchor normally requires a 34 inch (863 mm) funneling distance, compared with the 4 inch (102 mm) used here--it was necessary to jack the two pieces together (figure 2.15) before the weld could be applied. Even though all internal surfaces had been machined and ground to effect a smooth transition between the pulling head and the pipe, industry spokesmen cautioned of the possibility of shearing prematurely the outer strands at high loads. On this basis the mix design strength of the concrete was lowered from f'_c = 4000 psi (27.6 MPa) to f'_c = 2500 psi (17.25 MPa) and the tests were carried out without difficulty. The assembled disk, stem, and loading tendon are shown in figure 2.16. It was tacitly assumed that the presence of the loading head below the disk would not adversely affect the state of stress along the critical failure surface. Additionally, the composite thickness (8 inches) of the disk and loading head is within the current allowable limit of 0.5 times the diameter of the disk as specified in ASTM C-900.

The dimensions of the cast concrete specimen measured 80 inch (2 m) square and 48 inch (1.2 m) high. This was approximately a 12:1 scale up from specimen dimensions originally used on a pilot test by Kierkegaard-Hansen [2]. Later tests by many researchers utilized standard 6 inch (152 mm) x 12 inch (304 mm) cylinders with the pullout inserts embedded in one or both ends. Adopting a 12:1 scale for this situation would have called for a scaled-up specimen measuring 12 ft (3.7 m) in height! A somewhat more workable figure of 48 inch (1.2 m) was arbitrarily assigned. In essence the size of the specimen needed only to be large enough to suppress any perturbations in the vicinity of the failure surface that might be induced by the specimen's boundary geometry.

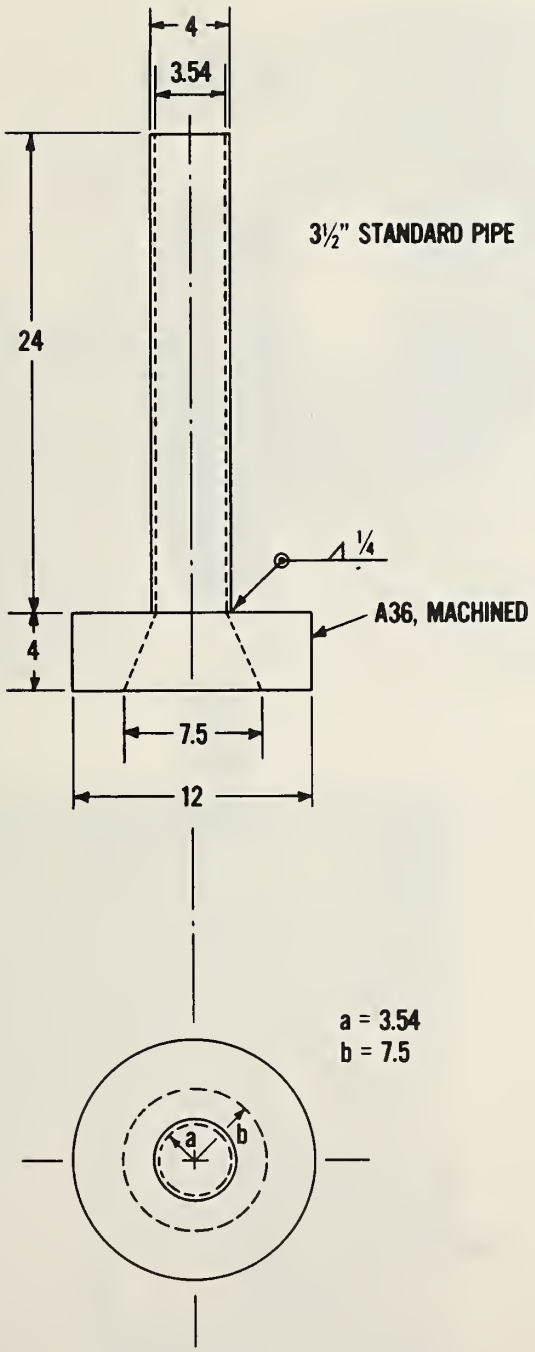

Figure 2.13 Pull-out insert specifications (all units inches)

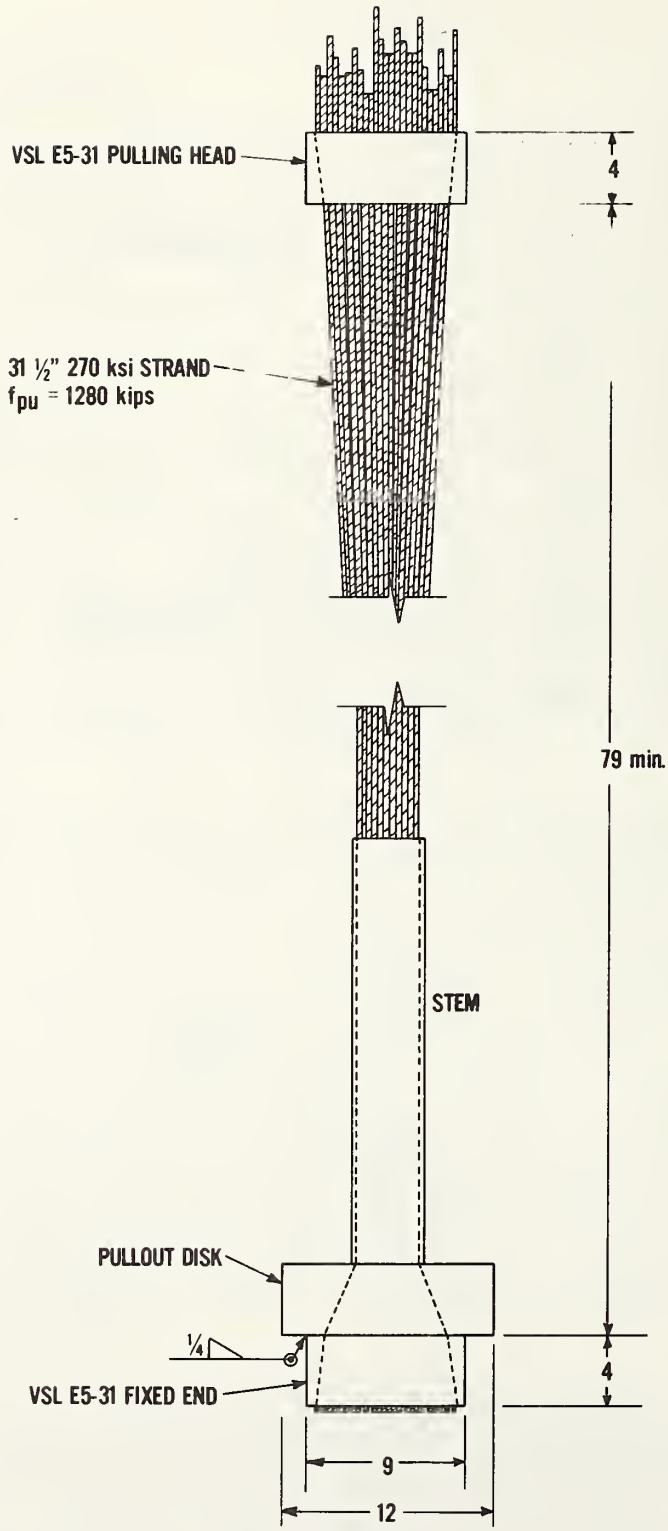

Figure 2.14 Assembled loading tendon and pull-out insert (specifications) (all units inches)

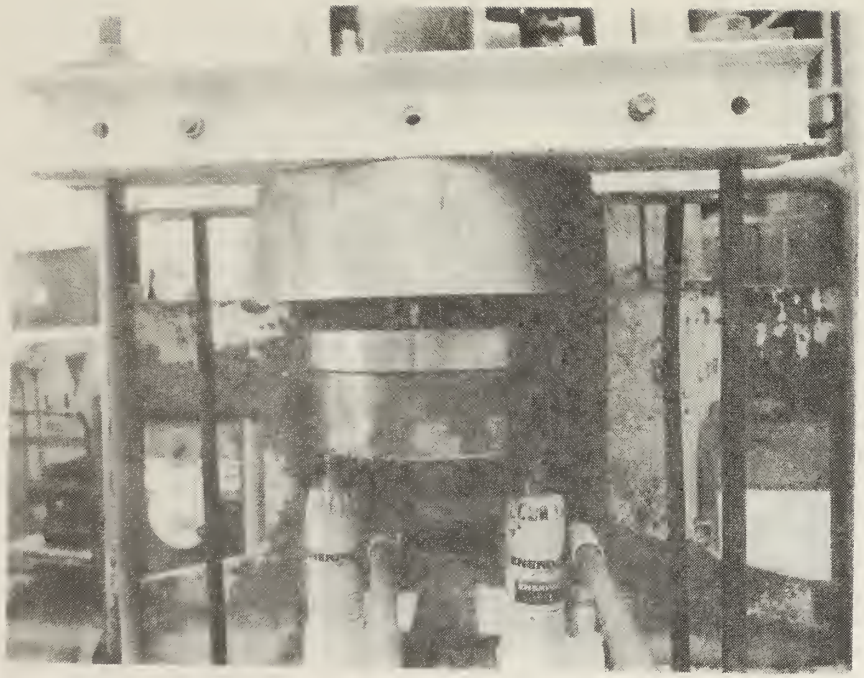

Figure 2.15 Mating disk and laoding head (with hydraulic jacks) prior to welding

Figure 2.16 Assembled loading tendon and pull-out disk (as built)

In his pilot test, Kierkegaard-Hansen noted that some 30 percent of his specimens failed when flexurally induced tensile stresses split the entire specimen in two--thus invalidating the test, as far as pullout results were concerned. Behavior of this type in the present study was to be avoided. Two supplementary sets of reinforcement were designed to prevent such an occurrence in the scaled-up pullout tests. These are shown in schematic form in figure 2.17 and as-built in figure 2.18. The primary containment grid consisted of #2 (6.35 mm) hoops (f_y = 40 ksi (276 MPa)) 54 inch (1.37 m) in diameter at 3 inch (76 mm) spacing tied to #3 (9.5 mm) bars (f_y = 40 ksi (276 MPa) oriented vertically at a 6 inch (152 mm) spacing around the hoop. This hoop was 11.25 inch (286 mm) larger in diameter than the outside diameter of the counterpressure device and thus was felt to constitute no interference with the pullout test, while effectively preventing flexural splitting. The remaining reinforcement consisted of a uniform orthogonal grid of #3 bars (f_y = 40 ksi (276 MPa)) at 6.5 inch spacing placed at the sides and bottom of the specimen with a concrete cover of 1 1/4 inch (31.75 mm). This was to prevent the propagation of any cracks that might arise due to temperature and shrinkage effects.

After the forms had been assembled the disk and stem were positioned in the center at the proper elevation (h = 10 inch (254 mm) and h = 13.5 inch (343 mm) for specimens 1 and 2 respectively). This elevation was established as the distance from the top face of the disk to a reference string that had been set across the top of the forms. Precision leveling and final positioning were accomplished by clamping the stem to a C-channel cross frame which spanned the top of the forms (see figure 2.18). A secondary frame, constructed from lightweight perforated 2 inch (51 mm) angle stock (figure 2.19), provided the upper support for the gage strings which were inserted at this time. The lower bracket for each gage string was attached to a special lug that had been welded to the disk edge. Figures 2.4 and 2.5 show the two types of connections used for mounting circumferential and radial gages respectively.

Each specimen--"pullout 1" (α = 35°) and "pullout 2" (α =27°)--had eight gage strings typically consisting of:

1. Ten radial gages (RN) spaced uniformly from the "north" edge of the disk to the inside edge of the reaction ring (figure 2.3, left hand string).

2. Six gages (RV) oriented parallel to the top face of the disk and uniformly spaced from the "north" edge of the disk to a point approximately 7 inch vertically above the north edge of the disk (figure 2.3, right hand string).

3. Ten radial gages (RS) spaced uniformly from the "south" edge of the disk to the inside of the counterpressure ring. (Specimen 1 (α =35°) had seven radial gages and six axial gages (AS) on the same grid, but this was modified for simplicity in specimen 2). (Figure 2.9, left-most string).

4. Ten circumferential gages (CE) spaced uniformly from the "east" edge of the disk to the inside of the counterpressure ring (figure 2.9, bottom string).

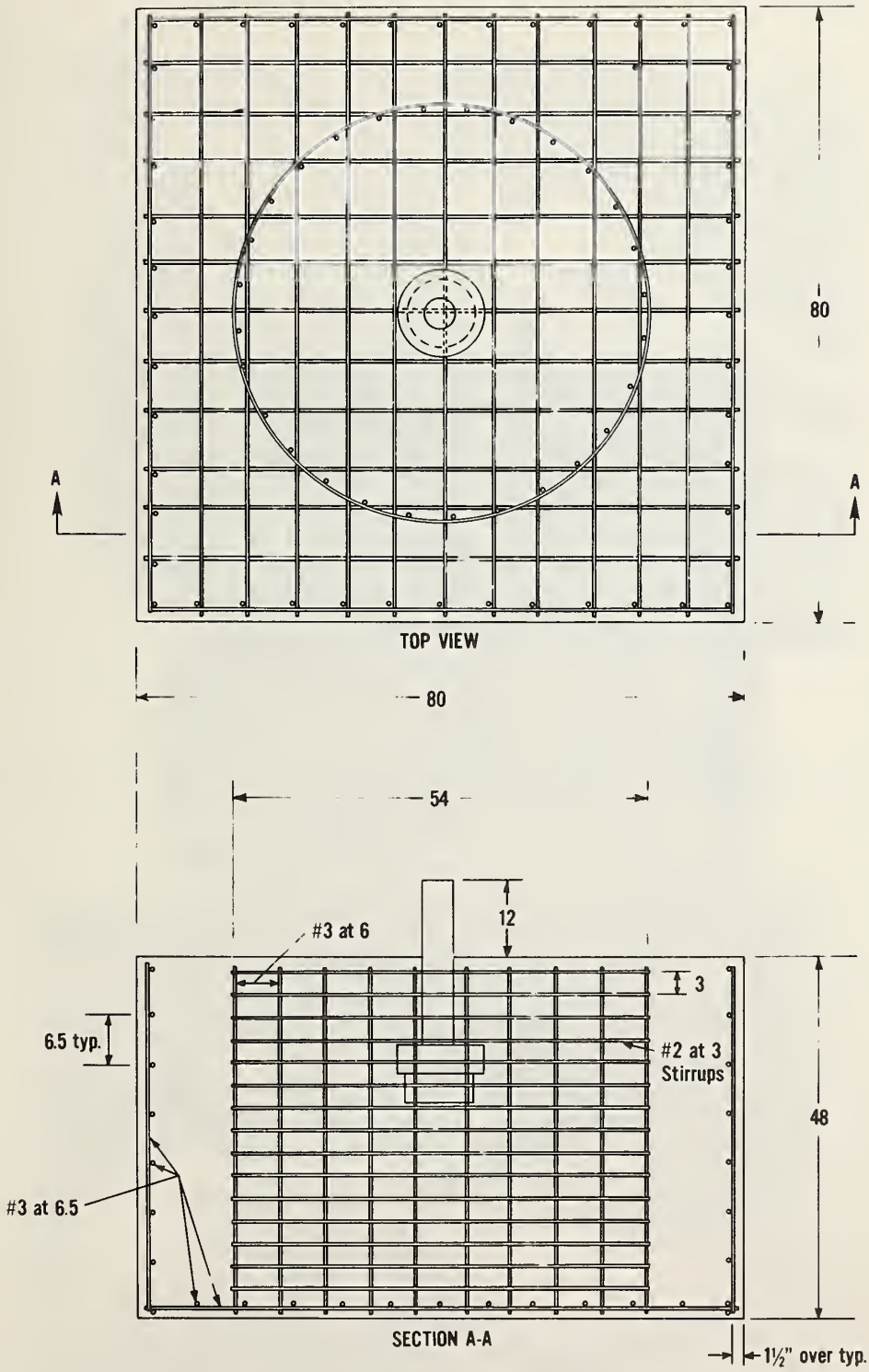

Figure 2.17 Supplemental reinforcement specifications (all units inches)

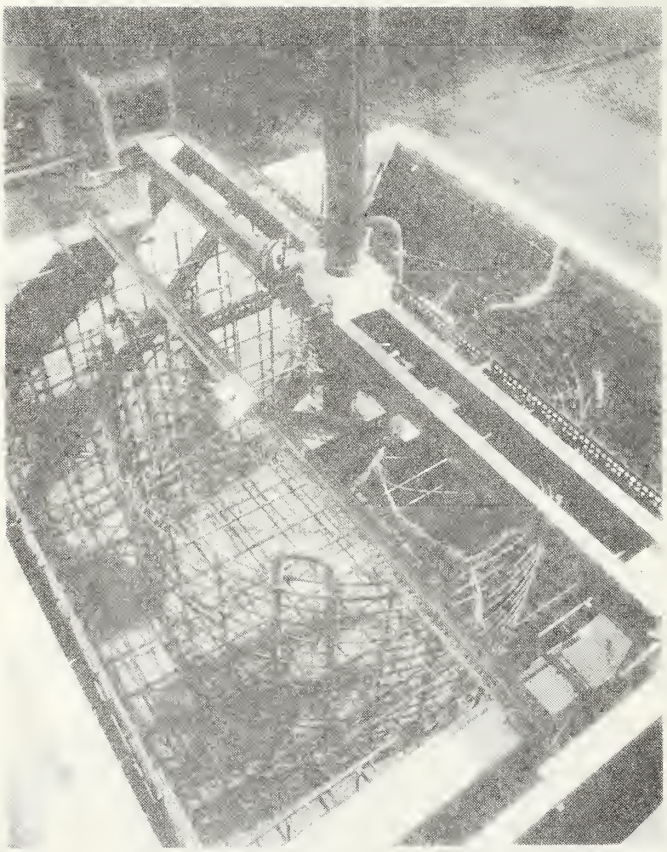

Figure 2.18 As built supplemental reinforcement

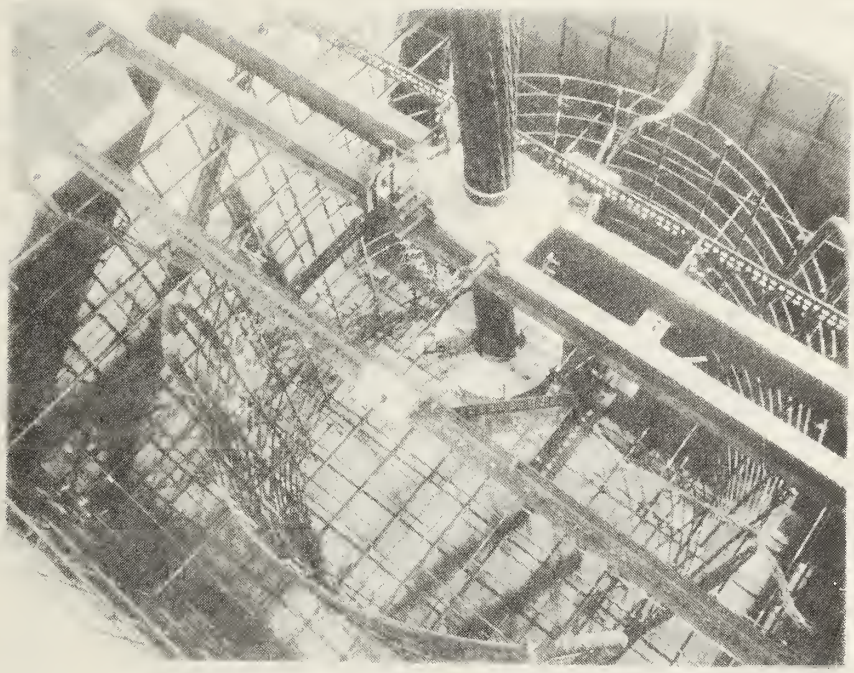

Figure 2.19 Perforated angle frame used to support gage strings. Cross channel frame is used to stabilize and level disk prior to casting

Figure 2.20 Checking embedment gage resistance

5. Ten circumferential gages (CW) spaced uniformly from the "west" edge of the disk to the inside of the counterpressure ring (figure 2.2, lower left string).

6. Fourteen axial gages (ANE) uniformly spaced in parallel overlapping strings from the "north east" edge of the disk to the inside of the counterpressure ring (specimen #1, shown in figure 2.5 had only 11).

7. Six gages (ET) oriented vertically and parallel to the side face of the disk. These were mounted approximately 1/2 inch (13 mm) away from the disk on the "south west" edge (figure 2.4).

8. Five gages (TC) mounted 1/2 inch (13 mm) above and parallel to the top face of the disk on the "north west" side, beginning at the stem and ending at the disk edge (figure 2.2).

Specific gage locations (numerical coordinates) are given in appendix A. Once all strings were in place, the slack was taken up via a nut and threaded rod which formed the upper support. To ensure that each string followed the proper angle (and the idealized failure surface) a properly trimmed wooden block was used so that the threaded rod (which exitted through the perforated support, then through the wooden block) could be tensioned parallel to the desired angle (see figure 2.19). This tensioning procedure imparted no pre-tension in any of the gages (due to the method of attachment--flexible copper wires) and was primarily for ensuring that the gages underwent no undesirable relocation during casting.

At this point the electronic integrity of the gages was rechecked (figure 2.20) using a digital ohmmeter. Gages were rejected (and replaced) if readings fell outside a window of 120 Ω to 123 Ω. The foil gages normally have a factory specification of 120 Ω ± .5 Ω. However, most embedment gages fell into the former window; the higher resistances resulted from the 10 ft (3m) lead wires and impurities in the soldered connections. This did not adversely affect the performance of the gages, but occasionally led to difficulties in balancing the bridge circuits (which used 120 Ω precision resistors, instead of temperature compensating gages) of the data acquisition system due to insufficient range in the balancing potentionmeter in the event that a particular circuit could not be balanced additional precision resistors were added in 1 ohm increments until balance was achieved.

The specimen was now ready for casting. A standard ready mix concrete, with 1/4" (6 mm) pea gravel aggregate, was used.* Total volume per cast, including

---

* The pea gravel aggregate was chosen because it was the smallest readily available commercial aggregate. The intent of this choice was to make the concrete mix as homogeneous as possible from the perspective of the scaled up pullout insert. This would then allow for better correlation with the analytically model which assumed the concrete to behave as a perfectly homogeneous material.

Table 2.2

Concrete Mix Proportions

	Specimen 1 (α =35°)		Specimen 2 (α =27°)	
Type 1 cement (lbs)	3172	(1442 Kg)	2961	(1346 Kg)
Silicious Sand (lbs)	12015	(5461 Kg)	12816	(5825 Kg)
Pea Gravel (lbs)	11437	(5198 Kg)	12200	(5545 Kg)
Water (lbs)	2200	(1000 Kg)	2384	(1083 Kg)
W/C (Approximate)	.693		.805	

test cylinders, was 7.5 yards (7.2 m^3). The mix design for both specimens is given in table 1.2. Concrete was delivered with only a portion of the total mix water; additional water was added at delivery to achieve a slump of 3 to 5 inches (76 to 127 mm).

2.5 LOADING SYSTEM

The pullout load was applied via the counterpressure system shown in figure 2.21. The bearing ring had an inside diameter of 26 inch (660 mm), an outside diameter of 42.75 inch (1.09 m), and was made from 1 inch (25.4 mm) thick plate stock. Eight W8 x 31 rolled A36 sections, 33.72 inch (856 mm) in length, were welded to the base as shown in figure 2.22, and tapered inward so as to form a pedestal for a 26 inch (660 mm) O.D. top plate, also made from 1 inch (25.4 mm) plate. The loading system consisted of six 100-ton (892 kn) hydraulic rams, with a maximum operating pressure of 10,000 psi (69 MPa). These were mounted in a hexagonal cluster on top of the counterpressure pedestal. Two steel retainer rings, made from 2 inch (51 mm) x 0.25 inch (6.35 mm) bar stock, were used to secure the ram cluster. The lower ring (figure 2.21) was welded to the top plate on the loading pedestal. To transmit the load from the ram cluster to the post-tensioning tendon (and thus, to the embedded disk) a jacking head 4 inch (102 mm) thick and 22.5 inch (572 mm) in diameter was machined to fit on top of the six hydraulic piston heads (figure 2.23). A 7.5 inch (191 mm) diameter hole in the center permitted the 31 strand tendon to pass through.

The assembled loading system was placed on top of the cured specimen and leveled using a base of high strength gypsum plaster (figure 2.24). The strands were then threaded through a 31 strand pulling head which rested on top of the jacking head. Each strand was pretensioned to 300 lb (1.33 kn) (figure 2.25) and its conical chucks were firmly seated. When all strands had been set the pistons for the ram cluster were retracted to remove any pre-load. This procedure was to ensure that all strands would have close to the same load at all times, thus avoiding a premature "zipper" type failure of the tendon. The six rams were linked to a load maintainer via two-six port manifolds. Two in-line, 10,000 psi (69 MPa) pressure transducers were used as the primary load monitors, while two additional in-line pressure gauges were used for backup spot-checks.

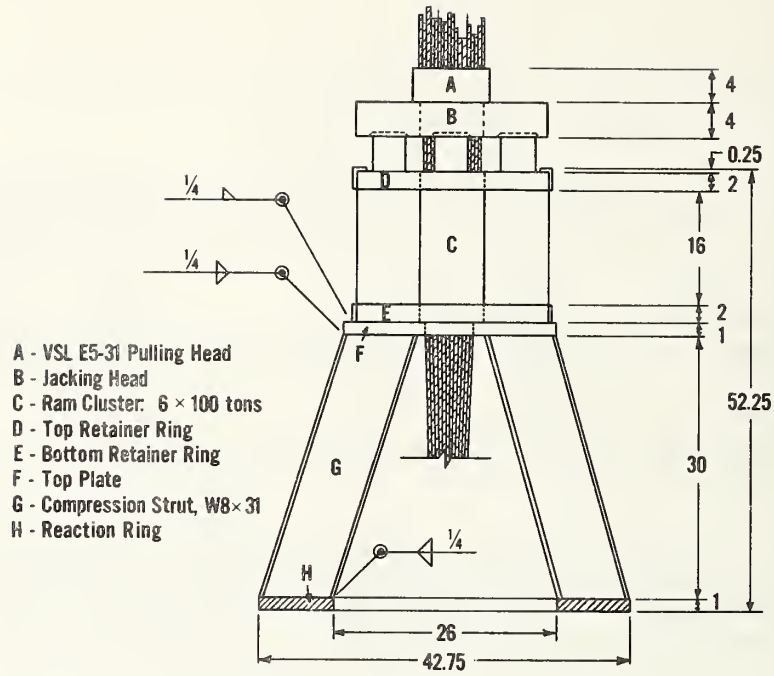

Figure 2.21 Jacking - counter pressure system (schematic) (all units inches)

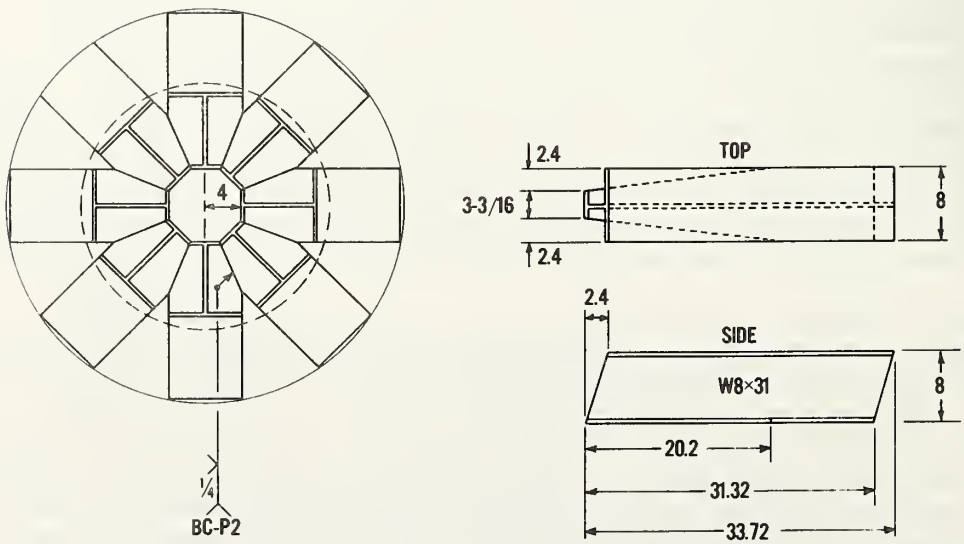

Figure 2.22 Compression frame specifications (all units inches)

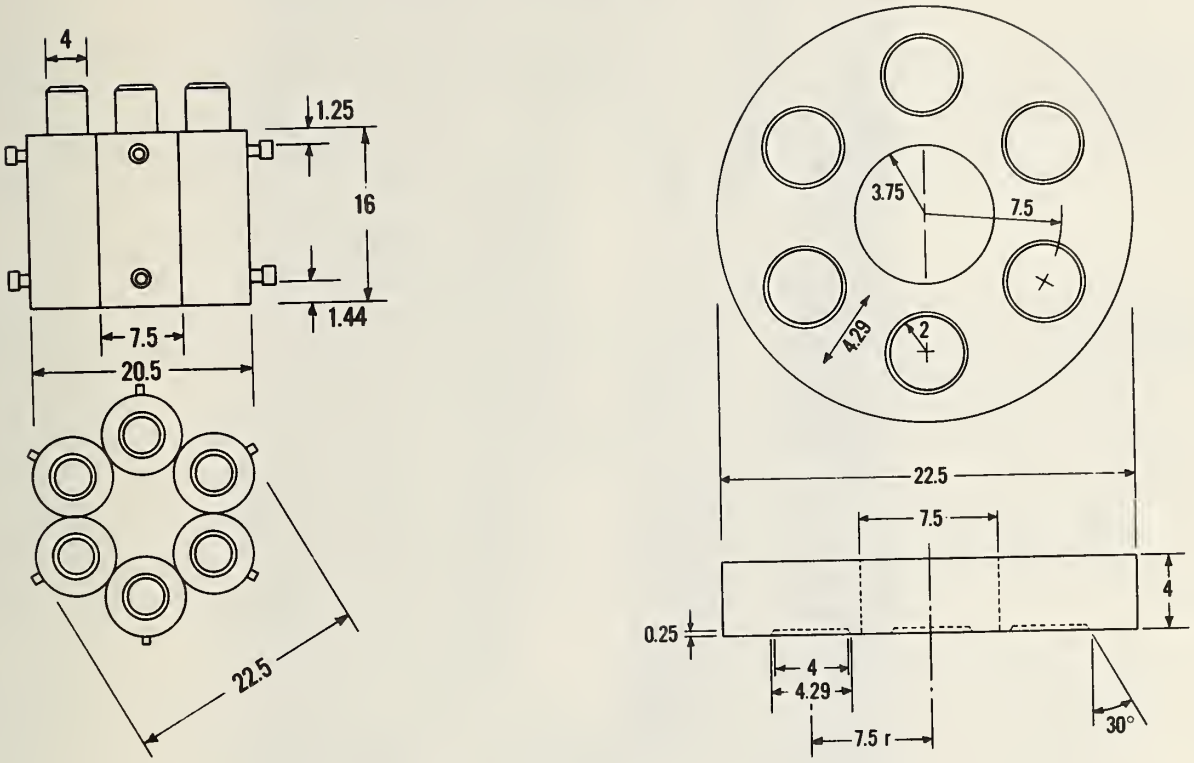

Figure 2.23 Jacking head and ram cluster specifications (all unit inches)

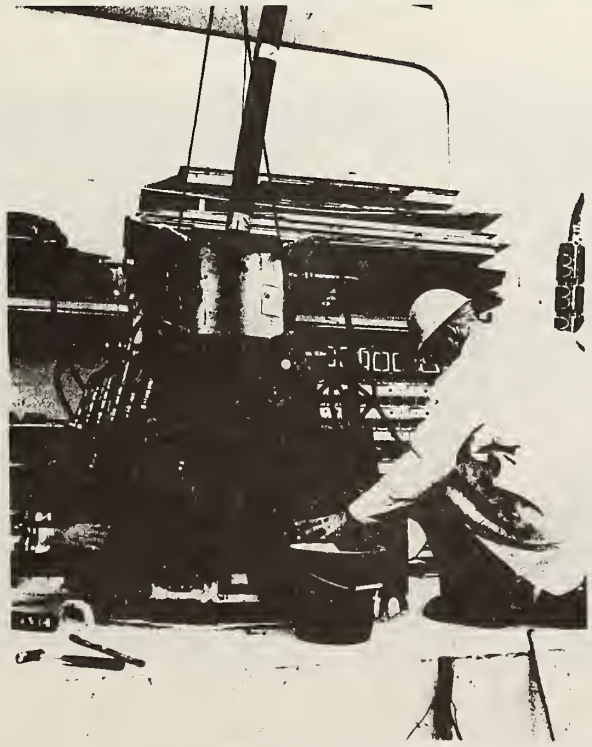

Figure 2.24 Seating jacking-counter pressure system on plaster grout

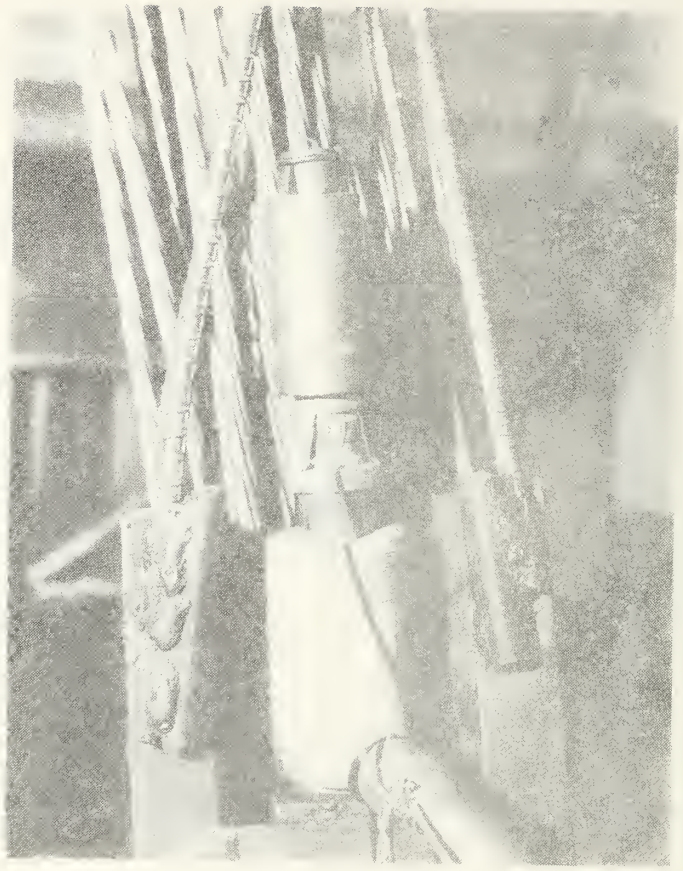

Figure 2.25 Pre-tensioning loading tendon strands

Figure 2.26 Calibrating jacking-counter pressure system

The load maintainer was driven by a 40 GPM (0.16 M^3/min), 10,000 psi (69 MPa) portable electric hydraulic pump. The load was advanced manually at a constant rate in 10 kip (44.6 kn) increments to failure. Before conducting the first test, the assembled loading unit was calibrated to 1,200,000 lb (5.3 mn) using the NBS 12,000,000 lb (54 mn) Universal testing machine (figure 2.26).

2.6 INPLACE STRENGTH OF CONCRETE

To aid in interpreting the test results, it is necessary to know the strength of the concrete in each specimen. Because of specimen size, it was anticipated that there would be a significant rise in the internal temperature during the early stages of hydration. It was felt that using ordinary cylindrical test specimens might not give accurate indications of the inplace strength, due to differences in thermal history. Therefore, it was decided to use cast-in-place pushout cylinder (CIPPOC) molds (figure 2.27), as described in standard test method ASTM C 873 (ref. 18), which would be embedded in the test specimens. The concrete within the molds would be subjected to approximately the same thermal history as the concrete within the pullout specimens.

For each test, eight 4 x 6 inch (102 x 152 mm) pushout cylinder molds were filled with concrete and embedded in the top surface of the test specimens. Rodding was used to consolidate the concrete within the molds. The top surfaces of the cylinders were kept covered with moist rags. For comparison, 6 x 12 inch (152 x 305 mm) cylindrical specimens were molded and allowed to cure adjacent to the pullout specimens. These cylinders were kept in their molds, covered with plastic, and water was added periodically to the top surface to provide moist curing conditions.

Thermocouples were used to measure concrete temperatures. Four pushout and two 6 x 12 inch (152 x 305 mm) cylinders were instrumented. In addition, thermocouples were embedded within the pullout test specimens. The thermocouples were read automatically by a datalogger.

Figure 2.29 shows the temperature histories during the first 10 days for the first test (pullout #1). The thermocouple within the test specimen was located near the insert head. It is seen that the 6 x 12 inch (152 x 305 mm) cylinders did not develop the same temperature as the test specimen. The pushout cylinders, while they were similar for the first 12 hours, did not attain the same maximum temperature as the concrete near the insert head. The discontinuities in the thermal history of the pushout specimens were due to the removal of the plastic sheet covering the specimen which resulted in a cooling off of the top surface of the test specimen.

Because the pushout molds were embedded in the surface of the test specimen, the concrete within them did not experience the same temperature rise as the interior concrete. Thus, an alternative procedure was used for the second test (pulllout #2). An additional set of 6 x 12 inch (152 x 305 mm) cylinders were made using plastic molds covered with plastic and stored under water. The temperature of the cylinders in the bath was compared with the temperature near the insert head, and an electric heater was turned on as necessary to maintain the cylinder temperature as close as possible to the temperature within the

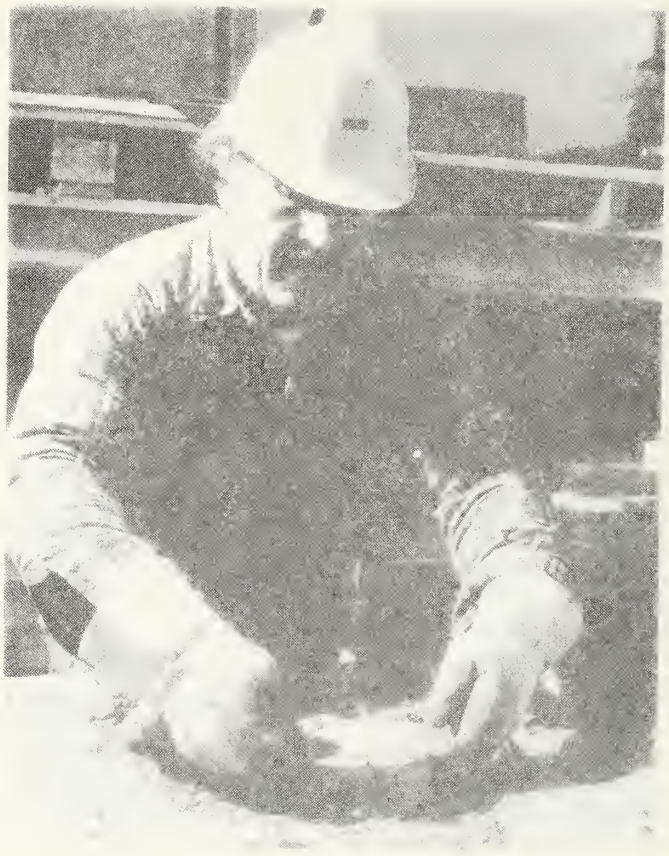

Figure 2.27 Placing CIPPOCS model in freshly cast specimen

Figure 2.28 Slave cylinders in temperature controlled water bath

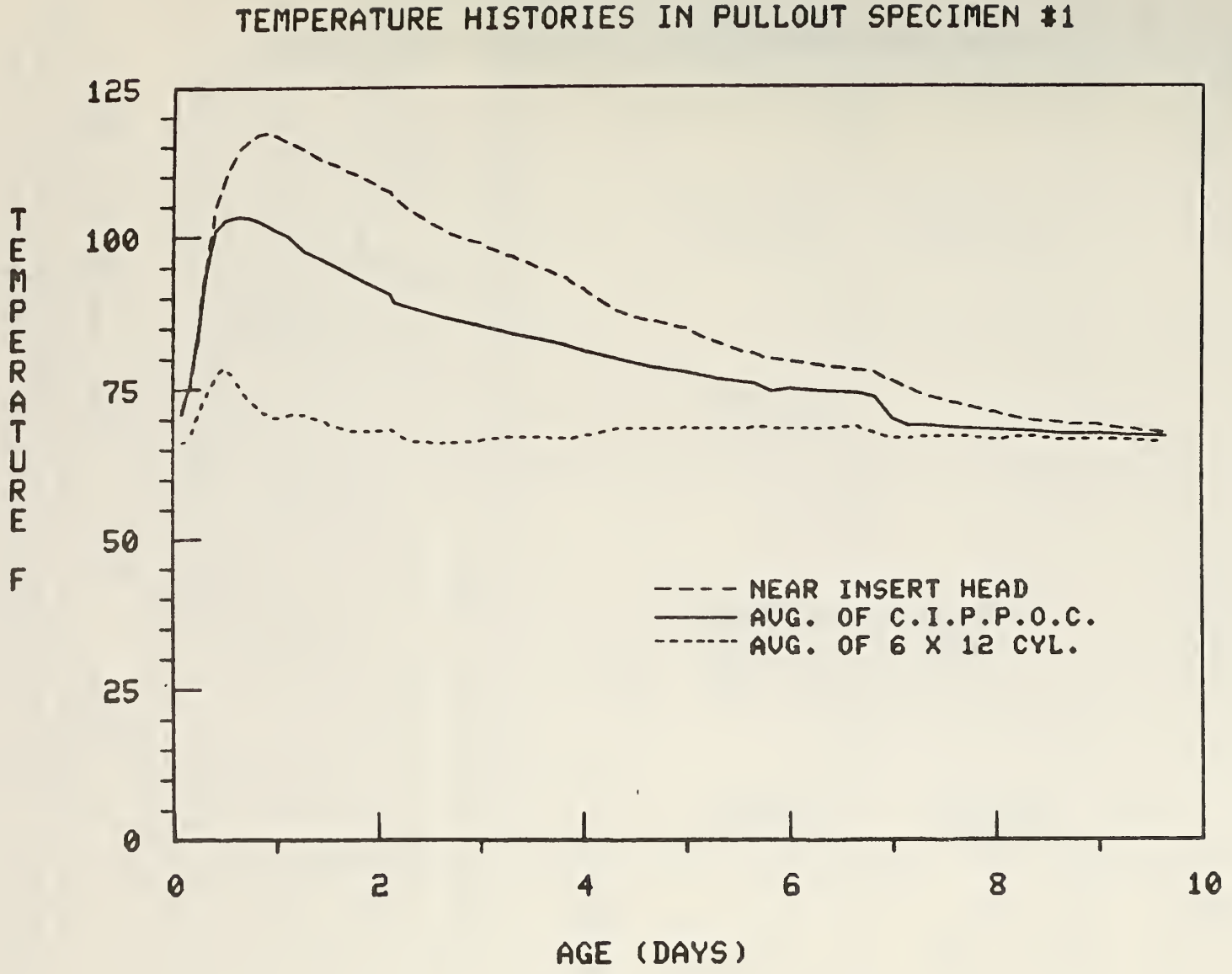

Figure 2.29 Temperature history for pull-out specimen #1 (h = 10 inches, $2\alpha = 70°$)

Table 2.3. Cylinder Strength Results

	Compressive (psi)			Splitting Tension (psi)	
	Room Cure	C.I.P.P.O.C	Slave	C.I.P.P.O.C	Slave
P.O. #1 (age = 27d)	2860 3020 2870 2920 (89)*	2735 2690 2675 2535 2660 (86)		358 331 322 334 336 (15)	
P.O. #2 (age = 13d)	1270 1370 1400 1345 (69)	1233 1330 1320 1275 1290 (44)	1220 1155 1170 1180 (34)	183 159 183 172 174 (11)	120 145 121 129 (14)

* Standard deviation, psi
1 psi = 0.0069 MPa

large specimen. An electronic circuit was designed and built that turned the heater on and off automatically (figure 2.28).

Figure (2.30) shows the thermal histories for the second test specimen. It is seen that the "slave" cylinders in the water bath did not heat up as rapidly as the interior concrete. This was due to a failure in the electronic circuitry and possibly also due to the lack of insulation around the water bath. At an age of 1 day, the damaged electronic component was fixed and insulation was placed around the tank. The "slave" cylinders then followed closely the interior concrete temperature. The rise in the "slave" temperature at four days was due to another electronic malfunction that was later corrected. Thus, except for some "shakedown" problems, the "slave" cylinder concept appears to have been a good solution to the problem of accounting for the inplace temperature rise in the massive test specimen.

On the day of the pullout test, the cylindrical specimens were also tested. Table 1.3 shows the measured compressive and splitting tensile strengths of the various specimens. The measured compressive strengths of the pushout cylinders were multiplied by 0.96 to account for their lower length:diameter ratio as specified in test method ASTM C 42 [27].

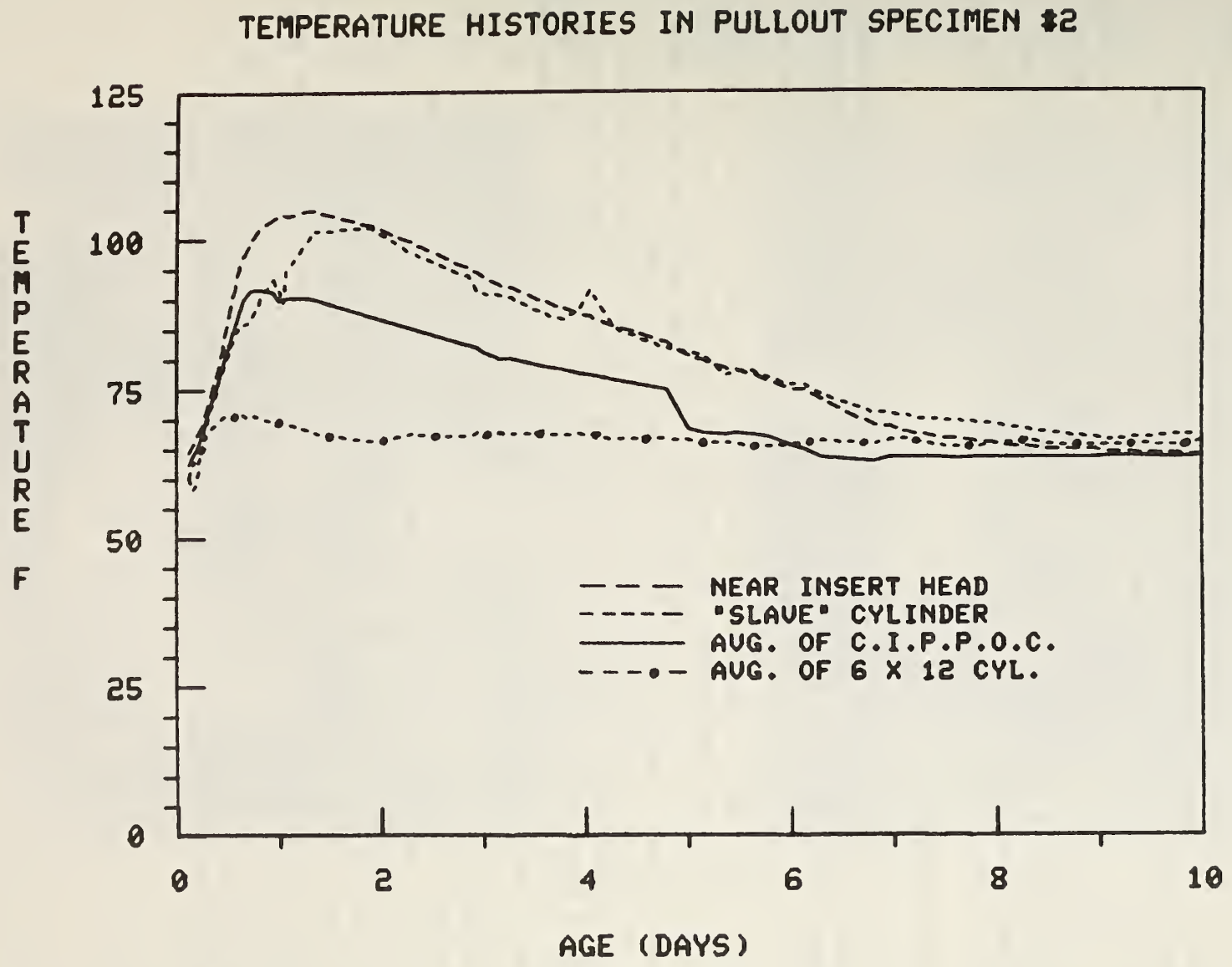

Figure 2.30 Temperature history for pull-out specimen #2
(h = 13.5 inches, $2\alpha = 54°$)

The compressive strength results are consistent with the known effects of initial curing temperature on later age strength, namely an increase in curing temperature lowers the long term strength. This may explain why the "slave" cylinders were weaker than the pushout cylinders which were in turn weaker than room cured cylinders. The splitting tensile strengths of the "slave" cylinders are lower than expected and there is no explanation for this, other than a "size effect" problem. For specimen #1 the average compressive strength of the C.I.P.P.O.C. cylinders (f'_c = 2660 psi) was used as the basic for material property inputs in the analytical model; for specimen #2 for average of the slave cylinder compressive strengths (1180 psi) was used, since this was considered to be a more accurate indicator of the concrete strength in the vicinity of the pullout insert.

2.7 TEST PROCEDURE

Once the electronics for the data acquisition system were checked, a pre-test data check run was made by loading each specimen to approximately 20 percent of ultimate load in 10 kip (4545 kg) increments. At each load stage a scan was made of all instruments and the data was stored on magnetic disk. At the peak load, plots of the observed strain distributions for the key gage strings were produced on site using a Tektronix 4014 terminal and a hard copy device (figure 2.31). If all gages checked out, the load was dropped to zero using the manual load maintainer and the actual test was begun. Load was monitored using both a digital voltmeter, which gave a direct reading of the pressure transducer output, and using the program TEXD. In the latter mode, the transducer channels were automatically converted by the program to give a visual display of the load in kips on the 4014 unit at the prompting of the operator. The digital voltmeter served as the primary queue for initiating a load scan. This was then verified on the 4014 as the load channel values appeared on the screen. The load was increased in 10 kip (4545 Kg) increments until ultimate failure. In order to assist in detecting the onset of failure, an acoustic emission receiving transducer (figure 2.32) was affixed to the counter pressure ring and the output signal amplified through a loud speaker system. The audible cracking sounds gave sufficient warning so that a large number of scans could be taken near the failure load. Each test required a full day to perform, including cylinder tests after the failure of the main specimen. The test data was backed up to tape from disk and individual strain-history plots for each embedded gage were generated; similarly, load versus deflection plots were made for each LVDT. Later, the loading system was disassembled and the pullout "cone" was removed for photographing and measurement. An overall view of the test setup is presented in figure 2.33.

Figure 2.31 Graphics terminal used to monitor real time strain histories during testing of specimens 1 and 2

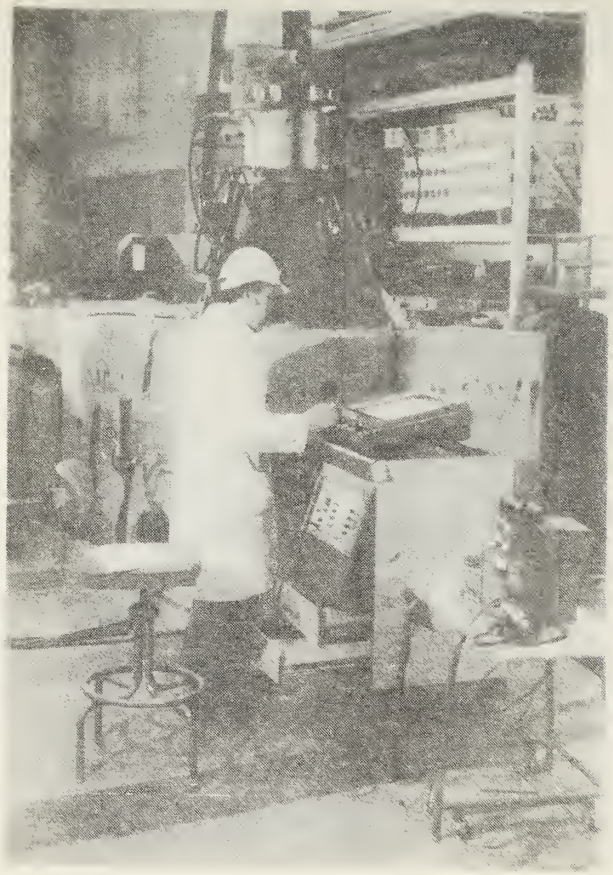

Figure 2.32 Acoustic emissions device and a amplifier used to provide advance warning of impending failure

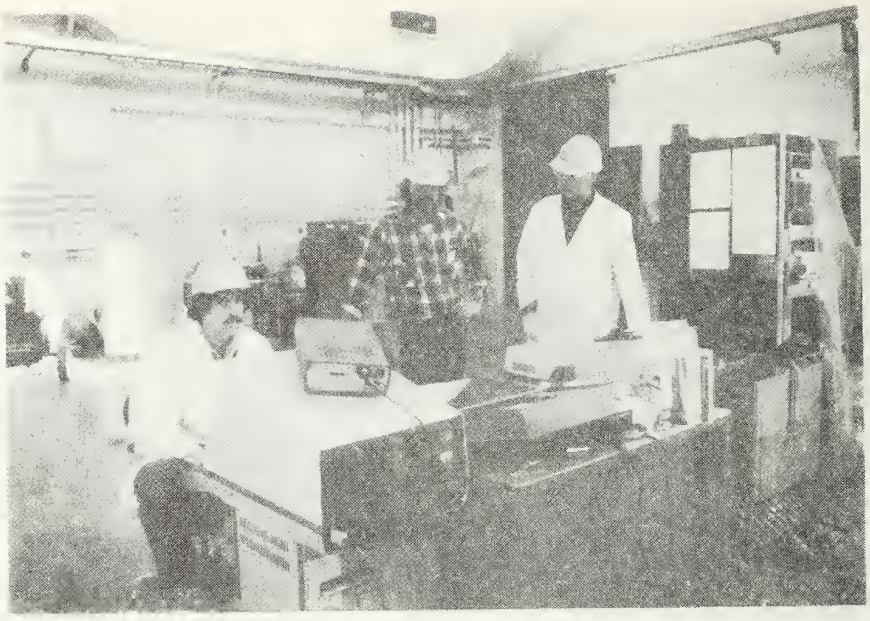

a) Tektronix 4014 terminal, digital voltmeter for monitoring load, x-y recorder for monitoring vertical displacement of pull-out disk, hard copy device for computer terminal, manual load maintainer, thermal data logger for embedded therocouples

b) Cast specimen, with loading device in operation

Figure 2.33 Overall view of lab test set-up

3. RESULTS

3.1 LOAD DEFLECTION CURVE

The experimental data obtained from each large pullout test are comprised of three parts: load-deflection data; the failure surface geometry; and internal strain histories as measured by embedded straingages. Figures 3.1 and 3.2 show load versus deflection plots for specimens 1 and 2 (2α =70° and 54°, respectively). Also indicated are values of compressive strength from CIPPOCS (for specimen #1) and slave cylinders (for specimen #2) and computed values of modulus of elasticity using the American Concrete Institute formula 8.5.1 ($E_c = w_c^{1.5} 33 \sqrt{f'_c}$). The leftmost curve in each figure represents the average upward deflection of the disk as measured by the three slip wire controlled, side mounted LVDTs. The right hand curve represents the average of the two vertical LVDT deflections. It can be seen from figures 3.1 and 3.2 that the failure sequence of the pullout test is marked by three phases signified by pronounced changes in the slope of the load-deformation curve. These load levels are listed in table 3.1, and their significance in terms of the failure sequence are discussed in section 3.5.

Table 3.1.

Ranges in Percent of Ultimate Load which Mark Pronounced Changes in the Slope of the Load Deflection Curve		
Phase	Specimen #1 (2α = 70°)	Specimen #2 (2α =54°)
I	30- 43	34- 39
II	63- 70	58- 66
III	83-100	84-100

In both specimens the slip wire deflections lagged behind those measured by the stem mounted gages. This may have been due to a taking up of slack in the piano wire--despite an effort to reduce this by spring loading the slip wire. Alternatively, as will be discussed, the load at which the slip gage picked up a significant deflection in specimen #2 corresonded almost exactly to the load at which circumferential cracks had completely formed from the outer disk edge to the inside edge of the counterpressure ring. This would indicate that large deflection begins only after circumferential cracking is complete.

For comparison of specimens 1 and 2 a normalized load deflection curve is shown in figure 3.3. Normalization was accomplished by dividing the applied load by the respective value of the compressive strength for each specimen and by multiplying the deflection by the calculated modulus of elasticity for each specimen. Each line represents the average of the vertical LVDT and slip wire

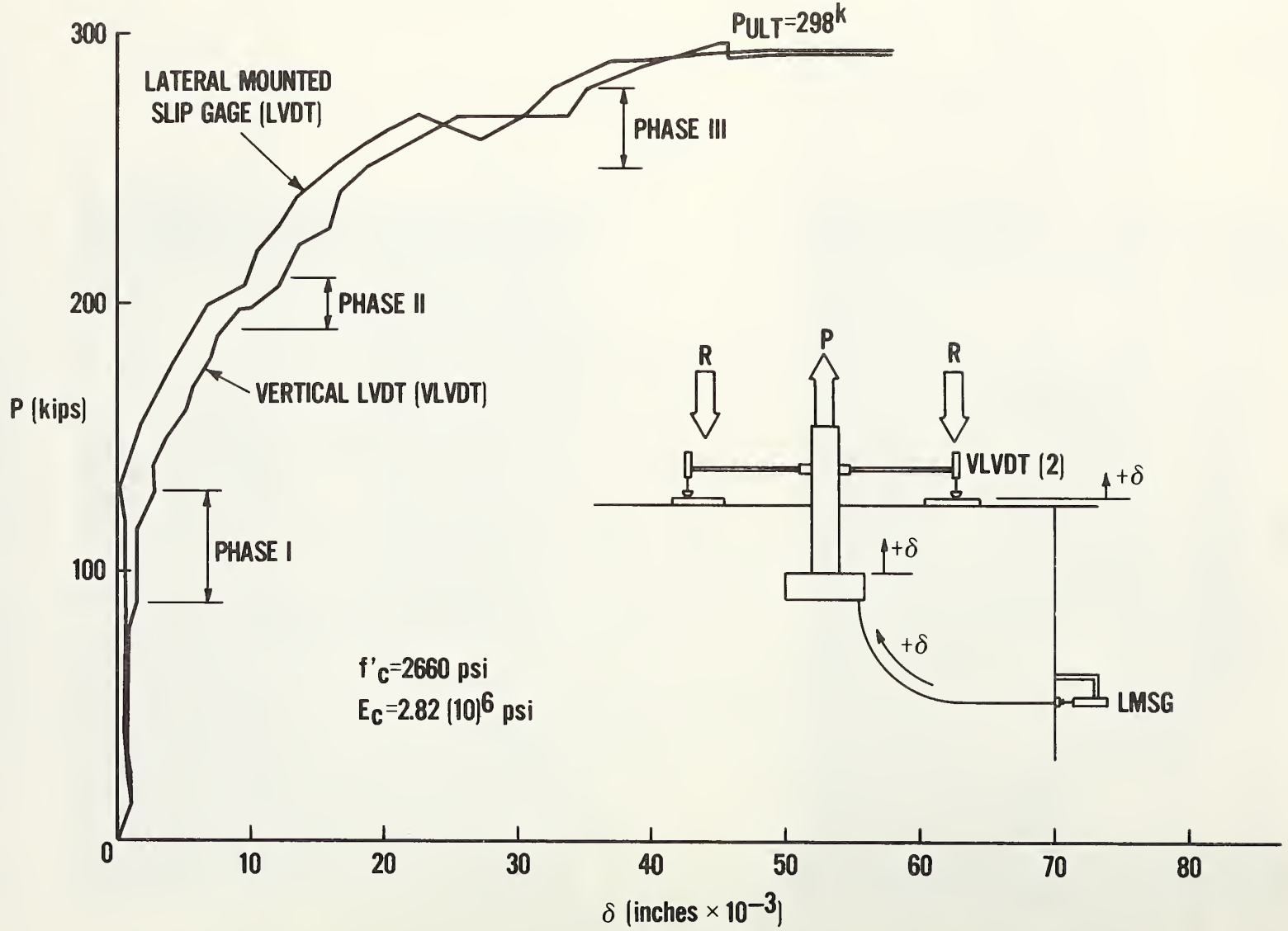

Figure 3.1 Vertical disk deflection vrs load
Specimen #1 $2\alpha = 70°$

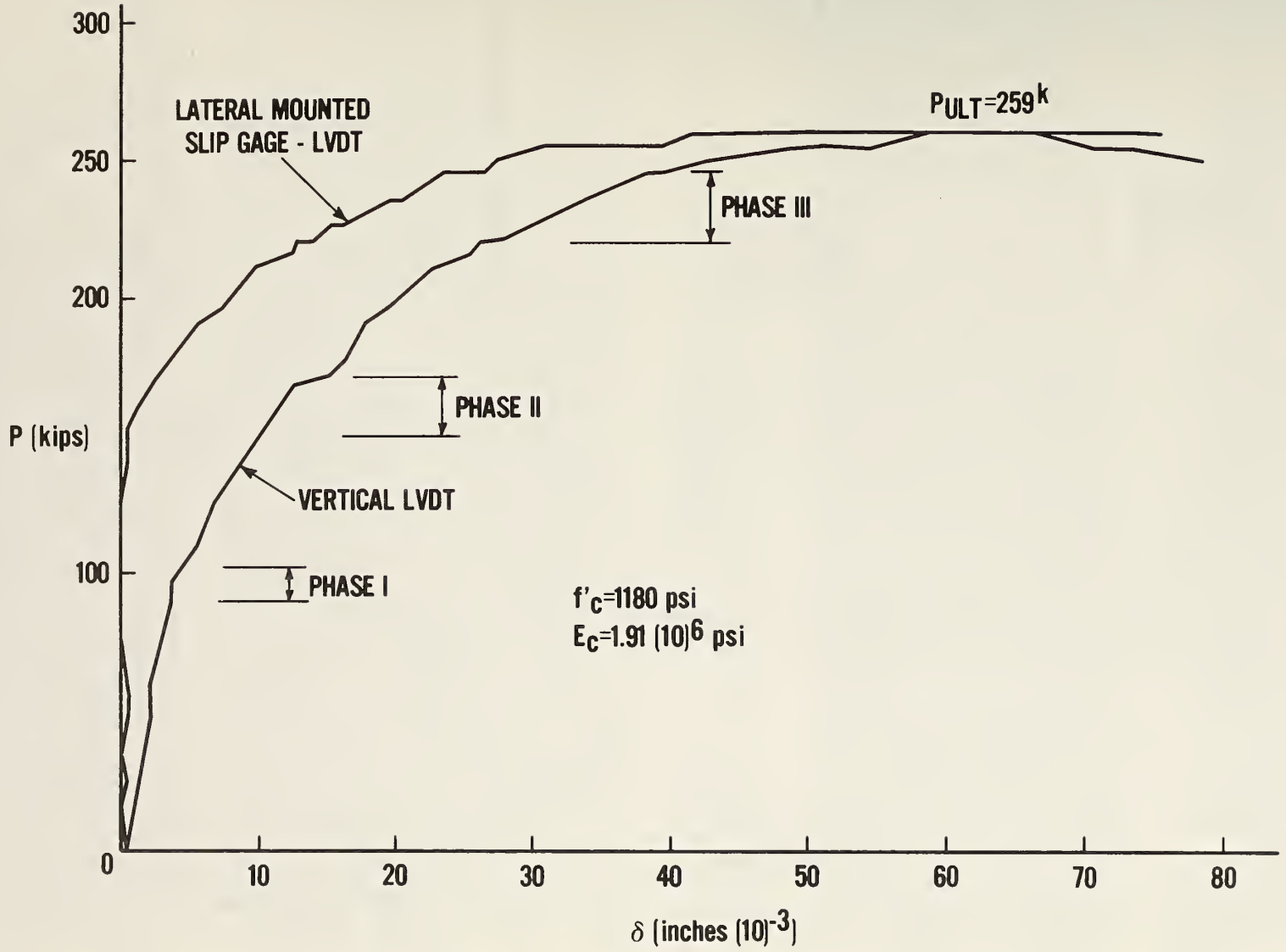

Figure 3.2 Vertical disk deflection vrs load Specimen #2
$2\alpha = 54°$

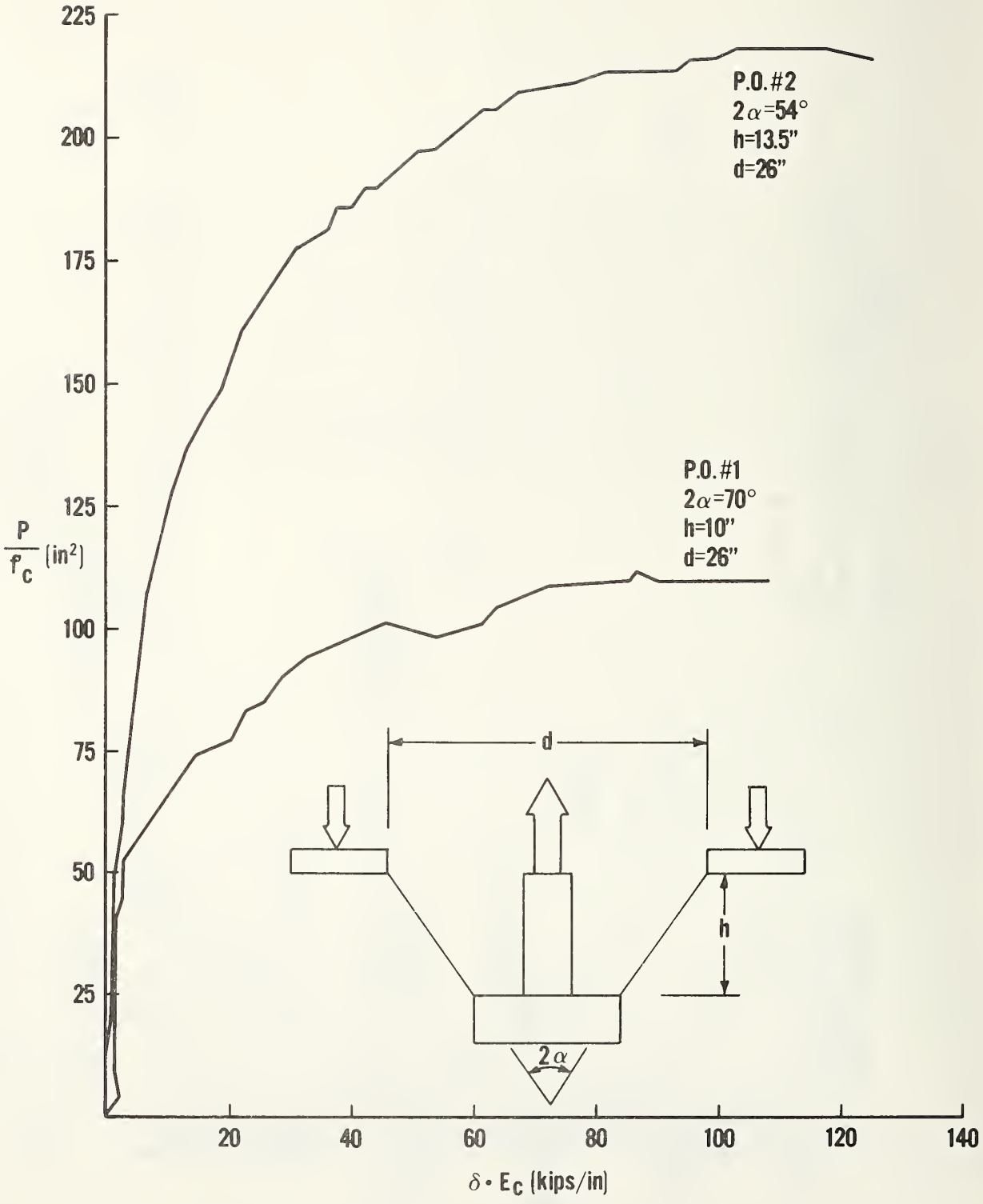

Figure 3.3 Normalized load deflection curve
Specimens 1 & 2

deflections. The normalized ultimate load for specimen #2 is twice that of specimen #1. Thus, a decrease in the apex angle (2α)--or increasing the depth of embedment, as in this case--leads to a higher pullout force. This was first observed in tests performed by Kierkegaard-Hansen [2] who changed the apex angle by varying the counterpressure ring diameter, rather than the depth.

3.2 SHAPE OF FAILURE SURFACE

Due to the size of the pullout "cones" (see figure 2.4) it was possible to make detailed measurements of their geometry. For each specimen several readings of the variation of radius with respect to height were taken around the circumference of the failure surface from the disk edge to the top edge of the cone which corresponded to the inside edge of the counterpressure ring. The readings were taken by dropping a plumb line from the top of the cone and measuring the perpendicular distance to the failure surface by means of a ring stand with an adjustable height horizontal reference rod. These are plotted in figure 3.5. The dashed line in each figure represents the idealized failure surface that would be defined by the frustum of a cone, as well as the line of location of the embedded strain gages. Two important observations that can be drawn from these figures are that:

a. the failure surface approaches a frustum geometry for low apex angles; and assumes a trumpet shaped, geometry which deviates further from the frustum line with increasing apex angles.

b. the failure surface geometry becomes more uniform about the circumference for lower apex angles. Stated differently, there was a greater scatter in the measurements taken from specimen 1 (figure 2.5a, $2\alpha = 70°$) than from specimen 2 (figure 3.5b, $2\alpha = 54°$).

3.3 COMPARISON OF EXPERIMENTAL AND ANALYTICAL STRAIN DISTRIBUTIONS

Examination of a typical embedment gage strain history, such as shown in figure 3.6, shows that the load versus strain behavior is nearly linear until roughly 30 percent of ultimate load. Below this load, the concrete can be assumed, for the sake of analysis, to be linear elastic, homogeneous, and uncracked. After cracking the state of stress will change continually as radial and circumferential cracks propagate through the concrete. As a precursor to possible future non-linear, finite element method (FEM) analyses of cracked specimens 1 and 2, it was felt necessary to first assure that the (FEM) modelling technique (FEM) would yield reliable reults in the precracked state.

For analyses, a linear elastic, isotropic, two dimensional, axisymmetric (solid) model was employed. The element meshes for modelling specimens 1 and 2 are shown in figure 3.7 and figure 3.8 respectively. The mesh generation and post processing stress contour plotting were done using the UNISTRUC II interactive graphics package. The problem solution was performed using ANSYS on a CDC cyber 175 computer. For both specimen models the applied load was 50 kips, or 17 percent and 19 percent of ultimate load for specimens 1 and 2, respectively, well below the level of first cracking. For each model, input values of the Elastic Modulus E_c corresponded to values calculated using the American Concrete

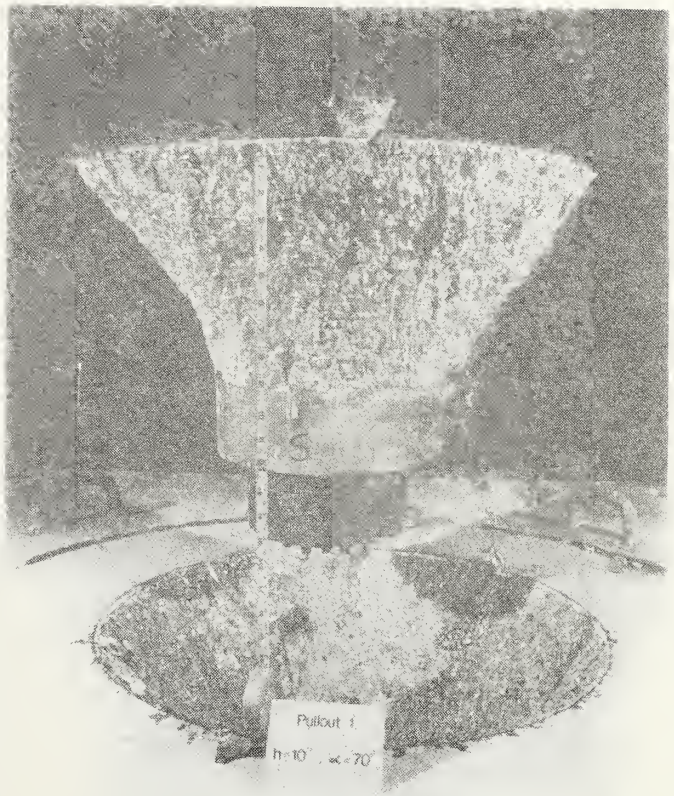

a) Specimen #1 (h = 10 inches, 2α = 70°C) viewed from the south

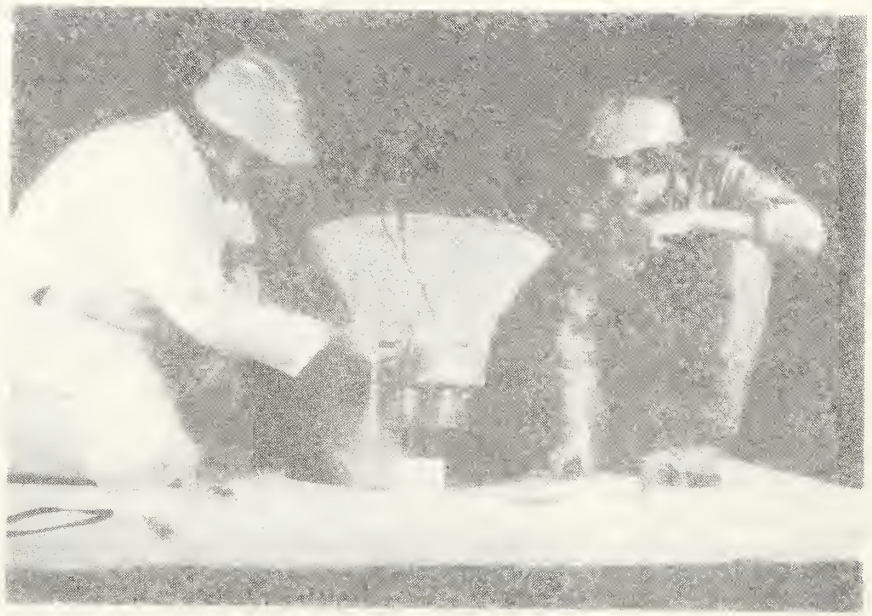

b) Specimen #1 pullout cone; relative scale

Figure 3.4 Experimental pullout cones

c) Specimen #1 (h = 10 inches, 2α = 70°C) viewed from the east

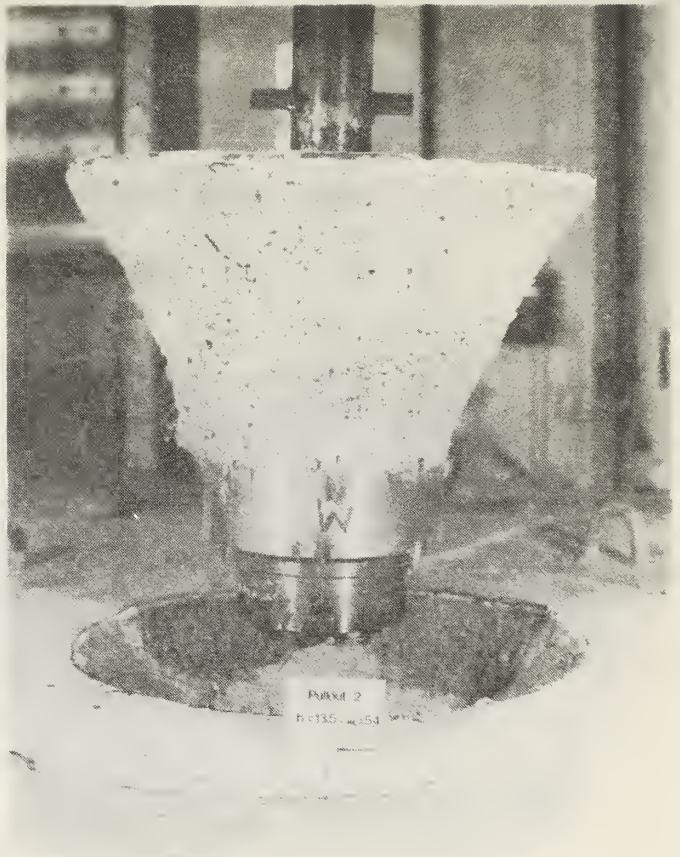

d) Specimen #2 (h = 13.5 inches, 2α = 54°C) viewed from the west

Figure 3.4 Experimental pullout cones

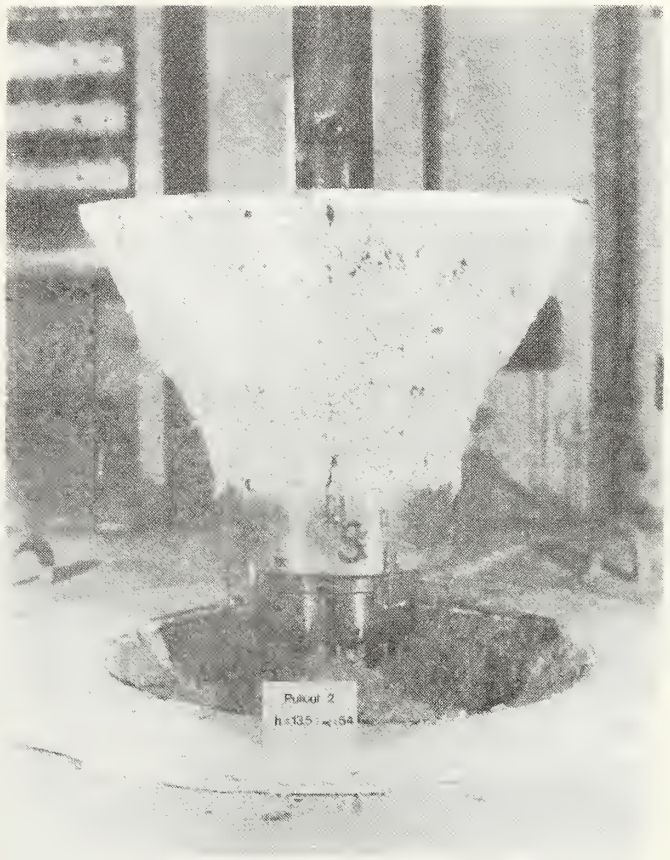

e) Specimen #2 (h = 13.5 inches, 2α = 54°C) viewed from the south

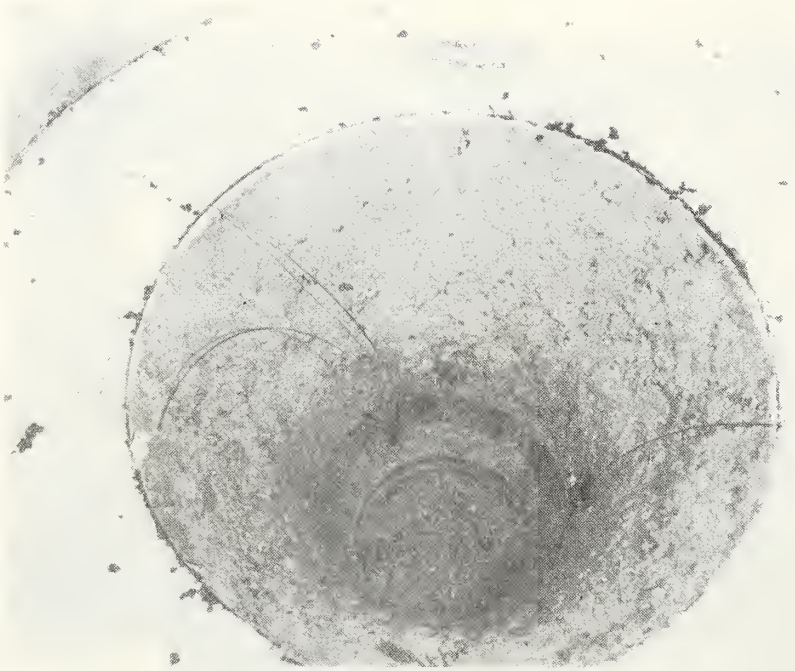

f) Specimen #2 base after removal of pullout cone. Note powdered aggregate and cement paste deposits on sides and bottom. This is indicative of a shear type failure

Figure 3.4 Experimental pullout cones

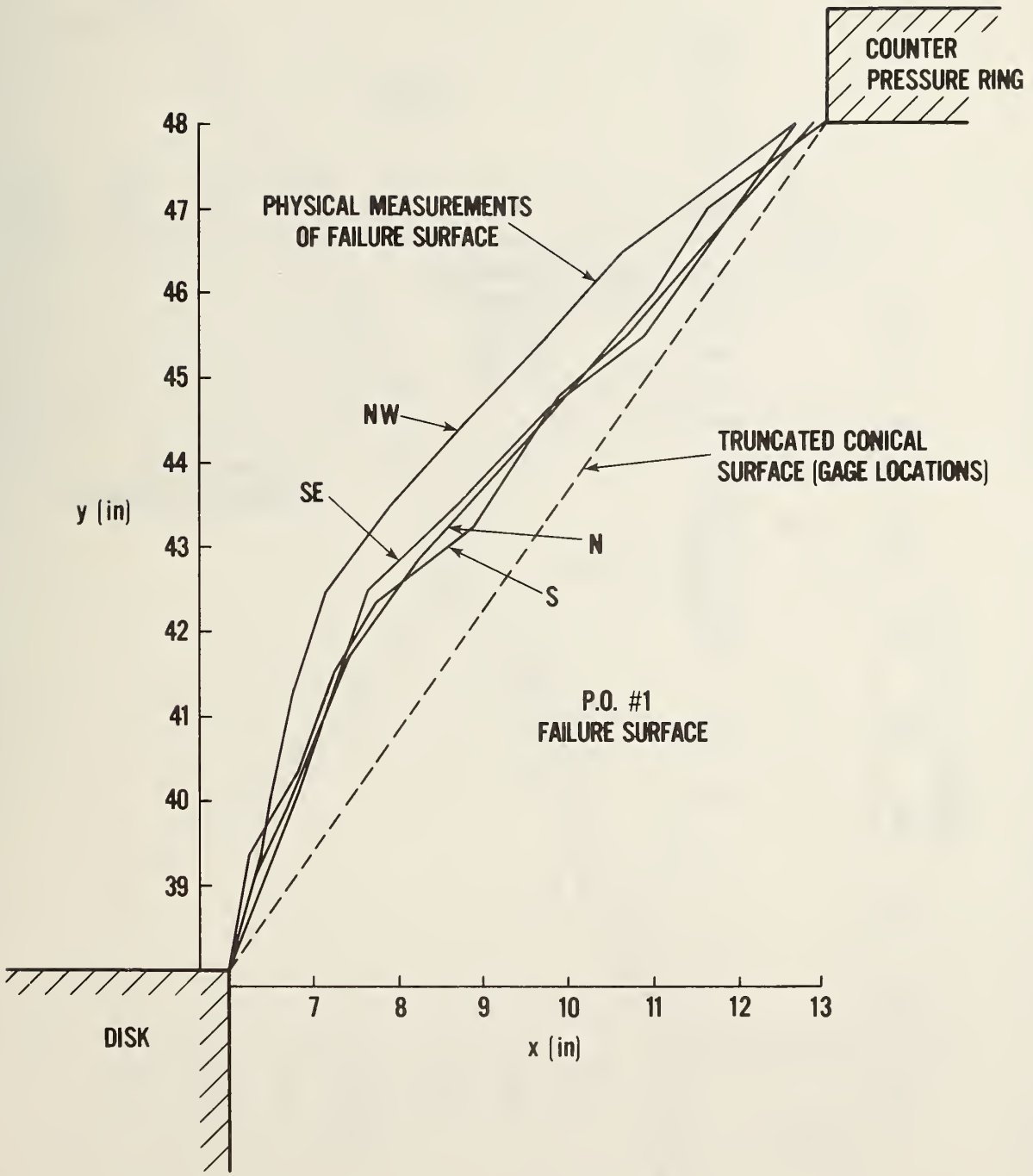

Figure 3.5a Measured failure surface for Specimen #1
$2\alpha = 70°$

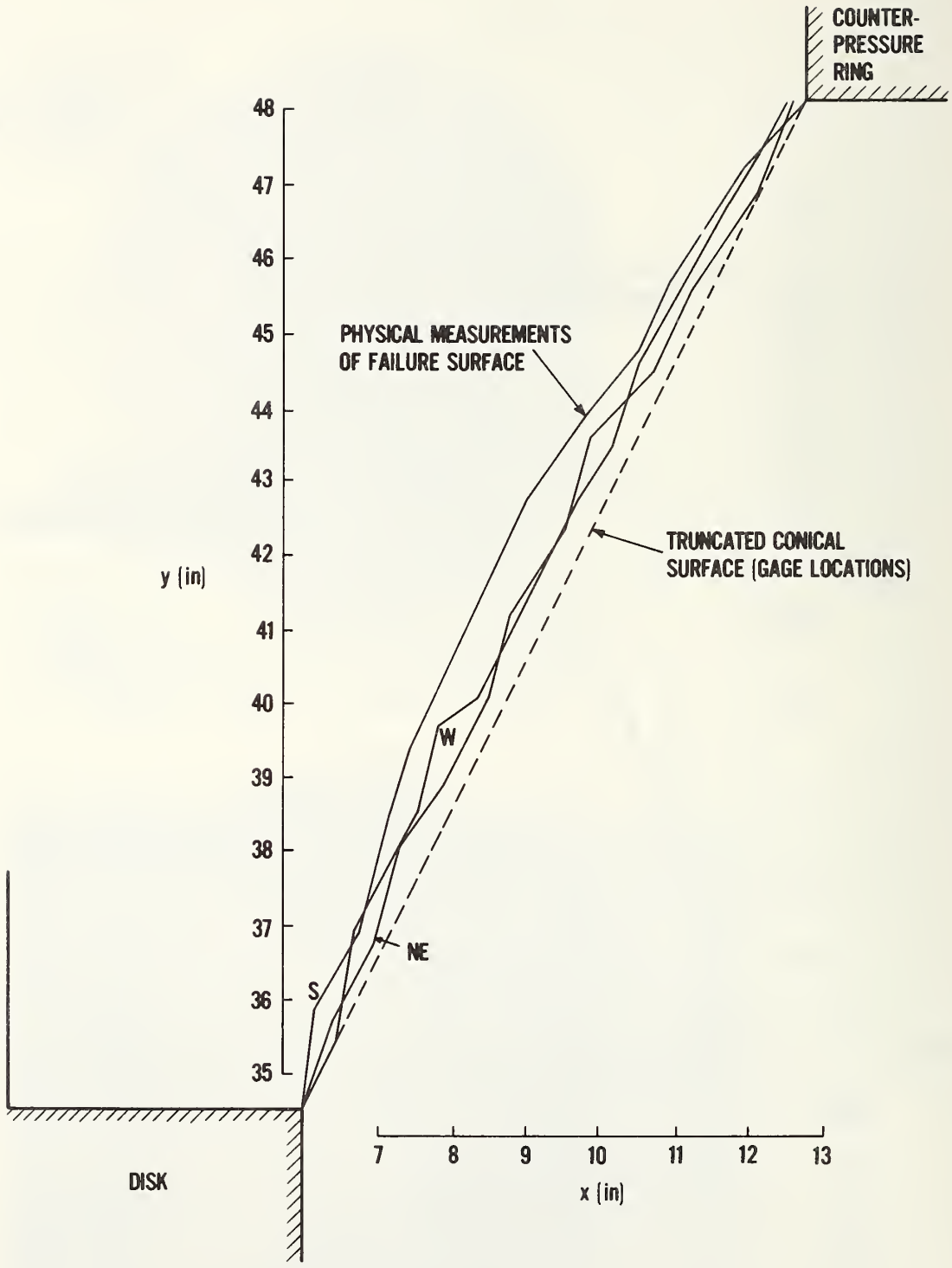

Figure 3.5b Measured failure surface for Specimen #2
$2\alpha = 54°$

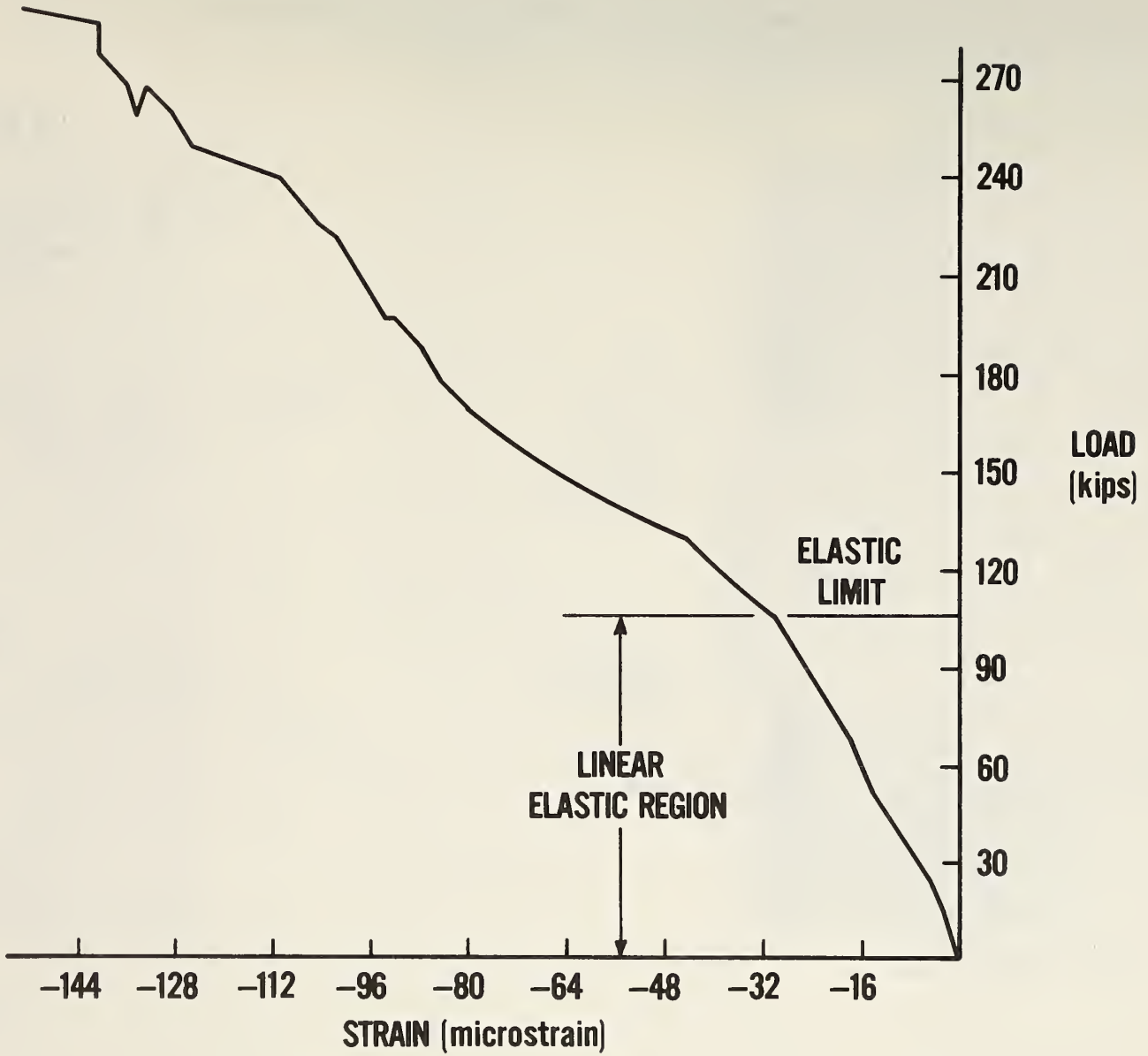

Figure 3.6 Typical embedded strain gage history -- axial gage #5 from Specimen 1

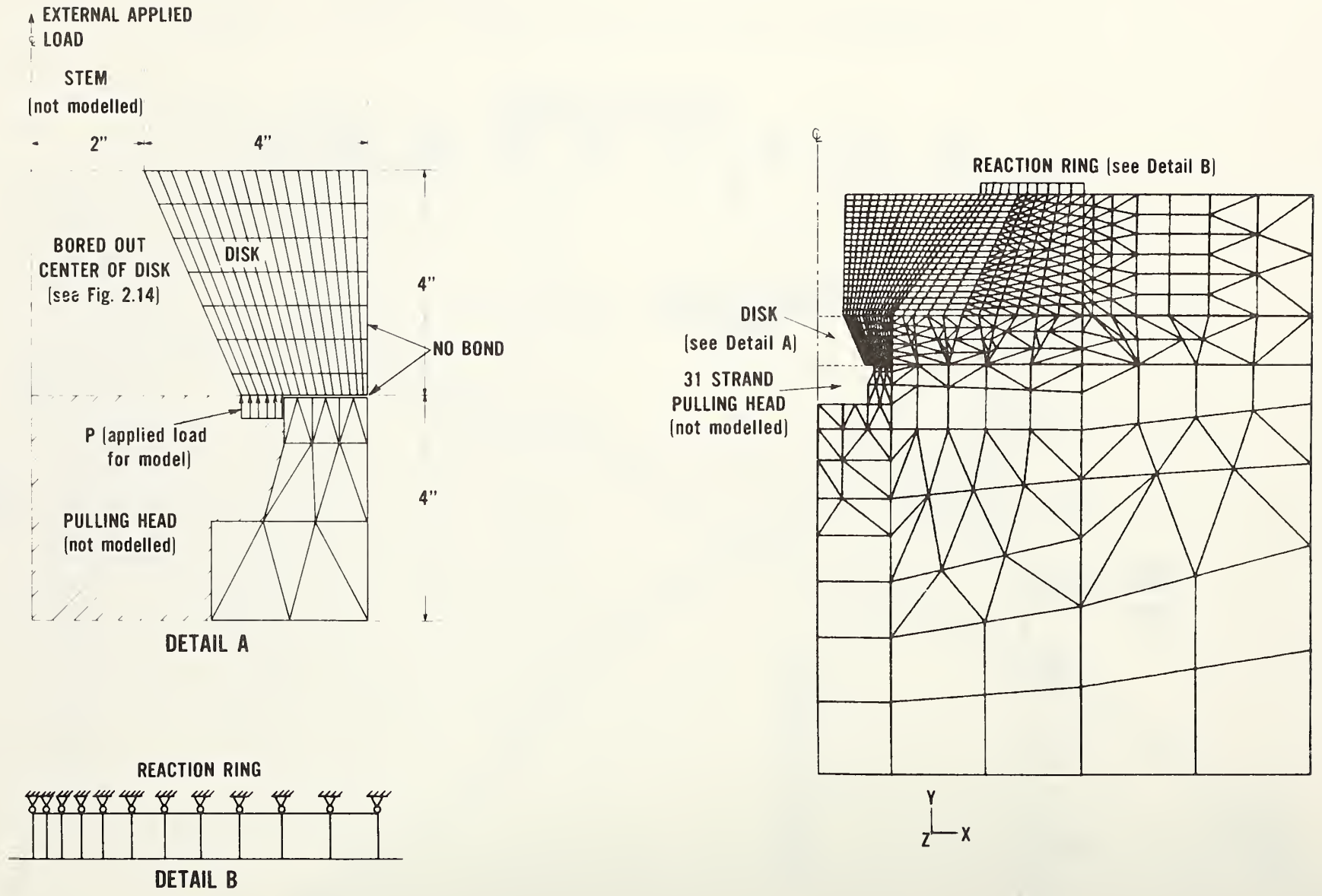

Figure 3.7 2D axysymmetric finite element mesh for Specimen #1

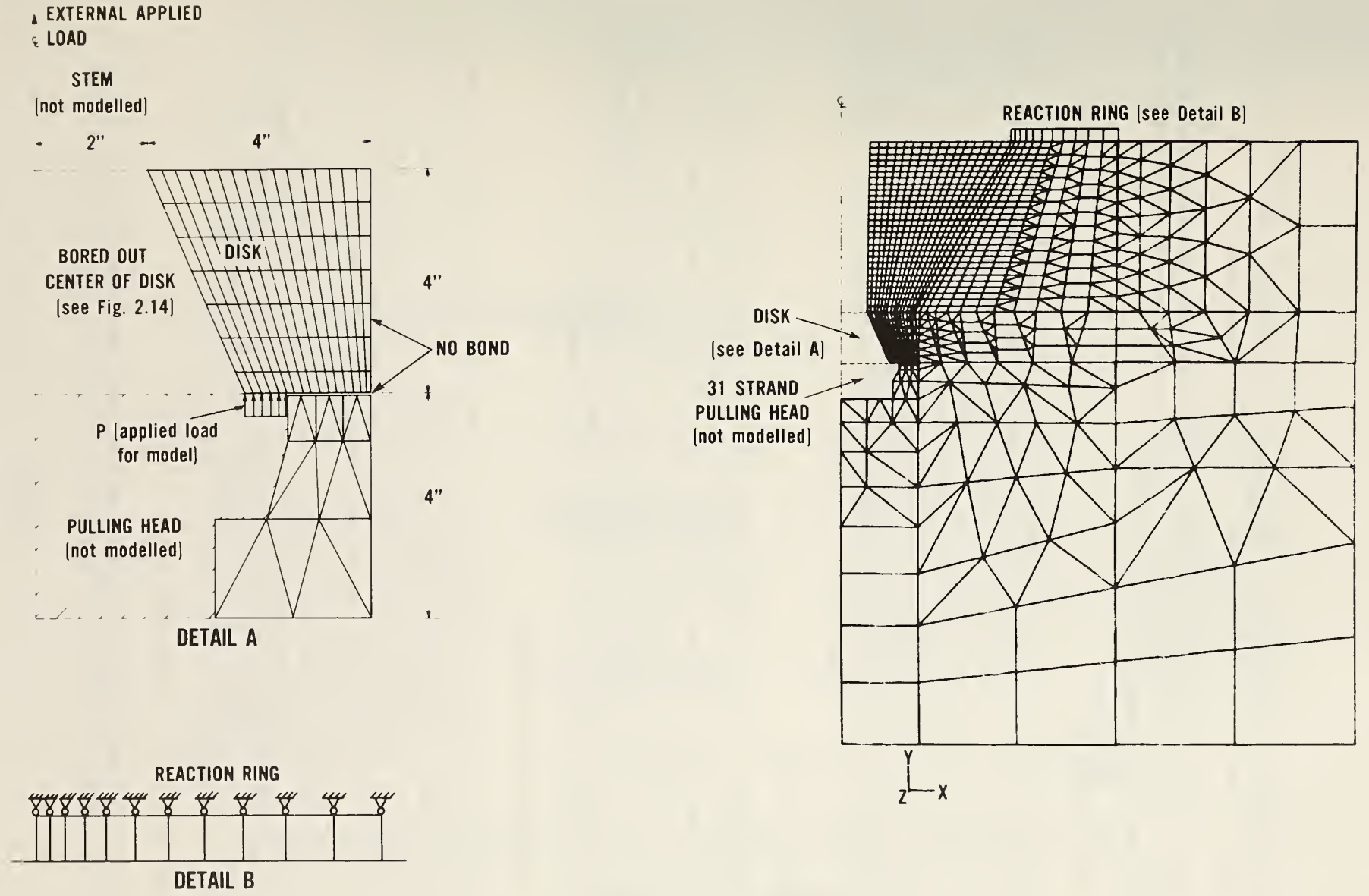

Figure 3.8 2D axysymmetric finite element mesh for Specimen #2

Institute formula 8.5.1. The value of Poisson's Ratio υ_c was obtained experimentally for each specimen. These were $E_c = 2.82(10)^6$ psi, $\upsilon_c = .16$ for specimen 1 and $E_c = 1.91(10)^6$ psi, $\upsilon_c = .16$ for specimen 2.

Comparisons between all experimental gage strings and the FEM predicted values are given in figures 3.9 through 3.20. For the most part the agreement between analytical and experimental values is good.

3.3.1 Axial Strain

The axial strain (i.e. the strain tangent to the surface of a conical frustum defined by the outer disk edge and inner reaction ring edge and parallel to the R-Z plane (figure 1.3)) is compressive and increases towards the disk edge and reaction ring. The maximum compressive strain occurs at the disk edge with a value approximately twice that of the compressive strain at the reaction ring. The minimum axial strain occurs at about 65 percent of the distance from the disk edge to the reaction ring (see figures 3.9 and 3.10). These latter two figures indicate a good fit with the FEM calculated strains, both in the general trend as well as the absolute numerical values.

3.3.2 Radial Strain

The radial strain (i.e., the strain perpendicular to the side of a conical frustum defined by the outer disk edge and inner reaction ring edge (figure 1.3)) decreases from a maximum tensile value at the disk edge to near zero at the reaction ring (see figures 3.11 and 3.12). The middle portion of the data (from x = 3 to x =10 for specimen #1 and from x =4 to x = 12 for specimen #2) indicates a relatively constant tensile strain in this region. While the general trends agree, the absolute numerical values predicted by the FEM analysis are substantially lower than those observed experimentally.

3.3.3 Circumferential Strain

The circumferential strain is tangent to the surface of the conical frustum defined by the outer disk edge and inner reaction ring edge, and perpendicular to the R-Z plane. Experimental data from specimen #1 ($2\alpha = 70°$) indicates that the circumferential strain is small and varies from slightly compressive near the disk edge to slightly tensile near the reaction ring. This contrasts with the analytical solution which indicates a nearly uniform low tensile strain between the disk and reaction ring. Specimen #2, on the other hand, agrees well with the analytical solution indicating a near uniform low (less than 10 microstrain) tensile strain from the disk edge to the reaction ring (see figures 3.13 and 3.14). With strains this small the experimental gage sensitivity (+/- 6 microstrain) could account for the majority of the differences between the analytically predicted and experimentally observed values.

3.3.4 Vertical Strain Near Side Face

The highest recorded tensile strains occurred near the side face of the disk, with the maximum values near the top edge of the disk (see figures 3.15 and

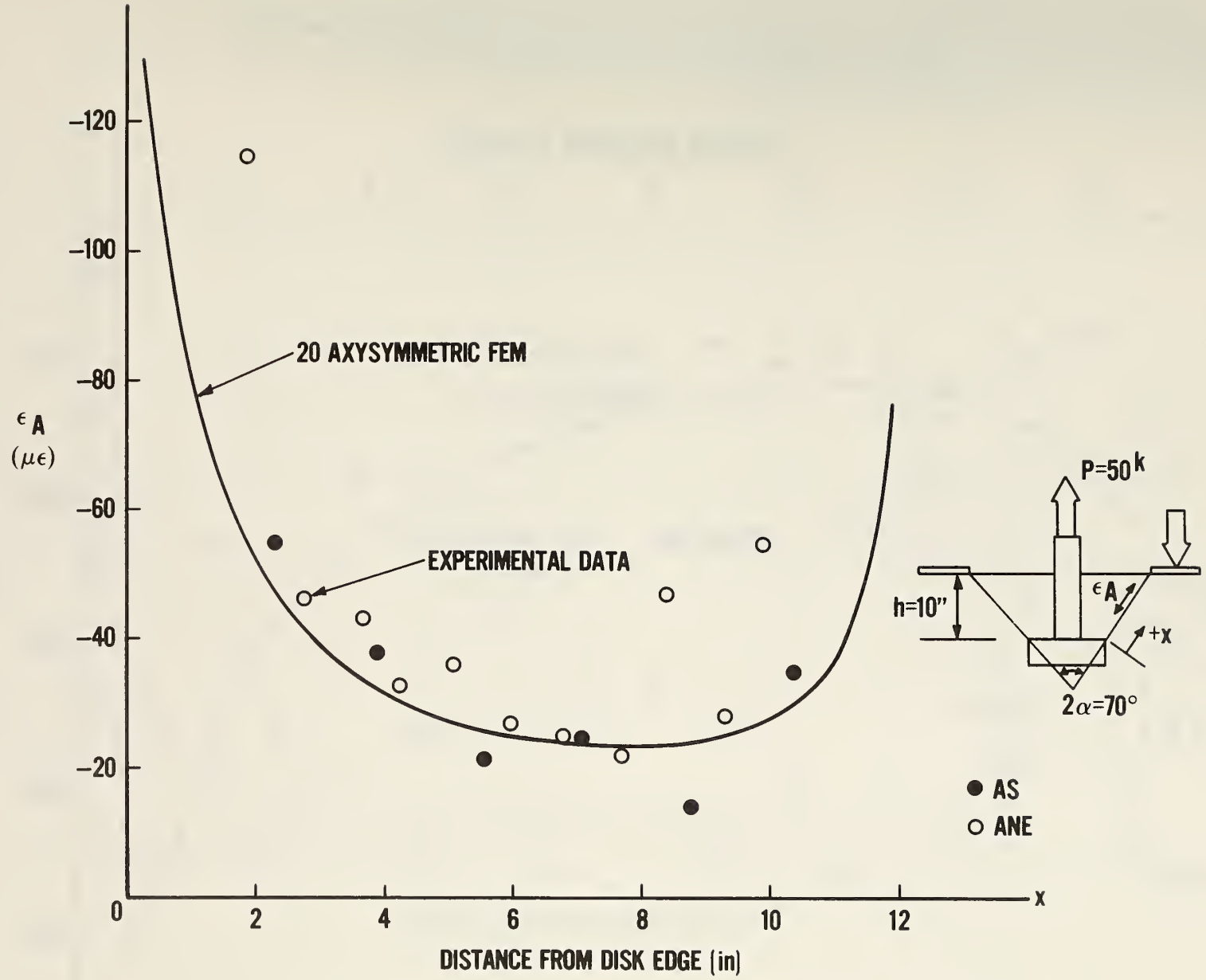

Figure 3.9 Axial strain along Frustum surface expermental vrs FEM
Specimen #1 $2\alpha = 70°$

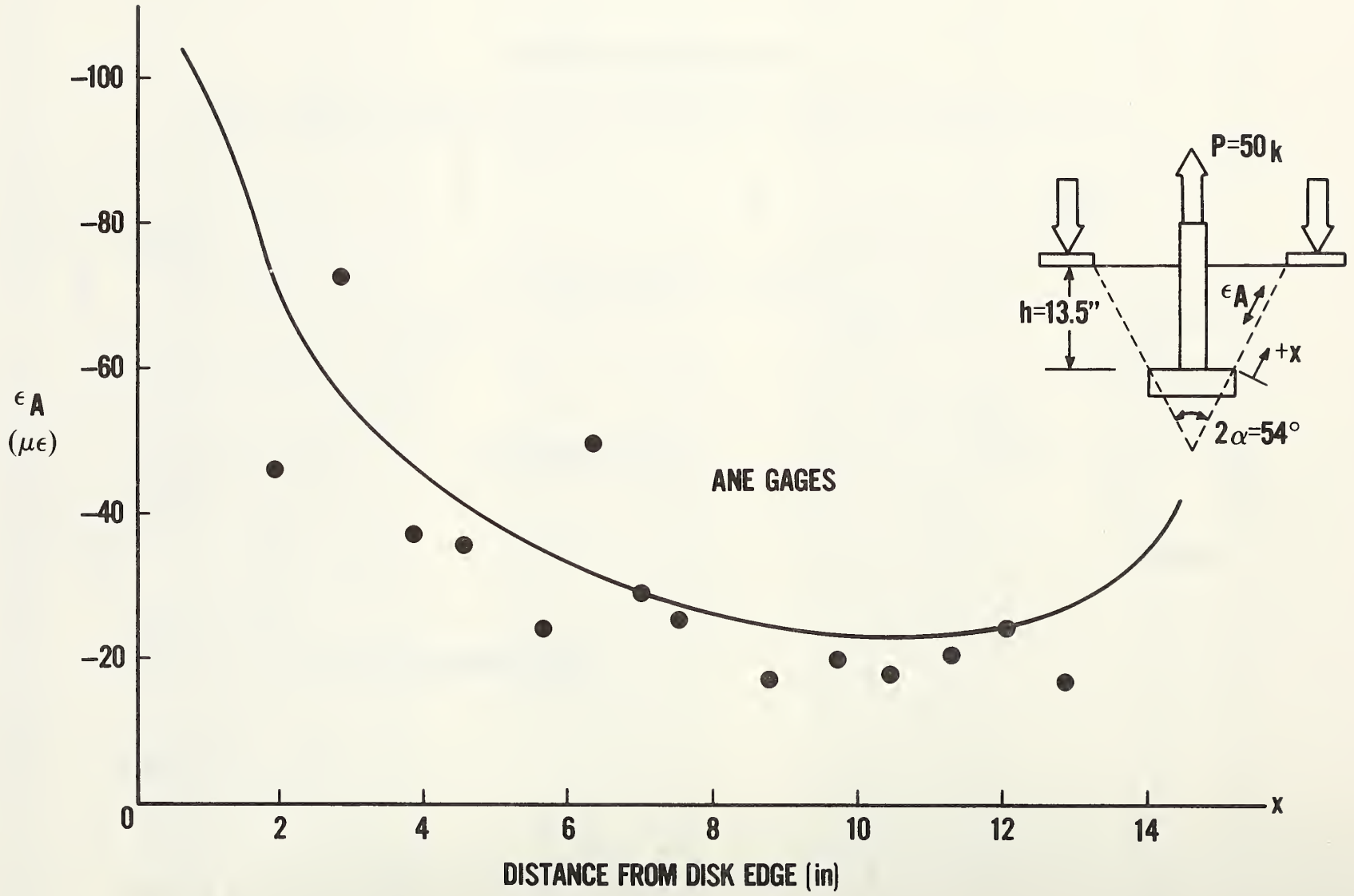

Figure 3.10 Axial strain along Frustum surface experimental vrs FEM
Specimen #2 2α = 54°

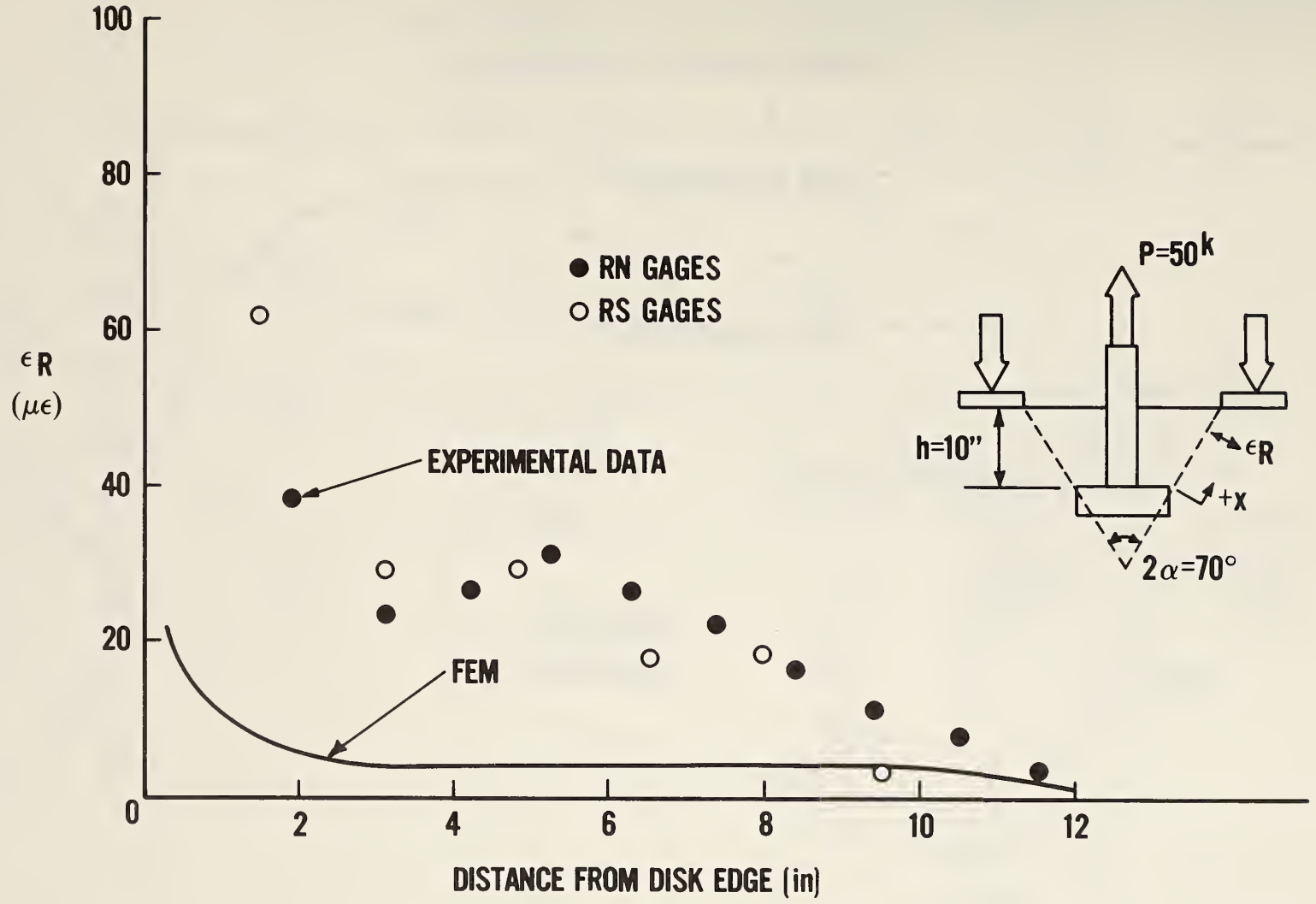

Figure 3.11 Radial strain along Frustum surface experimental vrs FEM
Specimen #1 $2\alpha = 70°$

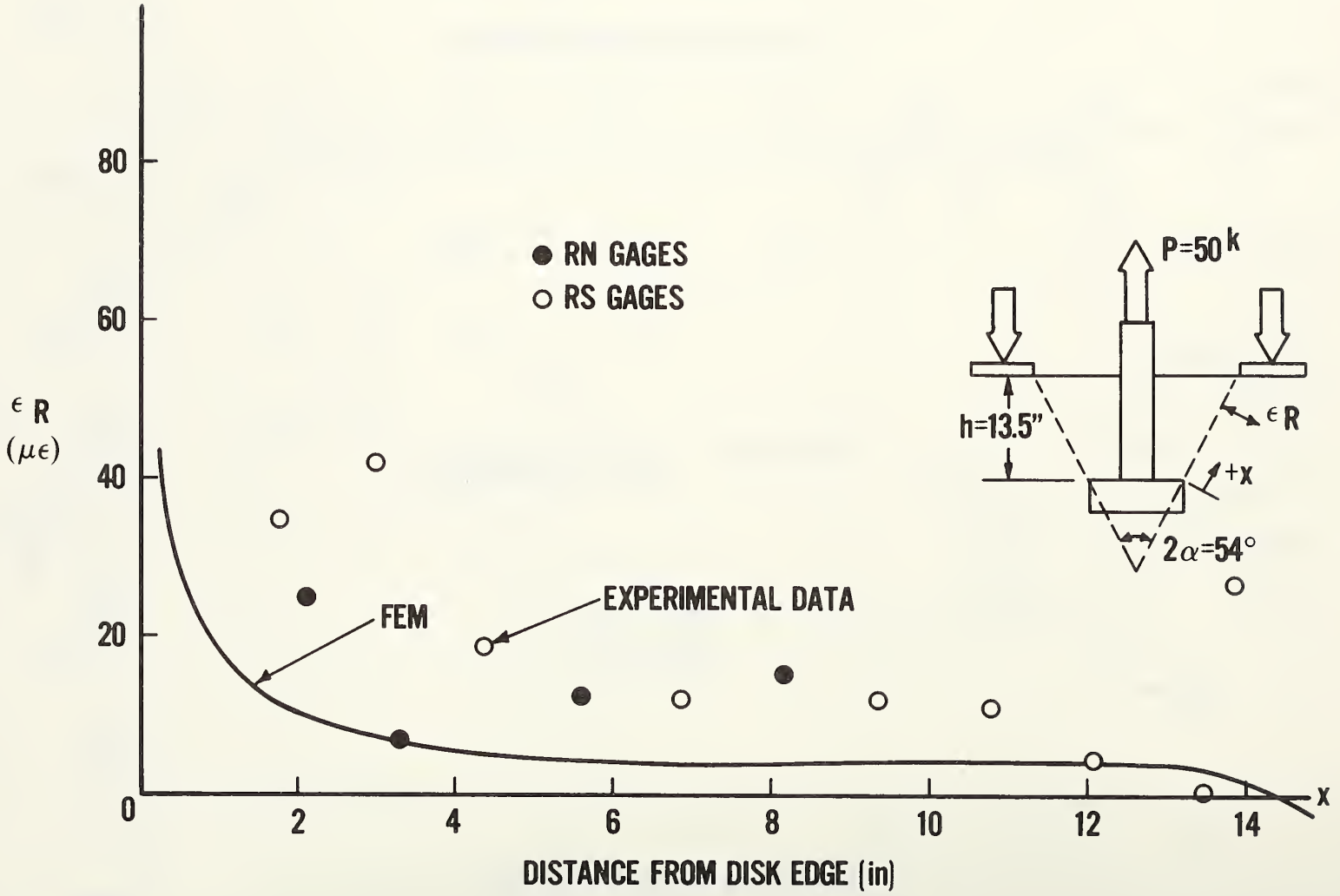

Figure 3.12 Radial strain along Frustum surface experimental vrs FEM
Specimen #2 $2\alpha = 54°$

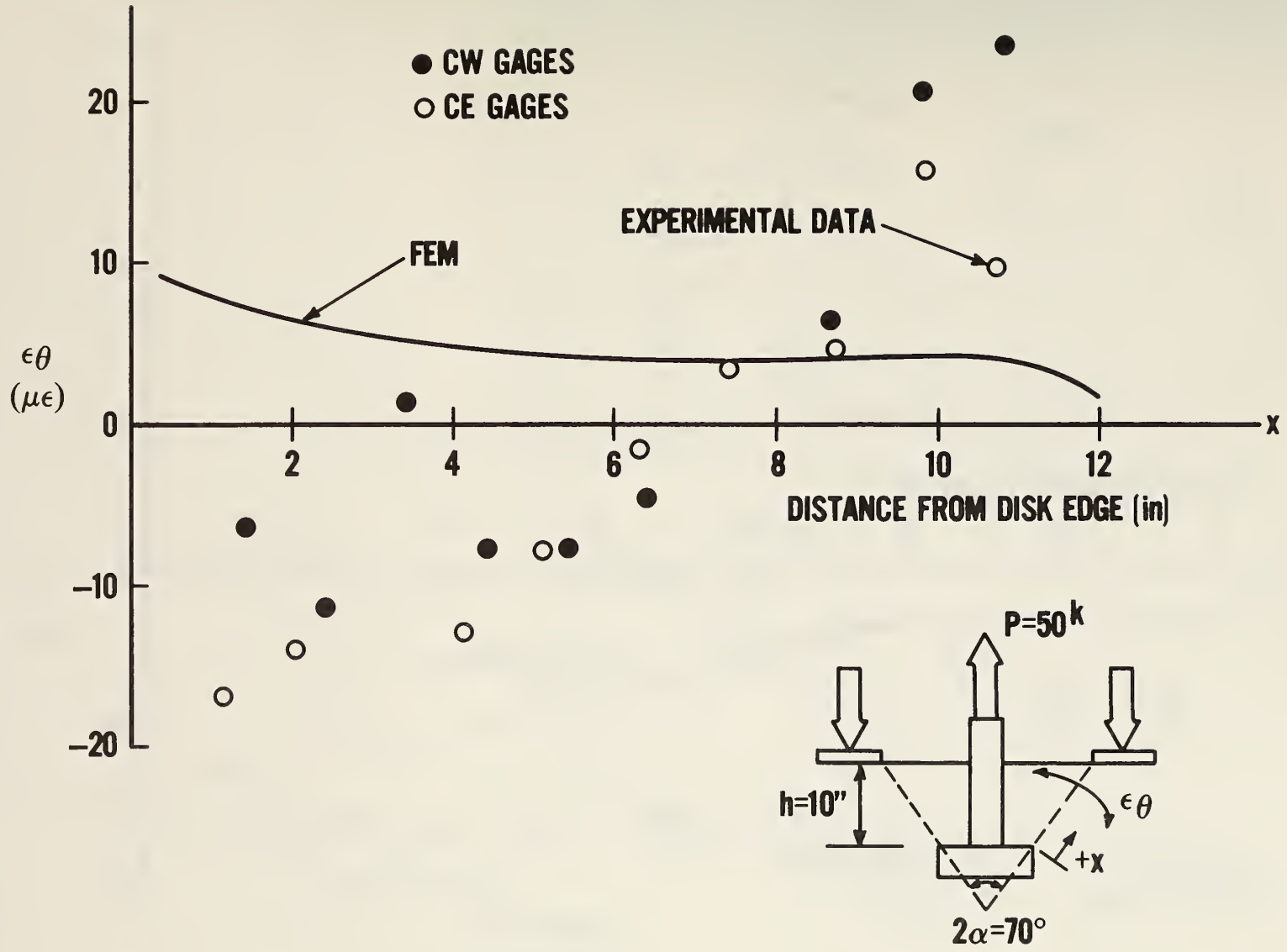

Figure 3.13 Circumferential strain along Frustum surface experimental vrs FEM
Specimen #1 $2\alpha = 70°$

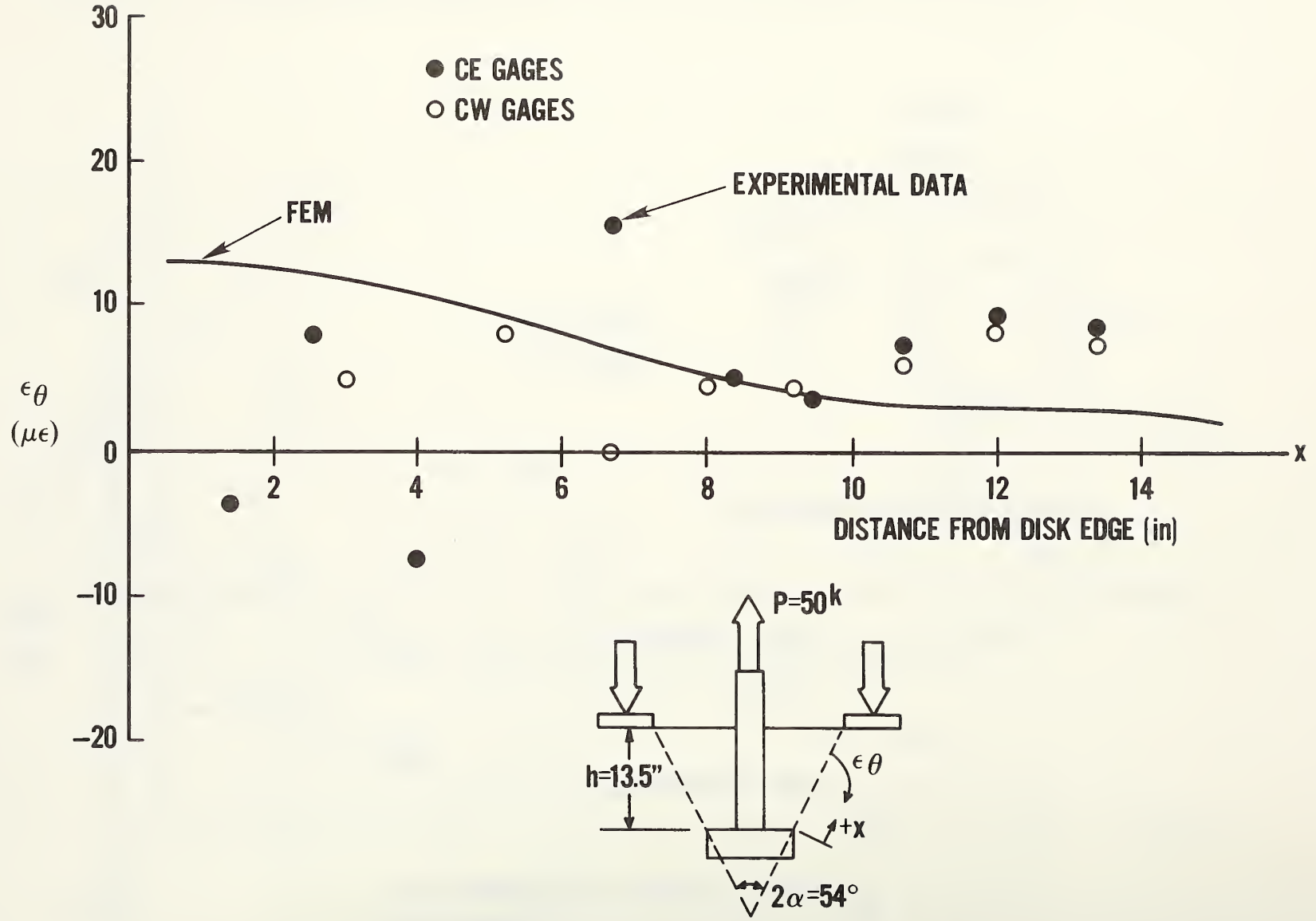

Figure 3.14 Circumferential strain along Frustum surface experimental vrs FEM
Specimen #2 $2\alpha = 54°$

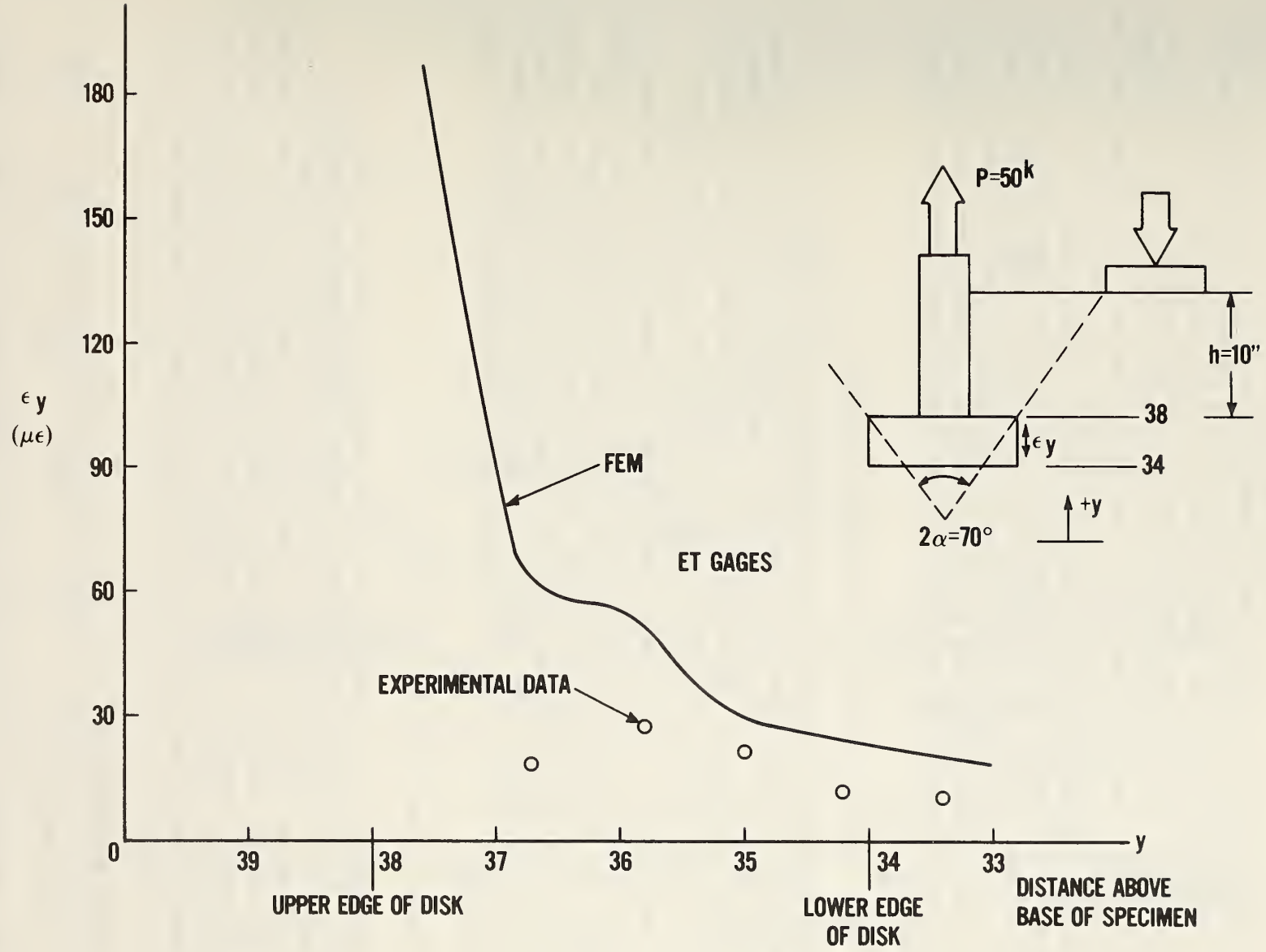

Figure 3.15 Vertial strain adjacent side of experimental vrs FEM
Specimen #1 2α = 54°

3.16). Because there is little bond between the concrete and the side face of the disk, the load is transmitted to the concrete primarily in compression via the top face of the disk. At the disk edge the load is applied to a right angle or "re-entrant" corner, giving rise to a large tensile strain concentration [15]. This strain concentration was monitored in specimen #2 as indicated by the high point near the top edge of the disk. Due to a faulty gage this was not seen in specimen #1. The maximum experimental value of 165 microstrain (specimen #2) exceeds the nominal limiting tensile strain capacity of concrete as recommended by Rusch [14]. We would thus expect that the concrete in the vicinity of the top edge of the disk would be cracked at this load stage, and indeed, further study showed this to be the case (see figure 3.40 section 3.5.3). The general trend, and absolute numerical values, agree fairly closely for experimentally observed and FEM predicted strains, with the latter being slightly higher than the former.

3.3.5 Radial Strain on Vertical Line Above Disk Edge

These data indicated the radial strain (parallel to the r-axis) to be compressive at the disk edge, but changing to a tensile state a short distance above the disk (see figures 3.17 and 3.18). The location of this cross over point varied, occuring at approximately 0.5 inches (12.7mm or 0.037h) above the top face of the disk for specimen #2, while occuring at 1.5 inches (38mm or 0.15h) above the top face of the disk for specimen #1. Good correlation between analytical and experimental results was obtained for both specimens. This strain pattern is very typical of concrete structures with post-tensioned anchorages and is usually referred to as the "bursting" strain/stress--the transverse tensile strain ahead of the loading plate. In thin web structures it was believed that this tensile strain caused cracking or "bursting" along the tendon path ahead of the anchor. For the pullout study these gages were used to attempt to detect the deviation of the failure surface from the linear conic frustum.

3.3.6 Radial Strain Near Top Disk Face

These gages were used to measure the strain parallel to the top disk face in an effort to study the triaxial state of stress which exists in this area. The experimental data indicate a linear increase in lateral compressive strain towards the outer edge of the disk. The analytical solution, for both specimens #1 and #2, agrees with the experimental edge compressive strains, but indicates a slight tension toward the stem (see figures 3.19 and 3.20). This difference may be due to the inability of the program to precisely model the complex friction boundary conditions existing at the interface of the concrete and the top face of the disk.

3.4 ELASTIC BEHAVIOR

3.4.1 Stress Contours

Given the reasonably good correlation between the results of the finite element model and the experimental gage data in the precracked state, we can proceed with an examination of the overall precracked state of stress by means of the

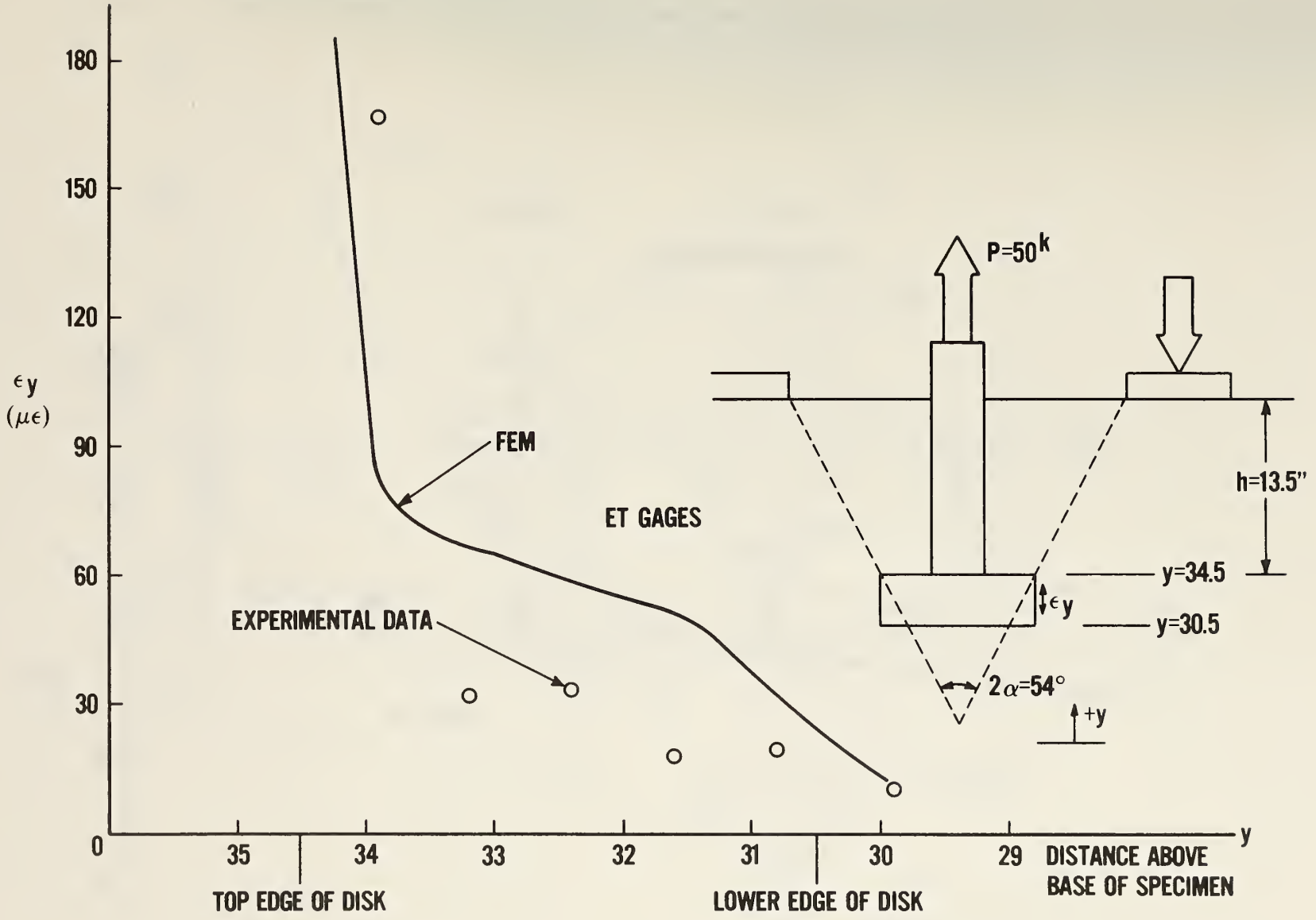

Figure 3.16 Vertical strain adjacent to side of disk experimental vrs FEM
Specimen #2 2α =54°

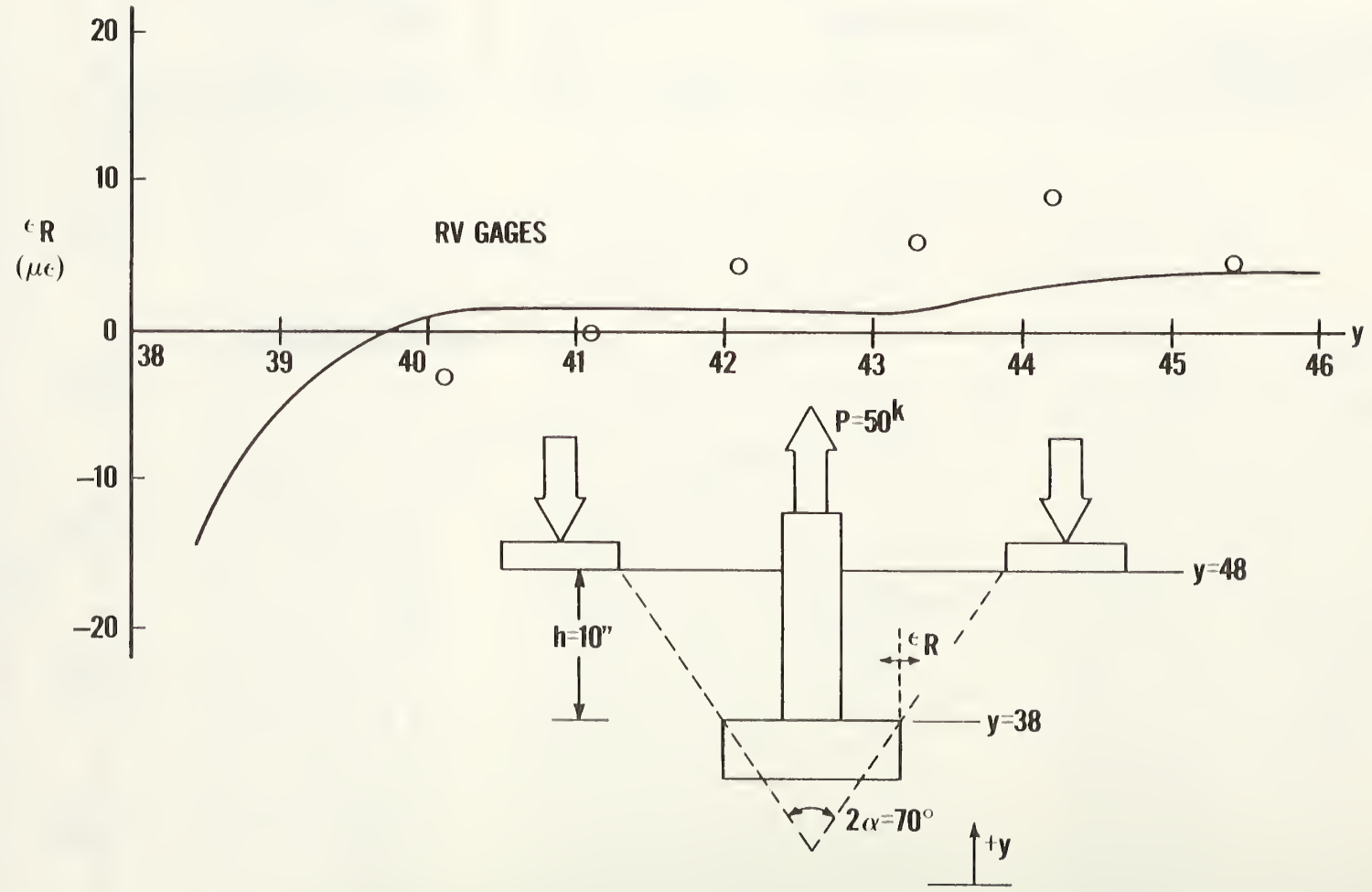

Figure 3.17 Radial strain on vertical line above disk edge experimental vrs FEM Specimen #1 $2\alpha = 70°$

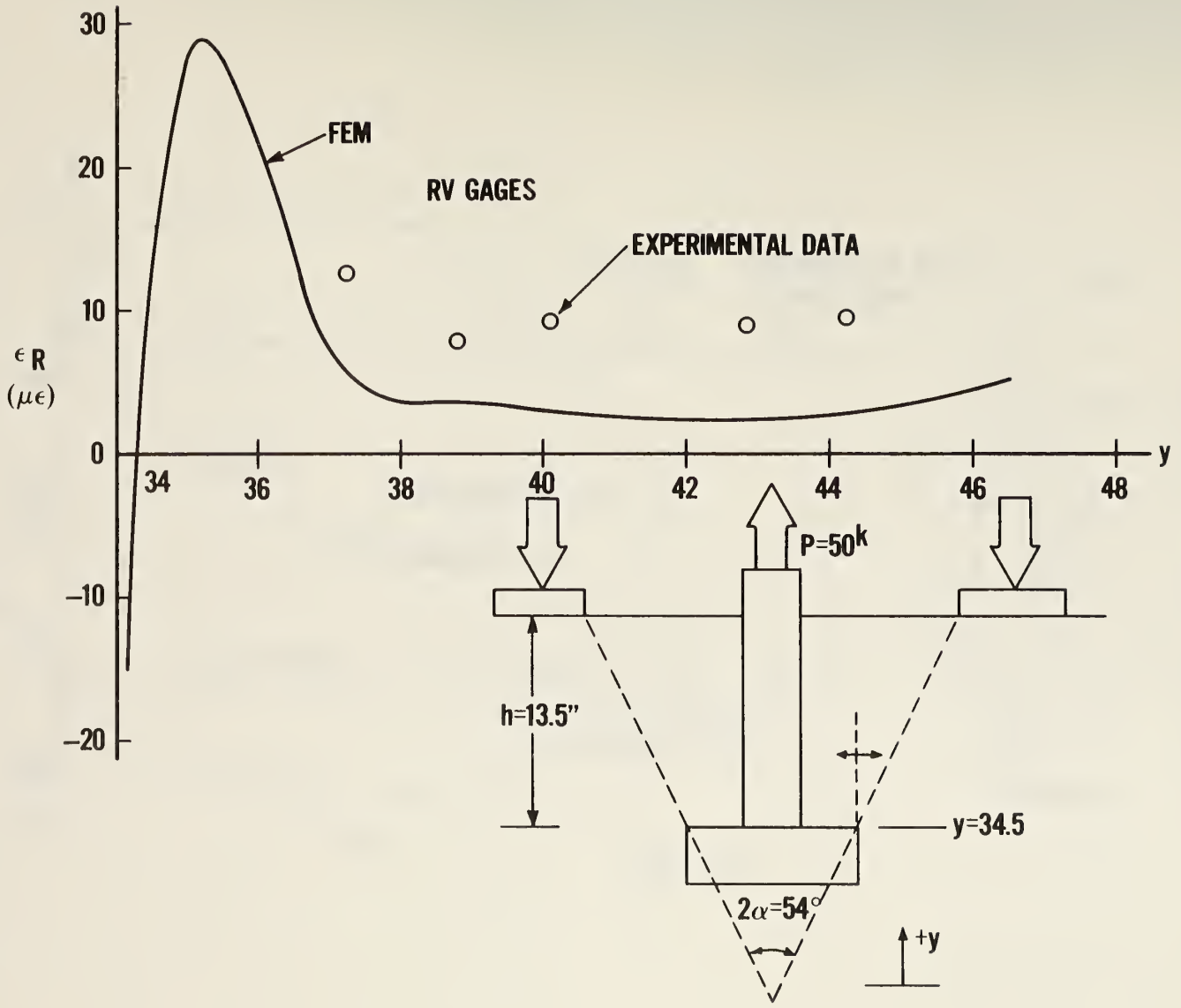

Figure 3.18 Radial strain on vertical line above disk edge experimental vrs FEM Specimen #2 $2\alpha = 54°$

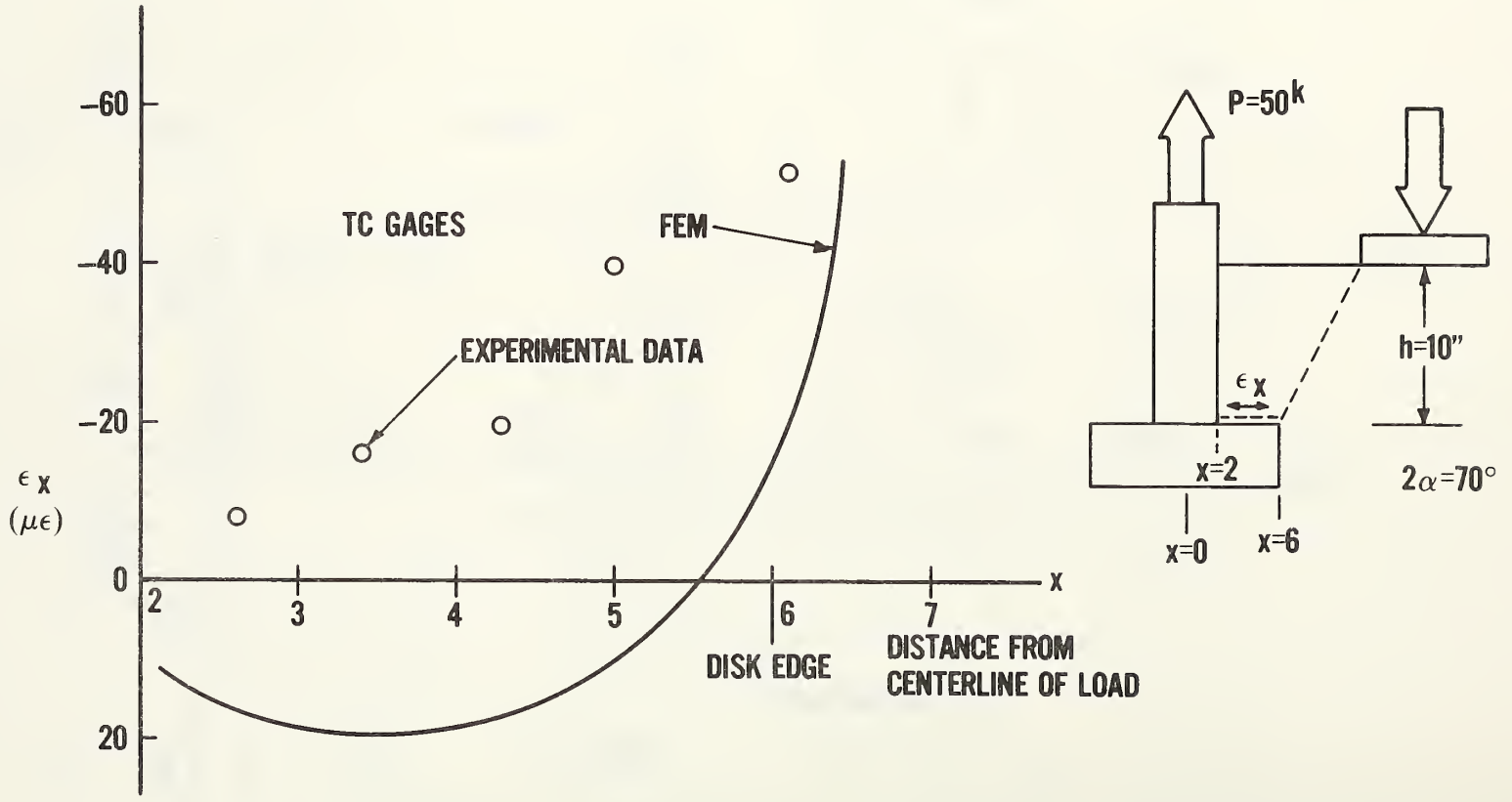

Figure 3.19 Radial strain along disk face experimental vrs FEM
Specimen #1 2α = 54°

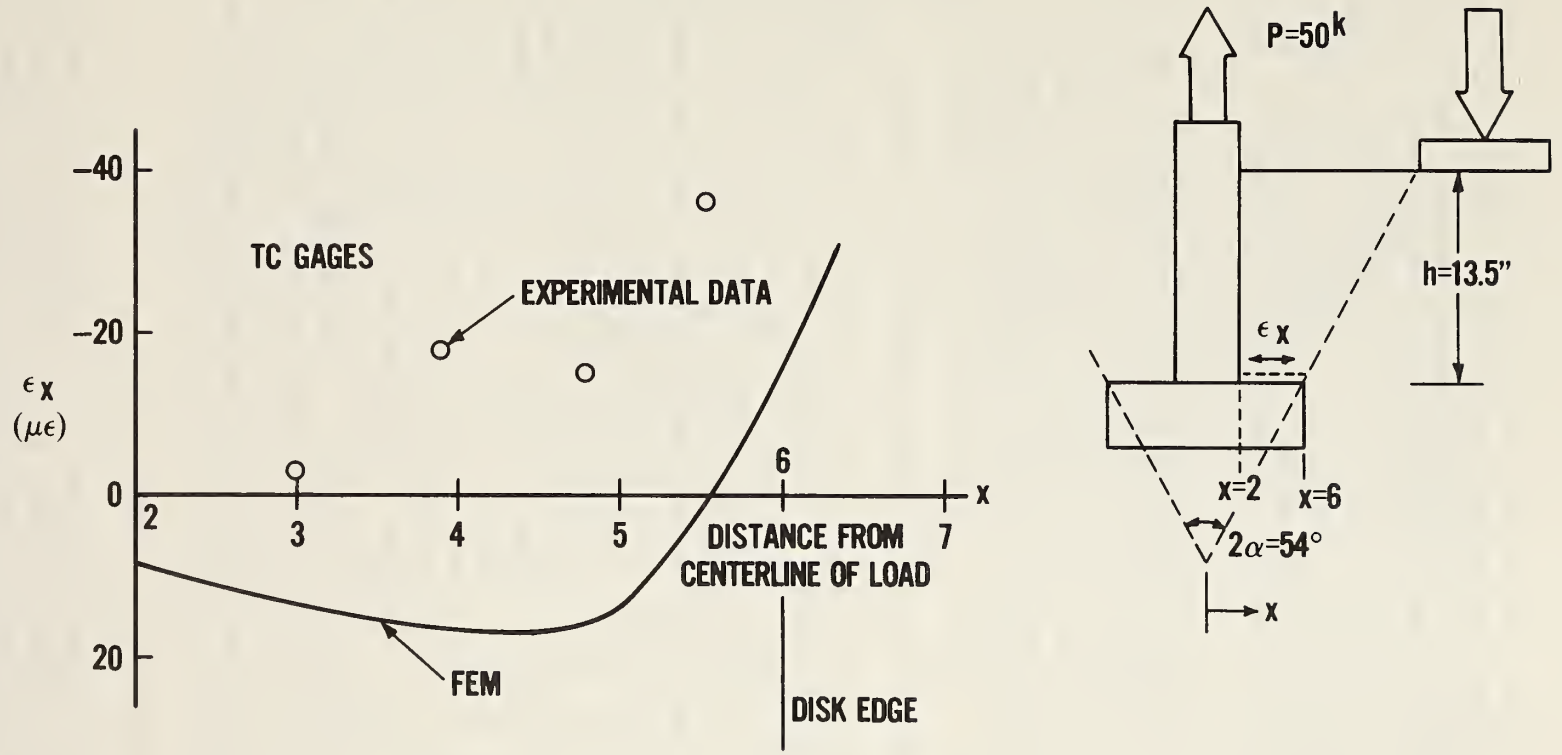

Figure 3.20 Radial strain along disk face experimental vrs FEM
Specimen #2 2α = 54°

analytical model. One of the most useful devices for identifying critically stressed regions is a stress contour plot. Figures 3.21 and 3.22 present the maximum principal stress contours for specimens 1 and 2 respectively. Tensile stresses are positive. From these plots it is clear that the maximum tensile stresses occur adjacent to the top edge of the disk. As mentioned previously this is due to the presence of the loaded re-entrant corner which creates a strain (and therefore a stress) concentration. This tensile stress decreases rapidly along the failure surface towards the reaction ring and a sign reversal occurs at approximately 90 percent of the distance to the reaction ring.

Contour plots of the minimum principal stress for specimens 1 and 2 are given in figures 3.23 and 3.24 respectively. From these it is apparent that the peak compressive stresses occur just ahead of the upper disk edge and beneath the reaction ring inner edge. The largest compressive stress at the disk is approximately three times the compressive stress at the reaction ring for specimen 1 and 3.75 times that at the reaction ring for specimen 2. There is a lower stress "saddle" between these two maxima, with the minimum value occuring at approximately 65 percent of the distance to the reaction ring.

3.4.2 Principal Stress Profiles Along Failure Surface

The variations in stresses along the idealized conic frustum failure surfaces are presented in figures 3.25 through 3.28. For these plots the analyses were conducted with $E_{c_1} = E_{c_2} = 2.82(10)^6$ psi and $\upsilon_{c1} = \upsilon_{c2} = .16$, such that the effect of the geometry change between specimens 1 and 2 could be isolated, independent of varying material properties. Figure 3.25 (maximum principal stresses) shows that the peak tensile stress for specimen 2 is, on the average, about 37 percent lower than for specimen 1 with the greatest difference (45 percent) occurring at the disk edge. Figure 3.26 (minimum principle stresses), on the other hand, shows a close similarity between specimens 1 and 2. The maximum difference occurs at approximately x/d = 0.1 where the minimum stress for specimen #2 is 25 percent below that for specimen #1. However, the peak compresive stresses at the disk edge and reaction ring edge show very little difference. The maximum shear stresses in the r-z plane (figure 3.27) exhibits the same trends as the minimum principal stress with nearly identical peak values for specimens 1 and 2. Figure 3.28 shows the circumferential stress variation along the frustum surface. Notably this stress is tensile, and nearly uniform over the majority of the surface. Towards the disk edge, and towards the reaction ring the circumferential stress becomes compressive. From figures 3.25, 3.26 and 3.28 it is apparent that the state of stress along the majority of the frustum surface (see figure 3.29) is biaxial tension-compression, with the highest tensile stresses occurring near the disk edge.

3.4.3 Principal Stress Trajectories

The principal stress direction (or trajectory) plots for specimens 1 and 2 are presented in figures 3.30 and 3.31 respectively. The solid lines represent the maximum principal stress directions while the dashed lines represent the minimum principal stress directions. Interestingly, the geometry of the experimentally measured failure surface coincides closely (more so with specimen #1 than with specimen #2) with the minimum principal stress trajectories between

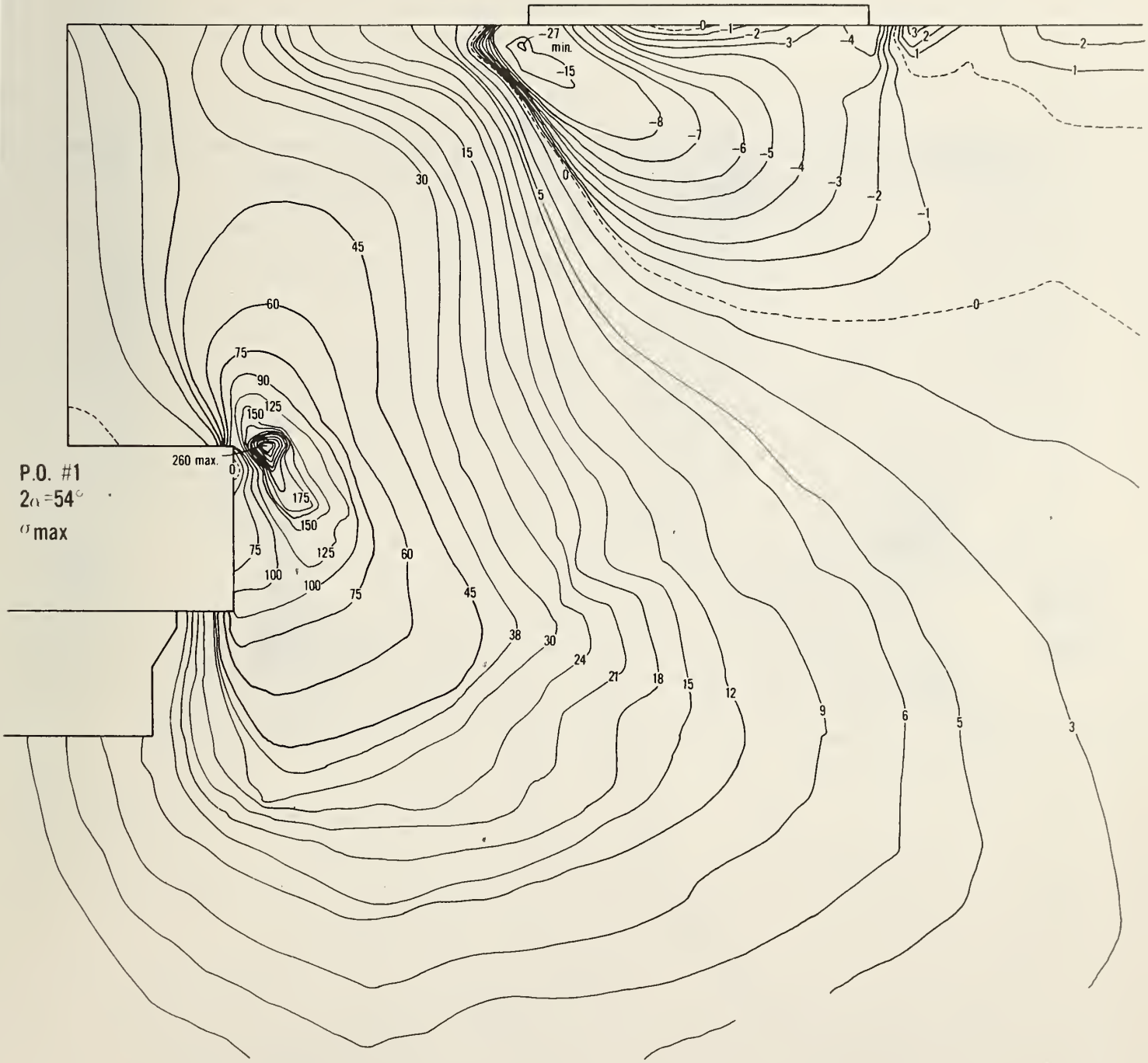

Figure 3.21 Maximum stress contours for Specimen #1 ($2\alpha = 70°$) for a load of P = 50 kips (17% of ultimate) (from 2D axisymmetric FEM analysis) All units are in psi (pounds per square inch)

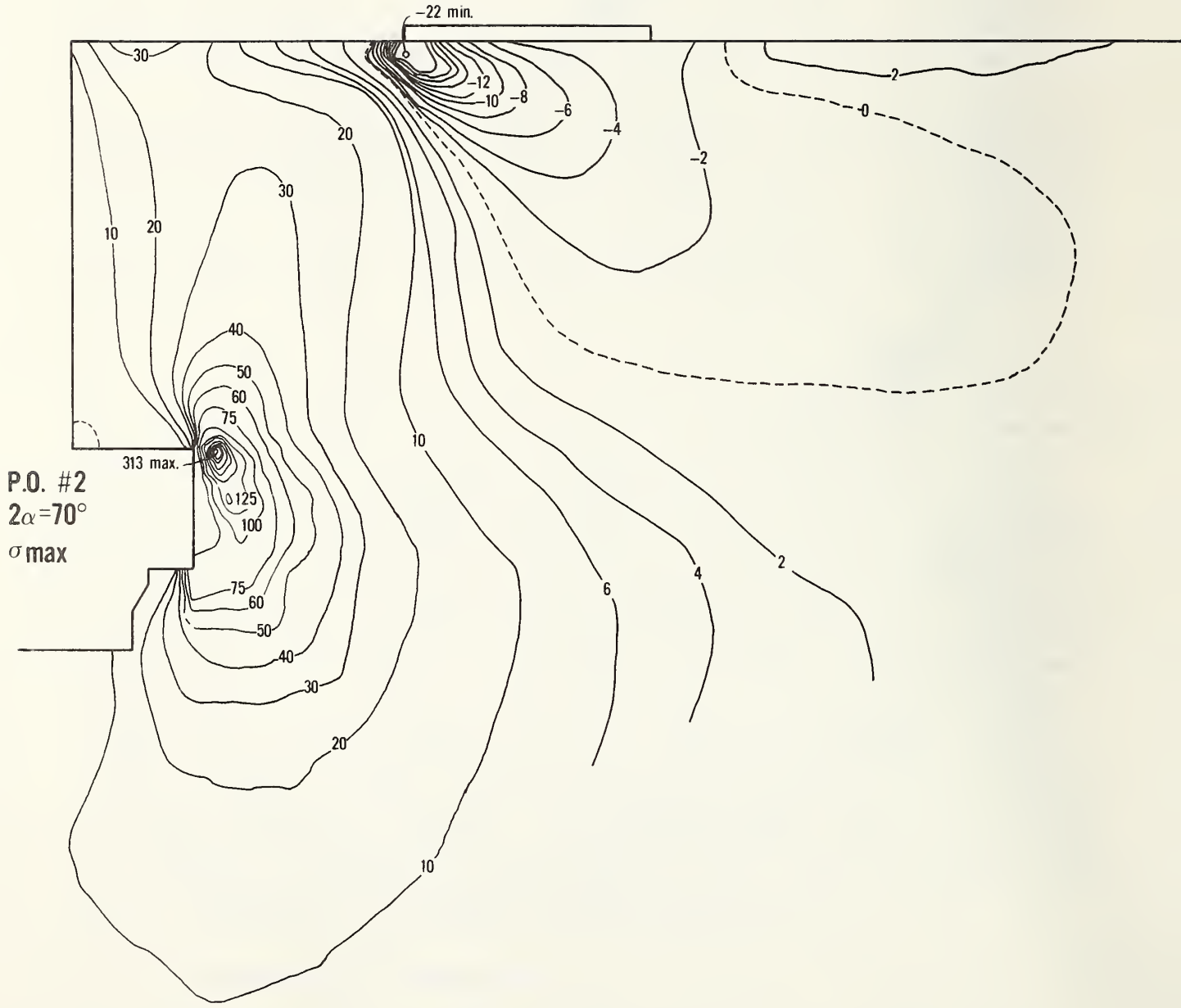

Figure 3.22 Maximum principal stress contours for Specimen #2 ($2\alpha = 54°$) for a load of P = 50 kips (19% of ultimate) (from 2D axisymmetric FEM analysis). All units are in psi (pounds per square inch)

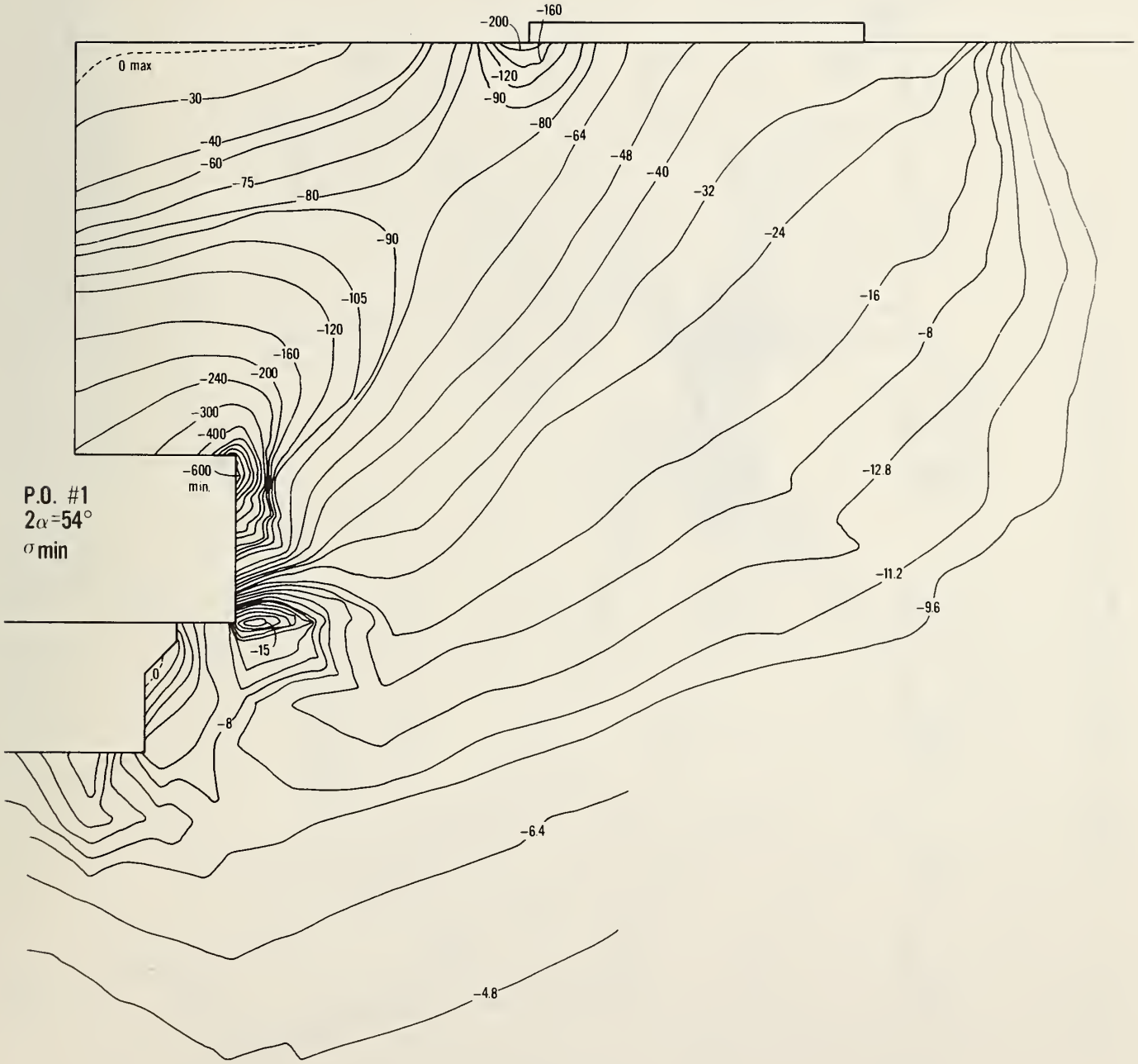

Figure 3.23 Minimum principal stress contours for Specimen #1 ($2\alpha = 70°$) for a load of P = 50 kips (17% of ultimate) (from 2D axisymmetric FEM analysis). All units are in psi (pounds per square inch)

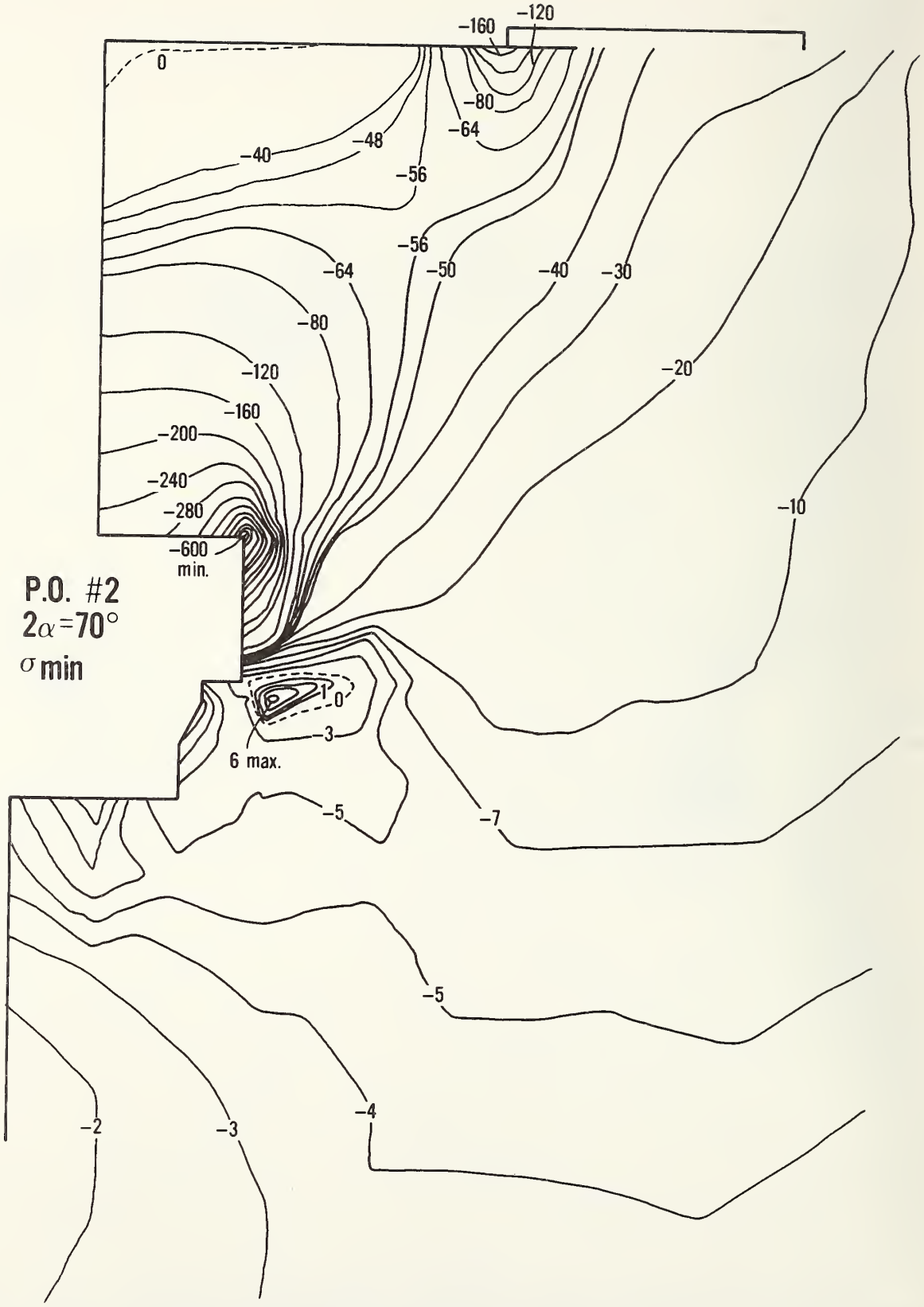

Figure 3.24 Minimum principal stress contours of Specimen #2 ($2\alpha = 54°$) for a load of P = 50 kips (19% of ultimate) (from 2D axisymmetric FEM analysis). All units are in psi (pounds per square inch)

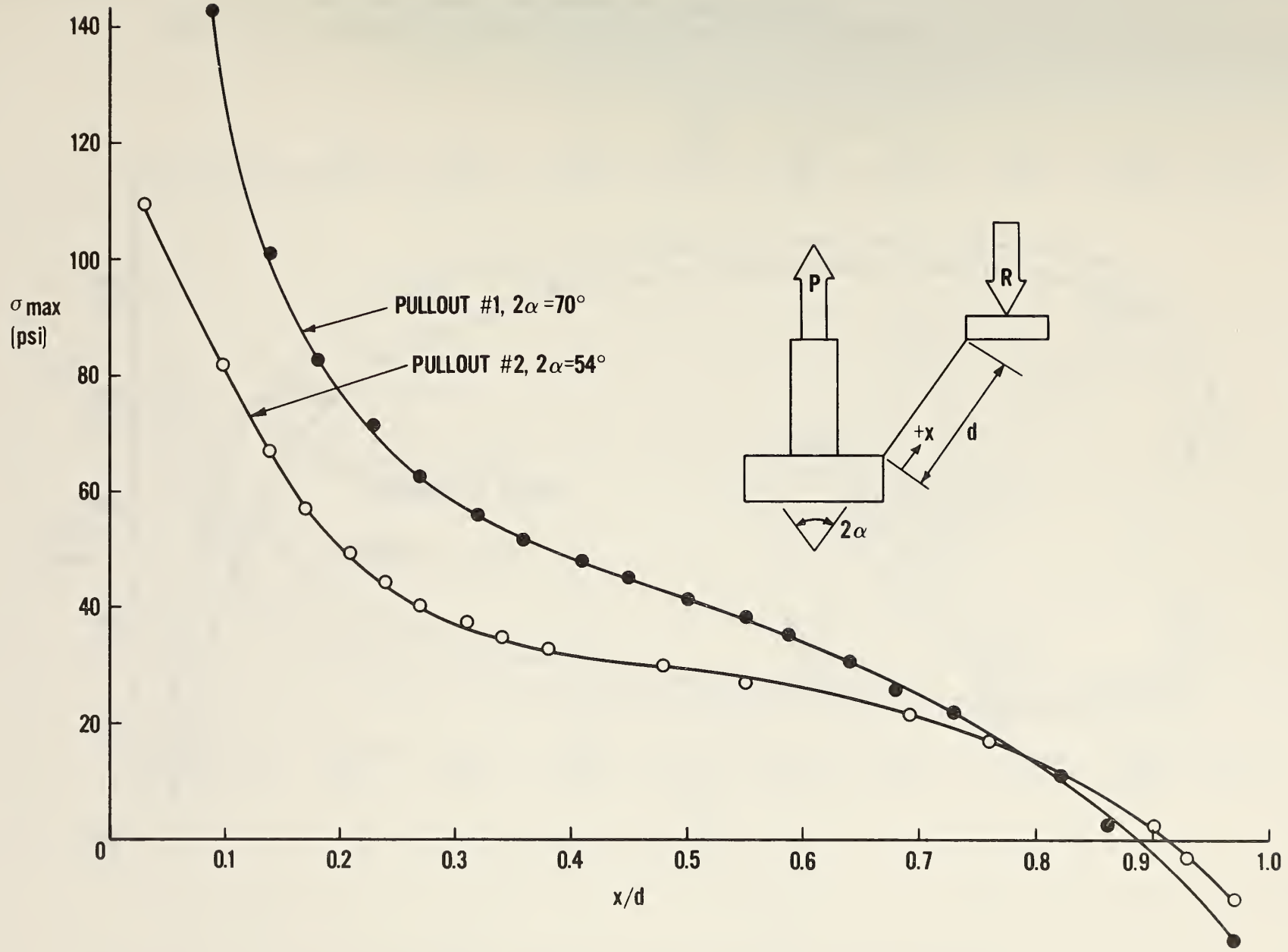

Figure 3.25 Variation of maximum principal stress along Frustum surface (from axisymmetric FEM analysis)

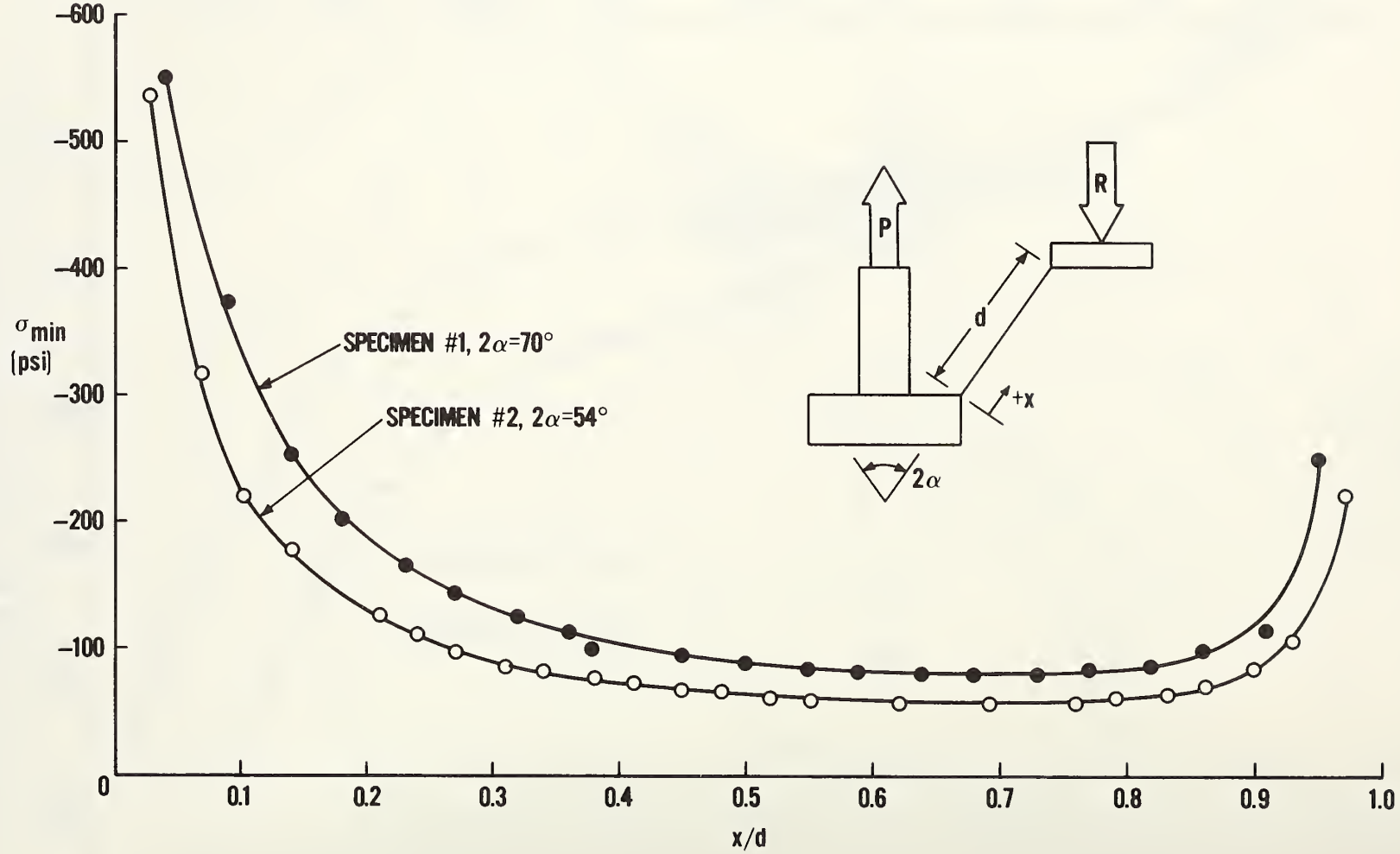

Figure 3.26 Variation of minimum principal stress along Frustum surface (from 2D axisymmetric FEM analysis)

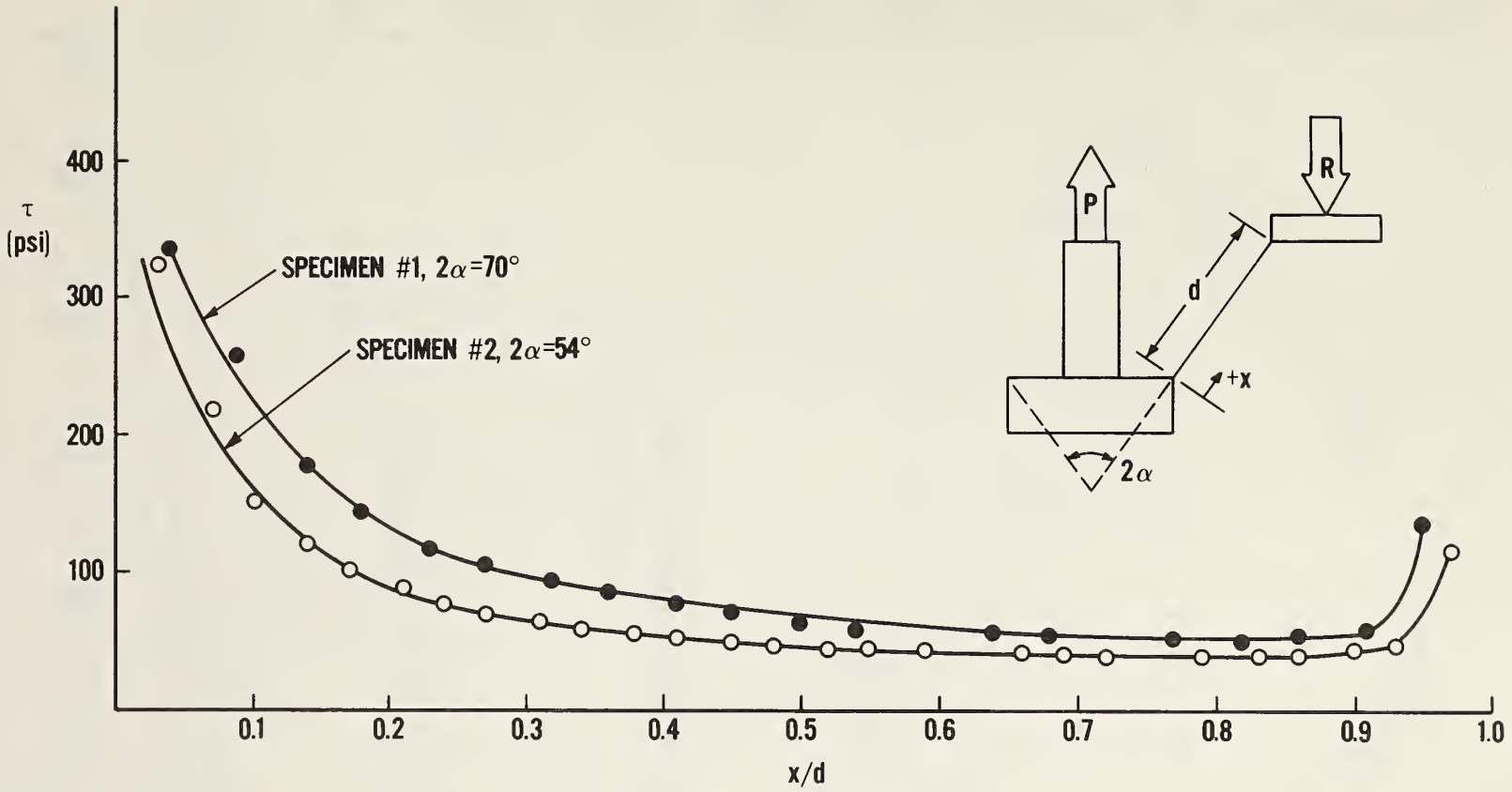

Figure 3.27 Variation of maximum shearing stress (R-Z plane) along Frustum surface (from 2D axisymmetric FEM analysis)

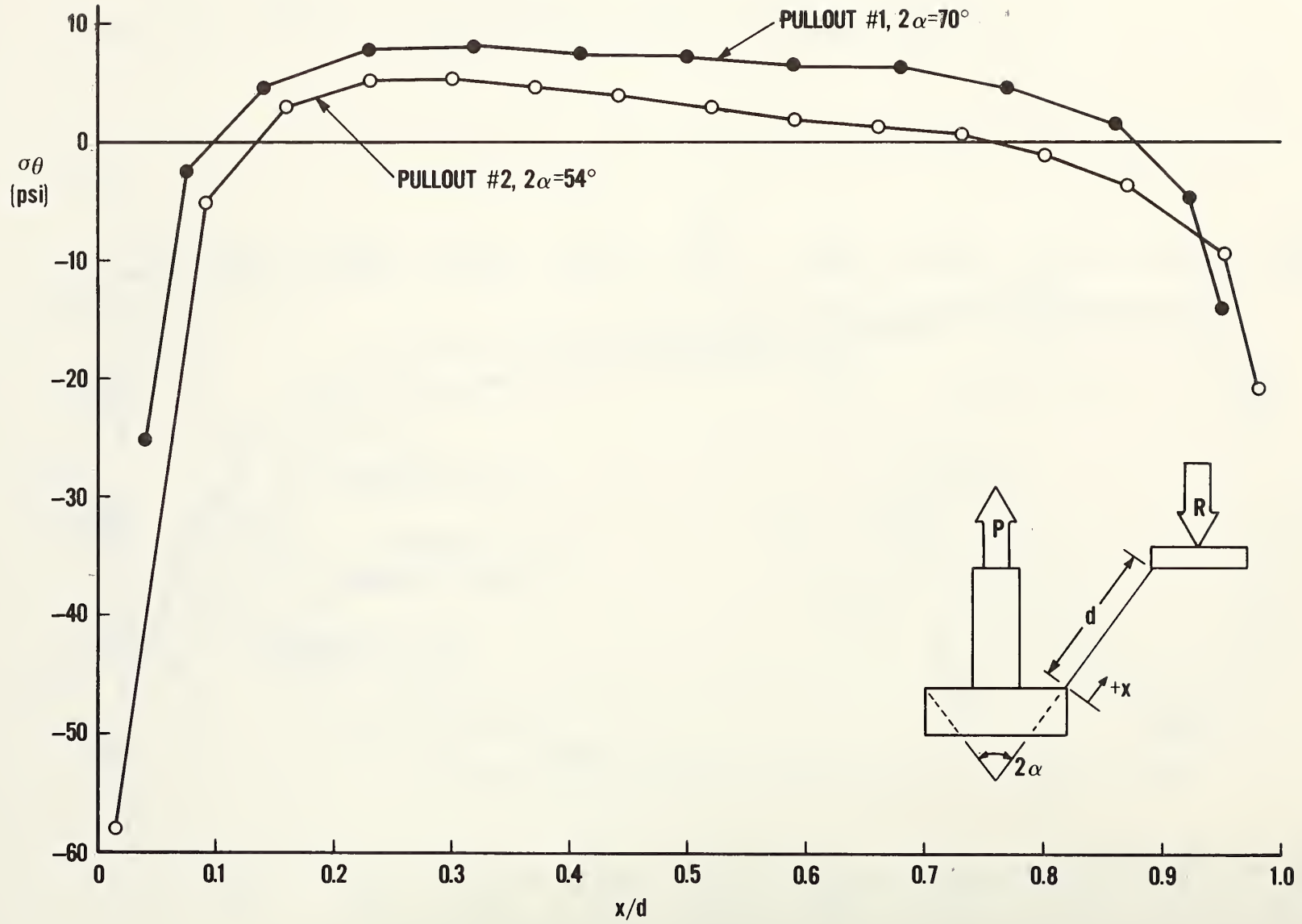

Figure 3.28 Variation of circumferential stress along Frustum surface (from 2D axisymmetric FEM analysis)

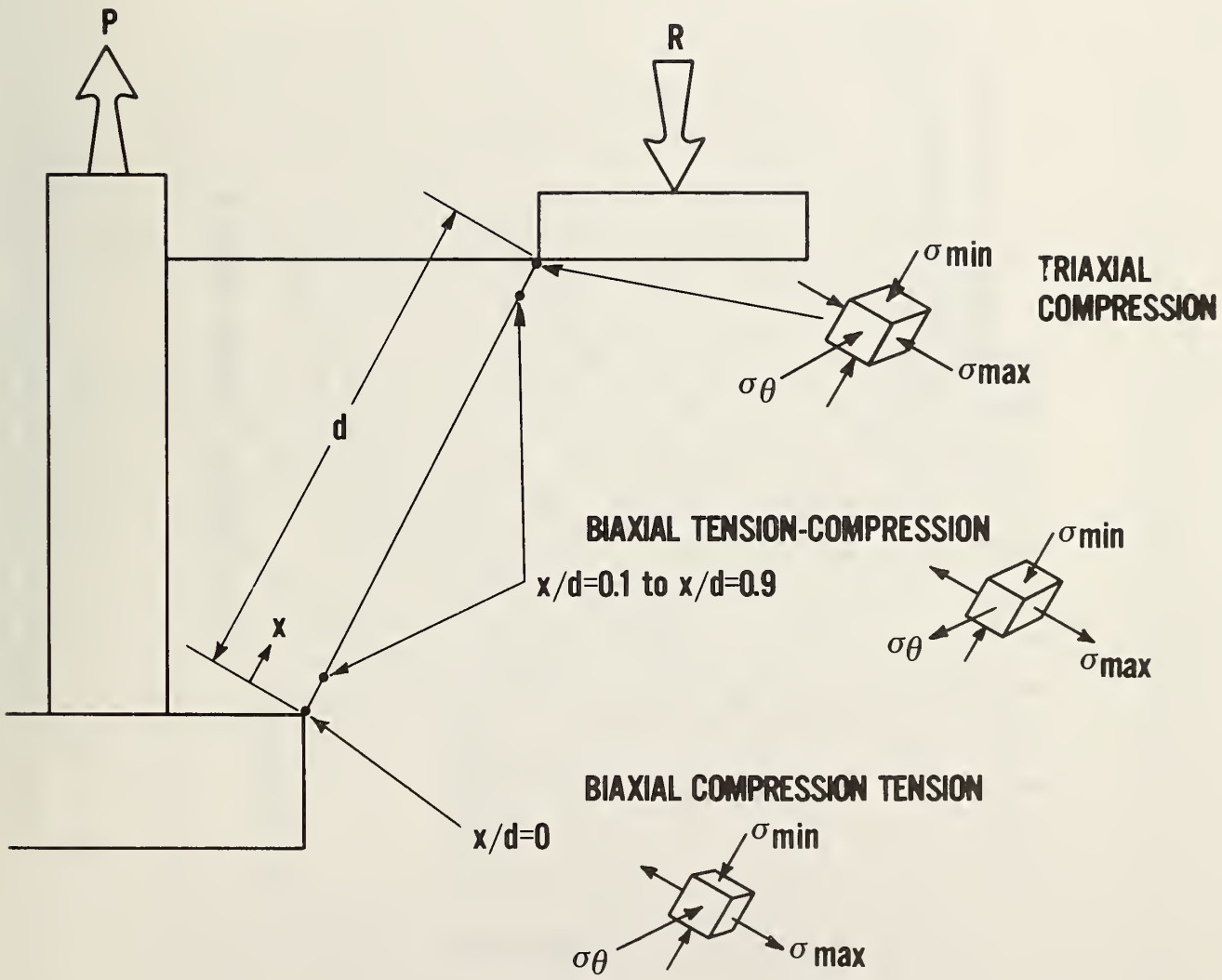

Figure 3.29 Elastic state of stress along idealized pullout failure surface

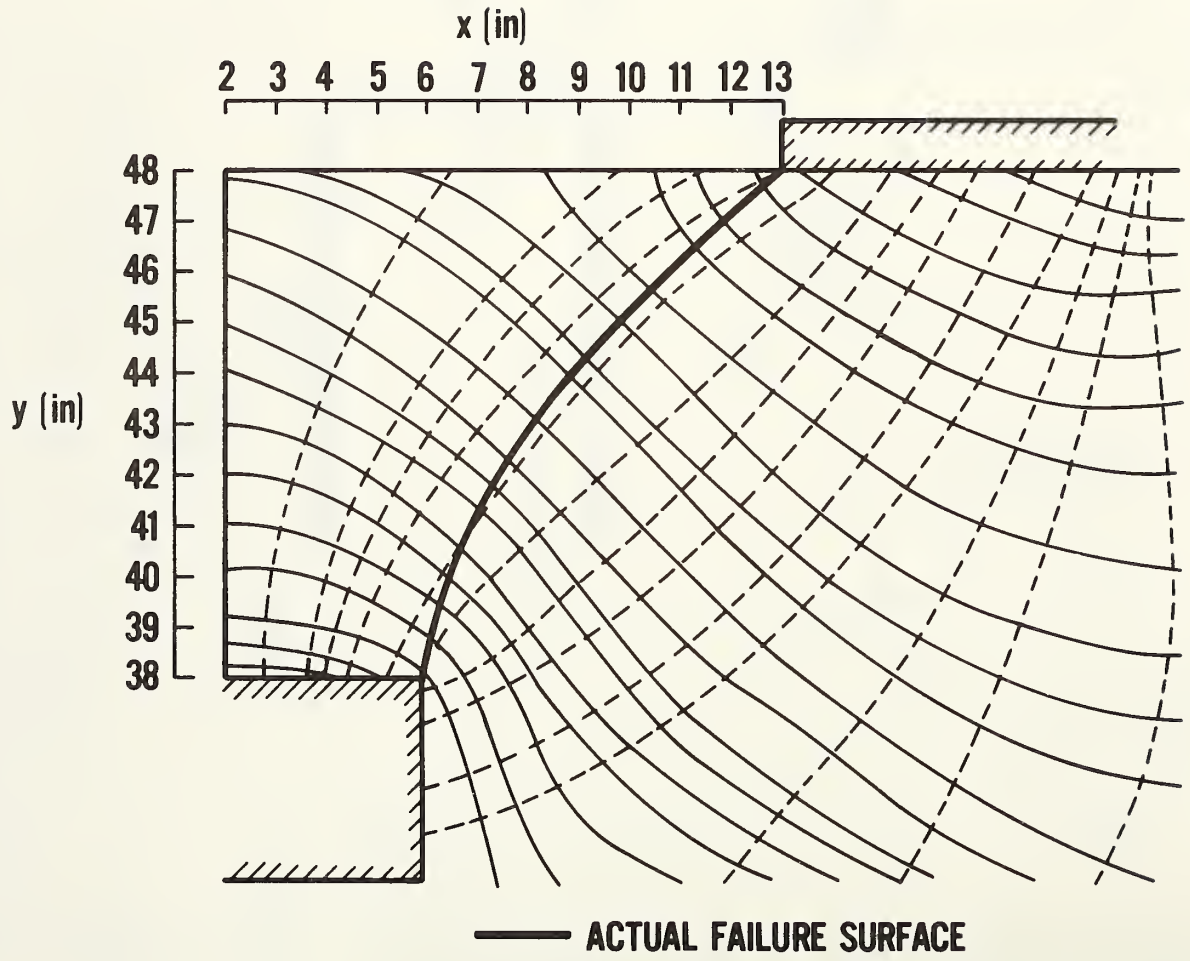

Figure 3.30 Principal Stress Trajectories for Specimen #1 = 70
(from 2D axisymmetric FEM analysis)

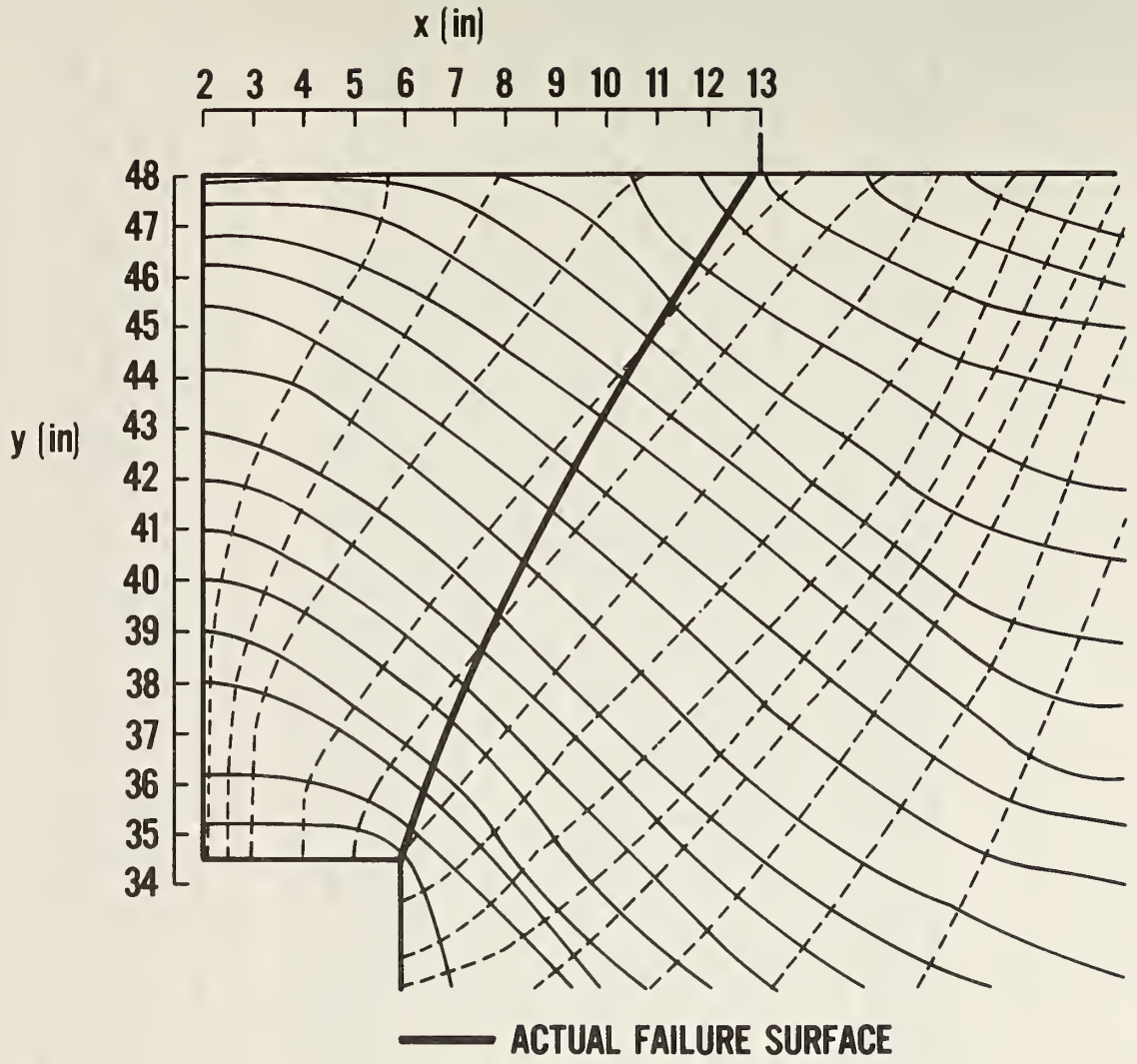

Figure 3.31 Principal stress trajectories for Specimen #2 = 54 (from 2D axisymmetric FEM analysis)

the disk and reaction ring. This means that the maximum (tensile) principal stress, for the most part, acts perpendicular to the failure surface while the minimum principal (compressive) stress acts parallel to the failure surface. The bold solid line in each of figures 3.30 and 3.31 represents the boundary of the observed failure surface. It is based on an average of the separate readings taken around the circumference shown in figures 3.4 and 3.5. It should be noted that the above comparison is for the concrete in the pre-cracked state, and the situation may change due to cracking.

3.5 CRACK PROPAGATION ANALYSIS

3.5.1 Post Cracking Behavior

As the load is increased towards ultimate failure two crack systems develop in the pullout test. These are:

1. Circumferential Cracks: Cracks which form the outer surface of the pullout "cone". As will be shown later these cracks begin at the disk edge and propagate towards the reaction ring as the load is increased. These cracks follow the curved paths previously shown in figures 3.4 and 3.5.

2. Radial Cracks: These cracks form parallel to vertical planes extending radially from the disk stem (r-z plane). Although the physical presence of these cracks was verified following testing -- absorbtion of methyl alcohol poured on the top surface of the pullout cone clearly revealed them -- the actual path of radial crack propagation was not monitored experimentally due to a lack of sufficient micro-embedment gages (which had to be meticulously hand crafted at the lab). However, FEM studies by Ottosen [7] and the ones by the author in this report indicate cracking initiates at the annulus formed by the top surface of the concrete and the disk stem and propagates as a curved wave from this point. Radial cracks are formed when the circumferential stresses exceed the tensile capacity of the concrete. The high circumferential stress values at the point of crack initiation are set up principally due to flexural type upward deformation of the top concrete surface. This as can be visualized in figure 3.23 which shows the peak vertical deformation, and from the circumferential stress contour plots shown in figure 3.33.

As these two crack systems propagate a discontinuity will occur in the load-strain history of any embedded gage in the vicinity of the crack. As previously shown, the actual failure surface did not follow the idealized conic frustum trajectory along which the gages were located. Because of this those gages oriented perpendicular to the principal cracking planes (radial gages for circumferential cracks, and circumferential gages for radial cracks) exhibited two types of load-strain behavior:

   a. For those cases where the gage crossed the failure surface a large change in the slope, or a large positive strain excursion indicated that cracking had propagated to that location. This type of behavior is shown in figure 3.34.

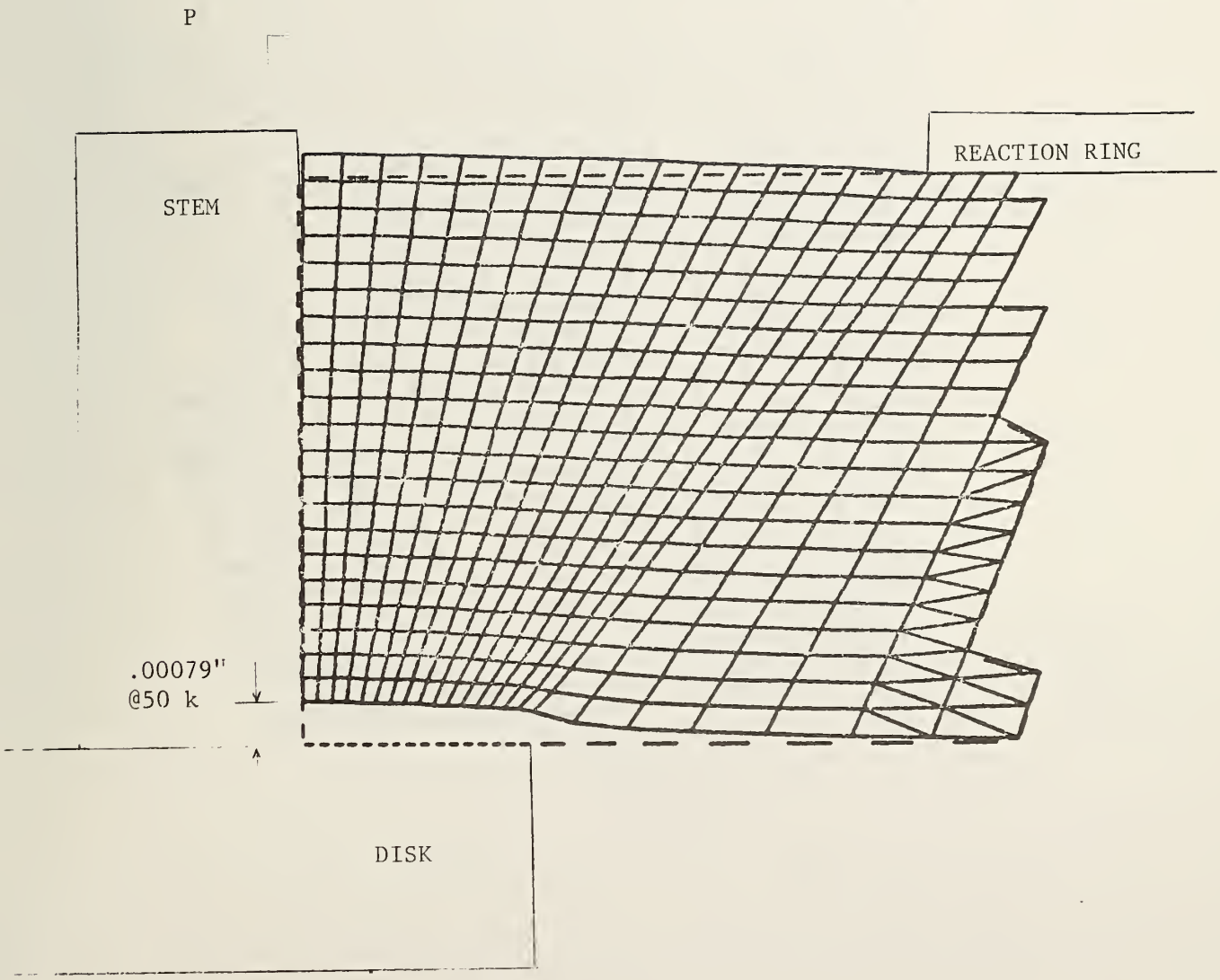

Figure 2.32a Elastic deformation of Specimen #1 ($2\alpha = 70°$) at a load of 50 kips (from 2D axisymmetric FEM analysis)

NOTE: Dashed lines denote undeformed shape

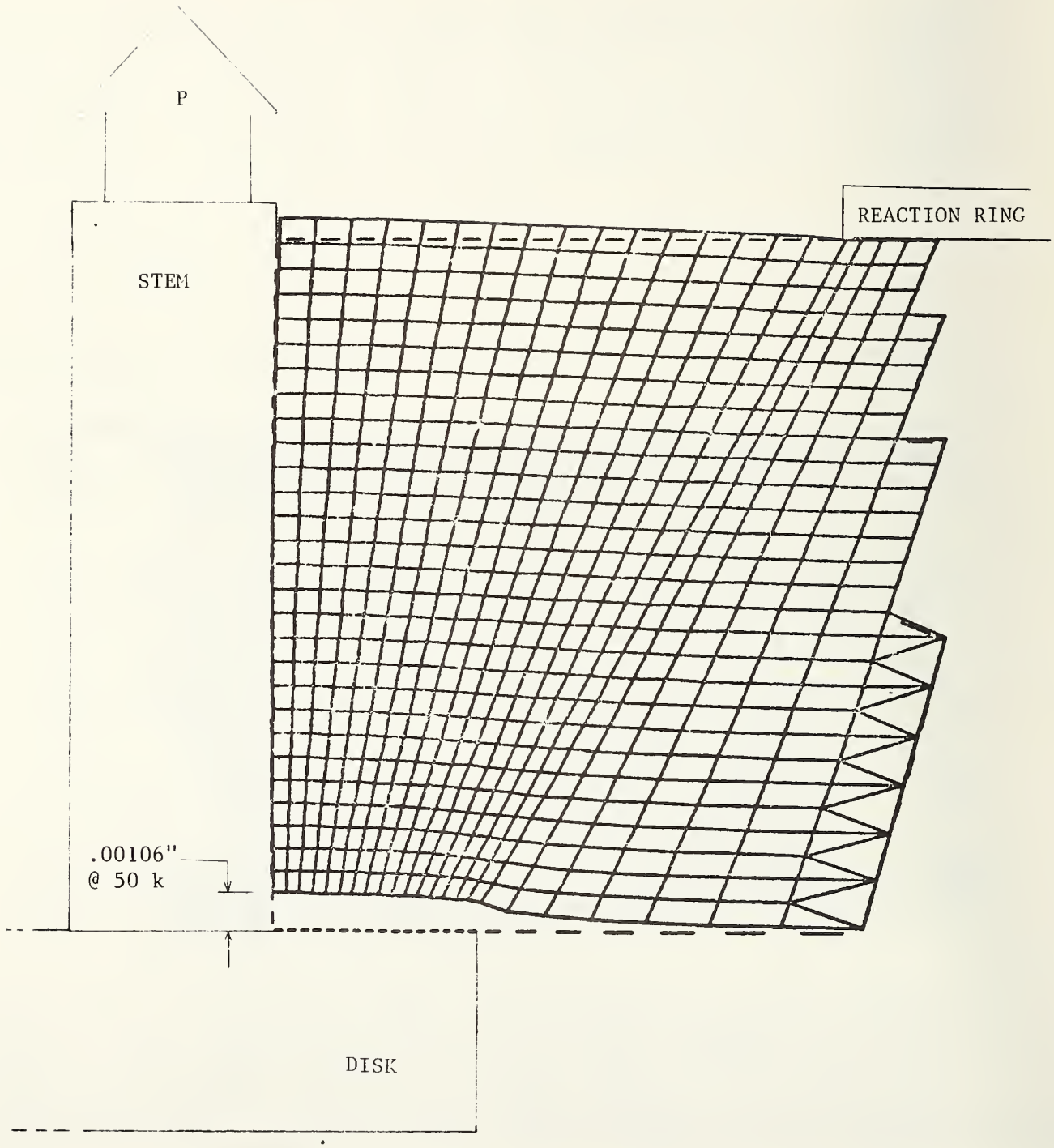

Figure 3.32b Elastic deformation of Specimen #2 ($2\alpha = 54°$) at a load of 50 kips (from 2D axisymmetric FEM analysis)

NOTE: Dashed lines denote undeformed shape

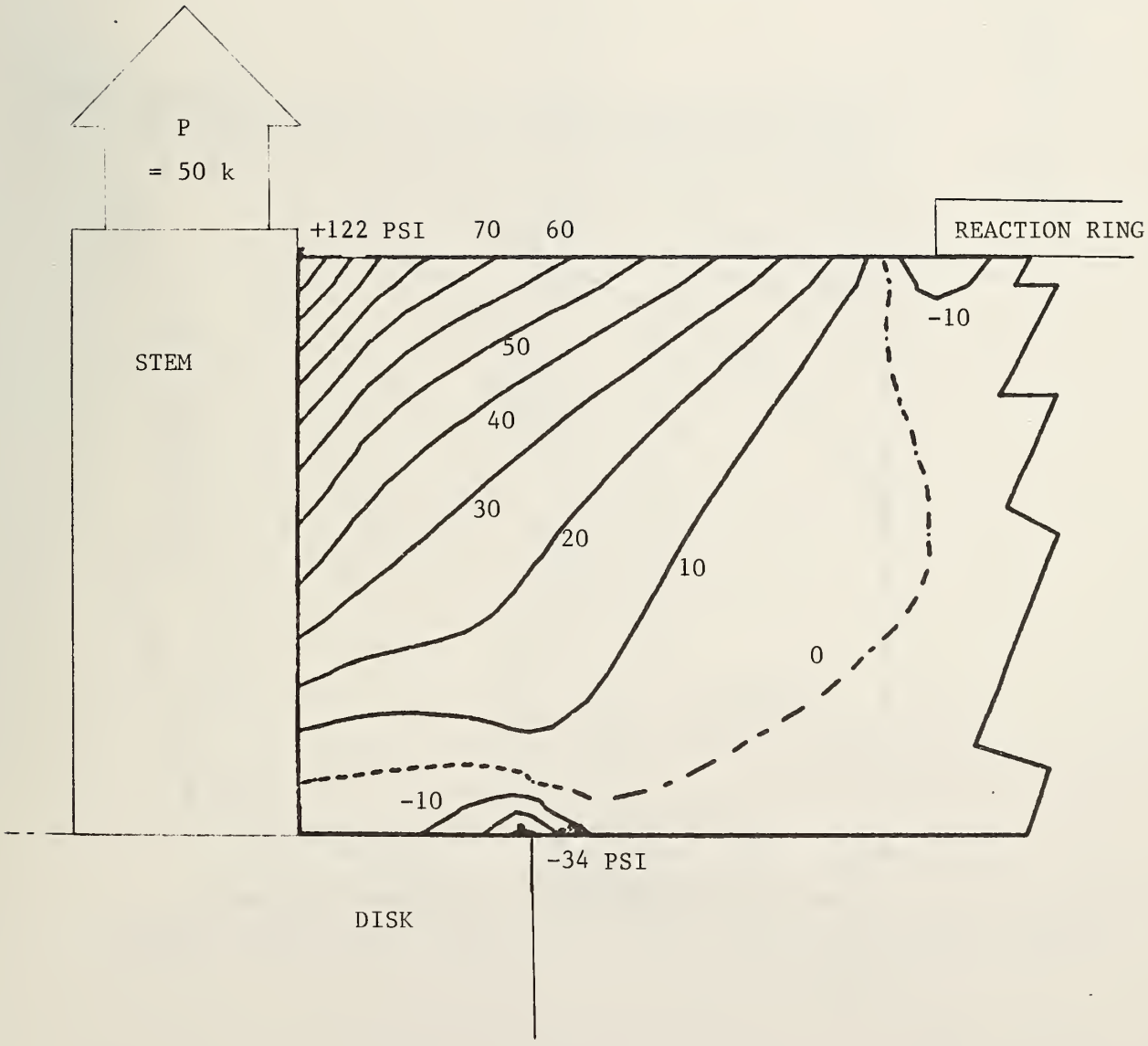

Figure 2.33a Circumferential stress contours for Specimen #1 ($2\alpha = 70°$) at 50 kips load (from 2D axisymmetric FEM analysis)

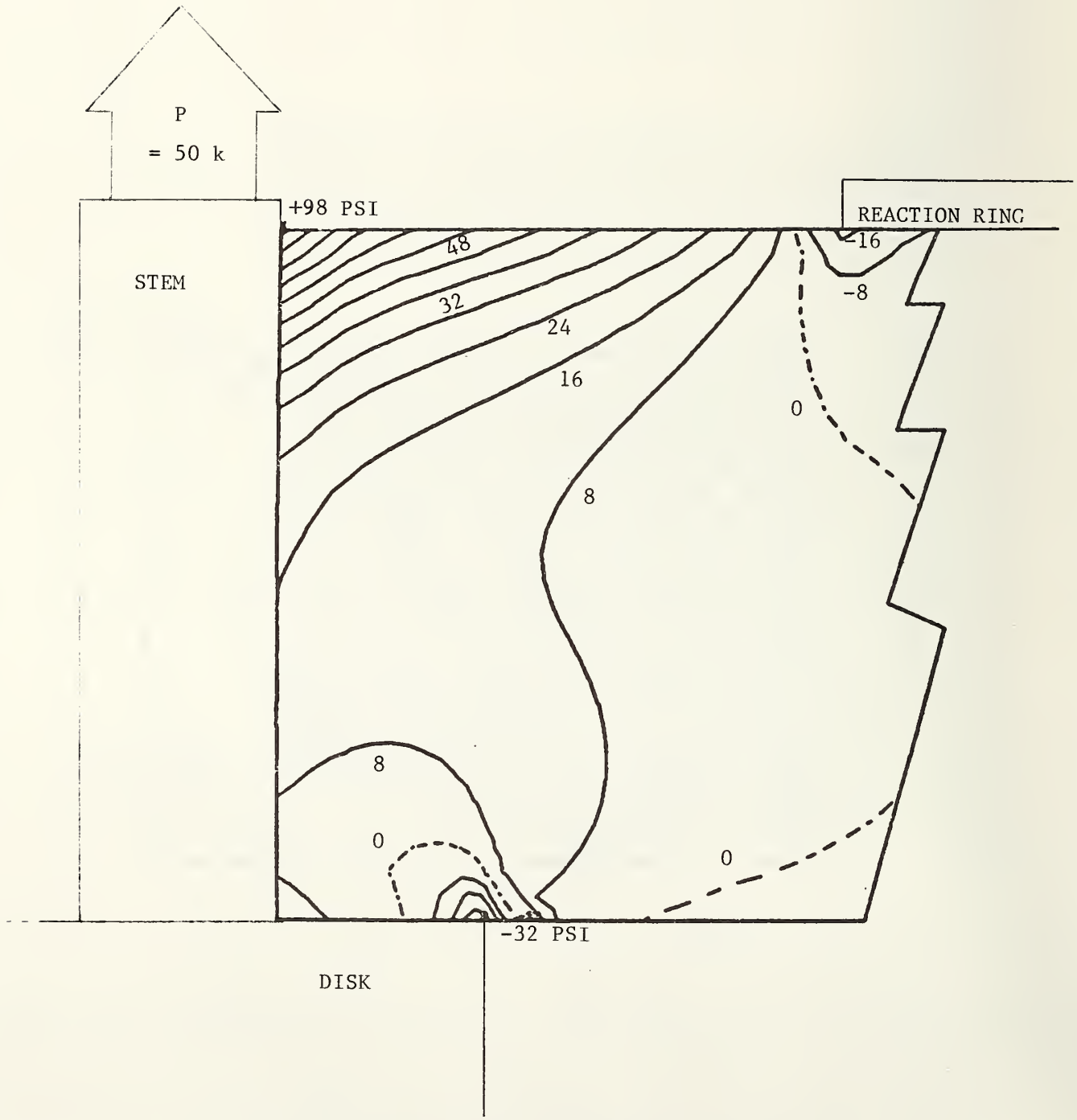

Figure 3.33b Circumferential Stress contours for Specimen #2 ($2\alpha = 54°$) at 50 kips load (from 2D axisymmetric FEM analysis)

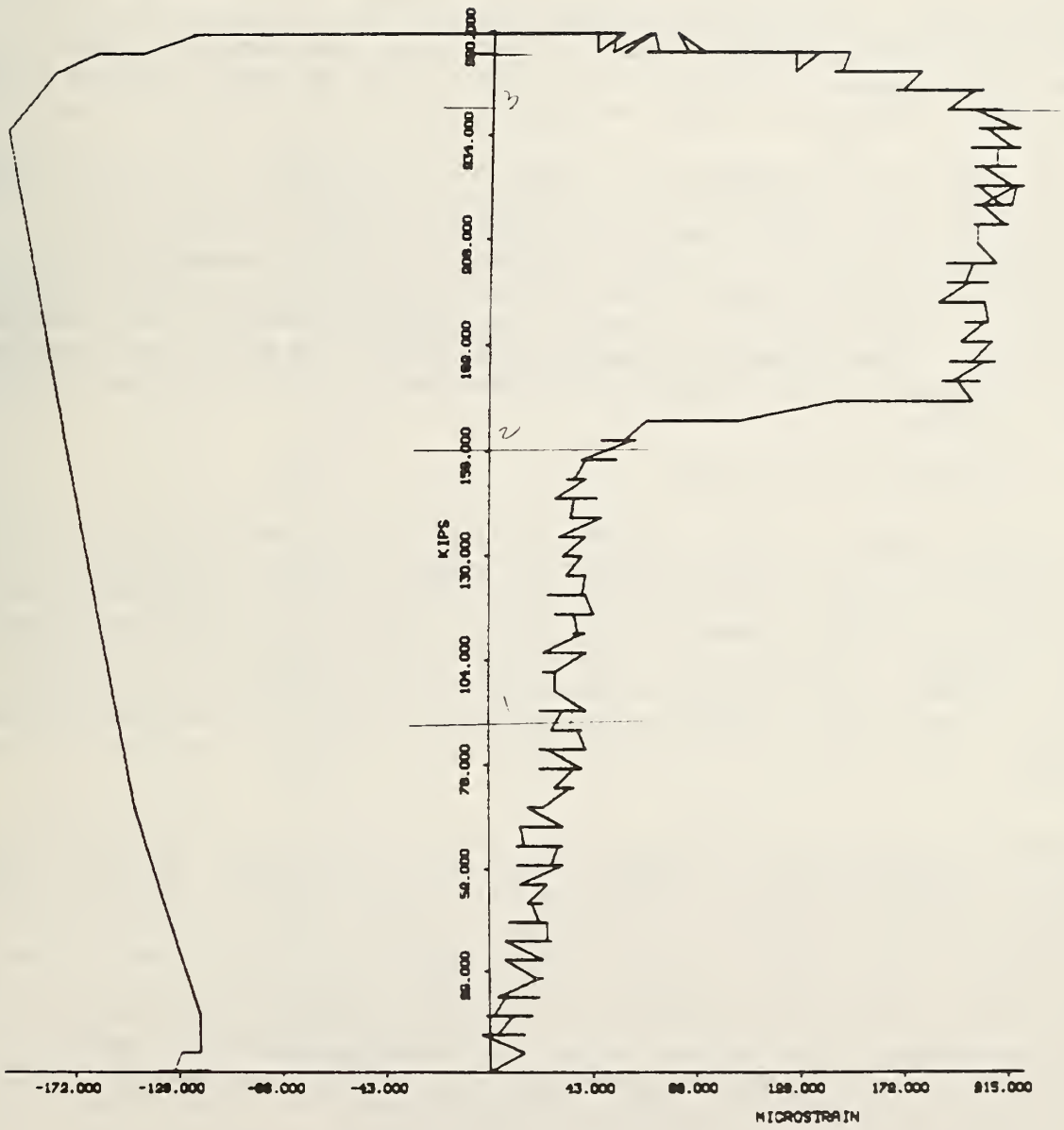

Figure 3.34 Gage RS5, Specimen #2 positive strain excursion indicating gage crosses crack surface

b. For gages not located along the failure surface the formation of a crack is evidenced by a sharp reversal or relaxation of strain. This type of behavior is shown in figure 3.35.

Although one would anticipate a monotonically increasing, compression strain history for gages oriented approximately parallel to the minimum principal stress (ANE and AS axial gages) this was not always the case. As cracking progressed those gages not on the failure surface (such as shown in figure 3.36) show a strain relaxation as the crack passes adjacent to the gage, unloading it.

Once the radial and circumferential cracks have propagated from the disk to the reaction ring -- as evidenced by large strain excursions having occurred for all key gages--there still remains a considerable reserve strength. At approximately 80 percent of ultimate load there begins a pronounced stiffness softening--a noticible change in slope of the load-strain plot--and finally, beginning at 97-98 percent of ultimate a large strain excursion is evidenced by all gages. These changes in the geometry of the load strain curve can be generally categorized as *discontinuities* each marking a specific phase of the failure process.

3.5.2 Discontinuity Histograms

By carefully inspecting the strain histories of each embedded gage a list of all discontinuities and the load stages at which they occur was compiled. As previously mentioned, a discontinuity was evidenced in the load-strain plots by either a pronounced change in slope or by a sharp strain excursion such as shown in figures 3.34 and 3.35. A bar chart of these points as a function of percent ultimate load is shown in figure 3.38. From this plot it is clear that there are three distinct phases which constitute the failure sequence of a pull-out test. These phases vary slightly for each specimen and are listed below in table 3.2.

The "peak" values indicate the percent of ultimate load at which the maximum number of discontinuities were observed within a given phase. Note the close correlation between the above ranges and the ranges listed in table 3.1, which represent the discontinuities observed in the external load-deflection plots of the specimen. This close similarity would suggest that future tests to investigate changes in the failure process due to changes in the geometry of the test could be more efficiently undertaken by carefully monitoring the external load deflection behavior, rather than using the tedious embedment gage method. The latter, of course, is considerly more precise, owing to the superior sensitivity of the strain gage over a typical displacement LVDT.

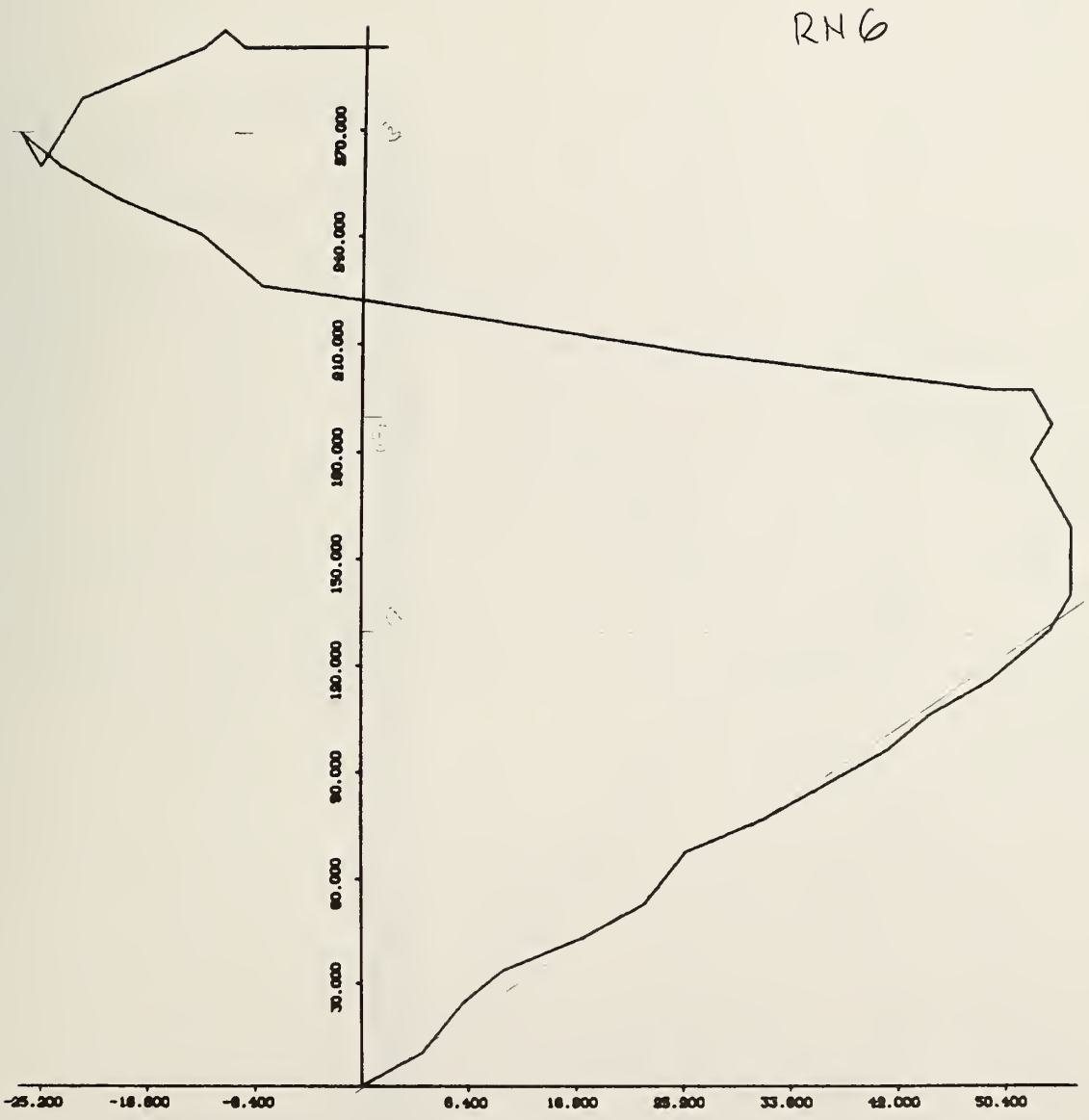

Figure 3.35 Gage RN6, Specimen #1 negative strain excursion (reversal) indicating crack has passed adjacent to gage

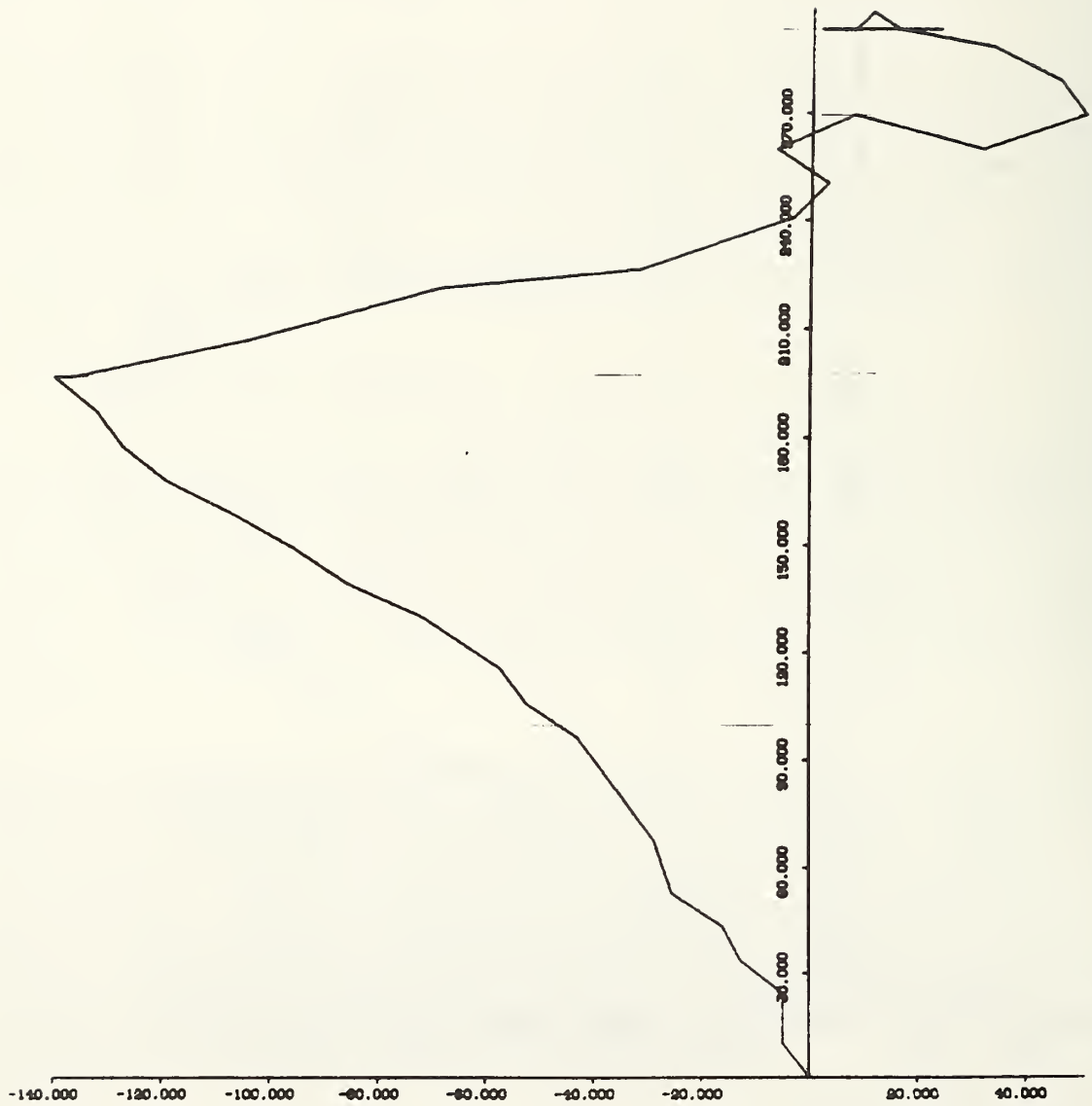

Figure 3.36 Gage ANE7, Specimen #1 axial gage showing strain reversal -- crack has passed adjcent to gage, thereby unloading it

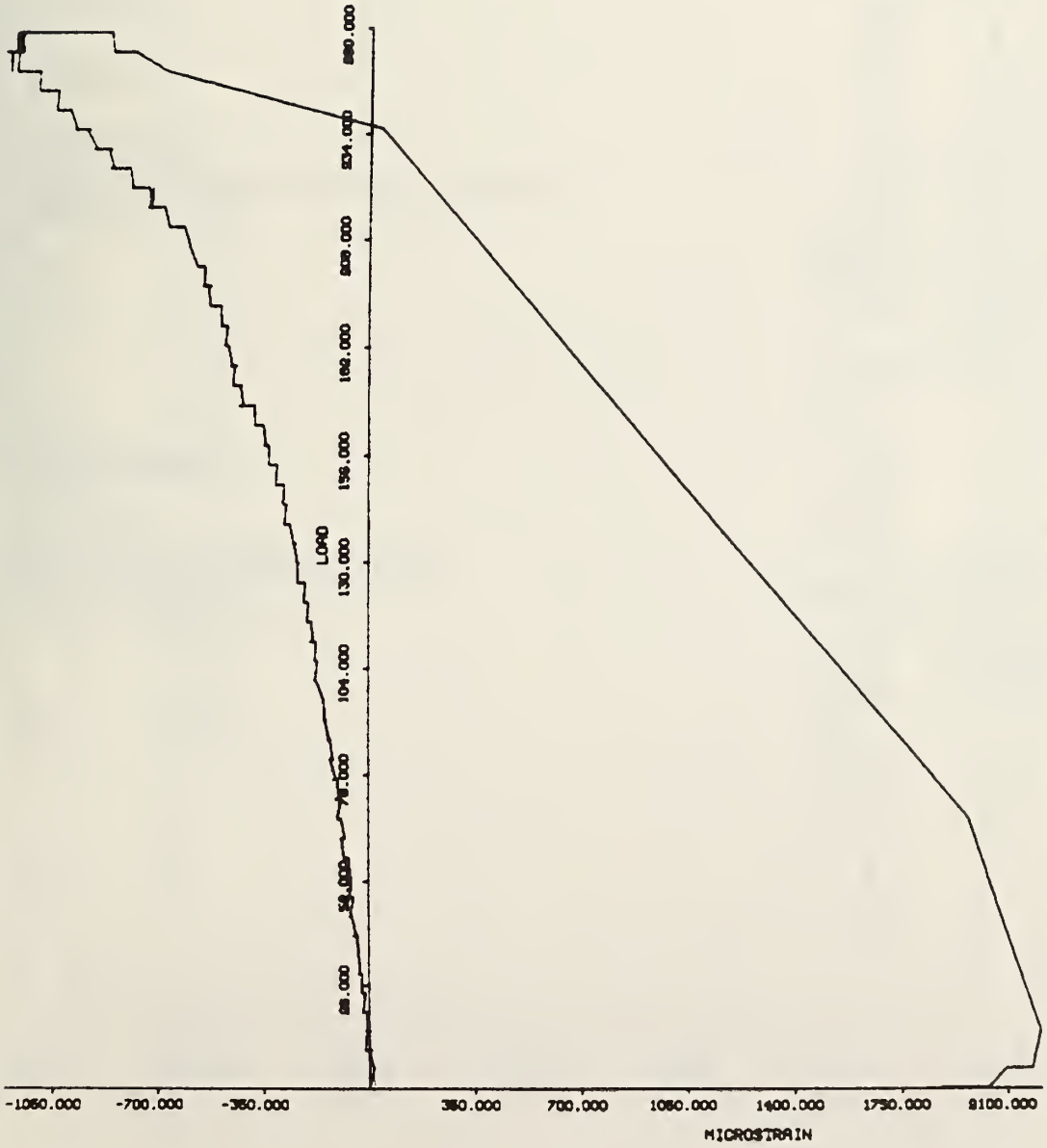

Figure 3.37 Gage ANE2, Specimen #2 typical monotonic axial strain history

Figure 3.38a

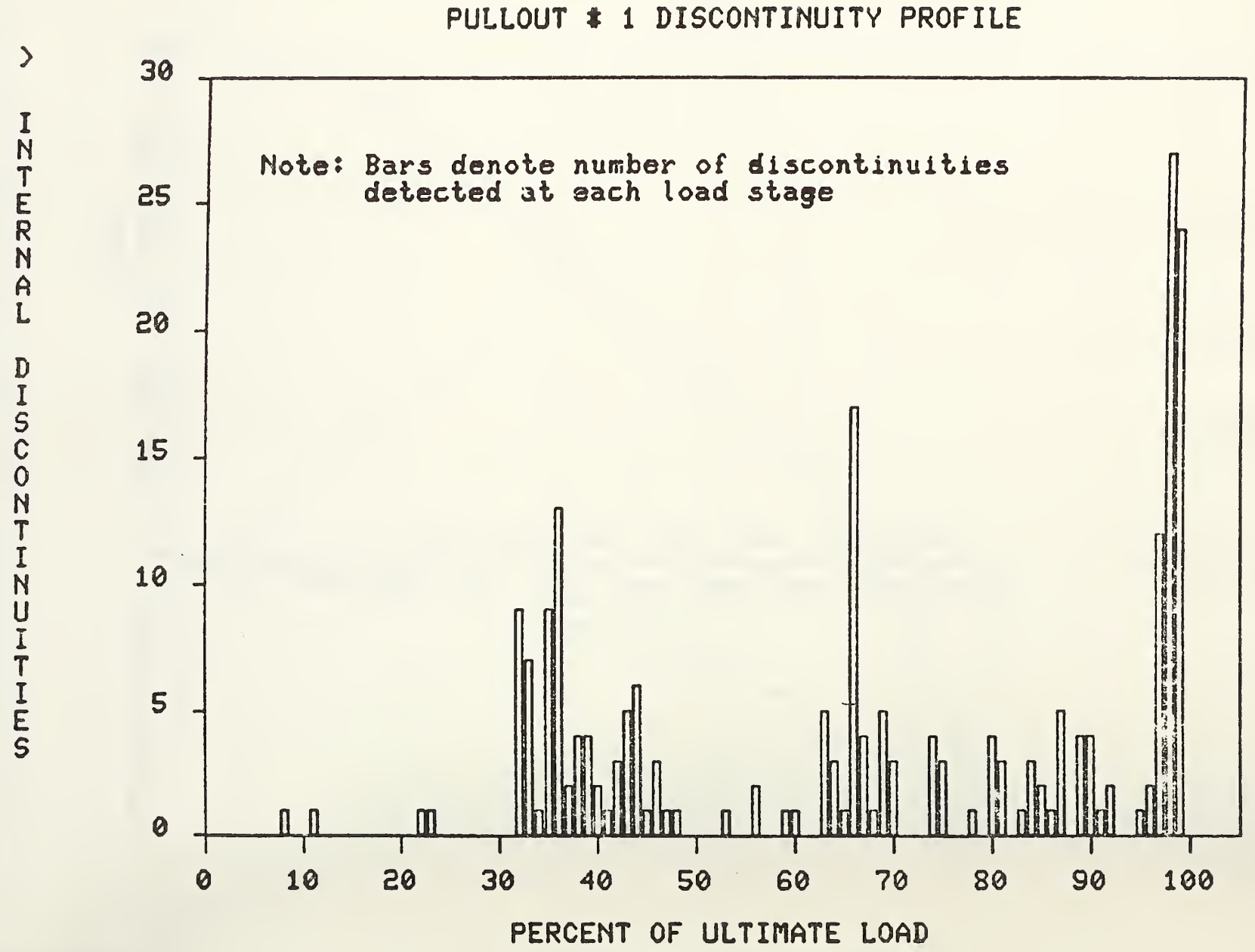
PULLOUT # 1 DISCONTINUITY PROFILE
Note: Bars denote number of discontinuities detected at each load stage
INTERNAL DISCONTINUITIES
0
5
10
15
20
25
30
0
10
20
30
40
50
60
70
80
90
100
PERCENT OF ULTIMATE LOAD

Figure 3.38b

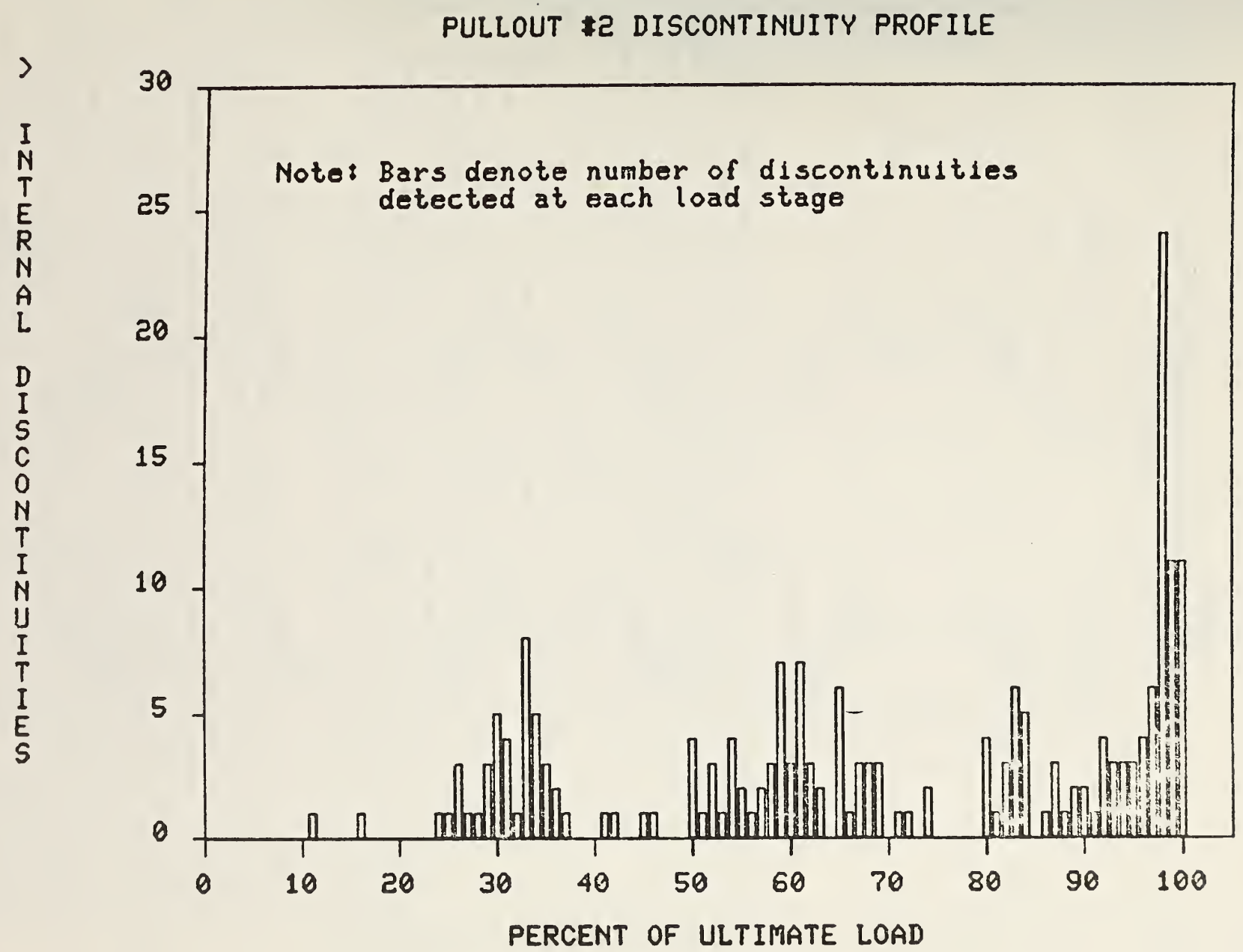
PULLOUT #2 DISCONTINUITY PROFILE
Note: Bars denote number of discontinuities detected at each load stage
INTERNAL DISCONTINUITIES
30
25
20
15
10
5
0
0
10
20
30
40
50
60
70
80
90
100
PERCENT OF ULTIMATE LOAD

Table 3.2. Ranges in Percent of Ultimate Load of Primary Discontinuity Zones Observed by Embedment Gages

	SPECIMEN #1		SPECIMEN #2	
PHASE	% ULT. LOAD Range	% ULT. LOAD Peak	% ULT. LOAD Range	% ULT. LOAD Peak
I	32 - 40	36	28 - 38	33
II	63 - 70	66	50 - 70	61
III	80 -100	98	80 -100	83/98

3.5.3 Crack Propagation Sequence

By tabulating the percent of ultimate load at which each "cross crack" gage records its first discontinuity it is possible to trace the formation and propagation of internal cracking during the pullout test. As previously mentioned, the key gage strings which most reliably monitored the progression of circumferential cracks were the gages oriented perpendicular to the plane of these cracks: the radial gages. Similarly, the circumferential gages were the most accurate indicators of radial crack propagation. Figures 3.39 and 3.40 present, in schematic form, the progression of circumferential and radial cracks as inferred from discontinuities in the strain histories for specimens 1 and 2. These figures are broken into eight load stages which mark significant crack propagation. The right hand diagonal columns for each sequential plot represent the radial gages in the proper relative positions within the specimen. The short vertical strings above and below the right disk edge represent the RV (radial) and ET (edge, tension) gages. All of the above gages monitored the progression of circumferential cracks. The left hand diagonal columns represents the circumferential gages which recorded radial crack development. A blackened circle indicates that the gage has undergone a strain excursion at or before the labelled load stage. From these plots it is clear that:

1. Circumferential cracking begins at the disk edge at low load levels--25 to 35 percent of ultimate load. Computer studies by Ottosen [7] and those by the author in the report have shown that the cracks may begin on the side face of the disk near the top edge at loads below 25 percent of ultimate. This was verified in pullout specimen #2 as shown in the first schematic drawing in figure 3.40. A faulty gage precluded monitoring this early cracking in specimen #1. Once the cracking threshold is reached the circumferential failure surface begins to propagate from the disk edge towards the inside edge of the reaction ring. It is interesting to note that for specimen #1 the RV (radial) gages--the short vertical string above the disk edge--indicate major cracking in their vicinity at early loads, while the same gages for specimen #2 indicate that no cracking occurs until much higher loads. This may be inferred to mean that the failure surface near the disk for specimen #1 ($2\alpha = 70°$) deviated significantly from the

Figure 3.39 Crack propagation sequence for Specimen #1 ($2\alpha = 70°$) black circles denote gages which have recorded cracking at a particular load stage. Left had diagonal columns represent circumferential gages; right hand diagonal columns represent radial gages

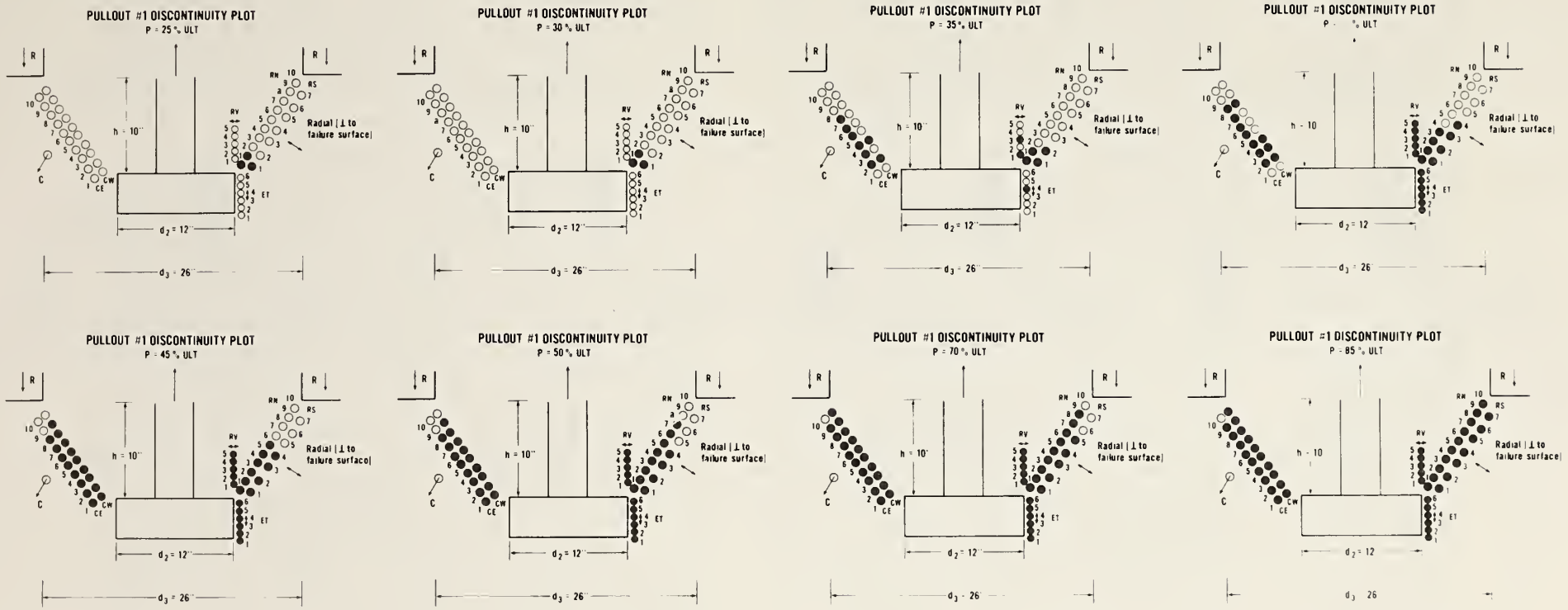

Figure 3.40 Crack propagation sequence for Specimen #2 ($2\alpha = 54°$). Black circles denote gages which have recorded cracking at a particular load stage. Left hand diagonal columns represent circumferential gages; right hand diagonal columns represent radial gages

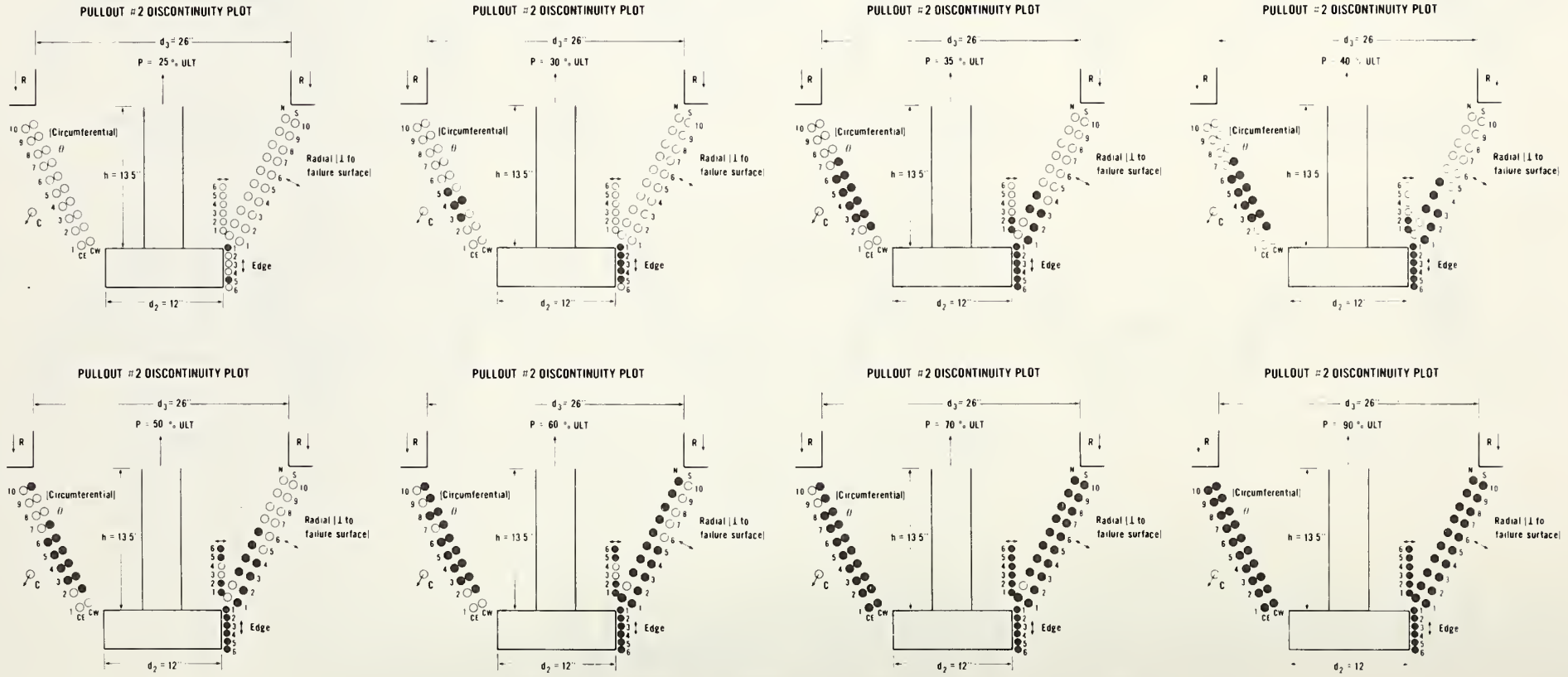

idealized conic frustum surface. This was born out in subsequent measurements of the failure cone following the conclusion of the test (figure 3.5). At approximately 65 percent of ultimate load it can be seen that in both specimens circumferential cracking has progressed from the disk edge to the reaction ring. This is an extremely important observation: with the failure surface completely formed there is still a 35 percent increase in load necessary to remove the cone.

2. Radial cracking, as previously mentioned, begins at the annulus formed by the intersection of the top concrete surface and the disk stem. This cracking probably begins at low load levels [7] and rapidly propagates away from this point. At approximately 35 percent of ultimate load the crack front reaches the circumferential failure surface. The experimental data shown in figures 3.39 and 3.40 indicate that the radial crack front is curved, since the circumferential gages in the middle of the string are the first to record cracking in both specimens. As the crack front progresses outwards the end gages near the disk and reaction ring eventually, with increased load, signal that radial cracks have extended beyond the middle region of the frustum. At approximately 65 percent of ultimate load both specimens had developed radial cracking from the stem to some point beyond the failure surface. Although an additional grid of circumferential gages towards the disk stem would have given a more complete picture of radial crack propagation, it was felt that radial cracking plays only a minor role in the failure process, and that the extra available embedment gages, which were in short supply and difficult to fabricate, should be used to monitor radial strain along a second position on the frustum.

In the paper summarizing his nonlinear, finite element, cracking analysis of the Lok-test, Ottosen [7] presented a figure which showed the analytically predicted cracking pattern. This pattern, reproduced in figure 1.2, shows a remarkably good correlation with the results above. However, two notable differences are evident: because Ottosen's model assumed perfect bond between the disk and concrete, large stresses--resulting in circumferential cracking--are developed at low loads beneath the pullout disk. In practice this is not the case. Most contractors have the disks and stems coated with oil to prevent rusting which, in effect, serves as a bond breaker along the side and bottom face of the disk. The stress concentration at the upper disk edge, as shown in the present study, is not accounted for in Ottosen's model. We would therefore not expect to see in the physical specimen the lowermost circumferential cracks shown in Ottosen's figures 1.2a and b. Furthermore, a comparison of Ottosen's figures 1.2c and d with figures 3.30 and 3.31 shows that the major circumferential cracks (from the disk edge to the reaction ring) generated by his analysis follow the minimum principal stress trajectories. Since these trajectories do not directly connect the disk edge to the inner edge of the reaction ring, the analytical failure surface will form such that a band of uncracked concrete between the disk and reaction ring remains after completion of circumferential cracking. After circumferential cracking is completed at approximately 60-65 percent of ultimate load, the uncracked concrete acts as a "compression strut" which carries the additional load. Ultimate failure, Ottosen asserts, is therefore due to compressive failure of the concrete in the uncracked strut.

If we ignore the fact that the measured failure surface for specimens 1 and 2 connected the disk edge and inner edge of the reaction ring, and assume that Ottosen's compression strut does indeed exist, then the compressive strain along the strut should approach the limiting value of approximately 3000 microstrain as the failure load is reached. Figures 3.41 and 3.42 show the measured axial strains along the frustum surface at the ultimate load for specimens 1 and 2, respectively. From these it is seen that the peak compressive strain is 1500 microstrain for specimen 1 and 1140 microstrain for specimen 2, both well below that required to produce a compressive failure in the concrete. Additionally, there was no observed evidence in either of the specimens of a strut having failed in compression. It is, therefore, necessary that the load beyond that required to complete circumferential cracking be carried by a mechanism other than the "compression strut".

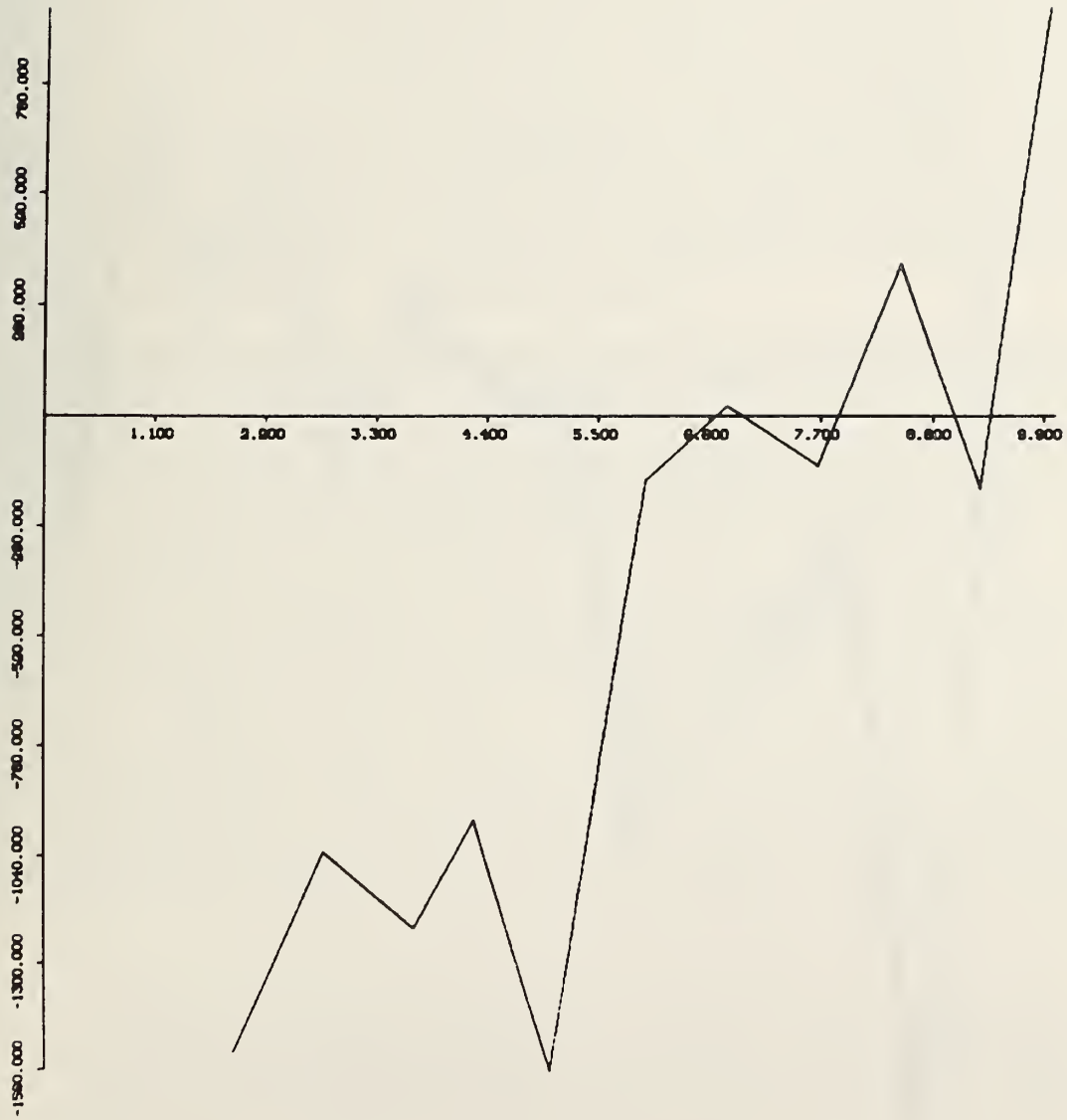

Figure 3.41 Axial strain profile along Frustum surface (experimental) at ultimate load for Specimen #1 ($2\alpha = 70°$)

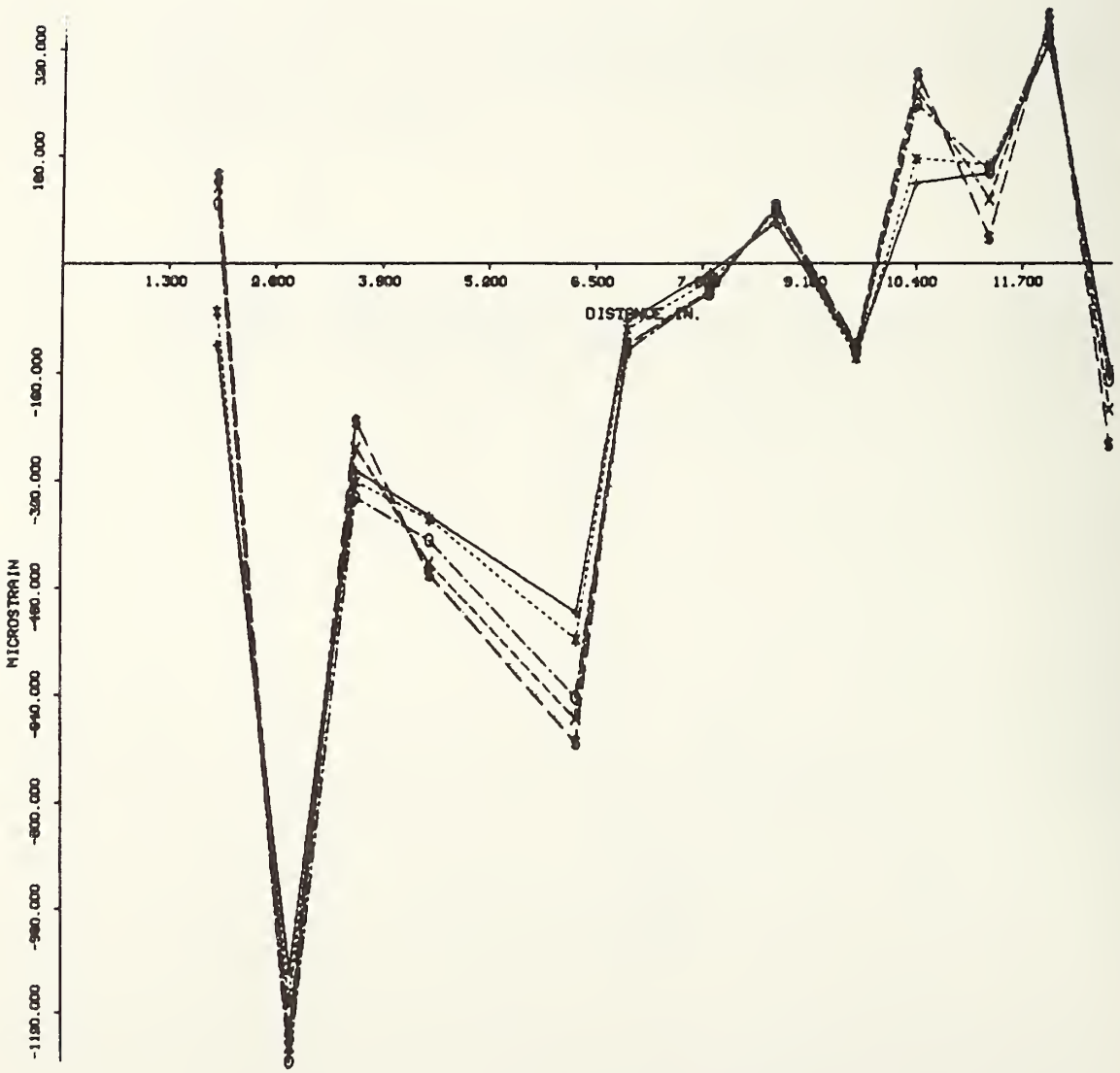

Figure 3.42 Axial strain profile along Frustum surface (experimental) at ultimate load for Specimen #2 (2α = 54°)

4. DISCUSSION

4.1 FAILURE MECHANISM

The close correlation between the internal discontinuity histograms (presented in figure 3.38) and the overall load-deflection response (figures 3.1 and 3.2) indicates that there are three distinct phases in the failure sequence of a pullout test. The first of these phases is marked by a deviation from elastic behavior. Previous work by Buyukozturk, et al. [16] has demonstrated that, under unaxial loading, the main cause which precipitates nonlinear response in concrete is microcracking at the aggregate-mortar interface. Under uniaxial loading nearly elastic behavior was obtained to about 40 percent of ultimate load in Buyukozturk's tests. For the pullout test, where the stress state along the majority of the failure surface is biaxial tension-compression, this value marking the beginning of nonlinear response will be less than 40 percent, as is evidenced in the discontinuity histograms.

As the load is further increased, circumferential cracks begin to propagate from the disk edge towards the inner edge of the reaction ring. This crack system appears to be completely formed at approximately 65 percent of ultimate load. Likewise, radial cracks, beginning at the intersection of the top surface of the concrete at the disk stem, have propagated through the entire failure surface by 65 percent of ultimate load (see figures 3.39 and 3.40). The above events constitute the second key phase in the failure mechanism. If the pullout test had been conducted using a perfectly homogeneous, brittle material, the completion of circumferential cracking would have marked the ultimate load of the test, since there would be no physical mechanism for load transfer between the pullout cone and the base material. For concrete it is thus likely that the entire load past 65 percent of ultimate must be supported by something other than a continuous stress field. The logical mechanism is one of aggregate interlock--by which the load is carried via the shear strength of the mortar in which the aggregates crossing the failure surface are embedded. Beyond approximately 80 percent of ultimate load, individual aggregates begin to shear free giving rise to a softening of the system, marked by a change in the slope of the load deflection curve.

It is, therefore, likely that the failure mechanism proceeds as follows:

Phase 1. Cracking initiates in the critical biaxial tension-compression zone near the disk at 25-30 percent of ultimate. This phase marks the initial load departure of the load-deflection curve from linear behavior.

Phase 2. Circumferential cracking, beginning at the disk edge, propagates toward the reaction ring forming the completed failure surface at approximately 65 percent of ultimate load.

Phase 3. Load past 65 percent of ultimate is carried entirely by discrete forces developed via aggregate interlock. Ultimate failure comes about through gradual shear failure of mortar as embedded aggregates which cross the failure surface are pulled free.

Note that the previously discussed phases are the same as those discussed in table 3.2.

4.2 AGGREGATE INTERLOCK MODEL

The load carrying mechanism of phase III can be demonstrated in the following simplified model. First, envision an idealized spherical aggregate with diameter d located on the failure surface such that one half of the aggregate is embedded in the pullout cone and the remaining half is embedded in the base material such as shown in figure 4.1a. For the sake of simplification we assume the failure surface to follow the idealized conic frustum previously discussed. The vertical force P required to pull the aggregate out of either side is equal to the shear strength of the cement paste times the shear area. The shear area A_v, as shown in figure 4.1b is calculated as:

$$A_v = 2 \int_0^{90} x\, r \sin \theta \, d\theta \qquad \text{(see figure 4.1b)}$$

$$= -2 \times r \cos \theta \Big|_0^{90}$$

$$= +2 \times r \qquad \text{but since } r = d/2$$

$$A_v = xd \tag{1}$$

where

θ = base angle for integration

r = radius of the aggregate

d = diameter of the aggregate

x = height of the shear surface = $d/(2 \tan \alpha)$

α = half the pullout apex angle

The force, P, to remove one aggregate is thus

$$P = \tau_c \times d = \tau_c \frac{d^2}{2\tan\alpha} \tag{2}$$

where τ_c = shear strength of the paste

We now investigate the more generalized case where the failure surface is represented as shown in figure 4.3. Here the aggregate spacing from the disk to the failure surface is arranged such that each aggregate will shear out an area equal to A_v as defined by Eq. (1). Assume also that the aggregates touch one another in the circumferential direction. In this manner, the number of aggregates around any circumference of the failure surface can be calculated as:

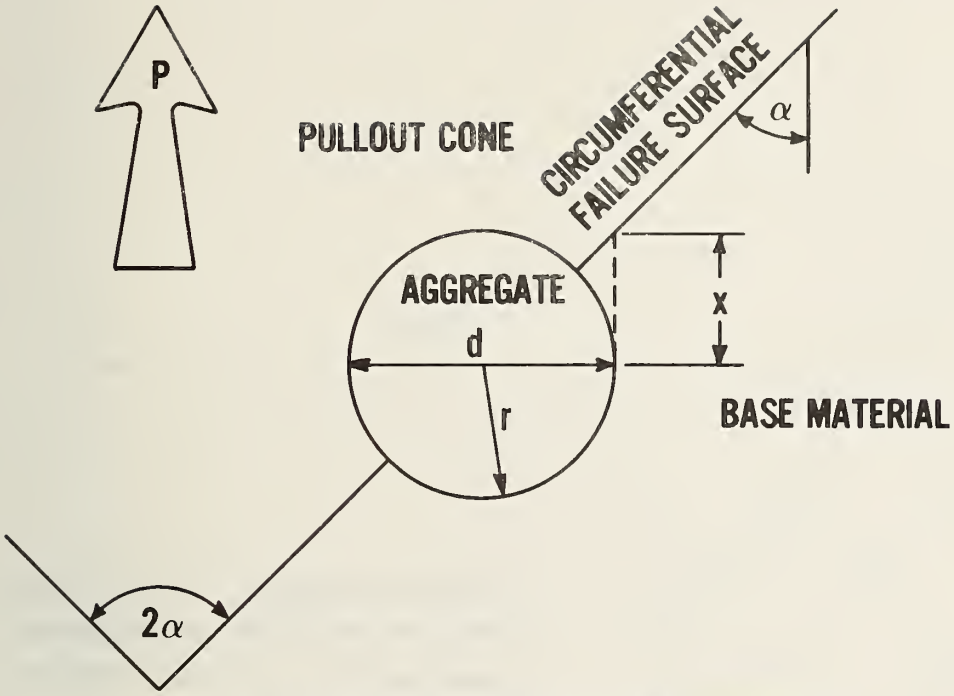

a) IDEALIZED AGGREGATE MECHANICALLY BRIDGING THE FAILURE SURFACE

$$dA = Zrd\,\theta$$

$$\frac{r \sin\theta}{Z} = \tan\alpha$$

$$Z = \frac{r \sin\theta}{\tan\alpha} = x \sin\theta$$

$$dA = xr \sin\theta\, d\,\theta$$

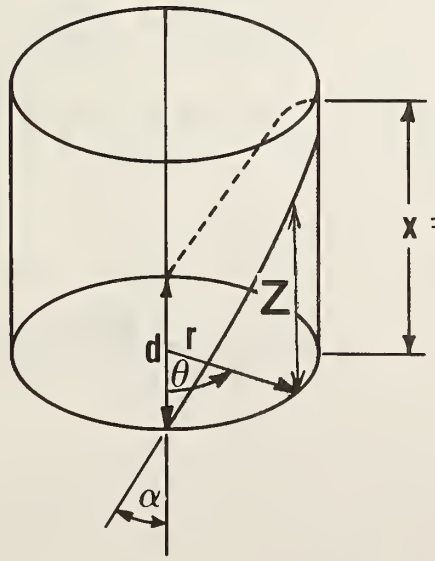

x = VERTICAL DISTANCE TO BE SHEARED
= d/2tanα

b) PASTE SHEAR AREA FOR SINGLE AGGREGATE = A_v

Figure 4.1 Basis for aggregate shear failure calculations

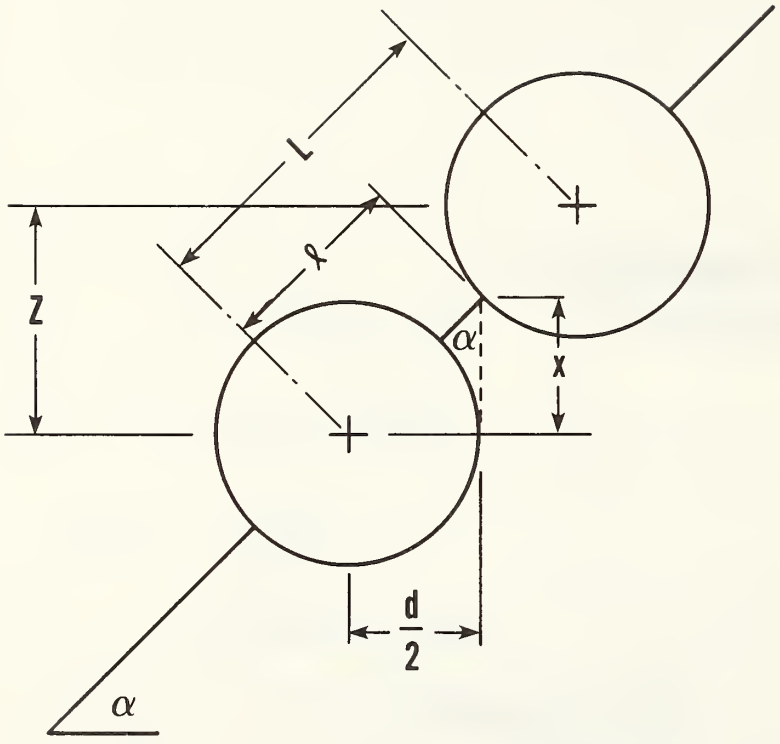

Aggregate spacing L is chosen so that there will be no interference between shear surfaces in adjacent levels of aggregates

$$\ell = \frac{d}{2} / \sin\alpha$$

$$L = \frac{d}{2}\left(1 + \frac{1}{\sin\alpha}\right) = \ell + \frac{d}{2}$$

$$Z = L\cos\alpha = \frac{d}{2}\left(\frac{\sin\alpha + 1}{\sin\alpha}\right)\cos\alpha$$

$$N = \frac{h}{Z}$$

$$N = \frac{2\,h\sin\alpha}{d\cos\alpha\,(1 + \sin\alpha)}$$

Figure 4.2 Basis for the calculation of n used in eq. (6)

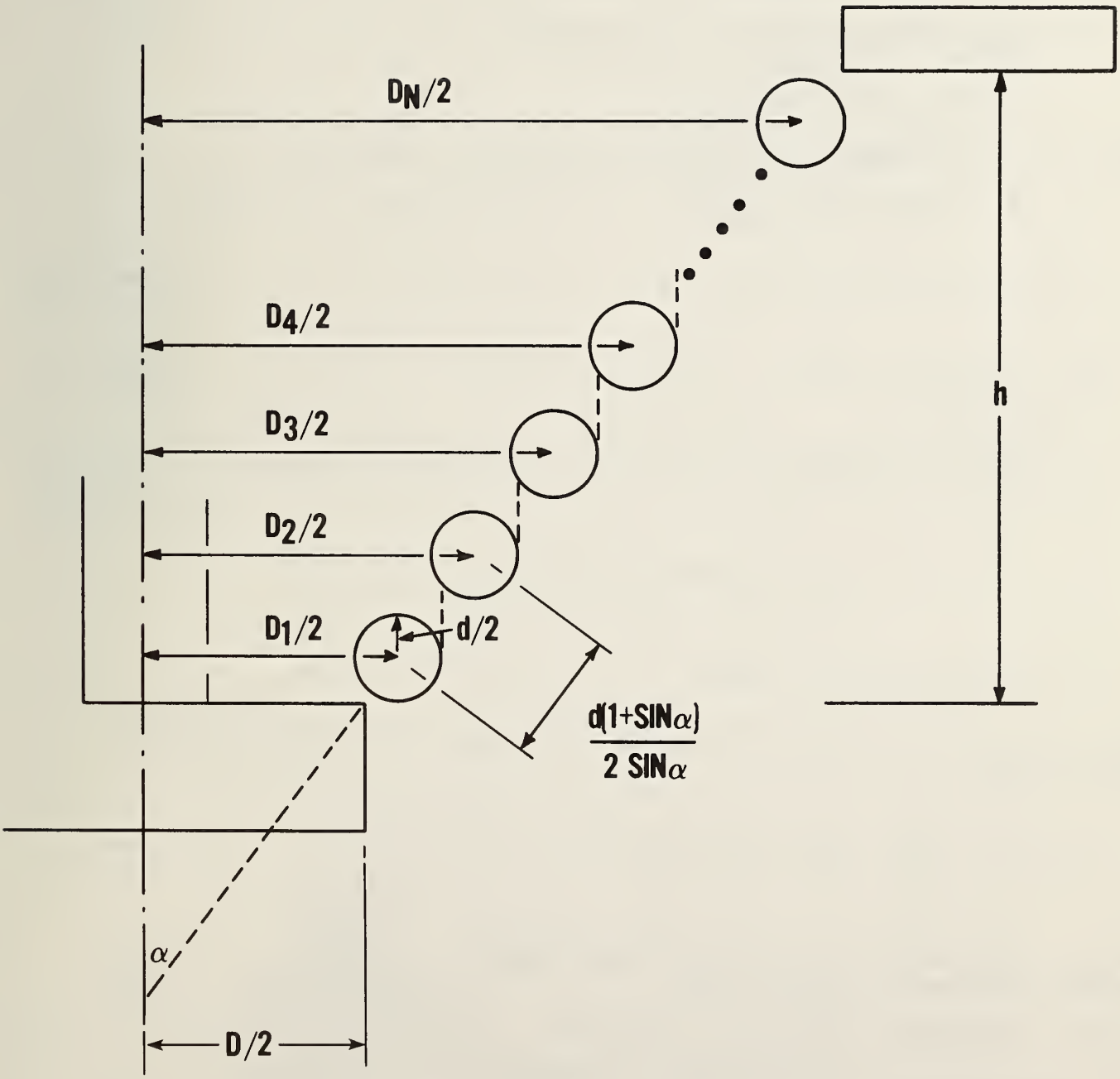

Figure 4.3 Generalization of idealized aggregate interlock failure

$$N_i = \frac{\pi D_i}{d} \tag{3}$$

where N_i = the number of aggregates around the circumference at a specified level.

D_i = the diameter of each successive aggregate ring. (D_1 is approximately equal to the diameter of the disk.)

d = the diameter of the aggregate

The number of aggregates in the following successive rings will be:

$$N_2 = \frac{\pi D_2}{d} = \frac{\pi D_1}{d} + \frac{\pi d(1 + \sin\alpha)}{d}$$

$$N_2 = \frac{\pi D_1}{d} + \pi(1 + \sin\alpha)$$

$$N_3 = \frac{\pi D_1}{d} + 2\pi(1 + \sin\alpha) \tag{4}$$

$$N_4 = \frac{\pi D_1}{d} + 3\pi(1 + \sin\alpha)$$

$$\vdots$$

$$N_n = \frac{\pi D_1}{d} + (n-1)\,\pi(1 + \sin\alpha)$$

The total number of aggregates along the failure surface for any given pullout test is thus:

$$T_n = \sum_{1}^{n} N_n = \frac{n\pi D_1}{d} + \pi(1 + \sin\alpha)\frac{(n-1)n}{2} \tag{5}$$

where n = the number of successive aggregate rings between the disk and reaction ring $= \dfrac{2h\sin^{\alpha}}{d\cos\ \alpha(1+\sin\alpha)}$ (6)

and h = the depth of embedment of the disk

The force required to overcome aggregate interlock is thus given by:

$$P = \tau_c A_t \tag{7}$$

where A_t = total shear area = $T_n \cdot A_v = T_n \cdot \frac{d^2}{2\tan\alpha}$ (8)

and τ_c = shear strength of the cement paste binding the aggregate.

A cursory search of the literature has revealed little definitive data relating this value to the compressive strength of concrete, f'_c. However, it is known that under combined states of stress the shear strength for concrete can vary from 20 to 90 percent of f'_c or higher [28]. Pending future experimental quantification, and a detailed literature search an intermediate value of $\tau_c = .4\ f'_c$ has been assumed arbitrarily for the sake of illustration in the following calculations.

Substituting eqs (8), (6), and (5) into (7), and assuming $D_1 = D$ pullout force is:

$$P_t = \frac{\tau_c \pi d^2}{2\tan\alpha}\left\{\frac{2h(\sin\alpha)D}{d^2\cos\alpha(1+\sin\alpha)} + \frac{(1+\sin\alpha)}{2}\left[\left(\frac{2h\sin\alpha}{d\cos\alpha(1+\sin\alpha)}\right)^2 - \frac{2h\sin\alpha}{d\cos\alpha(1+\sin\alpha)}\right]\right\} \quad (9)$$

Units are kips, inches and degrees. As an illustrative calculation we may substitute the following data from specimens 1 and 2 into eq (9) to obtain the pullout force:

	Specimen 1	Specimen 2
h	10 in.	13.5 in.
D	12 in.	12 in.
α	35°	27°
d	1/4 in.	1/4 in.
$\sigma_v = .4\ f'_c$	1.064 Ksi	0.472 Ksi
predicted ultimate pullout force	399 kips	257 kips
experimental ultimate force	298 kips	259 kips

The predicted pullout force value for specimen 1 is about 30 percent higher than the actual value. This is likely due to the large deviation of the actual failure surface for specimen 1 from the idealized conic frustum assumed in the

calculation. The aggregates at the top of the actual trumpet shaped failure surface would pull out at considerably lower loads than for aggregates on the steeper, idealized surface. It should also be noted that the model assumes that all aggregates pull out at the same time, and that the aggregates are packed as tightly as possible without interfering with adjacent shear surfaces. Both of these may lead to overestimations of the actual pullout force. The predicted and actual pullout forces are quite close for specimen #2. However, this should not be misconstrued as proof of accuracy for eq (9), since the value of τ_c is somewhat arbitrary.

What can be drawn from this hypothetical analysis is that a reasonable approximation of the pullout strength was obtained by assuming that after 65 percent of ultimate load--when circumferential cracks have propagated from the disk to the reaction ring--the entire load is carried by the mechanism of mechanical aggregate interlock. Ultimate failure thus appears to be governed not by tension, not by compression, but by shear failure of the cement paste which prohibits vertical displacement of those aggregates which cross the failure surface. For this reason analytical solutions, based on a continuum theory, are not applicable for predicting the ultimate pullout force, since beyond 65 percent of ultimate the load is carried via a noncontinuous, discrete mechanism.

An interesting corollary follows directly from this hypothesis: in an actual pullout test the spacing of the aggregates, and thus the number of aggregates, which cross the failure surface will be a random process; no where near as idealized as we have assumed for the above calculations. As was shown above, for a given concrete the pullout force will be directly proportional to the number of aggregates crossing the failure surface: for a smaller number of aggregates mechanically bridging the gap, there will be a lower pullout force. The "scatter" associated with the pullout strength for a given value of f'_c is thus likely to be a function of the random manner in which the aggregates are located along the failure surface. One might anticipate that greater precision for the test could be achieved by enforcing a homogeneous material state along the failure surface. This could be accomplished by selectively screening out random aggregates and essentially testing the cement paste with the pullout test. This, then, would have the effect of deleting aggregate interlock from the failure mechanism, and ultimate failure would occur upon completion of the circumferential failure surface. As previously mentioned, this latter phase (formerly phase II) is principally governed by the tensile strength of the concrete, which is known to have a direct correlation with the compressive strength.

5. SUMMARY AND CONCLUSIONS

At the inception of this study very little fundamental information was available concerning the internal behavior of the pullout test. The two notable exceptions involved a plasticity analysis by Jensen and Braestrup [1] and a non-linear, cracking finite element analysis by Ottosen [7]. Both analyses concluded that the pullout test directly measures the compressive strength of the concrete. In an effort to provide experimental data for the verification of these studies, as well as to calibrate further analytical methods, efforts were begun at the National Bureau of Standards in the summer of 1980 to design a scaled up version of the pullout test. These specimens were fabricated at a 12:1 scale based on commercial pullout test equipment and heavily instrumented with waterproof embedment gages to measure the internal strain field at critical locations. Two tests were conducted so as to achieve geometries at the upper and lower apex angle (2α) bounds currently recommended by ASTM C 900. The most important results of these tests, and of an auxiliary series of 2 axisymmetric finite element analyses, are as follows:

5.1 FAILURE SEQUENCE

The load-deflection curve and internal gage strain histories mark three distinct phases in the failure sequence of a pullout test. These are:

a. Phase I: Initiation of circumferential cracking near the upper edge of the disk between 30 to 40 percent of ultimate load.

b. Phase II: Completion of circumferential cracking between 60 and 70 percent of ultimate load.

c. Phase III: Shear failure of paste (or mortar) and degradation of aggregate interlock beginning at 80 percent of ultimate.

5.2 INTERNAL STRAINS

Six gage strings were oriented in each specimen so as to record the variation of internal strain with load along six paths in the vicinity of the pullout disk and failure surface. The significant findings for each string are as follows:

a. Axial strain parallel to the failure surface: Large compressive strains exist near the outer disk edge and beneath the inner edge of the reaction ring, the former being approximately twice the magnitude of the latter. Between these two points the compressive strain decreases, reaching its lowest point at about 60 percent of the distance to the reaction ring with a value roughly half that at the reaction ring. Studies of axial strain data at ultimate load revealed that the compressive strains adjacent the failure surface were *insufficient to initiate a compression faiure.*

b. Radial strain perpendicular to the failure surface: Large tensile radial strains exist near the outer disk edge and decrease rapidly along the failure surface towards the reaction ring. Prior to the initiation of cracking the elastic radial strain reaches zero at approximately 90 percent of the distance to the reaction ring, and is slightly compressive at the reaction ring. The large tensile strains at the disk edge *are sufficient* to initiate circumferential cracking near the disk edge at approximately 30 percent of ultimate load. As circumferential cracking progresses towards the reaction ring all radial gages began to pick up large tensile strains.

c. Circumferential strain along the failure surface: These strains are small (less than 20 microstrain), nearly uniform, and tensile along the failure surface at a load equal to 20 percent of ultimate. One specimen, with $2\alpha = 70°$, indicated small negative (compressive) strains (< 15 microstrain) in the vicinity of the disk edge. These values disagreed with a companion finite element analysis which indicated small tensile strains near the disk edge.

d. Vertical near side face of disk: These strains are tensile and increase exponentially from the bottom disk edge towards the top disk edge. Peak values exceeding the average limiting tensile strain of the concrete (180 microstrain) were measured at the upper disk edge at only 17 percent of ultimate load. This indicates that there is little or no bond of the concrete along the side face of the disk. The force is thus transmitted only via the top face of the disk, producing a stress concentration at the upper disk edge.

e. Radial strains near top face of disk: These stains increase linearly from near zero at the disk stem to a maximum compresive strain at the disk edge. Peak values were between -40 to -50 microstrain at 20 percent of ultimate load, and reached a maximum of -350 microstrain at approximately 80 percent of ultimate, afterwhich the compressive strain rapidly decreased and became tensile for the outermost gage at the disk edge. The latter behavior was likely one to develop bending of the gage.

f. Radial strain on a vertical line above disk edge: This gage string indicated compressive radial strains at the disk face changing to tensile strain at a point approximately 1/10 the diameter of the disk above the upper disk face. The experimentally measured tensile strains were generally less than + 10 microstrain at 20 percent of ultimate. Large tensile strains at ultimate near the disk face for specimen #1 ($2\alpha = 70°$) showed that circumferential cracks had passed through these gages to a height of 37 percent of the embedment depth above the top face of the disk for these gages to monitor cracking the failure surface must deviate towards a trumpet shape (rather than a conic frustum) for higher values of 2α.

5.3 PRINCIPAL STRESSES

A two dimensional linear elastic axisymmetric, finite element analysis was performed for each experimental specimen. Following good correlation with the experimentally observed strains in the precracked state, the analysis was modified so that both specimens had identical material properties. It was thus possible to isolate the effect of geometric change on the stress field along the idealized frustum failure surface. These analyses indicate:

a. The maximum principal stress along the failure surface is positive (tensile) and decreases with a decrease in apex angle. For equal values of pullout force, the peak principal stress (near the disk edge) for the specimen with $2\alpha = 54°$ was 45 percent lower than for a similar specimen with $2\alpha = 70°$.

b. The minimum principal stress along the failure surface is compressive and, for the two specimens investigated, showed virtually no change in the maximum values. This would indicate that the minimum principal stress along the frustum surface is fairly insensitive to changes in geometry. The peak compressive stresses occur near of the disk edge and beneath the reaction ring with the latter being approximatley half the value of the former.

c. The circumferential stress magnitude is not greatly influenced by changes in the apex angle and is uniform and tensile over the majority of the failure surface. It is compressive just near of the disk (to 10 percent of the distance to the reaction ring) and just beneath the reaction ring (beginning at 90 percent of the distance to the reaction ring).

The variation of these three principle stresses indicate three states of stress along the idealized frustum failure surface (see figure 3.29):

1. Biaxial compression-tension from $x/d = 0$ to $x/d \approx .1$

2. Biaxial tension-compression from $x/d \approx .1$ to $x/d \approx .9$

3. Triaxial compression from $x/d \approx .9$ to $x/d = 1$

where x/d represents the fractional distance from the disk edge to the inner edge of the reaction ring. These values are identical for both specimens.

5.4 FAILURE SURFACE SHAPE

As the apex angle (2α) is increased the shape of the failure surface changes significantly. For the low apex angle ($2\alpha = 54°$) the failure surface is nearly linear, following the idealized shape of a conic frustum defined by the disk edge and the inner edge of the reaction ring. For increasing values of 2α the surface becomes more curved, assuming a trumpet shape. Correlations between experimental and analytical studies indicated that the failure surface *very nearly follows the minimum principal stress trajectory from the disk edge*

to the reaction ring. This means that the principal tensile stresses are acting almost normal to the failure surface. Experimental data show that the compressive stresses (and strains) along this path are *insufficient* to cause compressive failure and additionally, that the normal (radial) tensile strains do substantially exceed the average limiting strain of concrete along the circumferential failure surface. It can, therefore, be concluded that the propagation of circumferential cracks (which form the failure surface) is controlled by tensile strength rather than compressive strength.

5.5 FAILURE MECHANISM

It has been shown experimentally that three distinct phases occur prior to ultimate failure of a pullout test, which are marked by changes in the slope of the load deflection curve and by discontinuities in the load-strain histories of embedment gages placed along the idealized frustum failure surface. What precisely takes place during the first and last of these phases has been hypothesized in this study to be initiation of circumferential cracking, and a progresive ultimate failure by degradation of aggregate interlock across the failure surface. Both of the first and third phases will require further experimental work to quantify precisely. However, the second phase--that of the completion of circumferential cracking between the disk and reaction ring--has clearly been shown experimentally to take place via propagation beginning at the disk edge and ending at the inside edge of the reaction ring. Completion of circumferential cracking occurs at approximately 65 percent of ultimate load (regardless of variation in apex angle). At this point, for a homogeneous material, all continuity between the pullout "cone" and the base material would have been severed, and indeed, if the material were perfectly homogeneous, it would fail at this stage. But concrete is not homogeneous. Its fine grained cement paste binds together a matrix of larger particles--aggregates--which usually, but not necessarily, have material strengths greater than that of the binder. Even though complete propagation of circumferential cracking has taken place at 65 percent of ultimate load the presence of randomly spaced large particles mechanically bridging the failure surface prohibits failure until all such particles have pulled out of the retaining cement paste. This assertion is an extremely important one and means that beyond 65 percent of ultimate load any analytical model--including a nonlinear cracking finite element analysis--which bases its failure criteria on material failure in a continuum is *not applicable*. Beyond 65 percent of ultimate load in real concrete we are dealing with a discrete failure mechanism, not a continuous one. A rudimentary idealized, discrete shear failure model, developed in the present study, gave failure load estimates which were encouraging. Further experimental work is justified to address the roles which are played by both the aggregate and cement paste, and to further quantify material constants such as τ_c--the shear strength (in pure shear) of the cement paste--and to relate this quantity to f'_c.

5.6 FURTHER RESEARCH

As stated in the introduction, the ultimate goal of the NBS study is to determine which strength property of concrete is being measured in the pullout test, and to optimize the test geometry--perhaps even to modify the test--so as to reduce bandwidth scatter relating the pullout force to a key strength

property of concrete, be it compressive strength, tensile strength, or shear strength of cement paste. In essence the goal is to make the pullout test as reliable as possible. Realistically the strength property of concrete which best correlates with the pullout force, if it is not compressive strength f'_c, must eventually be related in terms of f'_c for it to be of practical use. Further experimental work is justified at this time to investigate the following topics:

1. The effect of aggregate on the pullout force (load-deflection study)

    a) shape of aggregate
    b) content of aggregate
    c) strength of aggregate
    d) size of aggregate

2. A study of the aggregate pullout mechanism

3. A study of the effect of apex angeeand aggregate content of the scatter associated with the pullout test for multiple tests at a given concrete strength.

REFERENCES

1. Jensen, B. C. and Braestrup, M. W., "Lok-tests Determine the Compressive Strength of Concrete," Nordisk Betong, V. 19, No. 2, 1975.

2. Kierkegaard-Hansen, P., "Lok-strength", Saertryk af Nordisk Betong, V. 3, 1975.

3. Malhotra, V. M. and Carette, G., "Comparison of Pullout Strength of Concrete with Compressive Strength of Cylinders and Cores, Pulse Velocity, and Rebound Number," ACI Technical Paper #77-20. ACI Jounral May-June 1980, pp. 161-170.

4. Malhotra, V. M., "Evaluation of the Pullout Test to Determine Strength of In Situ Concrete," Materiaux et Constructions, V. 8, No. 43, 1975.

5. Discussion: "Comparison of Pullout Strength of Concrete with Compressive Strength of Cylinders and Cores, Pulse Velocity, and Rebound Number," by Snell, L. M. and Rutledge, R. B. and by Stamenkovic, H. Disc 77-20, ACI Journal, March-April 1981, pp. 152-155.

6. Bickley, J. A. and Fasullo, S., "Analysis of Pullout Data from Construction Sites", 16 Ann. Meeting Transportation Research Board, Jan. 12, 1981, Washington, D.C.

7. Ottosen, N. S., Nonlinear Finite Element Analysis of a Pullout Test, American Society of Civil Engineers, Structures Journal, Vol. 107, No. 4, April 1981, pp 591-603.

8. Richards, O., personal communication

9. Newman, K., "Criteria for the Behavior of Plan Concrete Under Complex States of Stess", Proc. Intl. Conf: The Structure of Concrete, Cement and Concrete Assoc., pp. 255-274, London, 1968.

10. Newman, K. and Newman, J. B., "Failure Theories and Design Criteria for Plain Concrete". Proc. Southhampton 1969, Civil Engineering Materials Conf., Wiley Interscience, pp. 963-993, London, 1971.

11. Carino, N. J. and Slate, F. O., "Limiting Tensile Strain Criterion for Failure of Concrete", Journal of the ACI, V 73, No. 3, pp. 160-163, March 1976.

12. Stone, W. C., Paes-Filhd, W. and Breen, J. E., "Behavior of Post-Tensioned Girder Anchorage Zones", Center for Transportation Research, #208-2, Austin, TX, 1981.

13. J. O. Jirsa, personal communications

14. Rusch, H., Grasser, E., and Rao, P. S., "Fundamentals of Design for Uniaxial Stress Conditions in Concrete Members", Translation from German, Oct. 1963 by J. V. McMahon and J. E. Breen, University of Texas at Austin, Department of Civil Engineering, Austin, Texas, 78712.

15. Peterson, R. E., "Stress Concentration Design Factors", Wiley, New York, 1953.

16. Buyukozturk, O., Nilson, A. H., and Slate, F. O., "Stress-Strain Response and Fracture of a Concrete Model in Biaxial Loading, Paper No. 68-52, ACI Journal, August 1971, pp. 590-599.

17. Richards, O. "Pullout Strength Tests of Concrete," Research Paper, American Concrete Institute, Annual Meeting, Dallas, Texas (1972).

18. C873 Ref. Tentative Test Method for Compressive Strength of Concrete Cylinders Cast in Place in Cylindrical Molds (C 873-77T), 1980, Annual Book of Standards, Pt. 14, American Society for Testing and Materials, Philadelphia.

19. "Lok-test LTD Brochure", 43 Baywood Rd., Rexdale, Ontario, M9V 3YB, Canada.

20. "Finite Element Cracking Models", Memo from Dave Darwin to Nick Carino, March 1980.

21. "Axisymmetric Punching of Plain and Reinforced Concrete" Braestrup, M. W. et al., Special Report, Structural Research Laboratory, Technical University of Denmark ( ).

22. ASTM C 900-78T, "Tentative Test Method for Pullout Strength of Hardened Concrete," 1980 Annual Book of Standards, Part 14, American Society for Testing and Materials, Philadelphia (1980).

23. Hsu, T. C., Slate, F. O., Surman, G. M. and Winter, G., "Microcracking of Plain Concrete and the Shape of the Stress Strain Curve", ACI Journal, February 1963, pp. 209-223.

24. Launay, P. and Gachon, H., "Strain and Ultimate Strength of Concrete Under Triaxial Stress", paper SP34-13, Symposium on Concrete for Nuclear Reactors, pp. 269-282 ( ).

25. "Determining Concrete Strength for Control of Concrete in Structures", Skrmtajew, B. G., ACI Proceedings, Vol. 34, Jan-Feb 1938, p. 285-303.

26. "Stress-strain Response and Fracture of Concrete in Uniaxial and Biaxial Compression", Liu, T. C., Nilson, A., and Slate, F. O., ACI Journal, May 1972, pp. 291-295.

27. ASTM C42

28. Concrete. Mindess, S. and Young. J. F., Prentice-Hall, Inc., Englewood Cliffs, N. J. 07632, 1981, pp 400-401.

Gage ID	Adjusted distance "X" wrt/Disk (inches)
RN 1	1.875
RN 2	3.075
RN 3	4.175
RN 4	5.375
RN 5	6.275
RN 6	7.375
RN 7	8.375
RN 8	9.375
RN 9	10.475
RN 10	11.475

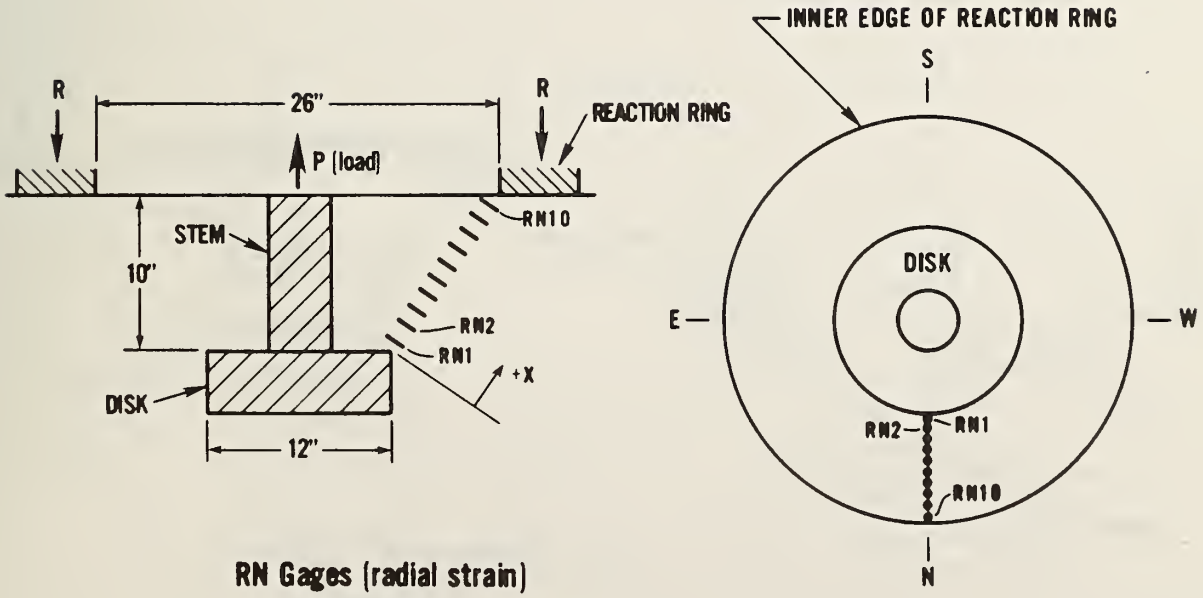

RN Gages (radial strain)
Specimen #1

Appendix A Table A.1 RN Gage locations, Specimen # 1

Gage ID	Adjusted distance "X" wrt/Disk (inches)
RS 1	1.625
RS 2	3.075
RS 3	4.775
RS 4	6.475
RS 5	7.975
RS 6	9.475
RS 7	11.275
AS 1	2.375
AS 2	3.875
AS 3	5.575
AS 4	7.075
AS 5	8.775
AS 6	10.375

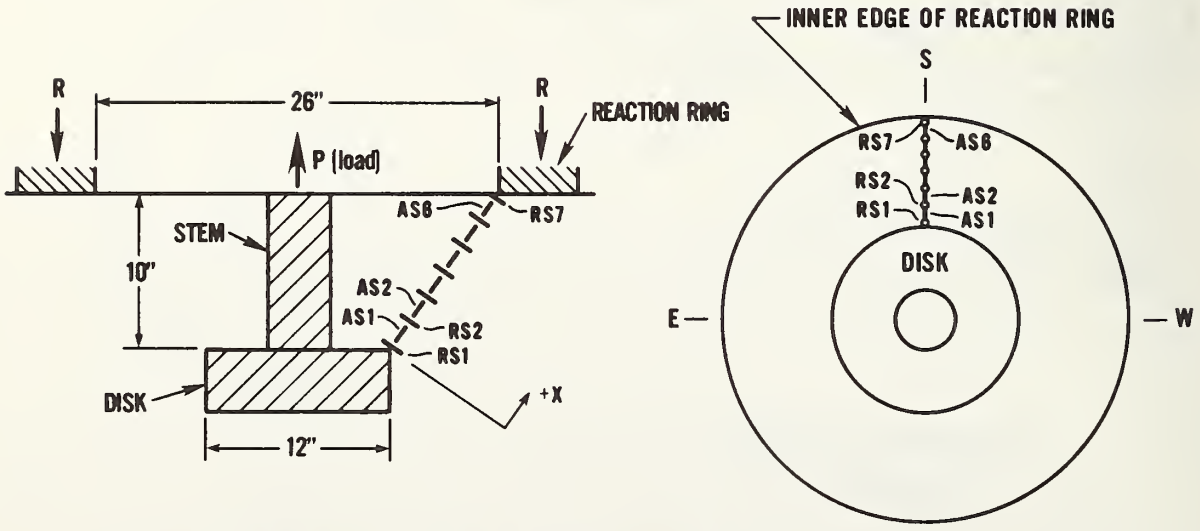

RS (radial strain) & AS (axial strain) Gages
Specimen #1

Appendix A Table A.2 RS & AS Gage locations, Specimen # 1

Gage ID	Adjusted distance "X" wrt/Disk (inches)
CE 1	1.125
CE 2	2.025
CE 3	3.025
CE 4	4.125
CE 5	5.125
CE 6	6.325
CE 7	7.425
CE 8	8.725
CE 9	9.825
CE 10	10.725

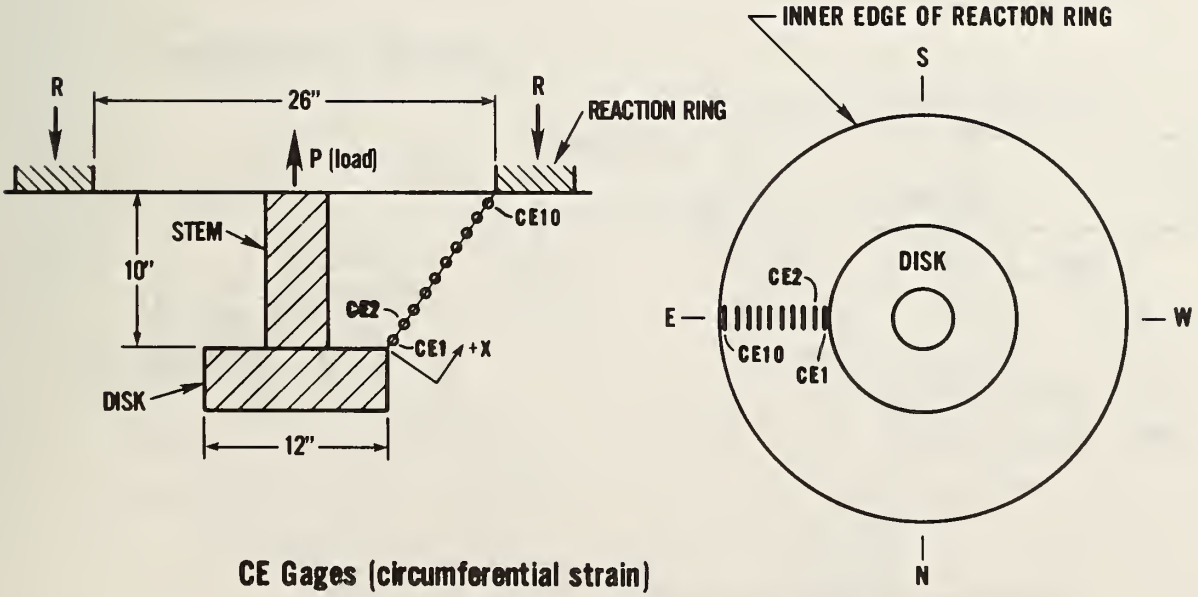

CE Gages (circumferential strain)
Specimen #1

Appendix A Table A.3 CE Gage locations, Specimen # 1

Gage ID	Adjusted distance "X" wrt/Disk (inches)
CW 1	1.375
CW 2	2.375
CW 3	3.375
CW 4	4.375
CW 5	5.375
CW 6	6.425
CW 7	7.575
CW 8	8.675
CW 9	9.775
CW 10	10.775

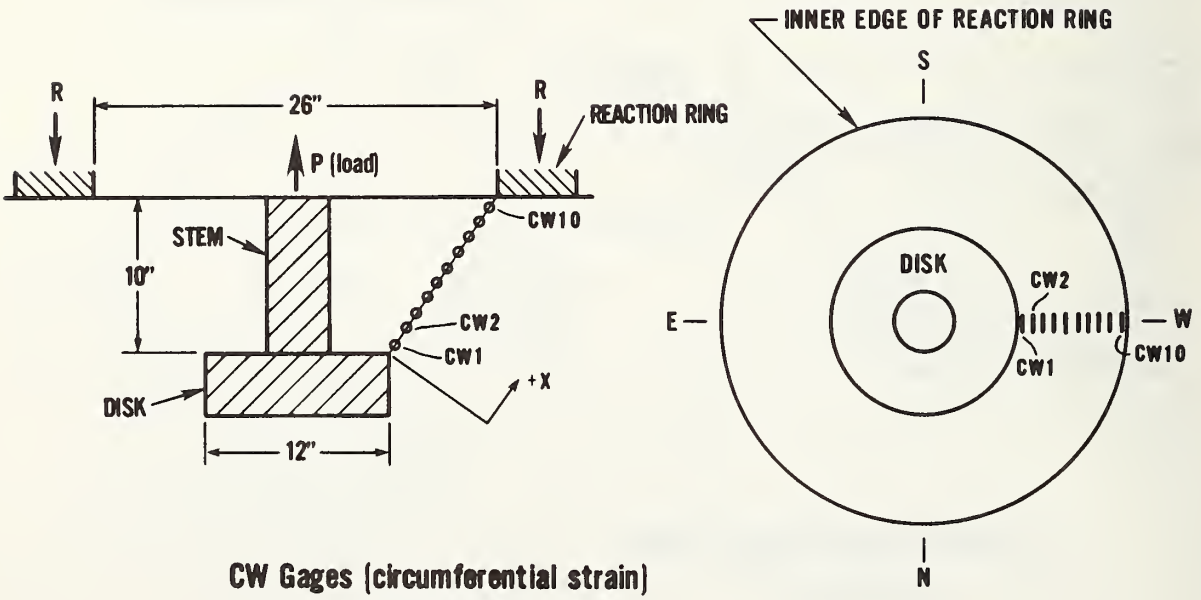

CW Gages (circumferential strain)
Specimen #1

Appendix A Table A.4 CW Gage locations, Specimen # 1

Gage ID	Adjusted distance "X" wrt/Disk (inches)
ANE 1	1.875
ANE 2	2.775
ANE 3	3.675
ANE 4	4.275
ANE 5	5.075
ANE 6	5.975
ANE 7	6.775
ANE 8	7.675
ANE 9	8.475
ANE 10	9.275
ANE 11	9.925

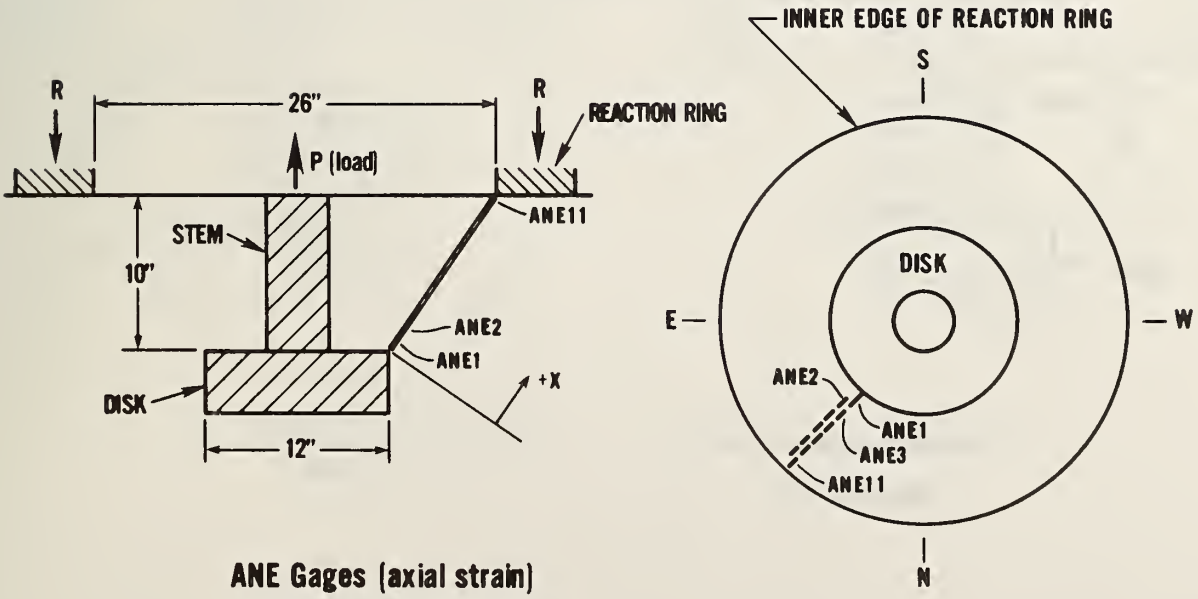

ANE Gages (axial strain)
Specimen #1

Appendix A Table A.5 ANE Gage locations, Specimen # 1

Gage ID	Adjusted distance "X" wrt/Stem (inches)
TC 1	.75
TC 2	1.45
TC 3	2.35
TC 4	3.05
TC 5	4.05

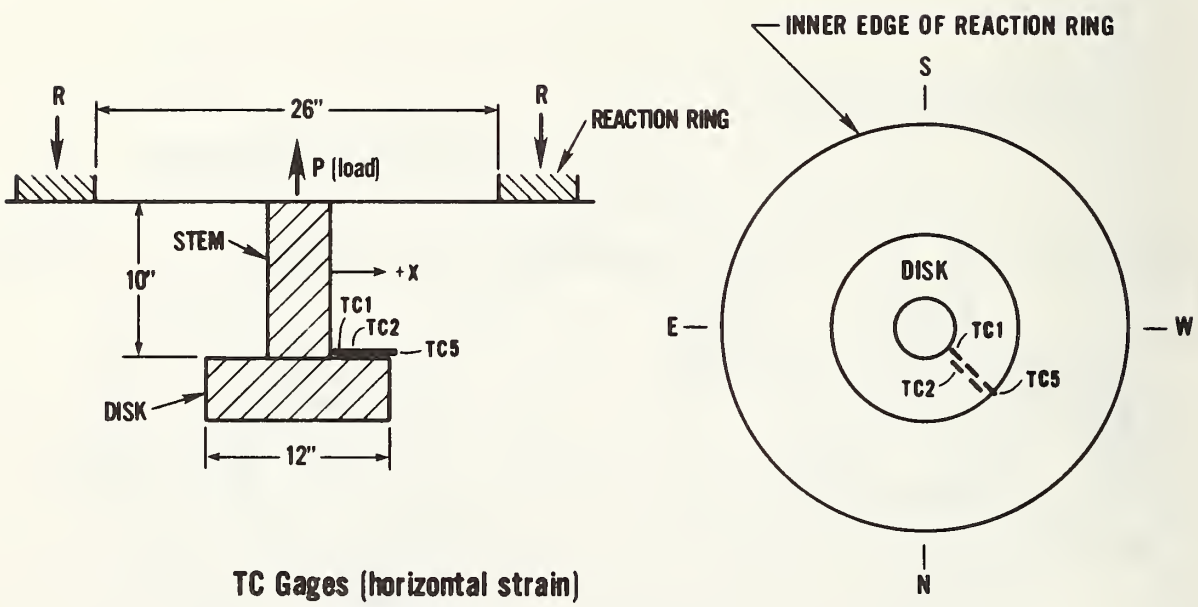

TC Gages (horizontal strain)
Specimen #1

Appendix A Table A.6 TC Gage locations, Specimen # 1

Gage ID	Adjusted distance "X" wrt/Disk (inches)
RV 1	2.125
RV 2	3.125
RV 3	4.125
RV 4	5.225
RV 5	6.225
RV 6	7.325

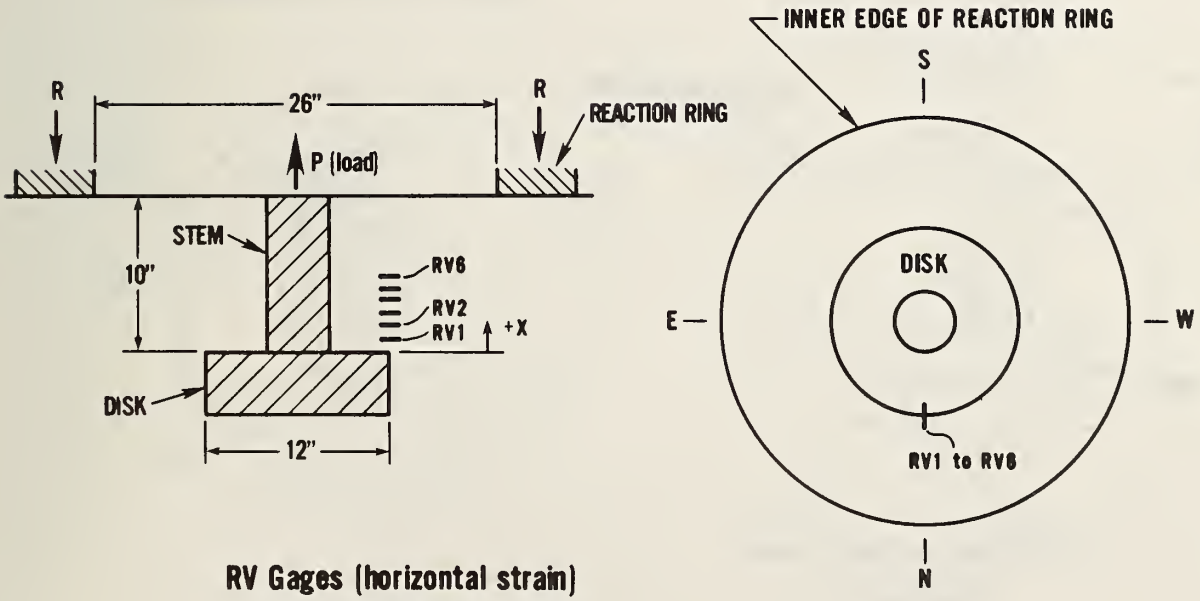

RV Gages (horizontal strain)
Specimen #1

Appendix A Table A.7 RV Gage locations, Specimen # 1

Gage ID	Adjusted distance "X" wrt/Disk (inches)
ET 1	4.5625
ET 2	3.76
ET 3	2.96
ET 4	2.16
ET 5	1.26
ET 6	.66

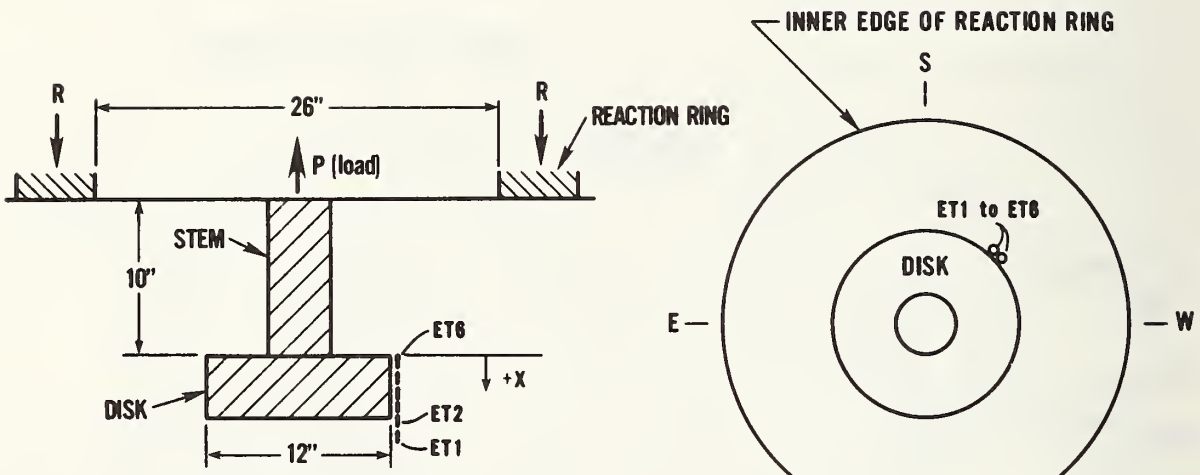

ET Gages (vertical strain)
Specimen #1

Appendix A Table A.8 ET Gage locations, Specimen # 1

Gage ID	"X" wrt/Disk (inches)
RN 1	2.125
RN 2	3.275
RN 3	4.575
RN 4	5.775
RN 5	7.075
RN 6	8.375
RN 7	9.775
RN 8	11.175
RN 9	12.475
RN 10	13.875

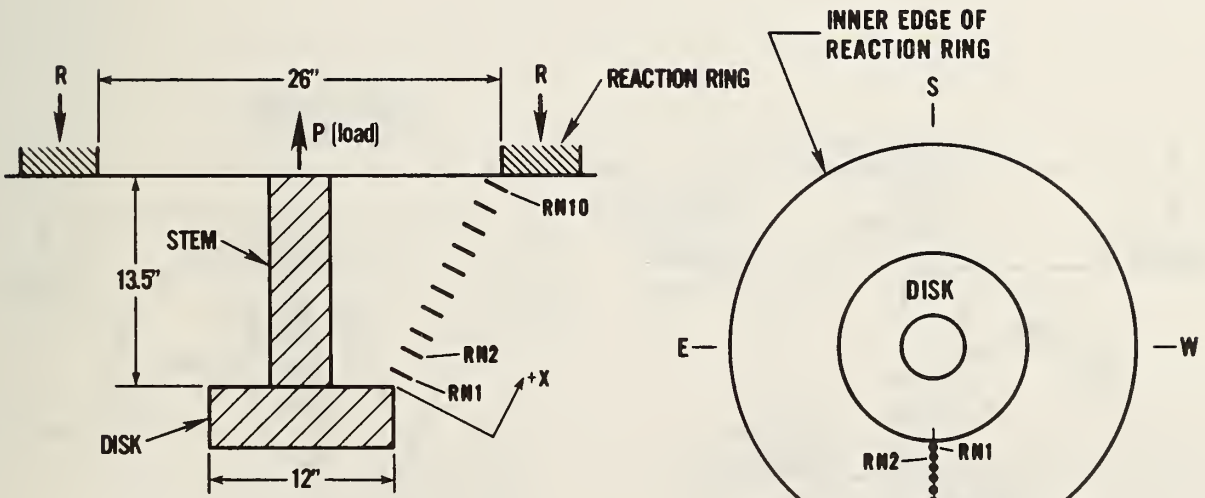

RN Gages (radial strain)
Specimen #2

Appendix A Table A.9 RN Gage locations, Specimen # 2

Gage ID	Adjusted Diameter "X" wrt/Disk (inches)
RS 1	1.77
RS 2	3.07
RS 3	4.37
RS 4	5.62
RS 5	6.92
RS 6	8.17
RS 7	9.37
RS 8	10.77
RS 9	12.07
RS 10	13.47

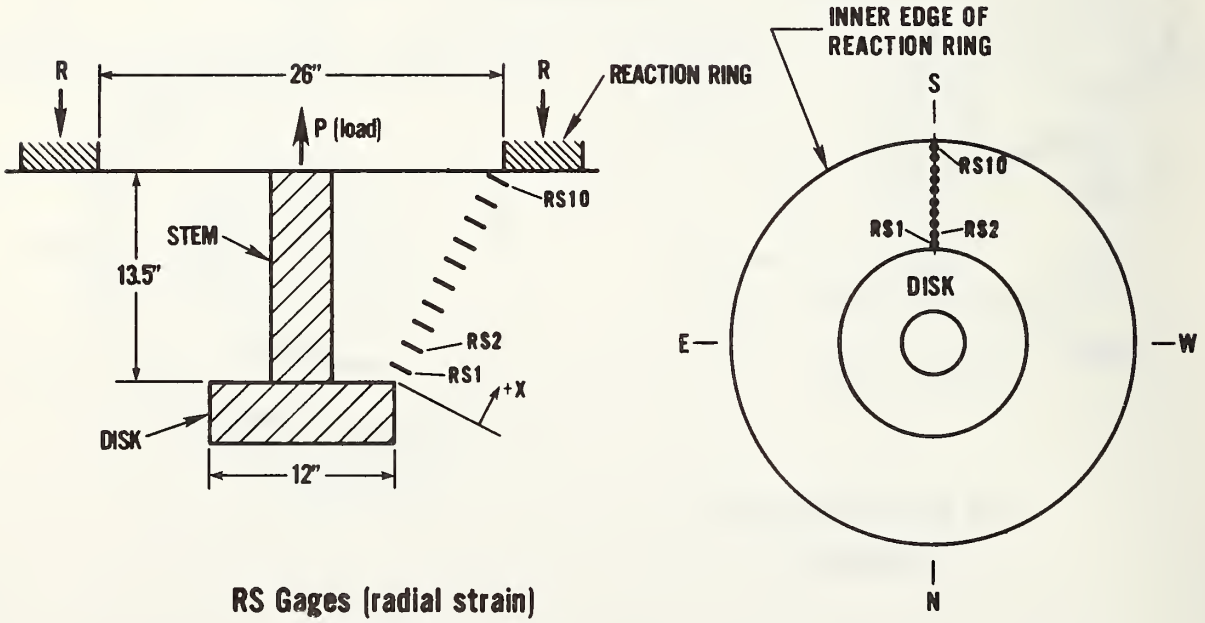

RS Gages (radial strain)
Specimen #2

Appendix A Table A.10 RS Gage locations,
Specimen # 2

Gage ID	Adjusted distance "X" wrt/Disk (inches)
CE 1	1.38
CE 2	2.68
CE 3	3.98
CE 4	5.28
CE 5	6.68
CE 6	8.08
CE 7	9.38
CE 8	10.68
CE 9	11.98
CE 10	13.28

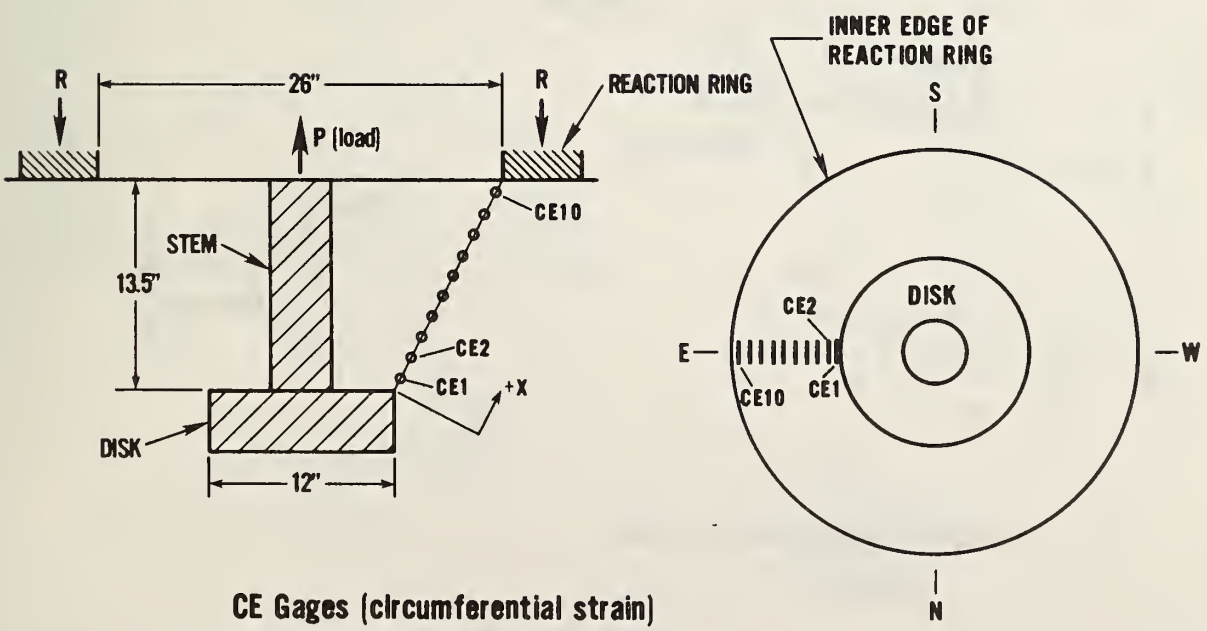

CE Gages (circumferential strain)
Specimen #2

Appendix A Table A.11 CE Gage locations,
Specimen # 2

Gage ID	Adjusted distance "X" wrt/Disk (inches)
CW 1	1.2
CW 2	2.6
CW 3	4.0
CW 4	5.3
CW 5	6.7
CW 6	8.0
CW 7	9.3
CW 8	10.7
CW 9	12.0
CW 10	13.4

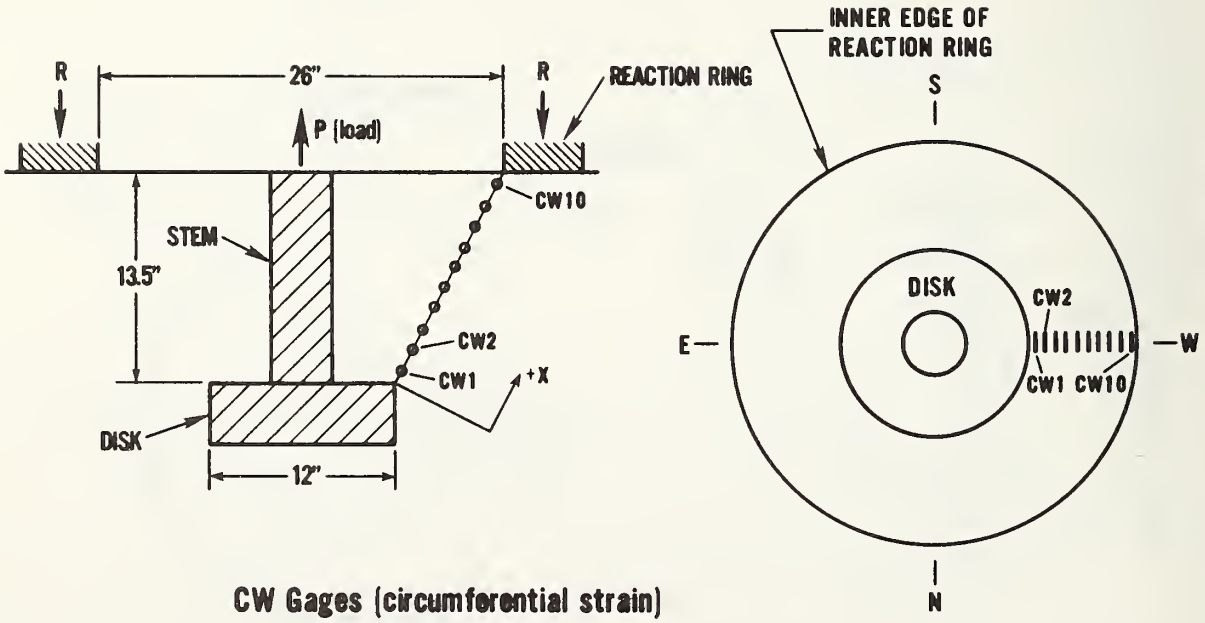

CW Gages (circumferential strain)
Specimen #2

Appendix A Table A.12 CW Gage locations,
Specimen # 2

Gage ID	Adjusted distance "X" wrt/Disk (inches)
ANE 1	1.89
ANE 2	2.79
ANE 3	3.59
ANE 4	4.49
ANE 5	5.29
ANE 6	6.29
ANE 7	6.89
ANE 8	7.89
ANE 9	8.69
ANE 10	9.69
ANE 11	10.39
ANE 12	11.29
ANE 13	11.99
ANE 14	12.79

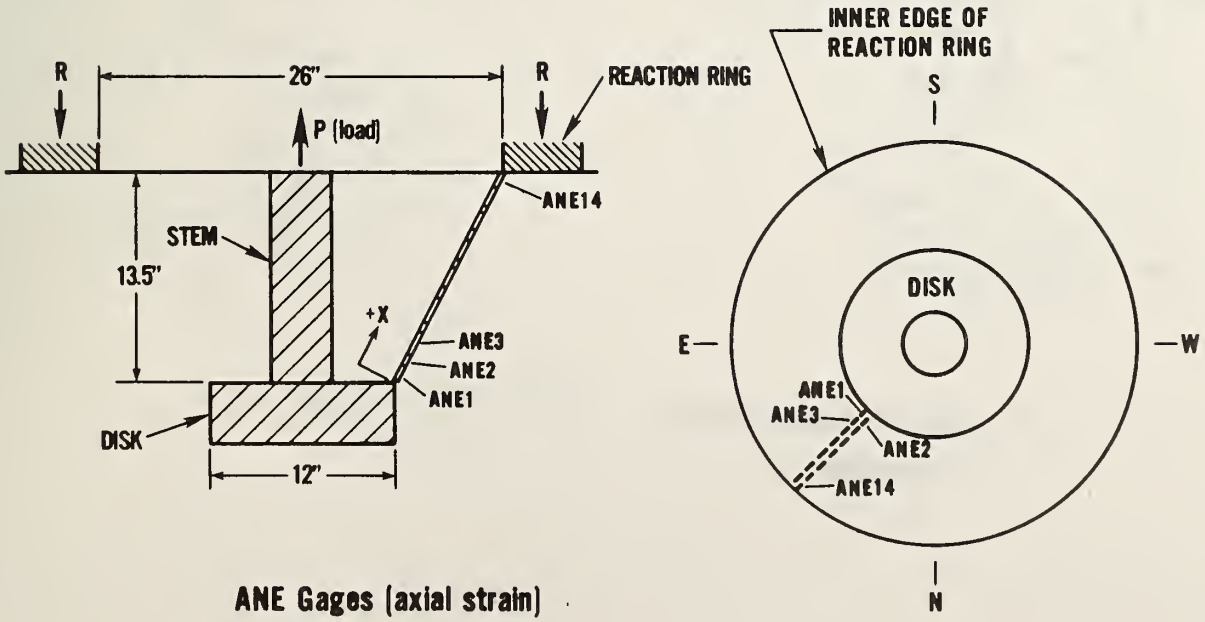

ANE Gages (axial strain)
Specimen #2

Appendix A Table A.13 ANE Gage locations,
Specimen # 2

Gage ID	Adjusted distance "X" wrt/Stem (inches)
TC 1	1.02
TC 2	1.82
TC 3	2.82
TC 4	3.52

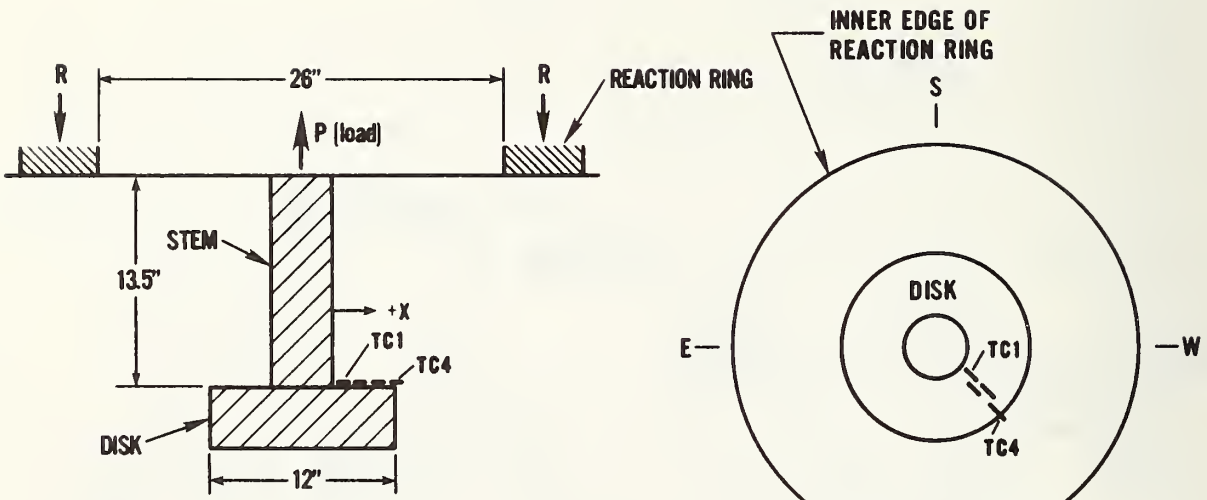

TC Gages (horizontal strain)
Specimen #2

Appendix A Table A.14 TC Gage locations,
Specimen # 2

Gage ID	Adjusted distance "X" wrt/Disk (inches)
RV 1	2.83
RV 2	4.28
RV 3	5.63
RV 4	7.03
RV 5	8.48
RV 6	9.68

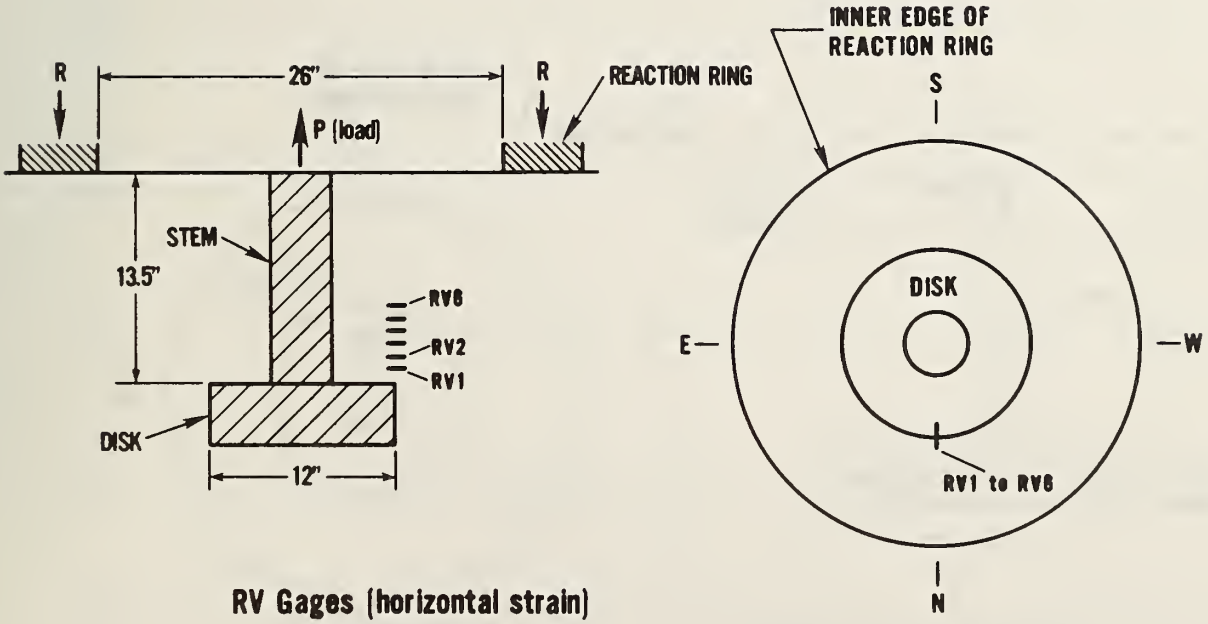

RV Gages (horizontal strain)
Specimen #2

Appendix A Table A.15 RV Gage locations,
Specimen # 2

Gage ID	Adjusted distance "X" wrt/Disk (inches)
ET 1	.63
ET 2	1.33
ET 3	2.13
ET 4	2.93
ET 5	3.73
ET 6	4.63

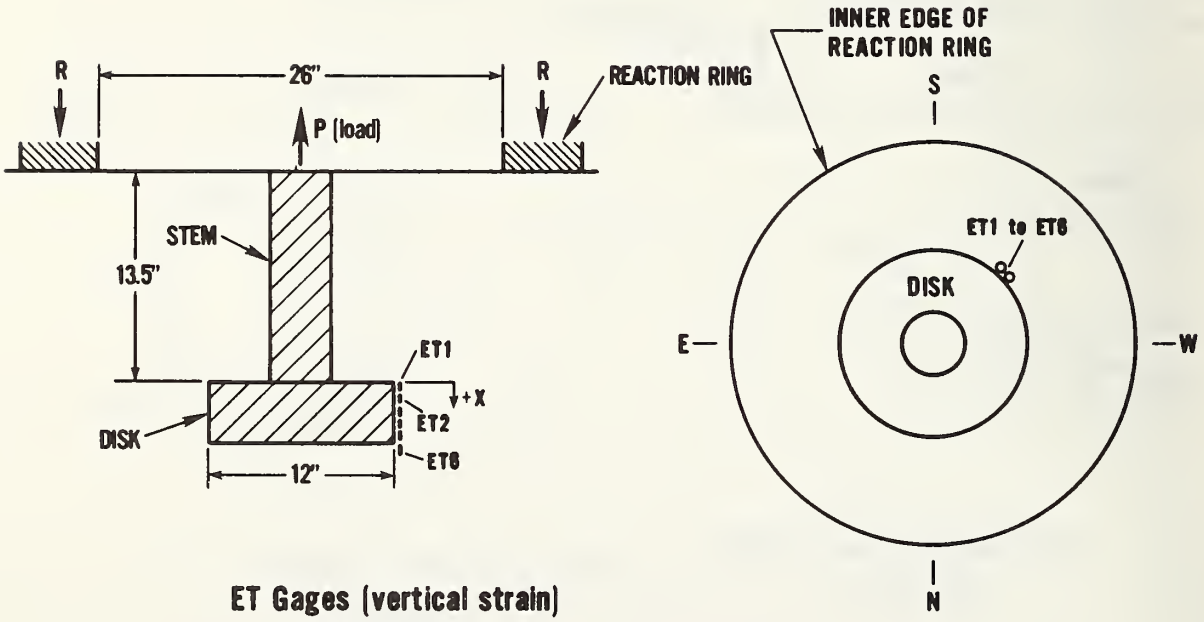

ET Gages (vertical strain)
Specimen #2

Appendix A Table A.16 ET Gage locations,
Specimen # 2

Appendix B - Table B.1 - Pullout #1
Raw Experimental Data
RN (north radial gages) see Appendix A
for gage location and orientation.

LOAD KIPS	SCAN #	RN1 MSTR*	RN2 MSTR	RN3 MSTR	RN4 MSTR	RN5 MSTR	RN6 MSTR	RN7 MSTR	RN8 MSTR	RN9 MSTR	RN10 MSTR
0	1	0	0	0	0	0	0	0	0	0	0
9.54	2	6	5	3	5	5	5	2	8	8	4
21.48	3	17	11	10	6	10	8	5	2	0	4
33.37	4	25	17	16	17	14	11	8	5	4	8
42.91	5	35	24	22	21	22	17	10	6	8	8
52.44	6	41	32	29	33	27	22	16	11	8	4
66.74	7	49	35	35	37	35	25	17	11	8	4
72.28	8	59	41	41	41	43	32	22	14	8	8
85.81	9	67	48	48	46	49	37	25	17	12	8
95.35	10	73	52	52	52	56	41	29	19	12	12
104.88	11	76	57	57	62	59	44	35	24	8	12
114.42	12	81	60	62	62	64	49	40	27	12	12
128.72	13	83	64	64	59	70	54	49	33	16	12
138.25	14	86	67	64	60	70	56	57	41	24	20
147.79	15	92	68	64	57	70	56	62	43	28	20
157.32	16	95	70	64	59	70	56	64	44	36	32
166.86	17	102	75	68	60	70	54	65	46	44	36
176.39	18	111	78	70	57	71	52	64	44	44	48
185.93	19	121	83	75	62	75	54	64	48	48	52
197.82	20	140	89	81	57	76	52	60	49	52	60
197.82	21	141	92	83	62	73	49	59	49	48	56
207.35	22	171	102	106	86	70	27	52	52	64	67
219.30	23	203	135	141	59	52	2	41	62	143	79
226.42	24	257	157	133	46	48	-8	37	67	266	83
238.37	25	305	170	141	37	48	-13	35	78	325	79
247.90	26	357	183	152	40	44	-19	38	100	389	91
257.44	27	435	200	171	24	44	-24	38	135	476	107
266.97	28	484	222	197	22	44	-27	40	181	564	131
257.44	29	518	246	221	19	41	-25	43	254	623	163
266.97	30	564	268	243	13	43	-24	44	330	663	187
278.86	31	591	284	254	19	44	-22	49	364	687	194
288.40	32	670	325	287	21	54	-16	60	465	754	242
293.17	33	778	381	322	17	65	-13	65	524	774	286
295.57	34	800	394	329	24	64	-11	67	522	770	290
293.17	35	829	405	335	17	67	-10	64	514	762	310
293.17	36	889	429	346	21	68	-6	54	489	766	345
293.17	37	1037	468	360	29	70	2	24	359	869	480

*MSTR = microstrain

Appendix B - Table B.2 - Pullout #1
Raw Experimental Data
RS (south radial gages) See Appendix A
for gage location and orientation.

LOAD KIPS	SCAN #	RS1 MSTR*	RS2 MSTR	RS3 MSTR	RS4 MSTR	RS5 MSTR	RS6 MSTR	RS7 MSTR
0	1	0	0	0	0	0	0	0
9.54	2	16	-2	4	4	-4	-8	-16
21.48	3	34	8	10	8	4	0	-20
33.37	4	46	14	16	12	-8	-8	-20
42.91	5	56	20	26	18	16	4	-20
52.44	6	73	26	32	20	20	4	-20
66.74	7	77	34	36	26	24	4	-20
72.28	8	85	38	46	30	28	12	-16
85.81	9	103	42	50	34	32	12	-16
95.35	10	113	46	58	38	36	12	-16
104.88	11	111	50	60	42	48	12	-16
114.42	12	125	50	64	46	56	16	-52
128.72	13	133	52	60	44	60	20	-48
138.25	14	153	52	56	42	71	16	-48
147.79	15	196	48	50	40	79	16	-40
157.32	16	204	48	50	38	79	8	-36
166.86	17	220	46	48	36	79	0	-36
176.39	18	244	44	50	36	83	-8	-32
185.93	19	272	46	52	38	83	-8	-32
197.82	20	310	50	56	38	95	-12	-32
197.82	21	316	48	56	36	99	-12	-36
207.35	22	327	54	60	30	103	-16	-64
219.30	23	369	62	65	30	111	-12	-67
226.42	24	411	67	75	28	127	-8	-67
238.37	25	522	93	99	-4	147	64	-60
247.90	26	812	127	95	-20	175	107	-52
257.44	27	1030	151	93	-24	183	79	-52
266.97	28	1175	161	99	-32	179	59	-44
257.44	29	1286	179	101	-38	175	48	-52
266.97	30	1280	196	107	-40	171	52	-71
278.86	31	1355	212	113	-40	175	56	-71
288.40	32	1449	260	127	-40	175	71	-67
293.17	33	1363	323	139	-40	163	119	-71
295.57	34	1411	335	139	-40	159	131	-71
293.17	35	1417	353	141	-40	156	151	-71
293.17	36	1469	383	139	-40	151	175	-71
293.17	37	1574	447	127	-40	147	226	-79

*MSTR = microstrain

Appendix B - Table B.3 - Pullout #1
Raw Experimental Data
RV (radial) gages. See Appendix A
for gage location and orientation.

LOAD KIPS	SCAN #	RV1 MSTR*	RV2 MSTR	RV3 MSTR	RV4 MSTR	RV5 MSTR	RV6 MSTR
0	1	0	0	0	0	0	0
9.54	2	-2	-2	0	-2	-2	-2
21.48	3	0	-2	5	3	3	3
33.37	4	-3	-2	2	3	5	3
42.91	5	-3	0	5	6	6	5
52.44	6	-6	0	3	6	10	5
66.74	7	-6	2	5	11	11	6
72.28	8	-6	2	6	13	13	6
85.81	9	-10	3	5	16	14	6
95.35	10	-11	2	6	17	16	10
104.88	11	-17	2	5	14	16	6
114.42	12	-30	-3	2	16	17	3
128.72	13	-51	-11	-3	11	14	-5
138.25	14	-76	-24	-10	2	10	-21
147.79	15	-106	-38	-21	-6	2	-35
157.32	16	-135	-54	-32	-16	-3	-44
166.86	17	-168	-70	-43	-29	-11	-57
176.39	18	-205	-90	-54	-38	-17	-65
185.93	19	-232	-102	-62	-46	-21	-71
197.82	20	-271	-122	-73	-52	-27	-76
197.82	21	-284	-129	-79	-56	-29	-79
207.35	22	-364	-160	-94	-70	-38	-86
219.30	23	-376	-138	-90	-105	-60	-102
226.42	24	-372	-92	-92	-148	-71	-105
238.37	25	-359	-68	-122	-186	-81	-106
247.90	26	-348	-59	-151	-227	-92	-116
257.44	27	-316	-54	-187	-284	-108	-122
266.97	28	-254	-54	-208	-335	-121	-127
257.44	29	-192	-62	-230	-391	-135	-130
266.97	30	-133	-70	-243	-435	-148	-132
278.86	31	-119	-64	-248	-446	-151	-133
288.40	32	-41	-35	-254	-478	-160	-133
293.17	33	64	27	-248	-486	-160	-127
295.57	34	81	40	-248	-487	-160	-127
293.17	35	103	56	-243	-483	-157	-125
293.17	36	141	94	-236	-478	-154	-124
293.17	37	198	175	-219	-464	-148	-121

*MSTR = microstrain

Appendix B - Table B.4 - Pullout #1
Raw Experimental Data
CE (east circumferential) gages. See Appendix A
for gage location and orientation.

LOAD KIPS	SCAN #	CE1 MSTR	CE2 MSTR*	CE3 MSTR	CE4 MSTR	CE5 MSTR	CE6 MSTR	CE7 MSTR	CE8 MSTR	CE9 MSTR	CE10 MSTR
0	1	0	0	0	0	0	0	0	0	0	0
9.54	2	-2	-2	-3	-2	-2	0	2	0	0	2
21.48	3	-3	-2	-5	-3	-2	0	3	3	8	6
33.37	4	-8	-6	-6	-6	-3	0	3	3	13	6
42.91	5	11	-8	-8	-10	-3	2	5	6	19	10
52.44	6	-17	-14	-13	-13	-8	-2	3	6	21	10
66.74	7	-19	-17	-13	-16	-10	2	6	11	29	13
72.28	8	-22	-21	-14	-19	-11	2	6	11	33	13
85.81	9	-27	-25	-19	-25	-14	0	6	13	38	16
95.35	10	-32	-30	-22	-29	-16	0	6	13	44	16
104.88	11	-38	-37	-27	-32	-22	-3	3	13	46	16
114.42	12	-46	-48	-32	-41	-30	-8	0	8	54	19
128.72	13	-57	-62	-44	-51	-40	-14	-6	0	56	19
138.25	14	-75	-78	-57	-62	-49	-17	-10	-5	59	19
147.79	15	-91	-100	-73	-78	-64	-25	-16	-14	60	22
157.32	16	-111	-121	-89	-92	-78	-30	-17	-16	67	24
166.86	17	-132	-143	-106	-108	-95	-37	-22	-21	70	25
176.39	18	-157	-170	-125	-125	-117	-44	-30	-25	78	30
185.93	19	-175	-187	-135	-137	-137	-49	-37	-25	78	33
197.82	20	-203	-216	-157	-159	-164	-54	-46	-25	81	40
197.82	21	-210	-225	-160	-165	-171	-57	-52	-27	81	40
207.35	22	-256	-275	-191	-200	-194	-75	-94	-30	73	48
219.30	23	-273	-294	-203	-211	-198	-81	-105	-29	79	54
226.42	24	-294	-318	-216	-221	-213	-83	-113	-27	87	60
238.37	25	-318	-341	-229	-230	-229	-94	-106	-25	105	71
247.90	26	-352	-372	-244	-243	-227	-79	-116	-29	129	83
257.44	27	-405	-402	-270	-267	-233	-73	-130	-35	168	105
266.97	28	-459	-419	-292	-294	-238	-71	-143	-37	206	122
257.44	29	-514	-414	-303	-316	-225	-68	-168	-41	213	137
266.97	30	-556	-406	-294	-335	-237	-62	-183	-35	213	149
278.86	31	-575	-419	-305	-348	-225	-64	-184	-32	222	152
288.40	32	-627	-410	-324	-381	-183	-60	-192	-22	232	164
293.17	33	-686	-383	-356	-445	-106	-41	-200	5	208	173
295.57	34	-699	-376	-365	-457	-95	-37	-206	6	198	168
293.17	35	-708	-372	-375	-467	-87	-35	-219	10	195	159
293.17	36	-727	-359	-399	-486	-84	-35	-262	5	194	137
293.17	37	-765	-354	-486	-495	-67	-95	-370	-32	287	92

*MSTR = microstrain

Appendix B - Table B.5 - Pullout #1
Raw Experimental Data
CW (circumferential west) gages. See Appendix A
for gage location and orientation.

LOAD KIPS	SCAN #	CW1 MSTR*	CW2 MSTR	CW3 MSTR	CW4 MSTR	CW5 MSTR	CW6 MSTR	CW7 MSTR	CW8 MSTR	CW9 MSTR
0	1	0	0	0	0	0	0	0	0	0
9.54	2	0	-2	2	-2	2	2	-2	3	5
21.48	3	0	-3	0	-3	2	0	-2	3	8
33.37	4	-2	-3	5	-2	-3	2	5	10	14
42.91	5	-3	-6	-2	-6	-6	-2	2	10	17
52.44	6	-6	-11	2	-8	-8	-5	5	16	24
66.74	7	-10	-14	0	-11	-13	-8	5	16	25
72.28	8	-10	-16	-3	-14	-16	-11	5	16	29
85.81	9	-10	-19	-3	-16	-19	-13	3	19	32
95.35	10	-13	-21	-3	-19	-24	-16	8	22	37
104.88	11	-16	-27	-3	-24	-29	-21	6	29	40
114.42	12	-24	-37	-8	-33	-37	-30	5	29	46
128.72	13	-32	-48	-21	-41	-46	-38	-3	29	49
138.25	14	-41	-60	-32	-46	-48	-40	-10	22	56
147.79	15	-52	-71	-43	-51	-51	-40	-11	17	60
157.32	16	-60	-83	-51	-56	-56	-40	-8	10	68
166.86	17	-73	-97	-64	-65	-59	-46	-14	5	73
176.39	18	-87	-113	-71	-73	-64	-49	-14	-2	75
185.93	19	-98	-122	-76	-76	-68	-54	-17	-5	79
197.82	20	-117	-137	-90	-89	-76	-65	-32	-24	78
197.82	21	-124	-140	-89	-90	-79	-67	-30	-24	79
207.35	22	-146	-157	-97	-110	-98	-79	-46	-37	73
219.30	23	-162	-164	-98	-116	-105	-76	-48	-37	73
226.42	24	-186	-168	-86	-129	-106	-79	-54	-40	65
238.37	25	-214	-167	-65	-137	-114	-87	-62	-41	52
247.90	26	-229	-167	-51	-135	-103	-83	-41	-37	51
257.44	27	-233	-181	-33	-132	-90	-57	-68	-40	46
266.97	28	-216	-203	-6	-125	-81	-49	-92	-67	52
257.44	29	-187	-224	43	-114	-83	-51	-135	-117	70
266.97	30	-170	-238	89	-111	-86	-54	-173	-146	83
278.86	31	-171	-248	102	-111	-84	-52	-178	-146	92
288.40	32	-156	-270	157	-106	-78	-51	-221	-159	108
293.17	33	-121	-284	218	-100	-67	-48	-203	-195	124
295.57	34	-110	-284	230	-97	-64	-48	-195	-218	137
293.17	35	-97	-284	241	-95	-62	-45	-194	-260	154
293.17	36	-70	-283	264	-90	-59	-48	-184	-327	187
293.17	37	14	-268	302	-83	-49	-49	-160	-449	321

*MSTR = microstrain

Appendix B - Table B.6 - Pullout #1
Raw Experimental Data
ANE (axial, northeast) gages. See Appendix A
for gage location and orientation.

LOAD KIPS	SCAN #	ANE 1 MSTR*	ANE2 MSTR	ANE3 MSTR	ANE4 MSTR	ANE5 MSTR	ANE6 MSTR	ANE7 MSTR	ANE8 MSTR	ANE9 MSTR	ANE10 MSTR	ANE 11 MSTR
0	1	0	0	0	0	0	0	0	0	0	0	0
9.54	2	-13	-8	-5	-3	-6	-3	-5	-3	-6	-5	-10
21.48	3	-35	-14	-13	-8	-11	-5	-5	-6	-19	-11	-21
33.37	4	-64	-24	-22	-17	-19	-14	-13	-13	-22	-16	-32
42.91	5	-87	-33	-32	-25	-25	-19	-16	-17	-37	-22	-44
52.44	6	-116	-46	-43	-33	-37	-27	-25	-22	-48	-29	-56
66.74	7	-143	-54	-51	-41	-43	-32	-29	-27	-59	-35	-67
72.28	8	-168	-65	-59	-49	-49	-35	-33	-32	-70	-40	-79
85.81	9	-195	-75	-68	-57	-59	-41	-38	-37	-79	-46	-90
95.35	10	-221	-84	-78	-65	-67	-48	-43	-41	-89	-52	-102
104.88	11	-251	-97	-90	-75	-78	-56	-52	-49	-102	-60	-114
114.42	12	-292	-108	-102	-81	-87	-68	-57	-60	-119	-73	-138
128.72	13	-348	-124	-116	-94	-100	-79	-71	-76	-149	-94	-171
138.25	14	-410	-140	-133	-111	-116	-92	-86	-92	-183	-122	-214
147.79	15	-475	-154	-151	-127	-130	-102	-95	-106	-216	-152	-265
157.32	16	-543	-170	-171	-144	-144	-113	-106	-119	-244	-186	-319
166.86	17	-613	-186	-192	-162	-160	-122	-119	-130	-279	-218	-375
176.39	18	-680	-197	-208	-183	-176	-132	-127	-143	-314	-243	-433
185.93	19	-735	-208	-222	-197	-187	-138	-132	-151	-343	-259	-476
197.82	20	-805	-219	-237	-210	-202	-141	-140	-157	-391	-265	-527
197.82	21	-819	-219	-238	-211	-202	-140	-137	-156	-400	-264	-538
207.35	22	-918	-244	-259	-271	-225	-94	-105	-103	-343	-267	-587
219.30	23	-968	-273	-281	-314	-248	-95	-68	-78	-279	-260	-626
226.42	24	-1037	-295	-302	-349	-284	-110	-32	-73	-187	-256	-653
238.37	25	-1124	-314	-325	-381	-316	-125	-3	-59	-78	-259	-672
247.90	26	-1227	-333	-354	-414	-356	-146	3	-38	49	-257	-684
257.44	27	-1321	-367	-392	-451	-414	-162	-6	8	191	-238	-672
266.97	28	-1357	-411	-440	-476	-506	-170	8	41	273	-208	-603
257.44	29	-1346	-468	-502	-487	-611	-165	32	75	324	-135	-394
266.97	30	-1370	-546	-573	-518	-727	-162	51	84	376	-46	-206
278.86	31	-1427	-576	-606	-537	-770	-173	46	83	381	-40	-210
288.40	32	-1477	-668	-705	-579	-908	-175	33	64	364	16	-21
293.17	33	-1515	-822	-856	-654	-1129	-178	16	30	381	-13	322
295.57	34	-1516	-865	-894	-675	-1178	-178	11	17	387	-21	391
293.17	35	-1511	-900	-932	-702	-1237	-173	8	0	367	-30	469
293.17	36	-1498	-960	-1022	-768	-1350	-164	2	-33	365	-62	641
293.17	37	-1519	-1030	-1213	-954	-1559	-151	24	-116	356	-170	959

*MSTR = microstrain

Appendix B - Table B.7 - Pullout #1
Raw Experimental Data
AS (axial, south) gages. See Appendix A
for gage location and orientation.

LOAD KIPS	SCAN #	ASE 1 MSTR*	ASE2 MSTR	ASE3 MSTR	ASE4 MSTR	ASE5 MSTR	ASE6 MSTR
0	1	0	0	0	0	0	0
9.54	2	-4	-5	-2	-5	-2	-12
21.48	3	-20	-11	-6	-8	-5	-12
33.37	4	-24	-19	-11	-14	-8	-24
42.91	5	-36	-29	-16	-19	-11	-32
52.44	6	-56	-38	-22	-25	-14	-36
66.74	7	-67	-48	-29	-32	-17	-44
72.28	8	-75	-56	-33	-37	-21	-48
85.81	9	-91	-65	-40	-43	-24	-56
95.35	10	-99	-73	-44	-49	-27	-60
104.88	11	-115	-83	-51	-56	-30	-67
114.42	12	-131	-95	-64	-71	-37	-79
128.72	13	-147	-111	-76	-87	-44	-87
138.25	14	-163	-129	-87	-105	-56	-107
147.79	15	-179	-146	-95	-119	-65	-131
157.32	16	-198	-164	-103	-132	-73	-155
166.86	17	-210	-183	-113	-141	-79	-175
176.39	18	-222	-200	-124	-152	-84	-187
185.93	19	-230	-216	-130	-160	-87	-198
197.82	20	-242	-237	-141	-171	-92	-210
197.82	21	-242	-240	-143	-171	-94	-210
207.35	22	-254	-259	-159	-189	-97	-222
219.30	23	-262	-275	-170	-198	-102	-242
226.42	24	-270	-289	-186	-210	-105	-246
238.37	25	-274	-316	-208	-225	-111	-238
247.90	26	-278	-325	-227	-243	-125	-210
257.44	27	-290	-330	-252	-256	-129	-191
266.97	28	-294	-333	-273	-265	-133	-191
257.44	29	-298	-324	-289	-265	-135	-183
266.97	30	-322	-327	-298	-271	-137	-163
278.86	31	-337	-341	-306	-281	-141	-167
288.40	32	-361	-354	-316	-287	-141	-159
293.17	33	-401	-379	-321	-291	-154	-131
295.57	34	-413	-384	-322	-292	-154	-127
293.17	35	-421	-392	-324	-292	-154	-123
293.17	36	-449	-408	-325	-294	-154	-107
293.17	37	-520	-449	-332	-297	-156	-83

*MSTR = microstrain

Appendix B - Table B.8 - Pullout #1
Raw Experimental Data
TC (triaxial, compression) gages. See Appendix A
for gage location and orientation.

LOAD KIPS	SCAN #	TC1 MSTR*	TC2 MSTR	TC3 MSTR	TC4 MSTR	TC5 MSTR
0	1	0	0	0	0	0
9.54	2	-4	0	-4	4	0
21.48	3	-4	-8	-8	-8	-11
33.37	4	-4	-8	-12	-16	-24
42.91	5	-4	-8	-12	-24	-40
52.44	6	-8	-16	-20	-40	-52
66.74	7	-12	-20	-28	-44	-64
72.28	8	-8	-24	-32	-48	-79
85.81	9	-16	-28	-32	-52	-103
95.35	10	-20	-36	-32	-60	-111
104.88	11	-20	-36	-48	-67	-115
114.42	12	-24	-40	-48	-83	-139
128.72	13	-28	-52	-60	-99	-159
138.25	14	-32	-56	-67	-119	-191
147.79	15	-40	-71	-83	-143	-214
157.32	16	-48	-83	-91	-159	-238
166.86	17	-52	-91	-103	-183	-270
176.39	18	-56	-103	-115	-210	-294
185.93	19	-64	-115	-123	-222	-318
197.82	20	-68	-119	-139	-250	-325
197.82	21	-64	-123	-143	-258	-329
207.35	22	-71	-143	-163	-302	-333
219.30	23	-79	-147	-163	-322	-345
226.42	24	-87	-167	-183	-349	-345
238.37	25	-91	-175	-194	-385	-341
247.90	26	-95	-191	-206	-405	-329
257.44	27	-99	-206	-226	-452	-310
266.97	28	-103	-222	-238	-488	-286
257.44	29	-99	-226	-250	-528	-250
266.97	30	-99	-234	-266	-556	-222
278.86	31	-107	-246	-278	-579	-226
288.40	32	-111	-262	-290	-623	-210
293.17	33	-119	-282	-306	-671	-206
295.57	34	-119	-282	-310	-687	-214
293.17	35	-119	-286	-318	-695	-222
293.17	36	-127	-294	-322	-714	-246
293.17	37	-131	-314	-345	-766	-345

*MSTR = microstrain

Appendix B - Table B.9 - Pullout #1
Raw Experimental Data
ET (edge tension) gages. See Appendix A
for gage location and orientation.

LOAD KIPS	SCAN #	ET1 MSTR*	ET2 MSTR	ET3 MSTR	ET4 MSTR	ET5 MSTR	ET6 MSTR
0	1	0	0	0	0	0	0
9.54	2	3	0	5	8	3	2
21.48	3	5	2	5	14	8	3
33.37	4	5	6	14	19	13	3
42.91	5	6	5	14	24	14	3
52.44	6	10	11	21	27	17	5
66.74	7	8	10	21	32	21	5
72.28	8	10	10	22	35	22	5
85.81	9	13	11	24	41	25	6
95.35	10	13	13	27	44	32	6
104.88	11	16	16	33	48	33	6
114.42	12	13	14	30	48	37	8
128.72	13	11	11	30	48	35	6
138.25	14	10	13	32	46	32	6
147.79	15	8	10	30	43	32	6
157.32	16	8	11	29	43	35	6
166.86	17	10	11	30	44	33	6
176.39	18	8	11	29	41	33	6
185.93	19	8	11	32	40	32	6
197.82	20	3	5	24	41	27	6
197.82	21	3	6	27	40	29	6
207.35	22	3	8	29	40	21	6
219.30	23	2	6	30	41	19	6
226.42	24	0	6	29	41	19	6
238.37	25	-2	3	25	40	17	6
247.90	26	3	8	30	37	19	6
257.44	27	-3	0	24	37	11	6
266.97	28	-3	0	25	37	13	6
257.44	29	-3	3	29	35	11	6
266.97	30	-8	0	25	35	11	5
278.86	31	-6	2	30	37	11	6
288.40	32	-5	0	29	37	10	5
293.17	33	-11	-5	25	41	11	5
295.57	34	-11	-2	30	43	13	6
293.17	35	-13	-6	25	44	11	6
293.17	36	-14	-8	25	46	11	5
293.17	37	19	25	46	62	14	5

*MSTR = microstrain

Appendix B - Table B.10 - Pullout #1
Raw Experimental Data
LVDT Displacements in thousandths of an inch.

LOAD KIPS	SCAN #	S VERT LVDT DISP*	N VERT LVDT DISP	NE HORIZ LVD DISP	SE HORIZ LVD DISP	W HORIZ LVDT DISP
0	1	0	0	0	0	0
9.54	2	0	-1	0	0	1
21.48	3	1	-2	0	0	1
33.37	4	3	-4	0	0	1
42.91	5	4	-5	0	0	1
52.44	6	6	-7	0	0	1
66.74	7	8	-8	0	0	1
72.28	8	8	-9	0	0	1
85.81	9	10	-11	0	0	1
95.35	10	11	-12	0	0	1
104.88	11	12	-14	0	0	1
114.42	12	13	-16	-1	0	0
128.72	13	14	-18	0	0	0
138.25	14	15	-19	0	0	-1
147.79	15	16	-21	0	0	-2
157.32	16	16	-23	-1	-1	-2
166.86	17	17	-25	-1	-1	-3
176.39	18	18	-27	-2	-2	-4
185.93	19	19	-29	-3	-3	-4
197.82	20	19	-31	-4	-4	-5
197.82	21	20	-33	-4	-4	-5
207.35	22	20	-36	-6	-5	-7
219.30	23	20	-39	-7	-6	-7
226.42	24	20	-41	-8	-7	-8
238.37	25	20	-43	-9	-8	-9
247.90	26	20	-45	-11	-9	-12
257.44	27	19	-49	-13	-11	-14
266.97	28	18	-52	-16	-15	-16
257.44	29	16	-55	-19	-17	-19
266.97	30	13	-58	-21	-20	-21
278.86	31	13	-60	-22	-21	-22
288.40	32	12	-65	-25	-24	-25
293.17	33	8	-70	-31	-28	-30
295.57	34	8	-70	-32	-29	-31
293.17	35	7	-72	-33	-30	-32
293.17	36	4	-74	-35	-32	-33
293.17	37	0	-78	-40	-36	-38

*thousandths of inches

Appendix B Table B.11. Pullout #2 Raw Experimental Data RN (North Radial) Gages.
See Appendix A for gage location and orientation.

Load*	Scan#	RN 1†	RN 2	RN 3	RN 4	RN 5	RN 6	RN 7	RN 8	RN 9	RN10
0	0	0	0	0	0	0	0	0	0	0	0
11.88	4	0	0	35	24	25	27	29	13	13	43
26.18	22	17	5	70	38	35	36	38	40	16	2
35.70	30	13	5	135	75	76	78	89	78	44	27
45.23	39	22	6	152	70	82	84	87	71	40	33
61.93	53	33	10	203	98	113	108	111	98	57	13
73.81	63	16	8	231	116	155	135	152	141	78	16
85.74	74	32	10	255	125	200	160	181	140	84	46
100.03	84	32	8	216	116	228	168	182	138	89	-20
109.56	89	35	8	217	119	252	179	198	136	100	-40
116.68	94	25	6	240	144	286	192	217	159	125	-40
123.85	100	40	8	225	132	287	186	203	132	113	-81
133.38	108	30	6	203	121	305	159	181	87	82	-165
142.90	111	40	8	241	148	395	136	160	63	106	-180
152.43	118	51	8	314	231	368	144	114	173	237	141
161.96	129	89	10	290	236	293	102	81	405	267	1996
171.48	140	171	11	295	212	220	67	79	853	309	3493
181.01	152	206	13	311	216	206	71	76	979	324	3493
190.54	163	251	14	349	216	173	67	73	1172	262	3493
200.06	174	300	16	384	230	146	67	67	1292	176	3493
209.59	179	351	19	454	260	133	75	84	1367	136	3493
214.12	200	460	24	598	338	82	71	102	1480	114	3493
228.65	235	596	33	766	409	-22	14	89	1597	95	3493
240.58	270	788	48	1100	574	-148	13	109	1733	111	3493
245.34	298	877	59	1258	663	-214	22	122	1788	127	3493
250.11	312	1021	82	1494	824	-308	33	136	1797	147	3493
254.87	368	1196	118	1860	1039	-428	79	155	1659	163	3493
257.26	390	1270	135	2004	1104	-509	79	149	1524	133	3493
257.26	439	1583	212	3087	1486	-801	212	267	1364	119	1124
254.87	442	1648	232	3201	1534	-895	211	255	1323	57	-1096
247.70	446	1811	298	3201	1802	-1077	283	309	1319	130	-3002
233.41	447	2303	1096	3201	3375	-1640	369	426	1336	171	-2233

* kips
† microstrain

Appendix B Table B.12. Pullout #2 Raw Experimental Data RS (South Radial) Gages.
See Appendix A for gage location and orientation.

Load*	Scan#	RS 1†	RS 2	RS 3	RS 4	RS 5	RS 6	RS 7	RS 8	RS 9	RS10
0	0	0	0	0	0	0	0	0	0	0	0
11.88	4	17	19	14	14	14	13	14	13	8	10
26.18	22	30	32	21	16	19	19	21	17	16	11
35.70	30	40	44	27	21	24	25	22	21	16	13
45.23	39 38	41	48	29	22	22	25	24	22	17	13
61.93	53	52	63	32	25	27	32	27	25	16	11
73.81	63	59	63	33	27	27	38	30	25	19	10
85.74	74	62	67	40	35	38	52	41	38	22	14
100.03	84	40	41	27	30	22	54	36	30	14	2
109.56	89	51	51	41	44	40	75	52	46	27	11
116.68	94	51	46	40	46	43	79	53	48	29	10
123.85	100	44	35	32	41	35	76	49	44	25	3
133.38	108	44	22	24	35	29	75	46	43	19	-8
142.90	111	52	19	24	38	35	82	49	44	22	-10
152.43	118	60	13	22	38	40	95	49	46	19	-14
161.96	129	84	24	32	46	65	130	67	57	27	-11
171.48	140	203	97	16	27	187	144	278	92	73	2
181.01	152	250	125	25	41	208	144	319	141	114	16
190.54	163	314	164	17	36	194	114	337	270	173	11
200.06	174	370	206	14	33	189	87	347	366	195	11
209.59	179	439	272	27	44	201	81	373	501	221	25
214.12	200	561	390	33	48	201	46	401	820	252	49
228.65	235	730	562	57	76	219	32	447	1243	289	70
240.58	270	939	763	62	94	197	-35	482	1545	277	92
245.34	298	1050	848	75	116	175	-61	506	1610	249	130
250.11	312	1183	925	73	125	135	-143	531	1648	182	198
254.87	368	1302	1016	68	149	54	-282	549	1600	103.1	243
257.26	390	1342	1008	68	155	17	-352	550	1534	87	228
257.26	439	1446	999	67	173	-105	-819	547	1116	174	166
254.87	442	1468	952	65	173	-124	-905	544	1016	189	120
247.70	446	1499	1194	49	163	-182	-1056	512	542	191	13
233.41	447	1472	1649	13	151	-201	-1080	466	-329	182	-412

* kips
† microstrain

Appendix B Table B.13. Pullout #2 Raw Experimental Data RV (radial) Gages. See Appendix A for gage location and orientation.

Load*	Scan#	RV 1†	RV 2	RV 3	RV 5	RV 6
0	0	0	0	0	0	0
11.88	4	14	10	10	10	11
26.18	22	22	17	14	11	16
35.70	30	22	16	14	16	14
45.23	39	19	13	10	14	10
61.93	53	27	22	14	24	14
73.81	63	22	22	13	22	13
85.74	74	24	29	21	33	22
100.03	84	-8	14	8	32	5
109.56	89	-10	24	21	43	8
116.68	94	-32	10	5	30	-14
123.85	100	-30	16	16	40	-11
133.38	108	-57	5	8	30	-30
142.90	111	-67	11	13	29	-33
152.43	118	-68	27	11	13	-56
161.96	129	-36	62	10	5	-48
171.48	140	19	62	-10	-22	-78
181.01	152	49	86	0	-14	-62
190.54	163	71	97	-16	-25	-81
200.06	174	71	106	-32	-30	-95
209.59	179	58	127	-40	-24	-98
214.12	200	-40	145	-63	-13	-119
228.65	235	-171	193	-63	10	-117
240.58	270	-574	246	-48	30	-152
245.34	298	-692	274	-2	52	-157
250.11	312	-731	290	59	76	-176
254.87	368	-836	297	162	22	-187
257.26	390	-896	295	211	-19	-188
257.26	439	-1518	324	463	-190	-195
254.87	442	-1616	339	517	-247	-190
247.70	446	-1906	379	690	-309	-190
233.41	447	-2479	422	926	-368	-187

* kips
† microstrain

Appendix B Table B.14. Pullout #2 Raw Experimental Data CE (Circumferential East) Gages. See Appendix A for gage location and orientation.

Load*	Scan#	CE 1†	CE 2	CE 3	CE 5	CE 6	CE 7	CE 8	CE 9	CE 10
0	0	0	0	0	0	0	0	0	0	0
11.88	4	-8	87	14	14	14	13	13	16	11
26.18	22	-4	20	14	21	13	8	11	16	14
35.70	30	0	44	16	24	16	14	17	21	16
45.23	39	-4	75	3	13	5	5	10	13	13
61.93	53	-4	4	3	22	10	8	14	19	19
73.81	63	-8	-48	2	24	10	11	19	24	21
85.74	74	-16	8	-8	22	6	13	21	30	29
100.03	84	-32	-20	-33	2	-13	2	14	24	25
109.56	89	-44	-4	-27	11	-2	17	30	41	41
116.68	94	-48	-44	-41	-5	-14	8	25	33	38
123.85	100	-56	-56	-49	-10	-16	10	27	40	46
133.38	108	-72	-40	-63	-16	-19	6	27	40	49
142.90	111	-83	-52	-75	-21	-22	6	29	41	56
152.43	118	-103	-99	-89	-27	-29	2	24	40	57
161.96	129	-131	-67	-94	-76	-36	-10	-4	33	52
171.48	140	-194	-75	-81	-186	-56	33	-54	33	51
181.01	152	-210	-32	-71	-187	-49	57	-54	49	65
190.54	163	-250	-52	-75	-159	-67	73	-81	43	63
200.06	174	-274	28	-73	-140	-82	94	-100	43	54
209.59	179	-301	-4	-62	-106	-86	122	-109	54	63
214.12	200	-361	-36	-62	-72	-102	140	-141	57	70
228.65	235	-420	-20	-44	-36	-86	168	-167	86	76
240.58	270	-503	40	-38	-25	-86	182	-206	116	-2
245.34	298	-551	20	-111	-8	-67	203	-198	167	-59
250.11	312	-623	143	16	-14	-36	211	-187	214	-175
254.87	368	-757	234	63	-27	21	252	-170	249	-373
257.26	390	-832	1047	84	-36	67	276	-179	240	-500
257.26	439	-1253	2494	192	-100	254	474	-423	-17	-1420
254.87	442	-1360	2506	201	-114	300	531	-487	-182	-1568
247.70	446	-1701	2522	200	-148	355	477	-706	-860	-1912
233.41	447	-2165	2399	189	-154	305	501	-1071	-2189	-2048

* kips
† microstrain

Appendix B Table B.15. Pullout #2 Raw Experimental Data CW (Circumferential West) Gages.
See Appendix A for gage location and orientation.

Load*	Scan#	CW 1†	CW 2	CW 3	CW 4	CW 5	CW 6	CW 7	CW 8	CW 9	CW 10
0	0	0	0	0	0	0	0	0	0	0	0
11.88	4	-513	0	-2	-2	5	5	2	5	0	5
26.18	22	-277	11	13	8	11	14	5	10	16	8
35.70	30	-434	2	0	5	8	8	5	3	8	2
45.23	39	-25	-3	-3	3	6	8	5	6	11	10
61.93	53	-106	3	8	10	13	16	10	14	19	14
73.81	63	-173	-10	-2	2	0	6	10	0	11	3
85.74	74	-228	-13	-8	-13	2	8	6	11	21	22
100.03	84	190	-36	-24	-25	-19	-11	0	-2	17	17
109.56	89	-371	-40	-25	-36	-19	-13	-3	2	25	24
116.68	94	-49	-62	-46	-46	-36	-30	-6	-13	11	13
123.85	100	-52	-56	-33	-50	-28	-19	-6	1.5	30	33
133.38	108	-67	-84	-57	-63	-51	-43	-10	-14	17	17
142.90	111	-181	-100	-65	-75	-56	-46	-13	-13	22	16
152.43	118	-140	-114	-76	-84	-65	-51	-17	-17	19	10
161.96	129	-409	-130	-87	-103	-78	-60	-29	-10	24	16
171.48	140	127	-146	-67	-94	-111	-41	-62	-32	11	-5
181.01	152	-219	-133	-56	-90	-97	-25	-65	-21	21	10
190.54	163	-29	-140	-65	-102	-89	-30	-78	-29	13	16
200.06	174	132	-133	-65	-109	-76	-32	-84	-35	8	16
209.59	179	-235	-132	-70	-125	-62	-32	-92	-33	6	16
214.12	200	-22	-130	-78	-163	-44	-22	-103	-25	10	25
228.65	235	-428	-108	-78	-209	-27	0	-113	6	25	44
240.58	270	-5	-87	-103	-292	-21	2	-131	38	24	51
245.34	298	-406	-62	-94	-328	-13	6	-138	46	11	49
250.11	312	-158	-22	-63	-418	10	11	-136	68	-33	50
254.87	368	-60	35	-29	-602	41	-6	-122	76	-149	89
257.26	390	-128	59	-22	-707	52	-25	-114	74	-199	107
257.26	439	-676	363	82	-1199	151	-68	-17	86	-323	210
254.87	442	-720	458	106	-1299	181	-66	-78	128	-293	250
247.70	446	-1193	793	163	-1596	285	-78	-106	241	-262	382
233.41	447	-2695	1753	178	-1862	392	-65	-17	603	-288	485

* kips
† microstrain

Appendix B Table B.16. Pullout #2 Raw Experimental Data ANE (axial, northeast) Gages.
See Appendix A for gage location and orientation.

Load*	Scan#	ANE 1†	ANE 2	ANE 3	ANE 4	ANE 6	ANE 7	ANE 8	ANE 9	ANE 10	ANE 11	ANE 12	ANE 13	ANE 14
0	0	0	0	0	0	0	0	0	0	0	0	0	0	0
11.88	4	11.88	6	-164	12	-8	-8	0	2	-3	-2	-5	-8	0
26.18	22	26.18	-25	-59	-8	-24	-16	-8	-6	-10	-10	-11	-12	-4
35.70	30	35.70	-33	-226	-8	-40	-20	-12	-11	-14	-13	-14	-20	-12
45.23	39	45.23	-63	-8	-32	-44	-28	-16	-14	-17	-16	-19	-20	-16
61.93	53	61.93	-89	-28	-42	-59	-32	-28	-22	-25	-22	-25	-32	-19
73.81	63	73.81	-101	-307	-49	-83	-40	-28	-24	-32	-30	-30	-36	-24
85.74	74	85.74	-131	-117	-69	-103	-44	-36	-29	-40	-38	-36	-44	-28
100.03	84	100.03	-175	-149	-105	-151	-44	-44	-35	-56	-56	-46	-56	-36
109.56	89	109.56	-182	-295	-99	-170	-48	-44	-38	-63	-65	-52	-63	-44
116.68	94	116.68	-202	-345	-115	-182	-48	-44	-40	-70	-71	-57	-67	-44
123.85	100	123.85	-226	-99	-127	-198	-52	-44	-41	-78	-79	-62	-71	-44
133.38	108	133.38	-249	-351	-135	-218	-52	-32	-40	-87	-87	-71	-83	-59
142.90	111	142.90	-274	-387	-151	-218	-44	20	-6	-86	-68	-81	-83	-59
152.43	118	152.43	-305	-375	-194	-222	-40	75	-10	-49	-48	-84	-51	-75
161.96	129	161.96	-349	-416	-230	-269	-44	134	-22	-46	-52	-8	67	-83
171.48	140	171.48	-442	-143	-288	-321	-44	103	-3	-41	-48	46	151	-91
181.01	152	181.01	-465	-165	-297	-349	-52	87	2	-46	-46	51	163	-103
190.54	163	190.54	-521	-87	-326	-376	-52	71	13	-56	-35	60	190	-111
200.06	174	200.06	-567	-194	-337	-404	-52	67	17	-60	-21	71	214	-119
209.59	179	209.59	-612	-370	-339	-420	-56	56	21	-68	-8	84	234	-127
214.12	200	214.12	-735	-282	-363	-456	-56	48	30	-81	21	109	278	-139
228.65	235	228.65	-858	-182	-367	-476	-59	36	44	-95	57	122	301	-151
240.58	270	240.58	-1055	-36	-387	-516	-83	-12	60	-124	116	132	325	-159
245.34	298	245.34	-1097	-259	-375	-539	-95	-24	67	-136	152	146	329	-155
250.11	312	250.11	-1196	-59	-407	-603	-115	-36	76	-140	221	154	349	-155
254.87	368	254.87	-1166	-85	-456	-694	-119	-36	84	-124	273	57	365	-246
257.26	390	257.26	-1154	-121	-482	-742	-123	-44	86	-116	305	-8	376	-309
257.26	439	257.26	-892	-510	-573	-948	-178	-47	73	-165	382	-585	202	-622
254.87	442	254.87	-863	-426	-597	-968	-175	-36	71	-187	390	-702	162	-662
247.70	446	247.70	-674	-356	-652	-1035	-167	-12	41	-236	463	-975	-71	-769
233.41	447	233.41	35	-767	-662	-1019	-139	4	-32	-169	496	-977	-503	-793

* kips
† microstrain

Appendix B Table B.17. Pullout #2 Raw Experimental Data TC (triaxial compression) Gages. See Appendix A for gage location and orientation.

Load	Scan#	TC 1	TC 2	TC 3	TC 4
11.88	4	2	-5	-3	-3
26.18	22	2	-5	-6	-14
35.70	30	-3	-14	-13	-25
45.23	39	-3	-17	-14	-33
61.93	53	-5	-21	-19	-43
73.81	63	-22	-43	-35	-68
85.74	74	-16	-48	-40	-92
100.03	84	-32	-70	-59	-132
109.56	89	-32	-79	-67	-152
116.68	94	-48	-102	-79	-168
123.85	100	-35	-98	-76	-182
133.38	108	-57	-125	-94	-203
142.90	111	-62	-140	-100	-219
152.43	118	-70	-160	-109	-236
161.96	129	-70	-178	-117	-255
171.48	140	-71	-203	-122	-278
181.01	152	-67	-209	-124	-274
190.54	163	-73	-228	-133	-262
200.06	174	-82	-246	-140	-246
209.59	179	-89	-263	-148	-227
214.12	200	-89	-284	-154	-197
228.65	235	-75	-293	-152	-146
240.58	270	-79	-323	-163	-54
245.34	298	-82	-335	-170	2
250.11	312	-73	-336	-175	98
254.87	368	-73	-351	-184	232
257.26	390	-76	-360	-189	289
257.26	439	-84	-378	-208	588
254.87	442	-78	-371	-205	648
247.70	446	-76	-371	-205	828
233.41	447	-79	-370	-200	1072

Appendix B Table B.18. Pullout #2 Raw Experimental Data ET (edge tension) Gages. See Appendix A for gage location and orientation.

Load	Scan#	ET 1	ET 2	ET 3	ET 4	ET 5	ET 6
11.88	4	27	13	16	12	12	12
26.18	22	97	25	32	20	28	16
35.70	30	135	29	32	20	24	16
45.23	39	157	29	32	16	20	8
61.93	53	189	35	36	20	16	16
73.81	63	195	33	28	8	12	24
85.74	74	194	27	32	16	4	12
100.03	84	190	25	28	-8	-16	0
109.56	89	187	24	36	8	-12	16
116.68	94	184	21	8	-12	-32	-4
123.85	100	181	19	32	0	-24	4
133.38	108	168	19	-24	-48	-44	4
142.90	111	166	17	20	-16	-44	12
152.43	118	162	13	-16	-28	-56	-8
161.96	129	163	6	16	-16	-56	0
171.48	140	162	6	0	-39	-87	0
181.01	152	160	5	16	-28	-87	-8
190.54	163	157	0	0	-44	-111	-20
200.06	174	157	-2	-8	-59	-123	-28
209.59	179	157	-5	-12	-56	-155	-19
214.12	200	155	-5	-24	-75	-138	-40
228.65	235	154	-14	-16	-67	-119	-32
240.58	270	140	-21	-36	-87	-131	-56
245.34	298	130	-25	-36	-87	-122	-52
250.11	312	127	-24	-43	-99	-126	-67
254.87	368	127	-32	-59	-115	-142	-83
257.26	390	127	-36	-63	-122	-151	-83
257.26	439	138	-47	-91	-131	-222	-99
254.87	442	138	-50	-83	-135	-238	-99
247.70	446	144	-59	-99	-167	-297	-115
233.41	447	152	-63	-135	-198	-428	-122

Appendix B Table B.19. Pullout #2 Raw Experimental Data LVDT Displacements (averages)

Scan#	AVG KIPS	AVG VERT. LVDT	AVG HOR. LVDT
4	11.88	0	0
22	26.18	-1.0	0.3
30	35.70	-1.5	0
39	45.23	-2.0	0.3
53	61.93	-2.5	0
63	73.81	-3.0	0
74	85.74	-3.5	0
84	100.03	-5.1	0
89	109.56	-5.6	0.3
94	116.68	-6.1	0
100	123.85	-6.6	0
108	133.38	-8.1	0.3
111	142.90	-8.6	0
118	152.43	-10.1	0
129	161.96	-11.6	-0.7
140	171.48	-15.2	-2.1
152	181.01	-16.7	-3.9
163	190.54	-18.7	-5.6
174	200.06	-20.2	-7.8
179	209.59	-22.2	-9.5
200	214.12	-26.3	-12.7
235	228.65	-30.8	-16.5
270	240.58	-38.4	-23.2
298	245.34	-42.4	-26.8
312	250.11	-48.5	-32.7
368	254.87	-58.1	-40.8
390	257.26	-62.6	-44.3
439	257.26	-83.3	-62.6
442	254.87	-87.9	-66.5
446	247.70	-101.0	-78.1
447	233.41	-124.7	-98.9

NBS-114A (REV. 2-8C)

U.S. DEPT. OF COMM. BIBLIOGRAPHIC DATA SHEET (See instructions)	1. PUBLICATION OR REPORT NO. NBSIR 82-2484	2. Performing Organ. Report No.	3. Publication Date May 1982

4. TITLE AND SUBTITLE

INTERNAL STRAIN, DEFORMATION, AND FAILURE OF LARGE SCALE PULLOUT TESTS IN CONCRETE

5. AUTHOR(S)

William C. Stone

6. PERFORMING ORGANIZATION (If joint or other than NBS, see instructions)

NATIONAL BUREAU OF STANDARDS
DEPARTMENT OF COMMERCE
WASHINGTON, D.C. 20234

7. Contract/Grant No.

8. Type of Report & Period Covered

9. SPONSORING ORGANIZATION NAME AND COMPLETE ADDRESS (Street, City, State, ZIP)

10. SUPPLEMENTARY NOTES

☐ Document describes a computer program; SF-185, FIPS Software Summary, is attached.

11. ABSTRACT (A 200-word or less factual summary of most significant information. If document includes a significant bibliography or literature survey, mention it here)

A study was performed to obtain detailed experimental data on crack propagation and internal strain distribution for the pullout test. A 12:1 scaled-up pullout test was designed, using a commercial pullout insert for the prototype dimensions, and was instrumented with small waterproof embedment strain gages so as to obtain internal strain profiles at critical locations. Two large scale specimens were tested with apex angles falling at the upper and lower bounds currently recommended in ASTM C-900. Two dimensional axisymmetric finite element analyses were performed for the two experimental specimens and the results were compared with measured strains for load stages below the onset of internal cracking. The results showed good correlation between the analytical and experimentally observed strains. The experimental data indicate that internal cracking, and the formation of the failure surface, are principally governed by the tensile strength of the concrete. The failure surface appears to have formed by 65% of ultimate load. Beyond this point, it is likely that the entire load is carried by the mechanism of aggregate interlock. Ultimate failure occurs when all aggregates mechanically bridging the failure surface pullout from the retaining cement paste. It is likely that the pullout test measures the shear strength of the cement paste or mortar which binds the concrete together.

12. KEY WORDS (Six to twelve entries; alphabetical order; capitalize only proper names; and separate key words by semicolons)

Concrete; crack propagation; failure surface geometry; failure theory; finite element method; internal strain; laboratory testing; large scale models; mathematical model; pullout test; stress contours

13. AVAILABILITY

☒ Unlimited

☐ For Official Distribution. Do Not Release to NTIS

☐ Order From Superintendent of Documents, U.S. Government Printing Office, Washington, D.C. 20402.

☒ Order From National Technical Information Service (NTIS), Springfield, VA. 22161

14. NO. OF PRINTED PAGES

170

15. Price

$15.00